International Journal of Antennas and Propagation

Bioengineering Applications of Electromagnetic Wave Propagation

Lead Guest Editor: Sandra Costanzo
Guest Editors: Lulu Wang and Alvaro Rocha

Bioengineering Applications of Electromagnetic Wave Propagation

International Journal of Antennas and Propagation

Bioengineering Applications of Electromagnetic Wave Propagation

Lead Guest Editor: Sandra Costanzo
Guest Editors: Lulu Wang and Alvaro Rocha

Contents

Hindawi
International Journal of Antennas and Propagation
Volume 2020, Article ID 5780243, 6 pages
https://doi.org/10.1155/2020/5780243

Research Article

Phaseless Microwave Tomography Assessment for Breast Imaging: Preliminary Results

Sandra Costanzo [1,2,3] **and Giuseppe Lopez** [1]

[1] *DIMES, University of Calabria, 87036 Rende (CS), Italy*
[2] *ICEmB, Inter-University National Research Center on Interactions between Electromagnetic Fields and Biosystems, 16145 Genova, Italy*
[3] *CNR—Institute for Electromagnetic Sensing of the Environment (IREA), Via Diocleziano 328, 80124 Naples, Italy*

Correspondence should be addressed to Sandra Costanzo; costanzo@dimes.unical.it

Received 19 July 2019; Accepted 23 January 2020; Published 22 February 2020

Academic Editor: Ping Li

In the present work, a phaseless approach for microwave imaging applications is presented. The proposed solution strategy is based on the formulation of the scattering phenomena in terms of contrast source, while no phase-recovery stage is involved into the numerical procedure, thus providing a phaseless single-step resolution method. The image recovering potentialities of the discussed method are numerically validated by successfully distinguishing different tissues of a slice breast model, with a tumor located wherein. The above preliminary assessment encourages the adoption of the proposed solution in the framework of biomedical imaging.

1. Introduction

Recent trends in biomedical imaging have raised some concerns about the safety of the imaging apparatus, as well as about the overall system costs. Microwave tomography (MWT) can be regarded as a safe, cost-effective, noninvasive supplement to the widely adopted imaging techniques. However, limited penetration depth and relatively low resolution put some constraints on a large-scale application of MWT. A major reason to move towards the microwave spectrum is given by the possibility to identify possible pathological alterations on biological tissues according to their water content. Furthermore, the use of nonionizing radiation in MWT techniques represents one of the main advantages as compared to computed tomography (CT) and positron emission tomography (PET). In this work, according to the preliminary assessment presented in [1], a Phaseless Contrast Source Inversion (P-CSI) method is successfully implemented for breast tissue reconstruction. Specifically, starting from the contrast source (CS) formulation described in [2, 3], the inverse scattering problem is solved with no linearization procedure, but recasting it into an iterative optimization problem, where the two problems unknowns, namely, the contrast source and the dielectric contrast, are alternatively updated according to a conjugate gradient scheme. The inversion procedure is performed by exploiting the amplitude-only data of the measured total field, locally defined as the sum of the incident field and the scattered field, the former obtained as a base-line measurement in the absence of the object under test (OUT), and the latter due to the interaction of the incident field with the OUT. The full-data information of the incident field inside the imaging domain, obtained through a wave expansion starting from the base-line measurement, is also required into the reconstruction process.

2. Phaseless Inverse Scattering Formulation

Let us consider a 2D tomography problem, aiming at retrieving the shape, the location and the dielectric properties of a generic OUT, hereby denoted as B. A TM-polarized incident field is assumed, and cylindrical targets are investigated.

In the whole scenario, a magnetic permittivity equal to that of free space is assumed, such as in a typical biomedical scenario, due to the nonmagnetic properties of the biological tissues. Therefore, the electromagnetic properties are fully described uniquely by the dielectric permittivity values. A circular acquisition setup is considered, where the measurement points are displaced on the acquisition curve S, as shown in the general scheme of Figure 1. It describes a multistatic and multiview setup, where the transmitter location is alternatively changed, thus determining N_{TX} angles of incidence and resulting into a number of $N_R \cdot N_{TX}$ measurements. The imaging domain, hereby indicated as D, fully contains the unknown OUT.

The inverse scattering problem is governed by the electrical field integral equations (EFIEs), known in the literature as *data equation* and *state equation*, and obtained as solution of the Helmholtz equation applied to the aforementioned setup [4]:

$$E^s(r) = E^t(r) - E^i(r) = k_b^2 \int_D G(r, r')\chi(r')E^t(r')\mathrm{d}r', \quad r \in S, \tag{1}$$

$$E^t(r) = E^i(r) + k_b^2 \int_D G(r, r')\chi(r')E^t(r')\mathrm{d}r', \quad r \in D. \tag{2}$$

In the above expressions, E^s represents the scattered field, while E^t, E^i give the total and the incident field, respectively; G denotes the Green's function of the background medium, while parameter χ gives the contrast function, normalized with respect to the permittivity of the background medium:

$$\chi(r) = \begin{cases} \dfrac{k^2(r)}{k_b^2} - 1, & r \in B, \\ 0, & r \notin B. \end{cases} \tag{3}$$

The considered approach is mathematically arranged into a local optimization problem, wherein a proper cost function is to be defined. The solution of the scattering problem is obtained as an iterative interplay of the EFIEs expressed by equations (1) and (2), which is formulated by the following cost function:

$$F(\omega_{v,n}) := F_S(\omega_{v,n}) + F_D(\omega_{v,n}, \chi_n), \tag{4}$$

with

$$F_S(\omega_{v,n}) = \alpha_S \sum_v \left\| |f_v|^2 - \left|E_v^i + G_S\omega_v\right|^2 \right\|_S^2, \tag{5}$$

$$F_D(\omega_{v,n}, \chi_n) = \alpha_D \sum_v \left\| \chi\left[E_v^i + G_D\omega_v\right] - \omega_v \right\|_D^2. \tag{6}$$

In the above expressions, parameters $\alpha_{S\text{-}D}$ denote proper normalization factors. The expressions shown in equation (5) represent the discrepancy between the measured total field in S, indicated as f, and the relative value according to the model defined into equation (1), while equation (6) considers the error affected by equation (2). Therefore, the cost function F combines the cumulative difference between

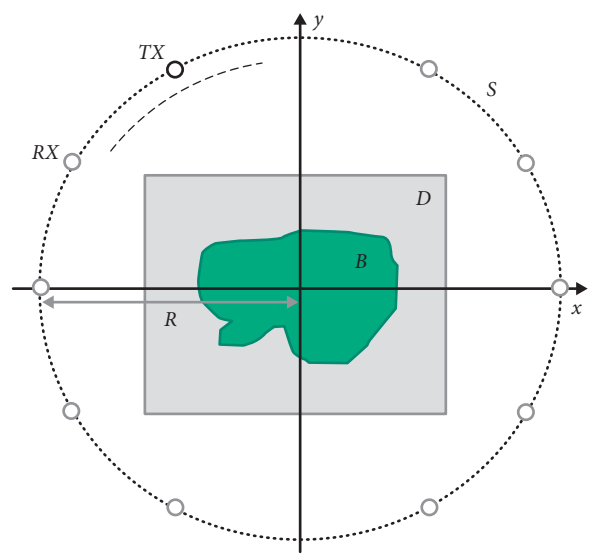

Figure 1: Acquisition setup for imaging.

the analytical data and the measured field for every illumination scenario v. The incident field in the OUT is determined starting from the incident electric field measurements performed along the acquisition curve S, by expressing the incident field as the sum of a limited number N of Hankel functions of the second kind [5, 6], so that the following relation holds true:

$$E_S^i(\rho, \theta) \cong -\frac{j}{4} \sum_{v=-N}^{N} c_v H_v^{(2)}(k_b\rho)\exp(jv\theta), \tag{7}$$

where ρ and ϑ represent the polar coordinates.

The truncation number N is determined by evaluating the variation of the Hankel function with respect to N, for a fixed parameter ρ equal to the radius R of the sampling curve, as shown in Figure 2. The computed c_v coefficients are subsequently implemented in the evaluation of the incident field inside the OUT [7–9].

The iterative process starts by updating the contrast source $\omega_{v,n}$, through the adoption of a nonlinear conjugate gradient scheme [10, 11], while the contrast function χ_n, after the evaluation of the current value of the total field at the n-th step, $E_{v,n}^t = E_v^i + G_S\omega_{v,n}$, is obtained as a minimizer of the state function, indicated as $F_D(E_{v,n}^t, \omega_{v,n})$. Since an iterative local-based optimization problem is involved, an initial guess for the contrast source $\omega_{v,0}$ occurs. Therefore, a proper initial value for the contrast source is considered, able to exploit all the available information provided by the measurement step. The initial guess is obtained by applying the steepest descent method to equation (5), thus resulting into the following expression:

$$\omega_{v,0} = -2\beta\alpha_S G_S^* \left[E_v^i\left(|f_v|^2 - \left|E_v^i\right|^2\right)\right] F_S, \tag{8}$$

where β is the step size, while the symbol $(*)$ indicates the adjoint operator. According to equation (8), all the available data are fully exploited in the initialization of the contrast

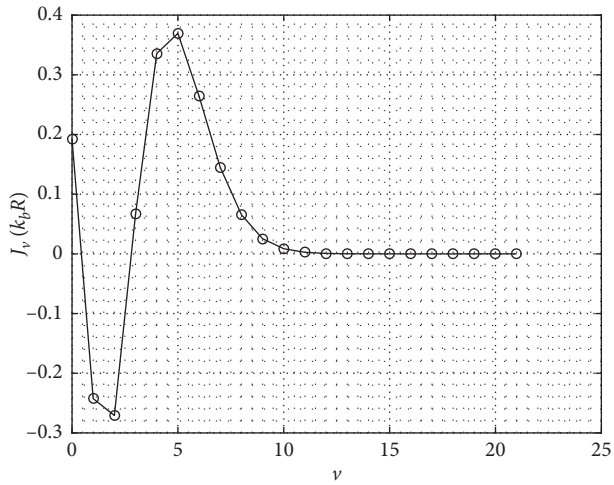

Figure 2: Bessel function behaviour versus the order ν.

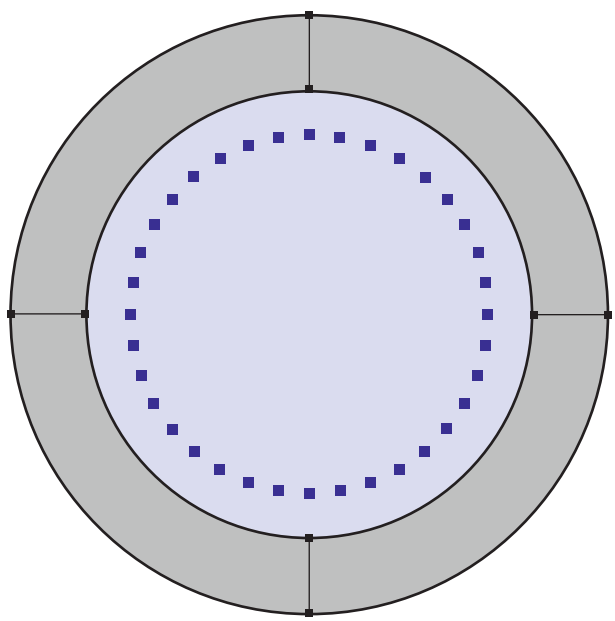

Figure 3: Acquisition setup on COMSOL : PML (grey), TX antenna positions (blue),. and matching medium (light blue).

source, with no arbitrary assumption on the unknown phase of the total field, which is instead proposed in [10, 11]. Furthermore, no a priori information about the dielectric contrast inside D is required, as compared to the approach outlined in [12].

3. Human Breast Modelling and Imaging Results

To perform a numerical validation of the proposed inverse strategy, a proper microwave imaging setup is simulated on COMSOL Multiphysics® [13], according to the proposed reconstruction method. The simulated setup is shown in Figure 3. It consists of a multistatic measurement setup, where N_{TX} point current source is uniformly arranged in a circular fashion, by surrounding the OUT. The 2-GHz operating frequency is considered, which is the most suitable one for microwave breast imaging, as it offers a considerable trade-off between spatial resolution and penetration depth into human breast tissues [14]. A perfectly matched layer (PML) surrounding the background medium is assumed as boundary condition. The forward data computation is performed by alternatively evaluating the total field and the incident field for a fixed position of the transmitting antenna. In order to speed up the simulation process, out-of-plane line currents are implemented as TM sources.

The dielectric profile of the breast is constructed similarly to the approach outlined in [14]. In particular, a simplified 3-tissue breast model is considered, whose dielectric properties are listed in Table 1. The implemented human breast model consists of a cylinder with a 45.5 mm radius, a fibroglandular region having a radius equal to

Table 1: Dielectric properties of breast tissues at 2 GHz [14, 15].

Tissue	Relative permittivity	Conductivity (S/m)
Fat	5	$5.0E-02$
Glandular/fibroconnective tissue	43	0.7
Malignant tissue	35	0.7

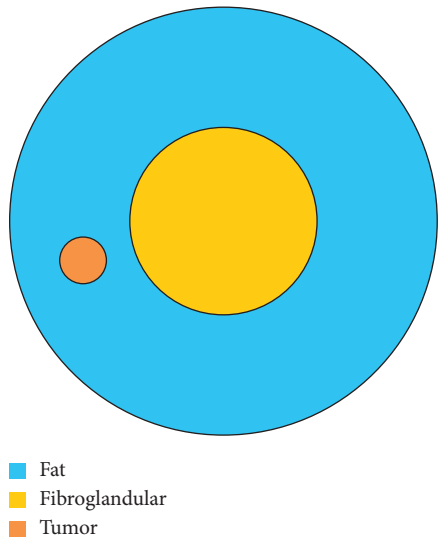

Figure 4: First scenario: tumor located inside the fat tissue.

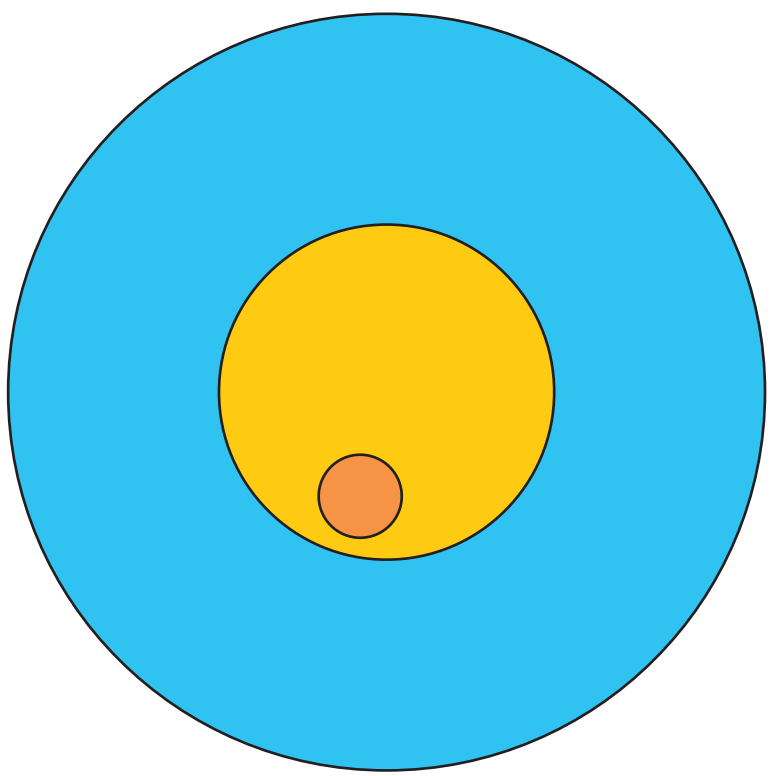

Figure 5: Second scenario: tumor located inside the fibroglandular tissue.

20 mm; the assumed tumor has a radius equal to 5 mm. The probe and the transmitter locations are placed 15 mm far from the breast, in a circular fashion. A lossless matching medium with $\varepsilon_r = 12$ is assumed.

4. Results and Discussion

Firstly, the cancerous portion is placed inside the adipose tissue (Figure 4), where a higher dielectric contrast can

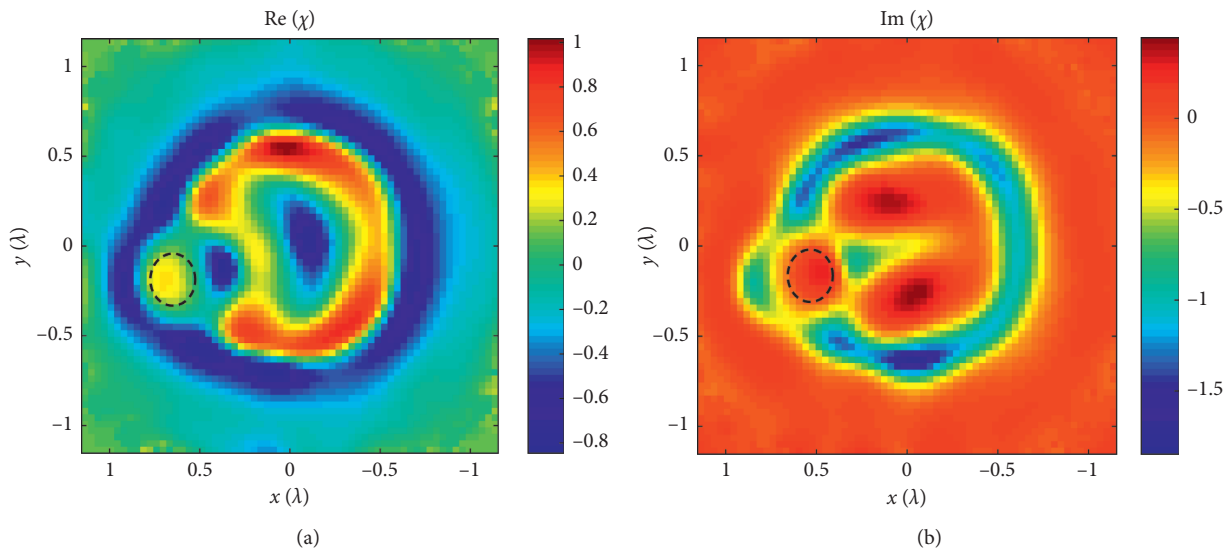

Figure 6: Real (a) and imaginary (b) part of the contrast function χ for the first scenario.

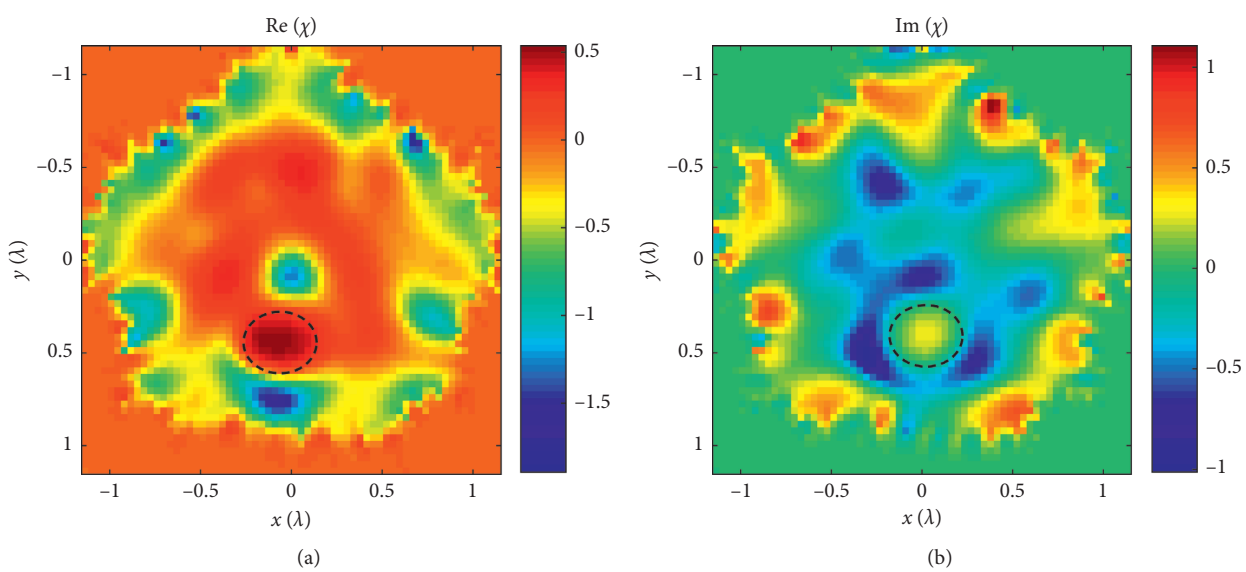

Figure 7: Real (a) and imaginary (b) part of the contrast function χ for the second scenario.

be experienced. A second case is then considered, with the tumor located inside the fibroglandular tissue (Figure 5), thus resulting into a lower dielectric contrast. As clearly shown in the contrast function map of Figures 6 and 7, for the two scenarios, the tumor is properly localized in both cases.

5. Conclusions

A single-step phaseless microwave tomography method for biomedical imaging has been proposed in this work. Firstly, the analytical formulation of the inverse scattering procedure has been discussed, by introducing a novel initialization for the algorithm. Secondly, some reconstruction results of a slice breast model have been presented, where the reconstruction capabilities of the proposed methodology have been confirmed. The discussed results represent a preliminary assessment for the use of MWT as a potential low-cost tool in the field of breast cancer detection and breast imaging applications. Further developments are currently being performed in order to achieve a quantitative reconstruction in terms of dielectric properties for the under test scenario.

Data Availability

The simulation data used to support the findings of this study are included within the article.

Conflicts of Interest

The authors declare that they have no conflicts of interest.

References

[1] S. Costanzo and G. Lopez, *Single-Step Approach to Phaseless Contrast-Source Inverse Scattering*, Springer, Cham, Switzerland, 2019.

[2] P. M. Van Den Berg and A. Abubakar, "Contrast source inversion method: state of art—abstract," *Journal of Electromagnetic Waves and Applications*, vol. 15, no. 11, pp. 1503–1505, 2001.

[3] P. M. v. d. Berg and R. E. Kleinman, "A contrast source inversion method," *Inverse Problems*, vol. 13, no. 6, pp. 1607–1620, 1997.

[4] S. Costanzo, G. Di Massa, M. Pastorino, A. Randazzo, and A. Borgia, "Non-invasive microwave characterization of dielectric scatterers," in *Microwave Materials Characterization*, InTech, London, UK, 2012.

[5] D. Colton and R. Kress, "The Helmholtz equation," in *Inverse Acoustic and Electromagnetic Scattering Theory*, pp. 13–38, Springer, Berlin, Germany, 2013.

[6] T. Tsuburaya, Z. Meng, and T. Takenaka, "Inverse scattering analysis from measurement data of total electric and magnetic fields by means of cylindrical-wave expansion," *Electronics*, vol. 8, no. 4, p. 417, 2019.

[7] E. Mallikarjun and A. Bhattacharya, "Method to calculate the incident fields in the investigation domain in the perspective of permittivity reconstruction," *IET Microwaves, Antennas & Propagation*, vol. 9, no. 3, pp. 252–263, 2015.

[8] F. Bürgel, K. S. Kazimierski, and A. Lechleiter, "A sparsity regularization and total variation based computational framework for the inverse medium problem in scattering," *Journal of Computational Physics*, vol. 339, pp. 1–30, Jun. 2017.

[9] F. Bürgel, K. S. Kazimierski, and A. Lechleiter, "IPscatt—a MATLAB Toolbox for the Inverse Medium Problem in Scattering," *ACM Transactions on Mathematical Software (TOMS)*, vol. 45, no. 4, pp. 1–20, 2017.

[10] Z. Hu, L. Lianlin, and L. Fang, "A multi-frequency MRCSI algorithm with phaseless data," *Inverse Probl*, vol. 25, no. 6, Article ID 065006, 2009.

[11] L. Li, H. Zheng, and F. Li, "Two-dimensional contrast source inversion method with phaseless data: TM case," in *IEEE Transactions on Geoscience and Remote Sensing*, vol. 47, no. 6, pp. 1719–1736, 2009.

[12] M. D'Urso, K. Belkebir, L. Crocco, T. Isernia, and A. Litman, "Phaseless imaging with experimental data: facts and challenges," *Journal of the Optical Society of America*, vol. 25, no. 1, p. 271, 2008.

[13] COMSOL AB, *"COMSOL Multiphysics®." v. 5.4*, COMSOL AB, Stockholm, Sweden, 2012, http://www.comsol.com.

[14] G. Bellizzi, O. M. Bucci, and I. Catapano, "Microwave cancer imaging exploiting magnetic nanoparticles as contrast agent," *IEEE Transactions on Biomedical Engineering*, vol. 58, no. 9, pp. 2528–2536, 2011.

[15] "Dielectric properties of body tissues," 2019, http://niremf.ifac.cnr.it/tissprop/#appl.

Hindawi
International Journal of Antennas and Propagation
Volume 2019, Article ID 5076139, 12 pages
https://doi.org/10.1155/2019/5076139

Research Article

RFID Double-Loop Tags with Novel Meandering Lines Design for Health Monitoring Application

Ibtissame Bouhassoune,[1] **Rachid Saadane**,[2] **and Khalid Minaoui**[1]

[1]*LRIT Laboratory, Faculty of Science, Mohammed V University, Rabat, Morocco*
[2]*SIRC/LaGeS-EHTP, EHTP Km 7 Route El Jadida, Oasis, Morocco*

Correspondence should be addressed to Ibtissame Bouhassoune; i.bouhassoune@gmail.com

Received 24 March 2019; Revised 16 July 2019; Accepted 25 August 2019; Published 1 October 2019

Guest Editor: Sandra Costanzo

In this paper, we propose a design of two compact and miniaturized RFID epidermal tags in the UHF band for health monitoring applications. The two conceptions of meandered double-loop antennas with *T*-match configuration, namely, a double-loop antenna with meandered line in the horizontal direction and a double-loop antenna with meandered lines in two directions, are placed at very close distance from the human body. The proposed tags are composed of bio-silicone substrate, to protect the human skin from the electromagnetic waves, and a copper conductor loaded by *T*-match configuration, to suit the complex impedance of the antenna to that of the chip. We have performed numerical simulations of these conceptions of two tags using the HFSS and CST solvers. Our results show two optimal sizes with a high communication performance, good matching features, and a large read range. We placed afterwards these two optimized tags in an elliptical environment to test their flexibility and examine their performance on different parts of the human body.

1. Introduction

One of the most striking evolutions of radiofrequency identification (RFID) is manifested in the epidermal RFID family for human health monitoring applications and indoor/outdoor tracking systems. This new RFID technology plays two roles, the first one is to identify different objects, and the second one is to sense physiological parameters of the human body (temperature, pressure, heartbeat, etc.). Therefore, the healthcare system can be highly developed and monitored in the long term.

The RFID system is composed of remote tags and interrogators or readers devices. The former has the potentiality to properly collect the energy from the readers and store the data in the microchip, while the latter transmit and receive the radio waves to communicate with tags [1] (see Figure 1).

The RFID tags can be passive without an internal power source, collecting energy from the interrogator, or semi-passive when a battery is used only to power and run the chip or other electronic components, and can be active when the tag has its own local alimentation system, which directly feeds a tag chip and the transmitting radio channel [2].

The epidermal RFID tags are placed in direct touch with human skin, and fabricated with a very thin, flexible, and biocompatible material, acting as an insulator between the conductor/electronic components and the skin. However, the cohabitation of passive tag elements with the human skin represents a complex challenge due to high losses in human tissues which strongly affect the general properties of the antenna. The electromagnetic waves emitted by the reader are either reflected or absorbed by the human tissue, and therefore, the performance of the wireless communication diminishes [3]. Most of the scientific researchers presented until now have been oriented to integrate the antenna with the lossy body, while maintaining the best characteristics of the antenna.

The epidermal RFID technology has been focused first on the near field, at 13.56 MHz (HF RFID), thanks to its insensitivity to the presence of living tissues and its

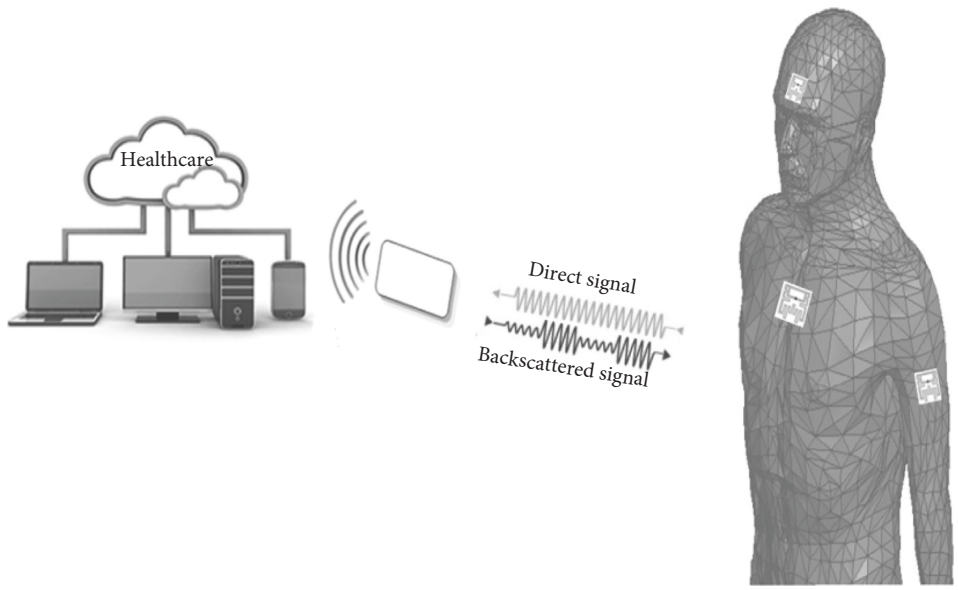

Figure 1: Concept of the RFID epidermal backscattering principle.

simplified design which consists of multiturn strip antennas attached to the chip. The basic function of this type of system is the inductive coupling which allows the readability by the reader only at small distances from the skin [4]. Thus, the feasibility of the HF standard in the wide environment, like supervising the body health in the hospital or at home, becomes limited.

Some successful works in the healthcare technology have extended the epidermal RFID systems to the UHF band (840–960 MHz). However, they are highly influenced by high dielectric objects as the human skin, but in principle, they can provide a long activation distance range. This potentiality opens additional possible sensing applications, where the patients can be monitored all the time by using the remote reader placed within environments like smart homes and hospitals [3]. Thus, the UHF RFID band is an attractive candidate than the HF band for this kind of applications, and it is therefore the subject of our study.

Various developments in the UHF RFID technology for human monitoring applications presented so far are interested to the innovative biosensor/tag with miniaturized size, reduced cost for wearable applications, like a famous slotted patch tag combined with a motion sensor, or fabricated with textile materials, which permits to decouple the antenna from the lossy human tissues [5, 6], and also double T-slotted patch designed for wristbands applications [7].

However, much less attention has been paid to the investigation and design of RFID antennas that are placed in direct contact with human skin and operated in the UHF band.

Recently considerable works on dual-loop tag placed in different body regions (stern, abdomen, limb, and head) [8] show the effects of each body regions of different volunteers on the antenna-matching features and realized gain. In ref. [9], the authors proposed a miniaturized dual-loop tag for temperature monitoring applications, with T-match configuration and tuning mechanism, to adapt its response to the specific placement over the body. This tag is used like a temporary epidermal RFID thermometer, and its read range can be significantly enhanced by adding a micro-battery [9].

In this paper, we address in detail the conception and optimization of the design and communication performances of the RFID double-loop epidermal tag for the UHF band, with a goal to reach smaller size, more flexibility, and better radiation performance.

Our paper is organized as follows. In Section 2, we present the energetic constraints of the epidermal RFID systems. Sections 3 includes (1) the design of the first proposed epidermal tag, (2) its performance characteristics and the comparison between the results obtained from the HFSS and those examined in the CST solver, in order to confirm the simulated performances of our novel proposed tag, (3) the effects of the elliptical reference model of human torso on the first proposed tag, and (4) the investigation of the placement of the proposed tag on some human body parts. Finally, (5) the miniaturization of the first proposed tag and its communication features are also discussed in this section, followed by a conclusion in Section 4.

2. Electromagnetic Equations for UHF RFID Technology

It is widely known that the passive and semi-active tags collect the energy from the reader. To setup the wireless communication between the reader and tag, first, the reader has to send an EM wave that bears the necessary energy to activate the tag. In this step, the microchip has an input impedance $Z_{\text{chip}} = R_{\text{chip}} + jX_{\text{chip}}$, where R_c is the microchip resistance and X_{chip} is the capacitive reactance.

The impedance mismatch between the antenna $Z_{\text{ANT}} = R_{\text{ANT}} + jX_{\text{ANT}}$ and the tag is described by the power transfer coefficient:

$$\tau = \frac{4R_{\text{chip}}R_{\text{ANT}}}{\left|Z_{\text{chip}} + Z_{\text{ANT}}\right|^2} \leq 1. \quad (1)$$

This accounts for the impedance mismatch between the antenna and microchip and is maximum in the case, where the microchip can use the entire power available at the tag antenna, and conjugate impedance condition is achieved, $Z_{\text{chip}} = Z^*_{\text{ANT}}$.

In the next step of the wireless communication, the activated tag receives the signal from the reader, and finally sends back the data stored in the microchip memory through a backscattered modulation of the EM wave transmitted by the reader.

Within the hypothesis of free-space interactions, the direct link power represents a power balance between the power transmitted from the reader towards the tag, and the power needed to activate the microchip, whereas the backward link power quantifies the capability of the reader to detect the tag response. These powers are given by the Friis formula and the radar equations [2]:

$$P_{R\longrightarrow T} = \left(\frac{\lambda_0}{4\pi d}\right)^2 P_{\text{in}} \cdot G_R(\theta,\phi) \cdot G_\tau(\theta,\phi) \cdot \eta(\theta,\phi),$$

$$P_{R\longleftarrow T} = \left(\frac{\lambda_0}{4\pi d}\right)^4 P_{\text{in}} G_R^2(\theta,\phi) \cdot G_T^2(\theta,\phi)\eta^2(\theta,\phi) \cdot \tau \frac{4R_A^2}{\left|Z_c + Z_A\right|^2}, \quad (2)$$

where $G_\tau(\phi,\theta) = G_T(\phi,\theta).\tau$ is the realized gain of the tag, P_{in} is the power emitted by the reader, G_R is the reader antenna gain, η and d are the polarization factor and the read range distance between the reader and tag antenna, respectively, and λ_0 is the free-space wavelength.

The realized gain $G_\tau(\phi,\theta) = G_T(\phi,\theta) \cdot \tau$ is given by the radiation gain G_T of the tag antenna reduced by the power transfer coefficient τ between the tag antenna and the microchip.

$G_\tau(\phi,\theta)$ can be expressed in terms of the minimum input power $P^{\text{to}}_{\text{in}}$, emitted by the reader, to activate the microchip P_{chip}:

$$G_\tau(\theta,\phi) = \left(\frac{4\pi d}{\lambda_0}\right)^2 \frac{P_{\text{chip}}}{G_R(\theta,\phi) \cdot \eta(\theta,\phi) \cdot P^{\text{to}}_{\text{in}}(\theta,\phi)}. \quad (3)$$

The maximum distance $d_{\max}$, at which a tag is detected by the reader, represents an important parameter of the whole communication performance and can be derived from Friis equations.

$$d_{\max}(\theta,\phi) = \frac{C}{4\pi f}\sqrt{\frac{\text{EIRP}_R}{P_{\text{chip}}}\tau G_T(\theta,\phi)}, \quad (4)$$

where $\text{EIRP}_R = G_R \cdot P_{\text{in}}$ is the equivalent isotropic radiated power emitted by the reader and fixed according to the regulations of different countries. In particular, within the 865.6–867.6 MHz Europe RFID band, the EIRP_R is fixed at 3.2 W EIRP, and within 902–928 MHz USA RFID band, the EIRP_R is fixed at 4 W [3].

The presence of the lossy body with its high permittivity and conductivity will be useful for antenna miniaturization but induces a great dissipation of the electromagnetic power, which leads to degradation of the radiation gain. Therefore, a much shorter reading range is expected for skin-mounted RFID.

3. Antennas Conception

Our proposed epidermal tag designs are based on the conception presented in [8]. However, our suggested tag layouts have a small size; contain a flexible bio-silicone substrate in the ground surface, and are fully covered by adhesive copper.

The two proposed tags form double-loop antennas with meandered strips. The first one is composed of an external, meandered radiating loop, which is curved in the horizontal direction to eliminate the nonuseful strips (Figure 2). The second one is composed of an external, fully meandered loop and is schematized in Figure 3. The meandered strip antennas of our two tags are connected to the microchip by the T-match technique to match the complex impedances of the chip and antenna [10].

The conceptions of two proposed tags were discussed and analyzed according to our electromagnetic simulations, where the geometrical parameters were performed by EM Simulators HFSS and CST software [11, 12].

Our modulations are based on the assumption that tags are placed on an estimated model of the layered anatomical phantom of human torso at 870 MHz. This model consists of stratified parallelepiped boxes with defined properties such as thickness, dielectric constant, and conductivity. We took these parameters from the database given in ref. [13] (Figure 4).

3.1. Epidermal Tag with Meandered Lines in the Horizontal Direction Design. The first tag layout contains a bio-silicone substrate (permittivity = 2.5, $\sigma = 0.005$·S/m, thickness 0.6 mm) that has the same shape of the antenna, and copper tapes forming two loops attached by the T-match structure, which is designed to connect the antenna to the microchip Zchip = 16−j148 Ω and Pchip = −15 dBm). The T-match technique also furnishes a degree of liberty to tune the desired conjugate impedance match between the antenna and the chip. The presence of the horizontal meandered line in the external loop permits an increase of the current flow, meaning that the electrical length of the antenna increases, and hence the antenna's radiation performance presents a good immunity of the tag to the human body. As it is known, this later represents a very lossy object that strongly degrades the radiation pattern and efficiency of the antenna. The design and geometrical parameters of the proposed antenna are presented, respectively, in Figure 2 and Table 1.

3.2. Matching Features and Radiation Performances of the First Proposed Tag. The return loss of this antenna was calculated based on the power reflection coefficient which considers the impedance of the microchip Z_c and the antenna's conjugate impedance Z^*_{ANT} is as shown in the following equation [14]:

$$\left|S^2\right| = \left|\frac{Z_{\text{chip}} - Z^*_A}{Z_c - Z_A}\right|^2. \quad (5)$$

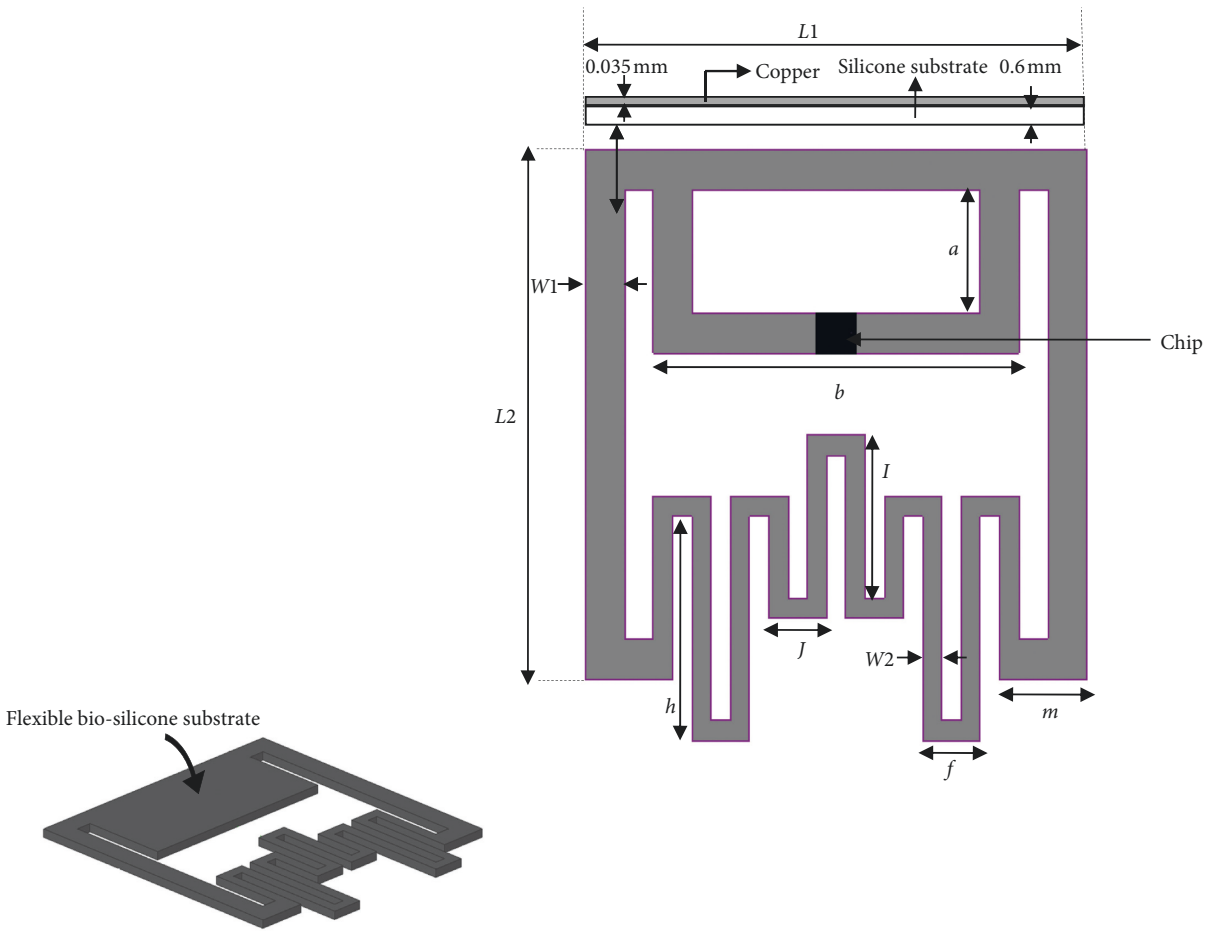

Figure 2: Geometrical design of dual loop tag with meandered line in the horizontal direction.

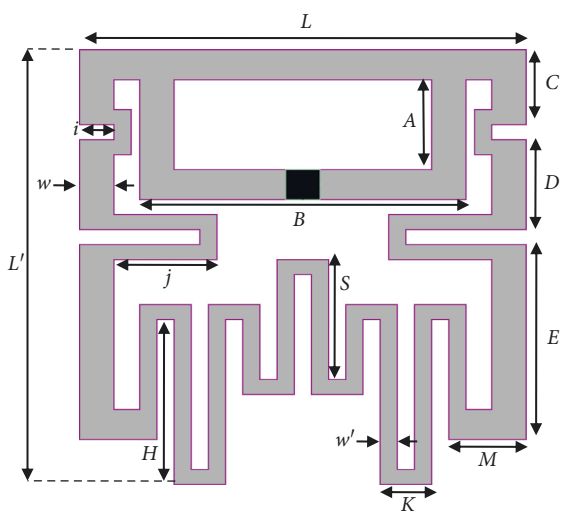

Figure 3: Geometrical layout of epidermal dual-loop tag with meandered lines in two directions.

Figure 5(a) shows the $S11$ plot against frequency of the first proposed tag antenna when it is placed on the human torso phantom.

The maximum simulated $S11$ of this tag has a value of −56.26 dB at the resonance frequency of 920 MHz.

The input impedance of the first proposed antenna is plotted in Figure 5(b). We can notice from the graph that the input impedance of the antenna, at the resonance frequency 920 MHz, is $Z_{\text{in}} = 16.5 + j148\,\Omega$. However, the input resistance of the antenna on the human torso is little higher

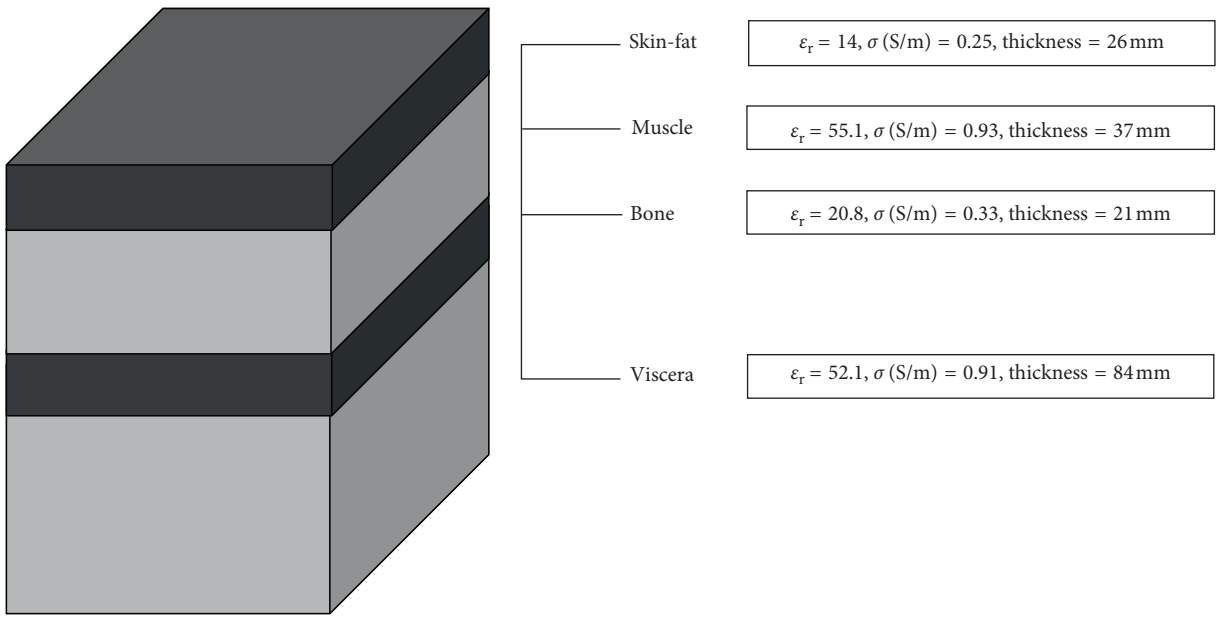

Figure 4: Geometrical and electrical parameters of the layered anatomical phantom of human torso at 870 MHz.

Table 1: Optimal dimensions of the first proposed epidermal RFID antenna.

Geometrical parameters	Dimensions (mm)
$L1 = L2$	26
A	6
B	19
M	4.5
F	3
I	9
J	3
H	12
$W1$	2
$W2$	1

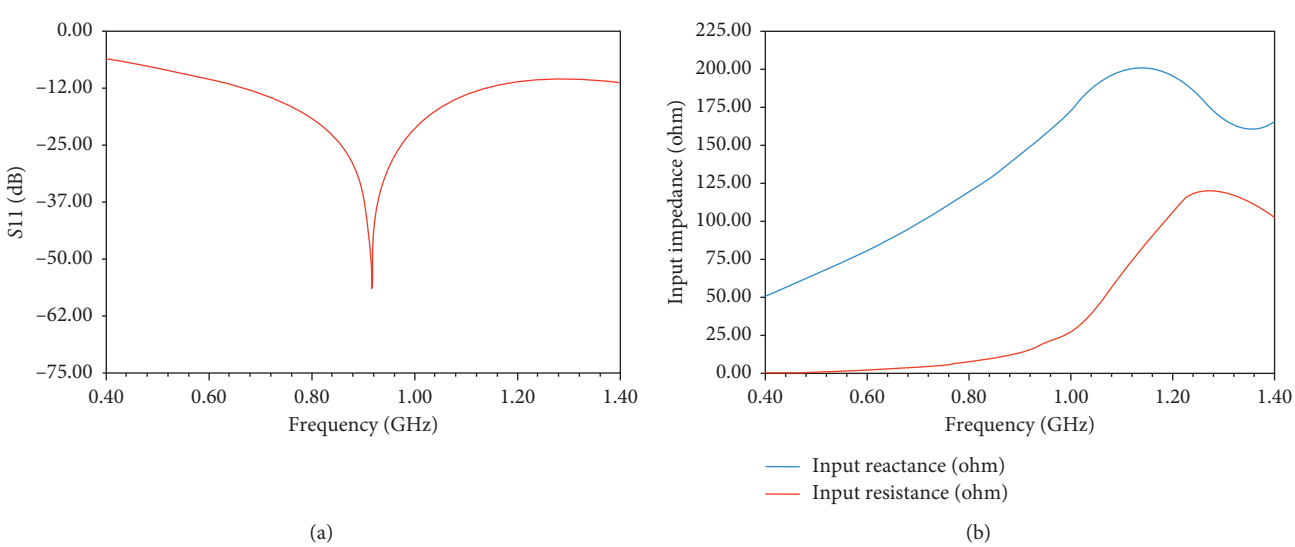

Figure 5: Simulated reflection coefficient S_{11} (a) and antenna input impedance (b) of the first proposed epidermal tag attached to the human torso model.

(about 16.50 Ω) than the resistance of the tag chip (16 Ω). The antenna input reactance is well conjugated to the tag chip reactance ($-j148\,\Omega$) around 920 MHz.

The realized gain simulation versus frequency, depicted in Figure 6, is obtained using a soft HFSS to simulate the performance of antenna radiation. In this case, the microchip was modeled by introducing the lumped port that simulates the behavior of the chip (with its complex impedance feed) [15]. The maximum value of the realized gain is −10.54 dBi, obtained around 960 MHz.

The 2 D radiation pattern of the first tag antenna attached to the planar torso model is presented in Figure 7. One can notice, from this figure, that the antenna represents a good omnidirectional radiation patterns in the two planes. Since the human tissues obviously absorb some of the received electromagnetic radiation, in our case, the peak gain is also reduced due to the effects of the human torso (−9.59 dBi around 960 MHz). In Figure 8, the simulated data refer to the estimated read range between tag and reader. When our first proposed tag was stacked onto the human body, the maximum read distance is almost 2.34 m in the case of the reader with circular polarization ($\boldsymbol{\eta}_{\mathbf{p}} = 0.5$), and it becomes above 4.68 m in the case of the reader with linear polarization ($\boldsymbol{\eta}_{\mathbf{p}} = 1$).

To verify the HFSS simulation results of our antenna characteristics, such as the S_{11} and the realized gain, we have used, for a comparison, another simulator (CST simulator) to design and simulate our first proposed antenna. The curves of S_{11} and the realized gain obtained from the CST and HFSS solvers are shown, respectively, in Figures 9(a) and 9(b). Nearly similar matching features and radiation performance are obtained from the two solvers. The slight differences between the results of the two simulators can be attributed to the difference between the numerical codes of each simulator and the mesh used during the simulation.

3.3. Deformation Effects on the First Proposed Tag Antenna. In order to take into account the effect of deformation, that also may happen to different parts of the human skin, we placed our epidermal tag on a layered elliptical model, of the human torso, taken from the database of ref. [16] (see Figure 10). This model helps us to see what happens to the antenna performance, compared to the previous planar model, when the effect of the curved meandered loop surface is taken into consideration.

Figure 11 shows $S11$ of our antenna by assuming two models of the human torso as described above: the planar (no simulated bending) and the elliptical layered model. We found that $S11$ in the antenna-bending format (elliptical model) at the resonance frequency ($S_{11} = -46$ dB) is slightly different from the one in the planar model ($S_{11} = -56$ dB). This effect can also be clearly seen in Figure 12 where a slight difference, in the input resistance between the elliptical and the planar form of the antenna, is noticed around the resonance frequency of 920 MHz.

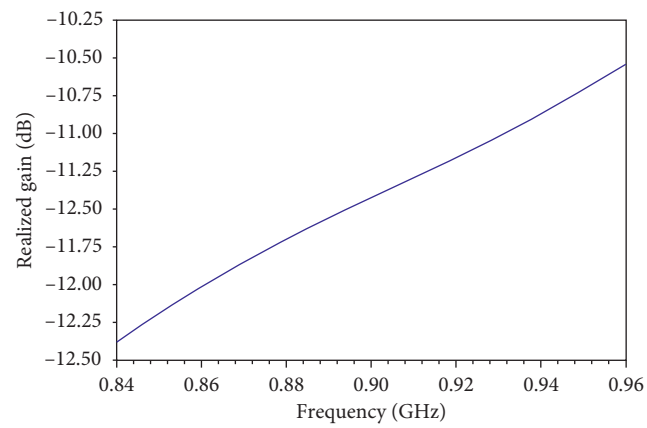

Figure 6: Simulated realized gain versus frequency of the first proposed epidermal tag over the human body reference model.

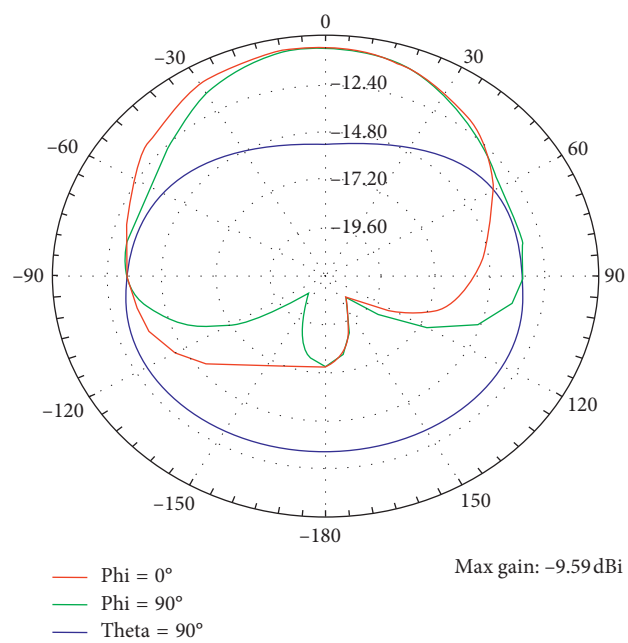

Figure 7: Radiation pattern (gain-total) in 2 D of the proposed epidermal tag over the human body reference model.

3.4. Simulated Performances of the First Proposed Antenna against Human Body Parts. In the following, we examine the properties of the first tag when it is bound to different parts of the body. Table 2 shows reference tissue thicknesses of some human body parts in the undistorted planar model. Figures 13(a) and 13(b) show, respectively, the simulated $S11$ and gain of our epidermal tag placed on four parts of the human body. The latter represents two regions according to the thickness of the fat tissue, i.e., the first region is characterized by small thicknesses (wrist and chest) while the second one has large thicknesses (abdomen and limb). We remark a decrease of $S11$ in the case when the tag is placed on the chest and wrist part. Moreover, we note that for the abdomen and the limb, the gain reaches higher values because of the high contents of fat tissue in the abdomen and limb compared to the chest and the wrist.

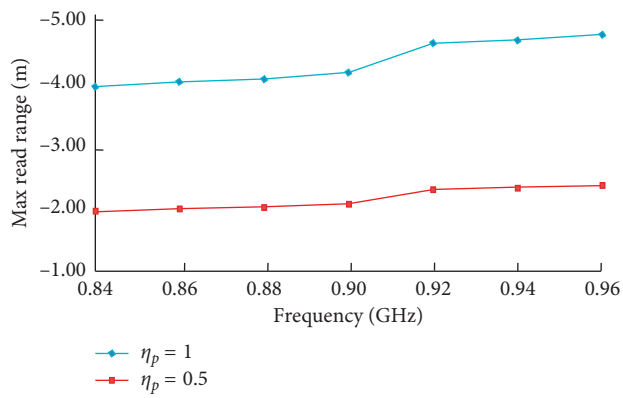

Figure 8: Read range of the epidermal RFID double-loop tag with meandered line in the horizontal direction.

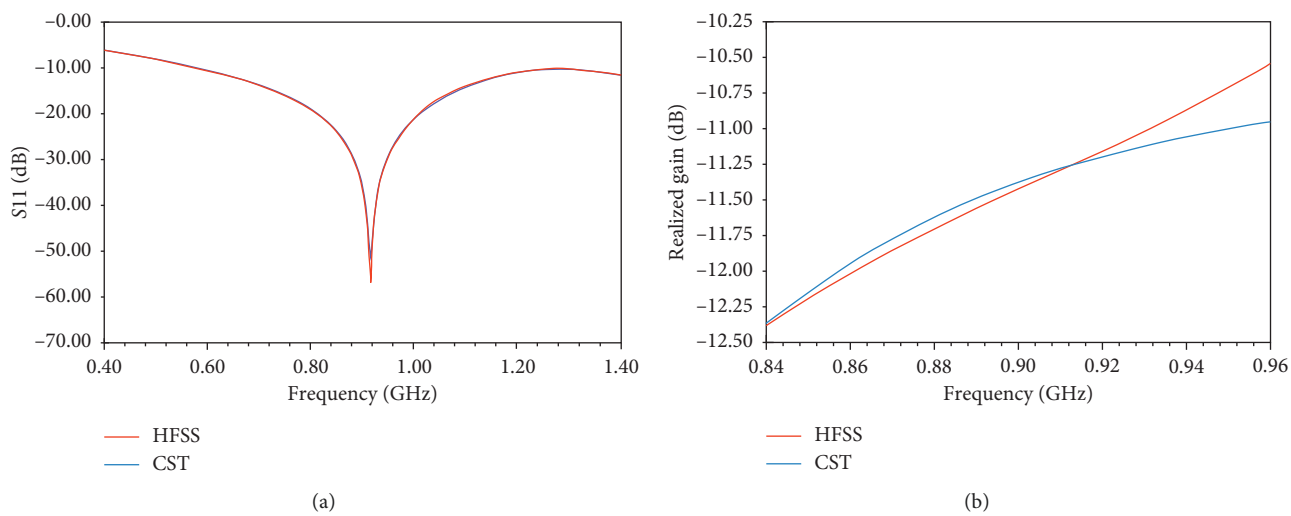

Figure 9: Comparison of the $S11$ results (a) and realized gain (b) of the first proposed antenna between the two simulators HFSS and CST.

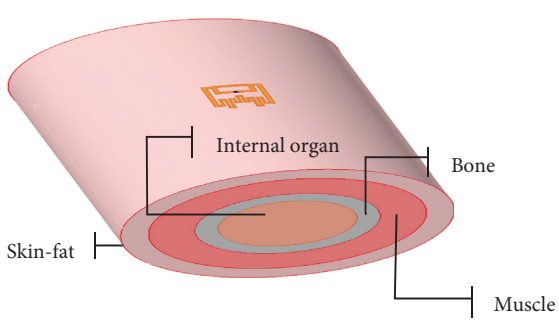

Figure 10: The first proposed tag placed on the layered elliptical model of the human torso: skin-fat axes, $335 \times 168\,\text{mm}^2$; muscle ellipse axes, $310 \times 142\,\text{mm}^2$; bone ellipse axes, $284 \times 105\,\text{mm}^2$; internal organ, $272 \times 84\,\text{mm}^2$ at 870 MHz.

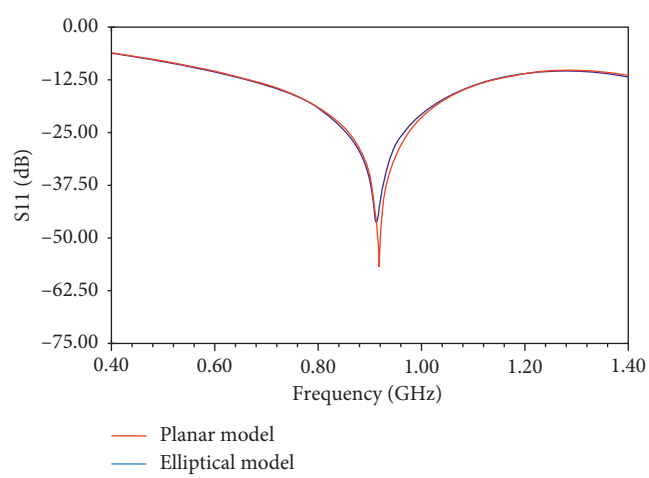

Figure 11: Simulated $S11$ of the first proposed tag on the layered elliptical model and planar model.

3.5. Epidermal Tag with Meandered Lines in the Two Directions Design. Figure 3 shows our second proposed tag whose shape is derived from the first tag addressed above, after miniaturization of the external loop, by adding meandered lines, not only in the horizontal direction but also in the vertical direction. The internal loop was connected to the chip by a T-match impedance transformer, and the chip has an input impedance $Z_{\text{in}} = 23.3 - j145\,\Omega$ and a power sensitivity (Pc = −4.5 dbmw). This tag is stuck over the human skin by a

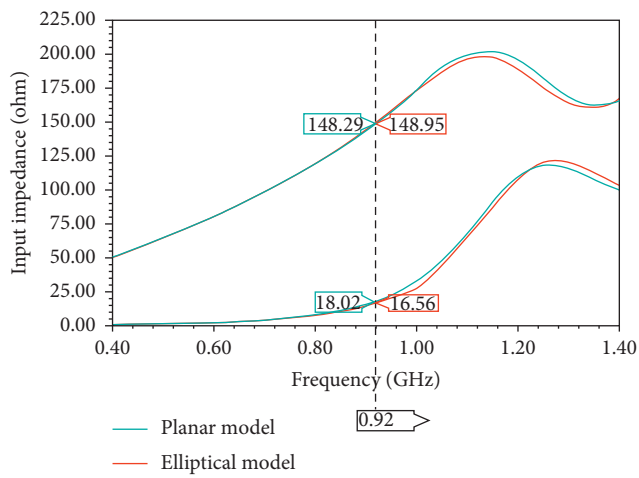

Figure 12: Simulated input resistance and reactance of the first proposed tag antenna on the layered elliptical model and planar model.

Table 2: Thicknesses of different tissues for some human body parts in the planar model.

Tissue thickness (mm)	Abdomen	Limb	Chest	Wrist
Skin	2	2.5	3	2
Fat	10	8	3	2
Muscle	20	25	20	24
Bone			11	10

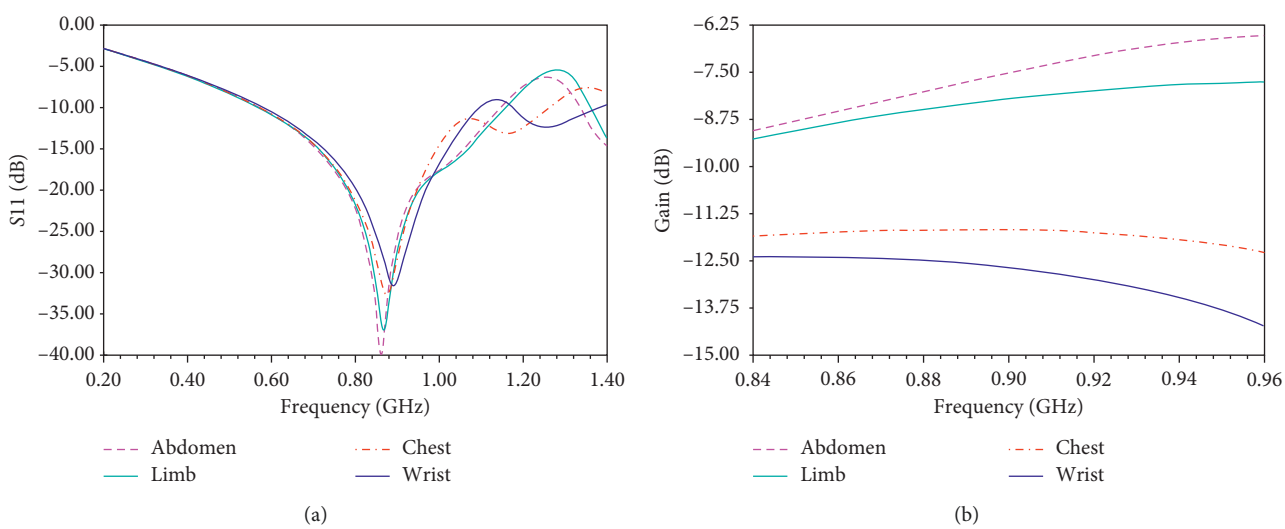

Figure 13: Simulated $S11$ (a) and gain (b) of the first epidermal tag placed on some human body parts (abdomen, limb, chest, and wrist).

sub-millimeter bio-silicone rectangular layer ($L = 26$ mm, L' = 29 mm and thickness = 0.6 mm) and is designed by numerical simulations using the finite element method implemented in the HFSS solver. As in the previous simulation, we consider the same human body reference model. The antenna geometrical parameters are tabulated in Table 3.

Figure 14(a) shows the reflection coefficient S_{11} of the epidermal double-loop tag with meandered lines in two directions. The peak $S11$ is now −46.35 dB at resonance frequency 900 Mhz. Figure 14(b) shows the input impedance plots of the second proposed antenna. The simulated resistance for the antenna in the UHF RFID frequency range maintains a value close to 23.3 ohms. The input reactance of the second antenna, as shown in Figure 14(b), maintains a positive value with a linear variation with frequency that equivalently cancels the effect of the capacitance of the chip. Therefore, the input impedance value of the antenna is almost matched with that of the tag chip around 900 MHz.

We note, from Figure 15, that the maximum realized gain of the second proposed tag is −10.80 dBi, at around 960 MHz. This value is lower than that of our previous tag, but it still maintains a good realized gain compared to other epidermal tags presented in the literature [8].

Figure 16 presents the 2 D radiation pattern of our second antenna which has similar omnidirectional radiation patterns as the first one, and as described above, the human

Table 3: Dimensions of the second proposed epidermal antenna.

Parameter	Dimension (mm)
L	26
L'	29
A	6
B	19
C	5
D	6
E	13
M	4.5
K	3
S	8
H	11
I	2
J	6
W	2
W'	1

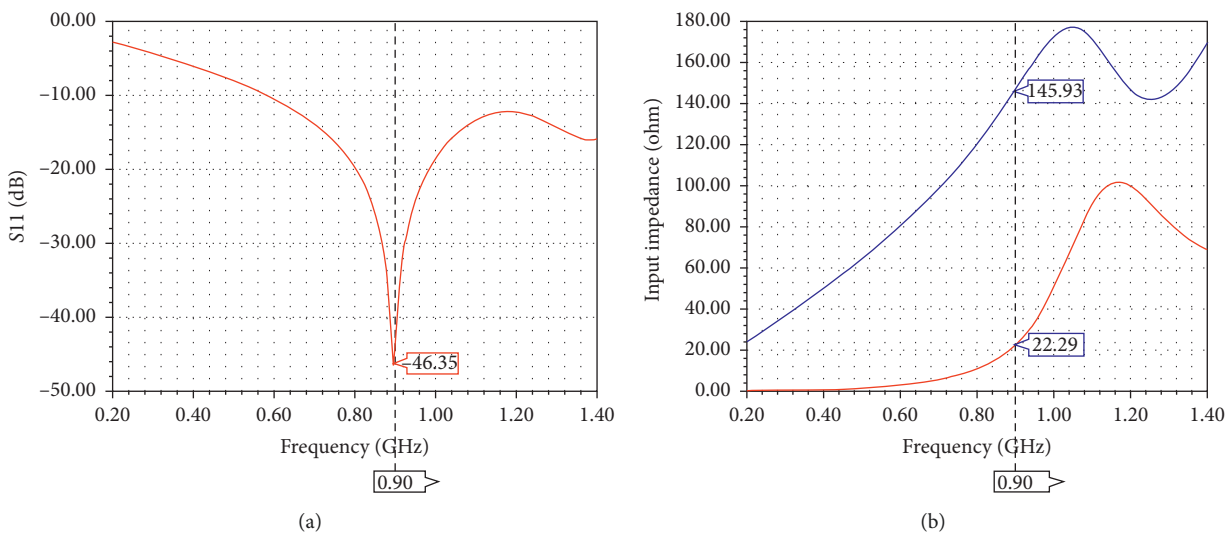

Figure 14: Simulated *S*11 (a) and antenna input impedance (b) of the epidermal double-loop tag with meandered lines in two directions.

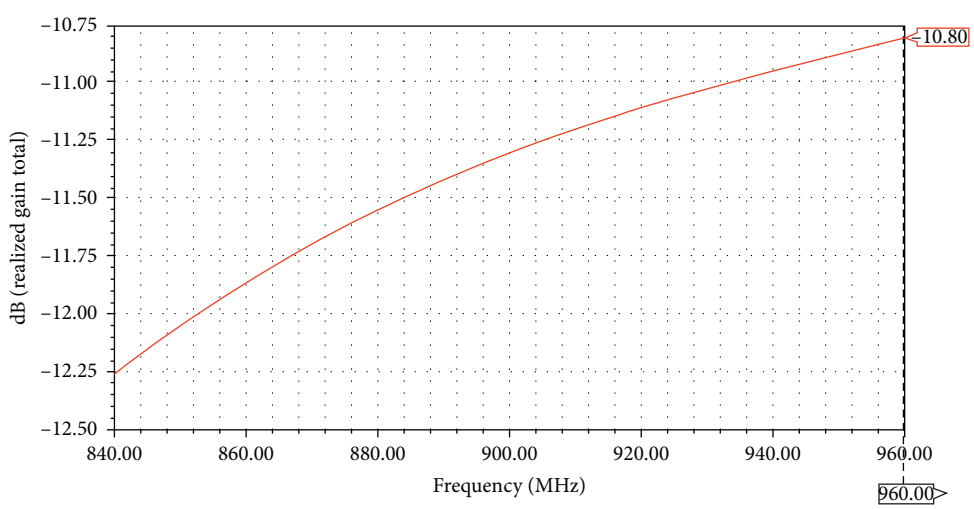

Figure 15: Simulated realized gain of the epidermal double-loop tag with meandered lines in two directions.

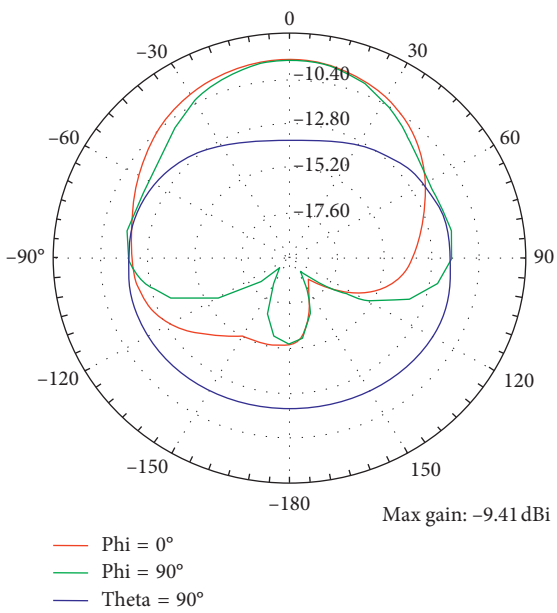

Figure 16: Radiation pattern (total gain) of the epidermal tag with meandered lines in two directions.

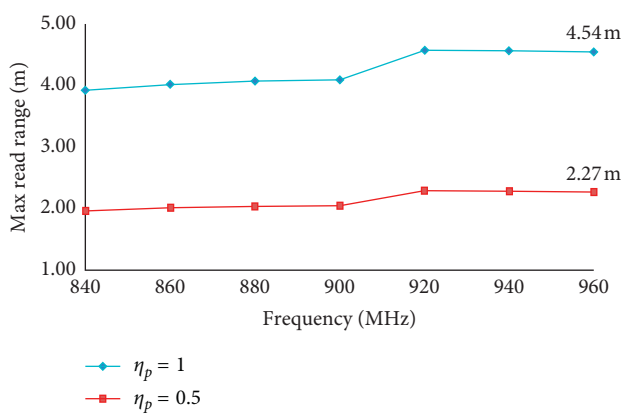

Figure 17: Simulated read range of the epidermal RFID double-loop tag with meandered lines in two directions for readers with circular (red line) and linear (blue line) polarizations.

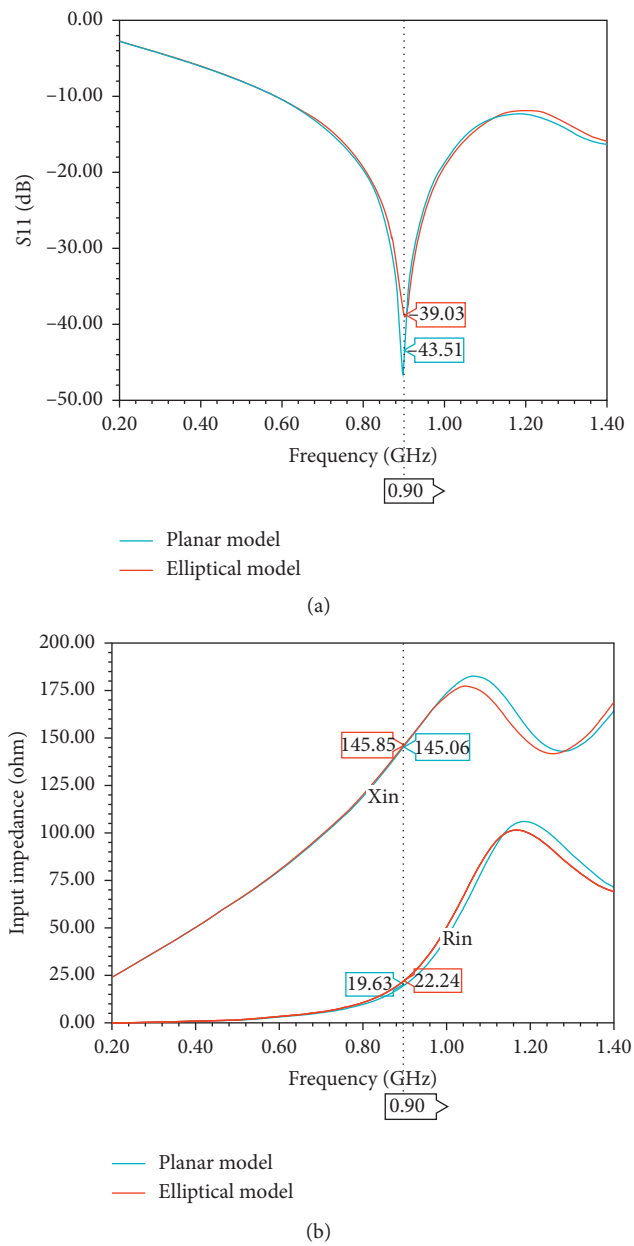

Figure 18: Simulated $S11$ (a) and antenna input impedance (b) of the second tag placed on layered elliptical and planar models.

tissues absorb some of the electromagnetic radiations. Therefore, accounting these losses in the human tissues, the total gain of the epidermal tag reaches −9.41 dBi in the (xy) plane at the resonance frequency of 960 MHz.

In Figure 17, the estimated reading range of the second epidermal tag is plotted versus the frequency, when the tag is placed directly on the reference model of human body. The maximum reading distance is almost 2.27 m in the case of the reader with circular polarization ($\eta p = 0.5$) and above 4.5 m in the case of the reader with linear polarization ($\eta p = 1$).

3.6. The Bending Effect on the Epidermal Tag with Meandered Lines in the Two Directions Design. Figure 18(a) shows simulated $S11$ of our second antenna by supposing, as above, the two reference models of the human torso: the planar and the elliptical model. $S11$, around the resonant frequency 900 MHz, of the second proposed antenna-bending format (−39 dB) is less than the one of the planar model (−43 dB). Figure 18(b) presents the input impedance of the second proposed antenna placed on the planar and elliptical model, and the elliptical model will slightly affect the impedance matching of the second proposed antenna which can be clearly described in this figure, showing a slightly change in the input resistance value at around 900 MHz, while its input reactance remains unchanged.

To confirm our results obtained by the HFSS solver, we proceeded by designing the same antenna in the CST

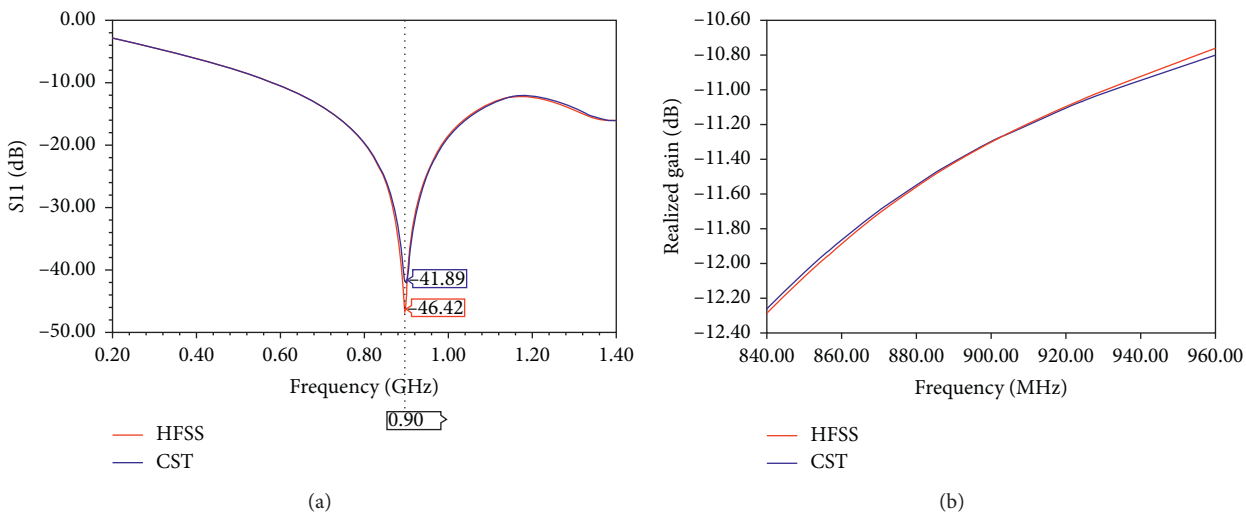

Figure 19: Comparison of $S11$ (a) and realized gain (b) results of the second antenna performed with the Ansoft HFSS and CST software.

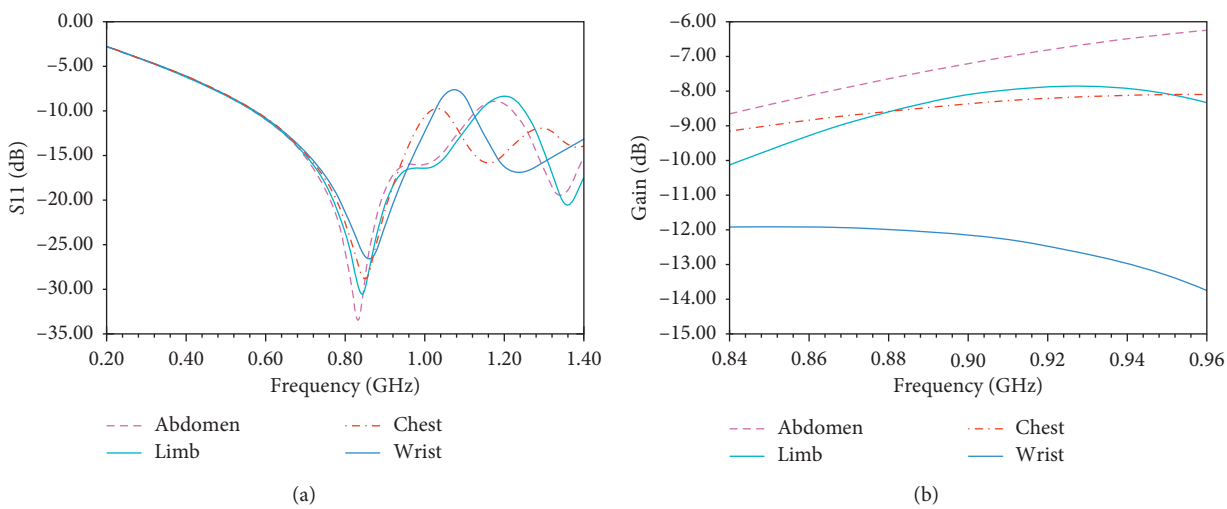

Figure 20: Simulated $S11$ (a) and gain (b) of the second epidermal proposed tag placed onto four reference layers models of some body parts.

simulator and performing the simulation of antenna properties. Figures 19(a) and 19(b) show a comparison between results of these two solvers. Similarly, $S11$ and realized gain values versus the frequency are obtained for both solvers. This indicates that using either HFSS or CST solvers converge to similar matching features and radiation performance.

3.7. Simulated Performances of the Second Proposed Antenna versus Human Body Parts. We have tested the matching characteristics and the gain of the second antenna by supposing, as above, different parts of the human body (limb, abdomen, chest, and wrist). Figure 20(a) shows a decrease of the simulated $S11$ of the second antenna around the resonance frequency, when it is placed in the limb and abdomen. This behavior is reflected in the total gain depicted in Figure 20(b) as a function of the frequency, where a difference is noticed between the human parts, the wrist, abdomen, chest, and limb. As stated above, this can be related to the larger fat tissue thickness of the abdomen, limb, and chest compared to the one of the wrist. Therefore, better total gains are obtained in the case of the abdomen and limb region.

4. Conclusion

The two proposed antennas configurations seem to be attractive to achieve miniaturized size and effective conjugate impedance to the microchip. Our simulations have demonstrated that the double-loop with meandered lines of epidermal UHF RFID tags insulated from the human skin by a flexible bio-silicone layer, provide a good realized gain. The wide bandwidths of the two antennas are enough to cover the worldwide UHF band. In addition, these two designed tags can be activated from a distance of almost 2.5 m up to 5 m depending on the position between the reader and the tag. We have verified and confirmed simulated features of

our designed tags obtained by the HFSS solver by using the CST simulator, especially in the case when the tag is bound to a rectangular anatomical human body shape. We have shown that these two particular structures are not much influenced by the detuning and absorbing effects on the human body.

Data Availability

We used in our work theoretical simulations with simulators; the data used to support the findings of this study are included within the article.

Conflicts of Interest

The authors declare that they have no conflicts of interest.

Acknowledgments

This work was supported by the Computer and Telecommunications Research Laboratory (LRIT), Associated Unit to CNRST (URAC29), Rabat IT Center, Faculty of Science, Mohammed V University, Rabat, and LaGeS, EHTP, Morocco.

References

[1] K. Finkenzeller, *RFID Handbook*, Wiley, Hoboken, NJ, USA, 3rd Edition, 2010.

[2] D. Dobkin, *The RF in RFID*, Elsevier, Burlington, MA, USA, 2007.

[3] G. Marrocco, "RFID antennas for the UHF remote monitoring of human subjects," *IEEE Transactions on Antennas and Propagation*, vol. 55, no. 6, pp. 1862–1870, 2007.

[4] J. Kim, A. Banks, H. Cheng et al., "Epidermal electronics with advanced capabilities in near-field communication," *Small*, vol. 11, no. 8, pp. 906–912, 2015.

[5] C. Occhiuzzi, S. Cippitelli, and G. Marrocco, "Modeling, design and experimentation of wearable RFID sensor tag," *IEEE Transactions on Antennas and Propagation*, vol. 58, no. 8, pp. 2490–2498, 2010.

[6] S. Manzari, C. Occhiuzzi, and G. Marrocco, "Feasibility of body-centric systems using passive textile RFID tags," *IEEE Antennas and Propagation Magazine*, vol. 54, no. 4, pp. 49–62, 2012.

[7] G.-L. Huang, C.-Y.-D. Sim, S.-Y. Liang, W.-S. Liao, and T. Yuan, "Low-profile flexible UHF RFID tag design for wristbands applications," *International Journal of Antennas and Propagation*, vol. 2018, p. 13, 2018.

[8] S. Amendola, S. Milici, and G. Marrocco, "Performance of epidermal RFID dual-loop tag and on-skin retuning," *IEEE Transactions on Antennas and Propagation*, vol. 63, no. 8, pp. 3672–3680, 2015.

[9] S. Amendola, G. Bovesecchi, A. Palombi, P. Coppa, and G. Marrocco, "Design, calibration and experimentation of an epidermal RFID sensor for remote temperature monitoring," *IEEE Sensors Journal*, vol. 16, no. 19, pp. 7250–7257, 2016.

[10] G. Marrocco, "The art of UHF RFID antenna design: impedance-matching and size-reduction techniques," *IEEE Antennas and Propagation Magazine*, vol. 50, no. 1, pp. 66–79, 2008.

[11] ANSYS HFSS 17.1, "EM simulation software," 2016, https://www.ansys.com/products.

[12] CST STUDIO SUITE 2016, "EM simulation software," 2016, https://www.cst.com/products.

[13] http://niremf.ifac.cnr.it/tissprop/.

[14] P. V. Nikitin, K. V. S. Rao, S. F. Lam, V. Pillai, R. Martinez, and H. Heinrich, "Power reflection coefficient analysis for complex impedances in RFID tag design," *IEEE Transactions on Microwave Theory and Techniques*, vol. 53, no. 9, pp. 2715–2721, 2005.

[15] L. Yang, A. Rida, and M. M. Tentzeris, "Design and development of radio frequency identification (RFID) and RFID-enabled sensors on flexible low cost substrates," *Synthesis Lectures on RF/Microwaves*, vol. 1, no. 1, pp. 1–89, 2009.

[16] C. Gabriel, S. Gabriel, and E. Corthout, "The dielectric properties of biological tissues: I. Literature survey," *Physics in Medicine and Biology*, vol. 41, no. 11, pp. 2231–2249, 1996.

Hindawi
International Journal of Antennas and Propagation
Volume 2019, Article ID 5459391, 7 pages
https://doi.org/10.1155/2019/5459391

Research Article

Anatomically and Dielectrically Realistic 2.5D 5-Layer Reconfigurable Head Phantom for Testing Microwave Stroke Detection and Classification

Tomas Pokorny,[1] **David Vrba**,[1] **Jan Tesarik**,[1] **Dario B. Rodrigues**,[2] **and Jan Vrba**[1]

[1]*Department of Biomedical Technology, Faculty of Biomedical Engineering, Czech Technical University in Prague, Prague, Czech Republic*
[2]*Department of Radiation Oncology, University of Maryland School of Medicine, Baltimore, MD, USA*

Correspondence should be addressed to Tomas Pokorny; tomas.pokorny@fbmi.cvut.cz

Received 19 October 2018; Accepted 17 July 2019; Published 25 August 2019

Guest Editor: Alvaro Rocha

This work presents the design and manufacturing of an anatomically and dielectrically realistic layered phantom of the human head that allows the insertion of ischemic and hemorrhagic stroke phantom models. A 2.5D physical phantom was designed using a representative anatomical image of the human head, which was simplified into 5 different layers that mimic the scalp, skull, cerebrospinal fluid, brain, and stroke regions in terms of anatomy and dielectric properties. Apart from the brain phantom, all other layers consist of a mixture of polyurethane rubber, graphite powder, and carbon black powder. The brain phantom is in the liquid form to facilitate the insertion of different stroke models (ischemic or hemorrhagic) with different positions and shapes. Phantoms were designed with dielectric properties valid within the frequency range 0.5–3.0 GHz, which is relevant for microwave stroke detection and classification. Molds for casting individual parts of the phantom were printed in 3D. The presented phantom is suitable for the development and testing of microwave systems and algorithms used in the detection and classification of vascular events relevant to stroke diagnosis.

1. Introduction

A stroke can cause lasting brain damage, long-term disability, and even death [1]. Recent developments in microwave imaging (MWI) have shown the potential for MWI to be used as a tool for detection and classification of different stroke types [2]. This technology is typically compact, light, portable, noninvasive, and inexpensive, which are advantages compared with traditional imaging techniques such as computed tomography (CT) or magnetic resonance (MR) [3, 4]. However, testing this imaging technique in patients who have their life at risk is not possible. The only solution is to develop an anatomically and dielectrically realistic human head phantom with layers that mimic the anatomy and dielectric properties of human head tissues as close as possible.

Dielectric properties vary depending on the stroke type, which can be classified into two main categories: hemorrhagic and ischemic. Ischemic strokes are caused by the interruption of blood flow within a region of the brain and are more common than hemorrhagic strokes, which are triggered by blood leakage/bleeding phenomena [1]. The dielectric properties of the blood are higher than the ones of the white and gray matter [5]. Furthermore, acute ischemic stroke causes a decrease in the dielectric properties of the brain tissue and the degree of such changes depends on the stage of ischemic disease [6]. Microwave systems should then be able to not only detect strokes but also classify different stroke types due to their different dielectric properties [2].

Most head phantoms [7–9] are made of water-based substances that consist of a single layer with dielectric

parameters corresponding to the average of human head tissues, which vary widely. Anatomical phantoms that contain individual tissues are available [10–12], but these phantoms are significantly simplified and use plastic materials, gels, and water-based substances that are not time-stable [13]. Furthermore, the insertion of stroke phantoms in different positions and their reuse are not possible with such phantoms.

Improved phantom properties can be obtained by using silicone or polyurethane rubber in combination with conductive powders [14–16]. These phantom materials show long-term stability both in shape and dielectric properties. They are also suitable for creating complex shapes and thin layers, but the ones available are still composed of one layer with average dielectric properties of tissues in the brain. In reference [17], a dielectrically and anatomically realistic solid 3D phantom was fabricated, resulting in a time-stable phantom that accommodates the insertion of stroke phantoms. However, only two predefined positions for the stroke phantom can be used and the head model only has two layers of tissue: an outer homogeneous layer exhibiting average dielectric properties of tissues outside the brain, that is, skin, fat, skull cortical bone, skull cancellous bone, meninges, and cerebrospinal fluid (CSF), and an inner homogeneous layer exhibiting average dielectric properties of the gray matter, white matter, and CSF.

Clearly, a more detailed and versatile human head phantom is required for testing microwave systems. The human head has several tissue layers: *epidermis*, scalp (skin, connective tissue, galea aponeurotic layer, loose areolar connective tissue layer, and pericranium), skull (outer middle and inner table layers), meninges (dura mater, arachnoid mater, and pia mater), and cerebrospinal fluid and brain parenchyma (white and gray matter) [18]. In this work, we propose a 5-tissue layer with scalp, skull, CSF, brain, and stroke compartments, where the stroke phantom can be positioned anywhere in the brain as is the case of naturally occurring strokes.

2. Materials and Methods

2.1. Phantom Mold Design. To fabricate a multilayer head phantom, we designed concentric phantom molds with anatomically realistic shapes. To this end, we analyzed MR scans from The Population Head Model V1.0 of the IT'IS Foundation database [19, 20] and selected model number 122317 due to its average head size. Using this model, we defined the baseline image for the molds production as the axial cross section that provided the largest brain portion of the head model (Figure 1(a)). The different layers of the human head were then segmented from the baseline image using the software 3D Builder (Microsoft Corporation) as shown in Figure 1(b). The molds are intended to be printed in 3D. Thus, the anatomy had to be simplified to create layers that are both feasible to be printed and mechanically stable. From our experience, a minimum thickness of 2 mm for each layer was chosen. The resulting simplified geometry can be seen in Figure 1(c) with 5 tissue layers: scalp, skull, CSF, brain, and a stroke model added a posteriori.

The 2.5D rendering of the phantom molds is shown in Figure 2 with a height of 20 cm. The outer shell (Figure 2(a)) dictates the head shape, and the molds in Figures 2(b), 2(c), and 2(d) will shape the skull, CSF, and brain regions, respectively. The mold for the stroke phantom (Figure 2(e)) is represented by a cylinder with a cross-sectional diameter of 4 cm. All phantoms will be made in the solid form, except the brain region which will be in the liquid form. A liquid brain region will allow immersion of stroke phantoms of different sizes and shapes.

2.2. Definition of Dielectrically Equivalent Phantom Models. The solid phantoms were prepared using mixtures of polyurethane rubber, graphite powder, carbon black powder, and acetone (Table 1). These materials were chosen due to their mechanical stability and their ability to match the dielectric properties of human tissues [21]. In total, 28 mixtures were fabricated in different proportions (Table 1).

A total of 28 mixtures were produced in 6 series in different compositions listed in Table 2. In each series, the weight percent of one component (graphite powder, carbon black powder, or acetone) was increased while the weight percent of the other component (graphite powder, carbon black powder, and acetone) was kept constant.

Dielectric properties of mixtures were measured using the SPEAG Dielectric Assessment kit (DAK, Schmid & Partner Engineering AG, Switzerland) with the probe DAK-12 in the frequency range 0.5–3.0 GHz. The frequency measurement range is given by the used measurement probe, and it covers the frequency range 0.7–1.3 GHz, which is currently considered the most suitable for MWI applications [22]. The relative permittivity and electrical conductivity of each sample were measured 10 times, and the measured data were supplemented with extended uncertainties with a coverage factor of $k = 2$. Based on the measured dielectric properties of the samples, the composition of the mixtures was determined so that the dielectric properties correspond to the five tissue layers at 1 GHz [6, 23], which is the center frequency of the MWI frequency range. The dielectric properties of each layer were determined from the IT'IS material parameter database V3.0 [24] as follows: scalp (weighted average of skin and fat with the ratio 2 : 1), skull (cortical skull), CSF (CSF), brain (average of gray matter, white matter, and cerebellum), hemorrhagic stroke (blood), and ischemic stroke (determined from the brain with 20% reduction of dielectric properties [6]). The tissues in parentheses are the ones listed in the IT'IS database.

2.3. Fabrication Process of the Head Phantom. The physical molds were printed on a 3D printer (Prusa i3 MK2, Prusa Research, Czech Republic) with 0.35 mm resolution in the longitudinal (Z) direction using polyethylene terephthalate glycol (PETG) as the base material. All molds are depicted in Figure 3. Due to the elasticity of the molds, it was necessary to reinforce them with plaster. The surface of the molds was treated with the Polyurethane separators Ease Release 200 (Smooth-On, US), detergent Jar (Procter & Gamble, US), or glossy adhesive tape to reduce the adhesion of the phantom mixtures.

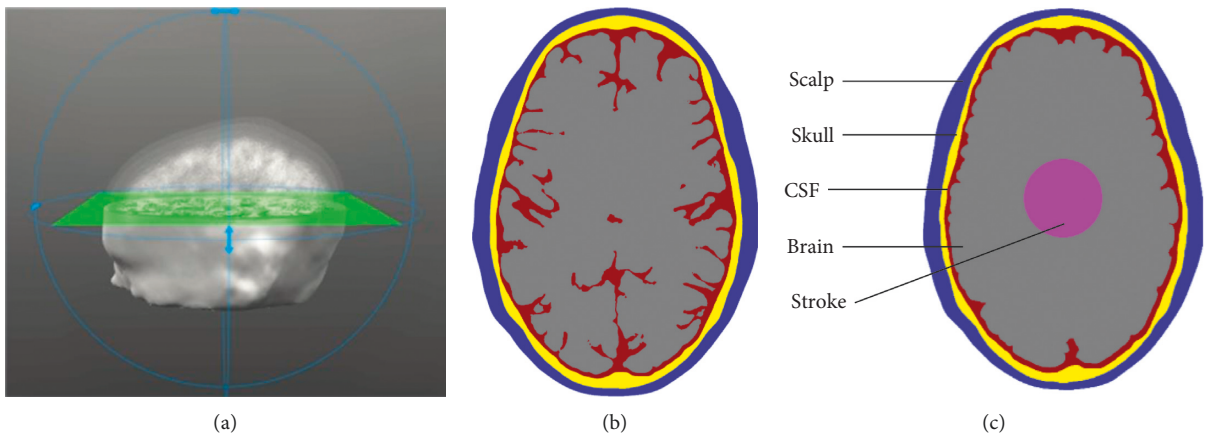

Figure 1: Baseline imaging for human head mold production: (a) cross section of the human head obtained from an MR image, (b) the 2D raw segmentation model of the main human head tissue layers, and (c) a simplified anatomical model with an added stroke model.

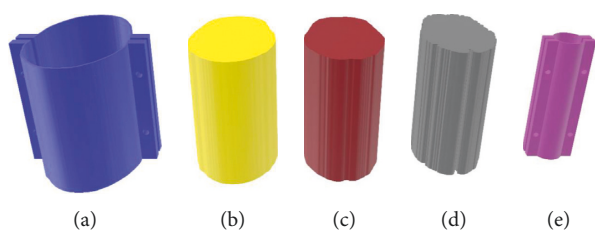

Figure 2: Computational design of the 2.5D human head tissue molds: scalp (a), skull (b), CSF (c), brain (d), and stroke (e) mold regions.

Table 1: Phantom materials to be used in the fabrication of the solid tissue layers of the human head phantom.

Material	Model	Manufacturer
Polyurethane rubber	PMC®-121 30/wet	Smooth-On, Inc. (US)
Graphite powder	282863-graphite	Sigma-Aldrich (US)
Carbon black powder	45527 carbon black	Alfa Aesar (US)
Acetone	99.9% acetone	Lach-Ner, s.r.o. (CZ)

Table 2: Phantom materials and their weight percentage used to prepare a series of samples to determine the most suitable composite to mimic the individual solid phantom layers of the human head physical model. For simplicity, the polyurethane rubber (% by weight) is omitted.

Series	Graphite powder (% by weight)	Carbon black powder (% by weight)	Acetone (% by weight)
1	10, 15, 20, 25, 30, 35, 40, 35, 50	0	0
2	0	1, 3, 5, 10, 15	0
3	25	2, 4, 6	0
4	10, 15, 20, 25, 30	4	0
5	20	2, 4, 6	0
6	40	0	10, 20, 30

The phantom mixtures were blended using a kitchen mixer (Bosch MUM 57860, Robert Bosch GmbH, Germany) with a dough kneading head for a total of 3 minutes to obtain a homogeneous phantom. The mixture was poured into the outer 3D printed mold (Figure 3(a)). Naturally occurring air bubbles were removed using a vacuum system. This is critical for dielectrically accurate phantoms since the presence of air would change the dielectric properties. The vacuum system consisted of a cylindrical vacuum chamber and an electric motor with a vacuum pump, where phantom mixtures were subjected to a vacuum of 0.8 bar three times for 30 seconds.

The inner 3D printed mold (Figure 3(b)) was slowly pressed into the homogeneous mixture to create the first layer (scalp). The insertion of inner molds had to be conducted with caution, and the position of the mold had to be controlled to guarantee that all layers were centered. The mixture was curated for 24 hours, and the internal mold was then carefully removed to avoid breaking the recently curated phantom layer. The same procedure was repeated with

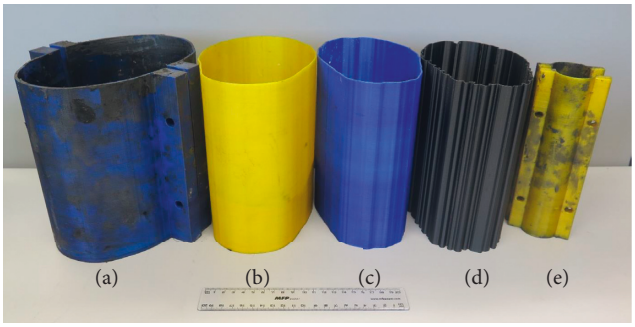

Figure 3: Molds printed in 3D for human head phantom fabrication: scalp (a), skull (b), CSF (c), gray matter (d), and stroke model (e).

the other two inner molds (Figures 3(c) and 3(d)) to create the skull and CSF domains. The resulting 3-layer solid phantom consisted of a waterproof container with an internal shape that mirrored the brain external anatomy. The container was then filled with a liquid brain phantom formed by adding deionized water and salt to isopropanol to achieve the desired brain dielectric properties [22]. Finally, the stroke phantom models were created by filling the cylindrical printed mold (Figure 3(e)) to mirror either ischemic or hemorrhagic tissue properties, yielding a total of 5 tissue layers.

3. Results

3.1. Phantom Materials and Dielectric Properties. The phantom mixtures that best represent the equivalent human tissue layers in terms of dielectric properties are summarized in Table 3. For simplicity, the dielectric properties are presented only at 1 GHz in Table 4 for all tissue layers.

The frequency-dependent relative permittivity and electrical conductivity of the human head phantom layers are shown in Figures 4 and 5, respectively. The plots were split into different tissue layers for clarity.

3.2. Human Head Physical Phantom. Using 3D printed molds, we built anatomically and dielectrically realistic 2.5D phantoms of scalp, skull, and CSF, which resulted in a stable multilayer phantom depicted in Figure 6(a). The final 5-layer phantom is shown in Figure 6(b), which includes the liquid brain phantom and a stroke model with realistic electrical properties.

4. Discussion

The main goal of this work was to design and manufacture an anatomically and dielectrically realistic 2.5D 5-layer head phantom with the possibility of adding stroke phantoms with different electrical properties, shapes, sizes, and positions.

The materials used for the mold production were suitable to compact five tissue layers into a single phantom. The resulting mixture of Polyurethane rubber, graphite, and carbon black powder had sufficiently low viscosity for pouring into the mold and, after curing, provided a time-stable and partially flexible phantom. Furthermore, the phantom mixtures analyzed proved to be adequate to match the phantom with the human-equivalent dielectric properties over a wide range of frequencies relevant to microwave imaging.

Table 3: Weight percentages of phantom materials for fabrication of a multilayer human head phantom for stroke detection.

Tissue phantom	Urethane rubber (%)	Graphite powder (%)	Carbon black powder (%)	Acetone (%)
Scalp	66.0	22.7	2.3	9.0
Skull	81.0	15.0	4.0	0
CSF	44.0	36.0	0	20.0
Hemorrhagic stroke	61.7	21.8	3.5	13.0
Ischemic stroke	53.6	37.3	0	9.1
Liquid brain	61.15% deionized water + 38% isopropanol + 0.85% NaCl			

Table 4: Dielectric properties at 1 GHz of the different tissue-equivalent layers of the human head phantom for stroke detection. The measured data are supplemented with extended uncertainties ($k = 2$).

Tissue layer	ε_r (−) human	ε_r (−) measured	σ (S/m) human	σ (S/m) measured
Scalp	31.06	34.16 ± 1.33	0.64	0.77 ± 0.08
Skull	11.97	12.17 ± 0.53	0.09	0.11 ± 0.01
CSF	68.44	82.81 ± 2.46	2.46	2.99 ± 0.04
Brain	46.57	45.33 ± 0.78	0.97	0.98 ± 0.01
Ischemic stroke	37.26	36.43 ± 0.66	0.78	0.87 ± 0.01
Hemorrhagic stroke	61.08	55.78 ± 2.18	1.59	1.80 ± 0.09

The 3D printing technology proved to be suitable for fast manufacturing of phantom molds. Using PETG as the base material provided solid yet partially flexible molds. The mixtures stuck to the mold surface, and it was necessary to use a separator. The polyurethane separator Ease Release 200 did not work well with the PETG molds. The most suitable separator was the detergent Jar that was applied by brushing the entire mold surface or glossy adhesive tape which was suitable for flat surfaces. Nonetheless, even with the use of a separator, it was challenging to remove the mold after the mixture cured. At the same time, it was critical to remove unwanted air bubbles from the mixture by means of a vacuum chamber. Emerging bubbles could be observed on the surface of the samples, indicating an effective air extraction.

Phantom mixtures with higher concentrations of graphite powder presented higher viscosity, an effect that was even more pronounced with higher carbon black powder concentrations. The high viscosity formed lumps that made the mixture heterogeneous. To lower the viscosity, we added a small amount of acetone. However, acetone increased both dielectric properties making the dielectric properties matching between phantom and human tissues challenging. Nonetheless, the largest difference between phantom and human dielectric properties is lower

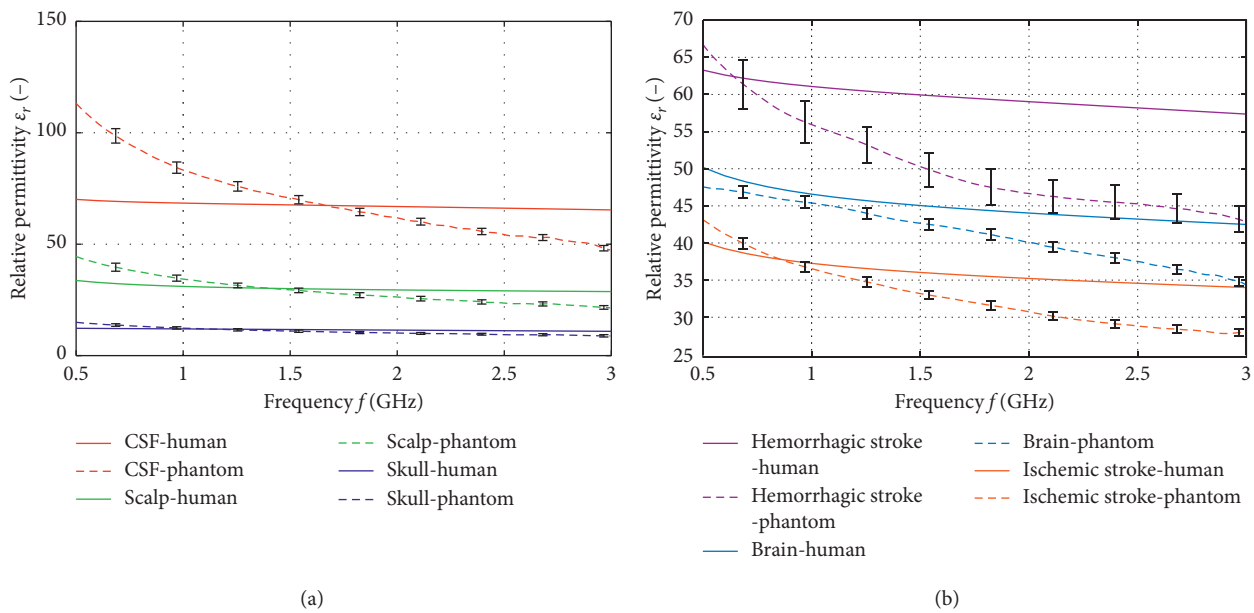

Figure 4: Frequency dependence of the human head phantom relative permittivity with extended uncertainties ($k = 2$): (a) scalp, skull, and CSF solid phantom layers; (b) liquid brain and solid stroke phantom layers.

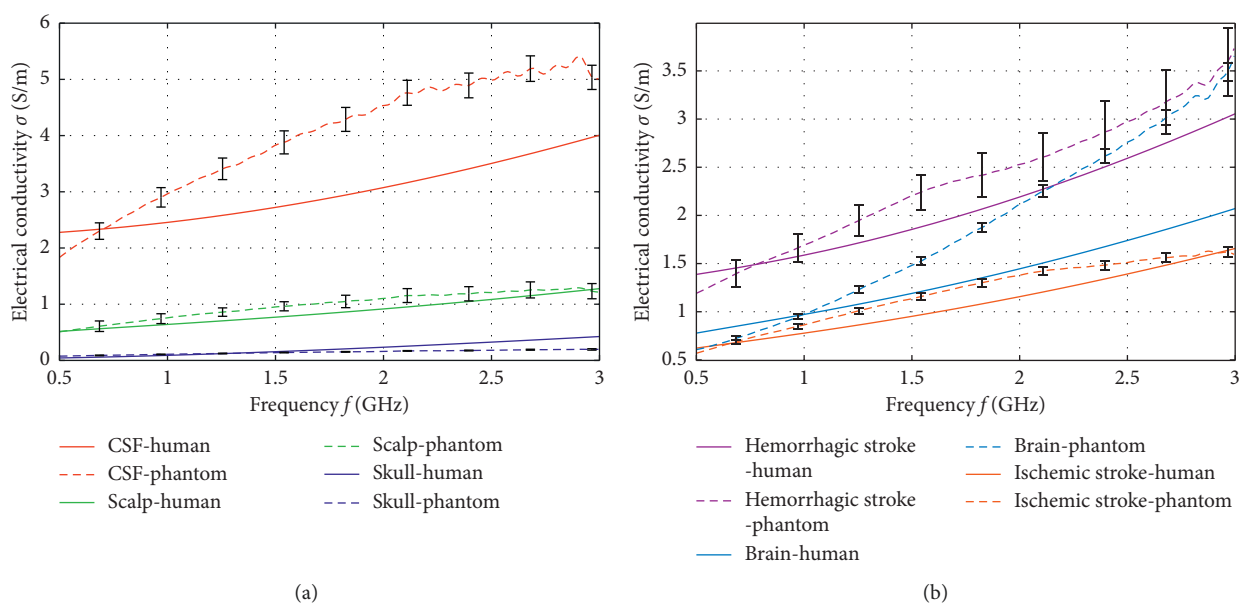

Figure 5: Frequency dependence of the human head phantom electrical conductivity with extended uncertainties ($k = 2$): (a) scalp, skull and CSF solid phantom layers; (b) liquid brain and solid stroke phantom layers.

than 25% at 1 GHz (Figures 4 and 5). Since the effect of relative permittivity on wave propagation is proportional to its square route, we consider the 25% difference acceptable. Moreover, the desired contrast in the dielectric properties between the different tissues in the human head phantom was preserved.

The dielectric properties of the solid phantoms were measured again one month after manufacturing, and they showed constant values. However, the liquid brain phantom changed its dielectric properties over time due to the evaporation of water and alcohol. Thus, we recommend measuring the dielectric properties of the mixture daily and, if necessary, adjust the composition or replace the mixture.

In reference [25], it was mentioned that extending the imaging system and the phantom of the head from 2.5D to 3D reduces the impact of the stroke area on the scattered EM field due to the significant reduction in stroke volume. On the other hand, the impact of the 2.5D phantom off the plane of the antenna array on the scattered field is not captured by the receiving antennas. Therefore, we believe that the 2.5D phantom [26] is a suitable platform for developing and testing algorithms, as well as microwave imaging hardware.

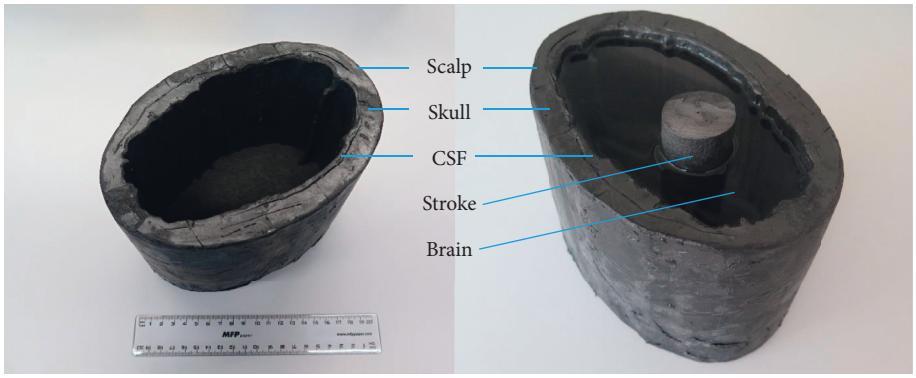

(a) (b)

Figure 6: Photograph of the anatomically and dielectrically realistic 2.5D human head phantom: (a) external solid layers corresponding to scalp, skull, and CSF that are snugly attached to each forming a waterproof container; (b) fully assembled 5-layer human head phantom with added liquid brain phantom and a cylindrical solid stroke model.

However, the phantom production methodology described here can be used in the future to produce anatomically and dielectrically realistic 3D phantoms of the head.

5. Conclusions

An anatomically and dielectrically realistic phantom of the human head was designed and manufactured for microwave detection and classification of strokes. The phantom contains 5 different layers including the scalp, skull, CSF, brain regions, and a reconfigurable stroke model. The outermost three layers and the internal stroke model are made with solid mixtures that can be as thin as 1 mm. The brain phantom was made in the liquid form to allow the insertion of different stroke models (ischemic or hemorrhagic) with different positions and shapes. The resulting structure of this head phantom resulted in a continuous multilayer environment without plastic walls between the different layers, making the phantom more dielectrically realistic. Furthermore, the phantom is time-stable and thus suitable for obtaining large measured data sets for testing new algorithms for stroke detection and classification based on machine learning methods.

Data Availability

The measured data used to support the findings of this study are available from the corresponding author upon request.

Conflicts of Interest

The authors declare that they have no conflicts of interest.

Acknowledgments

This work has been supported by a grant from the Czech Science Foundation (number 17-00477Y).

References

[1] National Heart, Lung, and Blood Institute, *Stroke*, National Heart, Lung, and Blood Institute, Bethesda, MD, USA, 2018, https://www.nhlbi.nih.gov/health-topics/stroke.

[2] M. A. Khorshidi, T. McKelvey, M. Persson, and H. D. Trefna, "Classification of microwave scattering data based on a subspace distance with application to detection of bleeding stroke," in *Proceedings of the 2009 3rd IEEE International Workshop on Computational Advances in Multi-Sensor Adaptive Processing (CAMSAP)*, pp. 301–304, Dutch Antilles, The Netherlands, December 2009.

[3] Y. Wu, M. Zhu, D. Li, Y. Zhang, and Y. Wang, "Brain stroke localization by using microwave-based signal classification," in *Proceedings of the 2016 International Conference on Electromagnetics in Advanced Applications (ICEAA)*, pp. 828–831, Queensland, Australia, September 2016.

[4] M. Pastorino, *Wiley Series in Microwave and Optical Engineering : Microwave Imaging*, John Wiley & Sons, Hoboken, NJ, USA, 2010.

[5] S. Semenov, J. Kellam, P. Althausen et al., "Microwave tomography for functional imaging of extremity soft tissues: feasibility assessment," *Physics in Medicine and Biology*, vol. 52, no. 18, pp. 5705–5719, 2007.

[6] S. Semenov, T. Huynh, T. Williams, B. Nicholson, and A. Vasilenko, "Dielectric properties of brain tissue at 1 GHz in acute ischemic stroke: experimental study on swine," *Bioelectromagnetics*, vol. 38, no. 2, pp. 158–163, 2017.

[7] M. Akter, T. Hirai, Y. Hiai et al., "Detection of hemorrhagic hypointense foci in the brain on susceptibility-weighted imaging," *Academic Radiology*, vol. 14, no. 9, pp. 1011–1019, 2007.

[8] B. A. J. Mohammed and A. M. Abbosh, "Realistic head phantom to test microwave systems for brain imaging," *Microwave and Optical Technology Letters*, vol. 56, no. 4, pp. 979–982, 2014.

[9] R. Scapaticci, L. Di Donato, I. Catapano, and L. Crocco, "A feasibility study on microwave imaging for brain stroke monitoring," *Progress in Electromagnetics Research B*, vol. 40, pp. 305–324, 2012.

[10] B. J. Mohammed, A. M. Abbosh, S. Mustafa, and D. Ireland, "Microwave system for head imaging," *IEEE Transactions on Instrumentation and Measurement*, vol. 63, no. 1, pp. 117–123, 2014.

[11] A. T. Mobashsher, A. M. Abbosh, and Y. Wang, "Microwave system to detect traumatic brain injuries using compact unidirectional antenna and wideband transceiver with verification on realistic head phantom," *IEEE Transactions on Microwave Theory and Techniques*, vol. 62, no. 9, pp. 1826–1836, 2014.

[12] D. B. Rodrigues, P. F. Maccarini, S. Salahi et al., "Design and optimization of an ultra wideband and compact microwave antenna for radiometric monitoring of brain temperature," *IEEE Transactions on Biomedical Engineering*, vol. 61, no. 7, pp. 2154–2160, 2014.

[13] J. Garrett and E. Fear, "Stable and flexible materials to mimic the dielectric properties of human soft tissues," *IEEE Antennas and Wireless Propagation Letters*, vol. 13, pp. 599–602, 2014.

[14] C. Gabriel, "Tissue equivalent material for hand phantoms," *Physics in Medicine and Biology*, vol. 52, no. 14, pp. 4205–4210, 2007.

[15] H. Tamura, Y. Ishikawa, T. Kobayashi, and T. Nojima, "A dry phantom material composed of ceramic and graphite powder," *IEEE Transactions on Electromagnetic Compatibility*, vol. 39, no. 2, pp. 132–137, 1997.

[16] T. Kobayashi, T. Nojima, K. Yamada, and S. Uebayashi, "Dry phantom composed of ceramics and its application to SAR estimation," *IEEE Transactions on Microwave Theory and Techniques*, vol. 41, no. 1, pp. 136–140, 1993.

[17] B. McDermott, E. Porter, A. Santorelli et al., "Anatomically and dielectrically realistic microwave head phantom with circulation and reconfigurable lesions," *Progress in Electromagnetics Research B*, vol. 78, pp. 47–60, 2017.

[18] J. F. Gillooly, J. H. Brown, G. B. West, V. M. Savage, and E. L. Charnov, "Effects of size and temperature on metabolic rate," *Science*, vol. 293, no. 5538, pp. 2248–2251, 2001.

[19] E. G. Lee, R. L. Hadimani, and D. C. Jiles, *Population Head Model Repository V1.0*, IT'IS Foundation, Switzerland, 2016.

[20] E. G. Lee, W. Duffy, R. L. Hadimani et al., "Investigational effect of brain-scalp distance on the efficacy of transcranial magnetic stimulation treatment in depression," *IEEE Transactions on Magnetics*, vol. 52, no. 7, pp. 1–4, 2016.

[21] J. Tesarik, T. Pokorny, and L. Holek, "Samples of dry head tissues phantoms for brain stroke classification," in *World Congress on Medical Physics and Biomedical Engineering 2018. IFMBE Proceedings*, L. Lhotska, L. Sukupova, I. Lacković, and G. Ibbott, Eds., vol. 68/3, pp. 775–778, Springer, Singapore, 2019.

[22] J. Tesarik, L. F. Diaz Rondon, and O. Fiser, "Prototype of simplified microwave imaging system for brain stroke follow up," in *World Congress on Medical Physics and Biomedical Engineering 2018. IFMBE Proceedings*, L. Lhotska, L. Sukupova, I. Lacković, and G. Ibbott, Eds., vol. 68/3, pp. 771–774, Springer, Singapore, 2019.

[23] M. Persson, A. Fhager, H. D. Trefna et al., "Microwave-based stroke diagnosis making global prehospital thrombolytic treatment possible," *IEEE Transactions on Biomedical Engineering*, vol. 61, no. 11, pp. 2806–2817, 2014.

[24] IT'IS Foundation, *Tissue Properties Database V3.0*, IT'IS Foundation, Switzerland, 2015.

[25] R. Scapaticci, J. Tobon, G. Bellizzi, F. Vipiana, and L. Crocco, "Design and numerical characterization of a low-complexity microwave device for brain stroke monitoring," *IEEE Transactions on Antennas and Propagation*, vol. 66, no. 12, pp. 7328–7338, 2018.

[26] I. Merunka, O. Fiser, D. Vrba, and V. Jan, "Microwave tomography system for methodical testing of brain stroke detection approaches," *International Journal of Antennas and Propagation*, In press.

Hindawi
International Journal of Antennas and Propagation
Volume 2019, Article ID 9014969, 12 pages
https://doi.org/10.1155/2019/9014969

Research Article

A Discrete Dipole Approximation Solver Based on the COCG-FFT Algorithm and Its Application to Microwave Breast Imaging

Samar Hosseinzadegan,[1] **Andreas Fhager**,[1] **Mikael Persson**,[1] **and Paul Meaney**[1,2]

[1]*Electrical Engineering Department, Chalmers University of Technology, 41296 Gothenburg, Sweden*
[2]*The Thayer School of Engineering, Dartmouth College, Hanover, NH 03755, USA*

Correspondence should be addressed to Samar Hosseinzadegan; samarh@chalmers.se

Received 26 February 2019; Revised 6 May 2019; Accepted 20 May 2019; Published 17 July 2019

Guest Editor: Sandra Costanzo

We introduce the discrete dipole approximation (DDA) for efficiently calculating the two-dimensional electric field distribution for our microwave tomographic breast imaging system. For iterative inverse problems such as microwave tomography, the forward field computation is the time limiting step. In this paper, the two-dimensional algorithm is derived and formulated such that the iterative conjugate orthogonal conjugate gradient (COCG) method can be used for efficiently solving the forward problem. We have also optimized the matrix-vector multiplication step by formulating the problem such that the nondiagonal portion of the matrix used to compute the dipole moments is block-Toeplitz. The computation costs for multiplying the block matrices times a vector can be dramatically accelerated by expanding each Toeplitz matrix to a circulant matrix for which the convolution theorem is applied for fast computation utilizing the fast Fourier transform (FFT). The results demonstrate that this formulation is accurate and efficient. In this work, the computation times for the direct solvers, the iterative solver (COCG), and the iterative solver using the fast Fourier transform (COCG-FFT) are compared with the best performance achieved using the iterative solver (COCG-FFT) in C++. Utilizing this formulation provides a computationally efficient building block for developing a low cost and fast breast imaging system to serve under-resourced populations.

1. Introduction

The mortality rate due to the breast cancer in women worldwide has led numerous research groups to investigate early diagnosis programs. Along with other imaging methods such as X-ray computed tomography [1], positron emission tomography [2], and magnetic resonance imaging [3, 4], microwave imaging has been tested in multiple settings. In this context, microwave imaging is performed in four primary forms: radar, holography, thermoacoustic imaging, and tomography. The radar approaches have been studied in an array of simulation experiments and have advanced to several clinical tests [5–8]. Holography approaches have been primarily tested in simulation and phantom experiments [9, 10]. Thermoacoustic imaging work has been evaluated in several phantom experiments along with early clinical studies [11, 12]. In this report, we focus on microwave tomography (MWT) which has been tested in several breast imaging clinical trials and has provided relevant diagnostic information regarding diagnosis of cancer and monitoring of tumor progression during neoadjuvant chemotherapy [13, 14].

In spite of the demand and interest for microwave tomography, the computational costs of various algorithms have remained a primary obstacle in translation to real applications [15, 16]. The choice of three or two-dimensional imaging algorithms has considerable impact on the computation time and necessary hardware resources [17, 18]. Investigations into 3D imaging are considerably more common than that for 2D because of the superior measurement model match despite the associated costs [16, 19]. For many groups investigating microwave imaging, the amount of

measurement data required is often a significant barrier to real 3D implementations [20, 21]. For most numerical techniques, solving the 3D imaging problem can be computationally expensive and requires use of multiprocessor computers working over many hours to even days to generate single images [16, 22]. While these 3D efforts are useful and necessary to advance the science of microwave imaging, the practical barriers to implementation, including measurement data costs and computation time, have greatly hindered its translation into the clinic and limited them primarily to simulation studies. Alternatively, 2D approaches have proved viable and have been demonstrated in numerous phantom and clinical studies [23–26]. In fact, largely due to continuing computer efficiency advances, 2D techniques are poised to be viable alternatives for conventional modalities in under-resourced settings where cost and portability are significant concerns. In this context, reducing memory requirements and computation time for the 2D algorithm is an important concern.

2D imaging algorithms and system implementations are not new to the microwave imaging community. One notable example is the Semenov group when they were associated with the Carolinas Medical Center in Charlotte, North Carolina. In a relatively early work, they concluded that the reason their imaging technique did not work as well as desired was because of the mismatch between their 2D algorithm and the inherent 3D nature of the actual propagating fields [27]. From that experience, they surmised that they would achieve improved results by transitioning to 3D imaging to avoid the measurement/model mismatch. However, no proof of this being a general conclusion was given. Notwithstanding, significant technological advances have made 2D imaging feasible and attractive. These include: (1) the use of the lossy coupling medium to suppress unwanted multipath signal corruption [28], (2) the use of monopole antennas which can be positioned very close to the target and which we have demonstrated improving the overall images [29], and (3) the use of the log transform which improves the algorithm convergence behavior, eliminates the conversion to local minima, and makes a priori information unnecessary [30, 31]. As such, 2D imaging is poised for an expanded clinical role.

Microwave tomographic imaging algorithms require solving two problems—forward and inverse problems. The forward solver is by far the more computationally expensive part of an iterative image reconstruction algorithm and requires substantial attention to reduce its impact. Additionally, the need to perform many iterations to recover accurate images further motivates the requirement for improving computation time. The most common numerical methods used to solve the forward problem are the finite-difference time-domain (FDTD) [32], finite element method (FEM) [33], and volume integral equations such as the method of moments (MoM) [34]. Recently, the 3D discrete dipole approximation was used as a forward solver for 3D imaging and was found to be highly efficient regarding computational cost and accuracy [35]. We have also introduced the 2D DDA as a forward solver for 2D imaging [36]. As part of that paper, comparisons were performed between the 2D DDA results and those modeled using COMSOL Multiphysics along with comparisons with actual measurements. The agreement was quite good for both. Each numerical method provides important advantages that can be exploited depending on the circumstances. For instance, the finite element method is particularly well suited for situations where nonuniform shaped scatterers are involved. Likewise, the uniform grid formulation of the FDTD problem facilitates fast computation times. While the DDA can be utilized on both uniform and nonuniform grid configurations, as will be demonstrated in this paper, the computational advantages are most significant for the uniform setting. In addition, the associated uniform setting is optimal when the objects in the domain are mostly dielectric in nature. While it would be possible to incorporate metallic scatterers in the domain, for an accurate representation, extra dipoles would need to be deployed on the boundaries of the objects. This would immediately preclude the uniform grid representation. Conveniently, the imaging system developed at Dartmouth [26] essentially provides this feature. The array of monopole antennas is naturally made of metal; however, their radar cross section is sufficiently small that they only slightly perturb the field distribution when another antenna is radiating. In addition, the use of a very lossy coupling medium (glycerin and water mixtures) further dampens any perturbations from scattering off the antennas.

In this work, the two-dimensional discrete dipole approximation (2D-DDA) for calculating the electric field distribution for our microwave imaging system is proposed. The iterative solver for 2D-DDA has the potential to significantly improve the computational speed. A conjugate gradient based method, i.e., the conjugate orthogonal conjugate gradient method (COCG), is used for which the computational cost of the COCG is remarkably reduced when incorporating the fast Fourier transform (FFT). This is made possible because the coefficient matrix for the 2D-DDA is complex, symmetric, and block-Toeplitz after removal of the main diagonal and enables the possibility for employing the FFT after expansion of the block matrices to circulant form. The computation times for the direct and iterative solvers are calculated and have been investigated in this comparison using both MATLAB and C++ implementations. It is useful to compare performance both with an interpretive language such as MATLAB and a classic compiler-based code. While the interpretive code struggles computation time-wise with constructs such as loops, it contains highly optimized matrix operations which can often overcome such disadvantages. These examinations show that the computation time for the 2D-DDA is significantly decreased in the COCG-FFT approach and that the best performance is achieved in C++ using an open source C++ package, FFTW, for fast Fourier transform calculations [37].

2. Derivations

In this section, we formulate the 2D-DDA and discuss possible computational efficiency for it as a forward solver of the reconstruction algorithms.

2.1. The 2D-DDA for the Forward Problem. The three-dimensional discrete dipole approximation (3D-DDA) has been widely used for calculation of scattering and absorption properties caused by an external electromagnetic field [38–40]. In the volume integral equations for techniques such as the discrete dipole approximation, an arbitrary geometry Ω is assumed to be a union of small volumes Ω_i such that $\Omega = \lim_{N\longrightarrow\infty} \bigcup_{i=1}^{N} \Omega_i$ [41]. For the purpose of microwave tomography, the electromagnetic field distribution is expressed in the imaging domain with the forward solver, the discrete dipole approximation. The total electric field at a point ρ in the imaging domain is

$$E_{tot}(\rho) = E_{inc}(\rho) + E_{scat}(\rho) \tag{1}$$

where E_{inc} and E_{scat} are the incident and scattered electric fields, respectively. The term E_{inc} represents the electric field propagation due to a waveguide or an antenna for a homogeneous domain. The scattered electric field E_{scat} is the electric field caused by scatterers in the domain. The Helmholtz equation solution in form of (1) is usually written as [42]

$$\begin{aligned} E_{tot}(\rho) &= E_{inc}(\rho) \\ &\quad + \int_{\Omega} G(\rho,\rho')\left[k^2(\rho') - k_{bk}^2\right] E_{tot}(\rho')\, d\Omega \end{aligned} \tag{2}$$

where $G(\rho,\rho')$ is the dyadic Green's function, $k(\rho)$ is wavenumber at $\rho \in \Omega_i$, and k_{bk} is the background wavenumber. The wavenumbers are expressed in terms of the material property and frequency as $k^2 = \omega^2\mu_0\varepsilon_0\varepsilon_r + j\omega\mu_0\sigma$. For the DDA, the idea is to approximate the total electric field, $E_{tot}(\rho')$ on the right-hand side of (1) such that we assume that the forward model zone consists of multiple number of dipoles. Each dipole represents the macroscopic field $E_{tot}(\rho')$ at the position of the dipole.

On the macroscopic level, the total electric field is proportional to the polarization P via

$$P = \varepsilon_0 \chi E_{tot} \tag{3}$$

where ε_0 is the permittivity of a vacuum and $\chi = \varepsilon_r - 1$ is the electric susceptibility. The term $k^2(\rho') - k_{bk}^2(\rho)$ in Equation (2) is related to χ such that

$$\begin{aligned} k^2(\rho') - k_{bk}^2(\rho) &= \omega^2\mu_0\left(\varepsilon(\rho') - \varepsilon_b(\rho)\right) \\ &= \omega^2\mu_0\varepsilon_0\left(\chi(\rho') - \chi_b(\rho)\right) \end{aligned} \tag{4}$$

On the microscopic level, the polarization field is related to dipole moments of individual molecules. Each individual molecule is affected by a local electric field E_{loc} and gets correspondingly polarized to exhibit dipole moment p. The total contribution from all molecules in a unit volume is defined as the polarization P:

$$P = Np = N\varepsilon_0\alpha E_{loc} \tag{5}$$

Here N is number of molecules per unit volume. The polarizability, α, expresses the relationship between the local and macroscopic field. In multiple applications, this interaction has been modeled by the Clausius-Mossotti relation. In the following section, we discuss the polarizability α for microwave breast imaging systems.

(1) Constant Polarizability (α) for the 2D DDA. The most common and well-known molecular polarizability, α, for the 3D-DDA is the Clausius-Mossotti relationship [43] and is defined for a sphere as

$$\alpha_{CM} = 3v\frac{\varepsilon_r - 1}{\varepsilon_r + 2} \tag{6}$$

where ε_r and v are the relative permittivity and volume of the sphere. The constant term α has different formulations depending on the volume and concentration of the medium [41, 44, 45]. Previously, Grzegorczyk et al. [35] used the following 3D Clausius-Mossotti relation for the microwave imaging system at Dartmouth:

$$\alpha_{3D} = 3v\frac{\varepsilon_t - \varepsilon_b}{\varepsilon_t + 2\varepsilon_b} \tag{7}$$

where ε_b and ε_t are the complex permittivities of the background and inclusion, respectively.

Since our imaging system shown in Figure 1 consists of a tank filled with a liquid mixture of glycerin and water with different polarization behavior on the molecular level, we select a more general form of the Clausius-Mossotti relationship, the Maxwell-Garnett formula. The main advantage of the Maxwell-Garnett model is that it is also valid for composite media which is the normal situation for many applications including our microwave imaging system. The Maxwell-Garnett formula can be expressed as

$$\frac{\varepsilon_{mix} - \varepsilon_b}{\varepsilon_{mix} + 2\varepsilon_b} = \sum_{k=1}^{K} c_k \frac{\varepsilon_k - \varepsilon_b}{\varepsilon_k + 2\varepsilon_b} \tag{8}$$

In (8), ε_{mix} denotes the composite medium consisting of K media with permittivities, ε_k. The coefficients, c_k, relate the volume of the inclusion to its concentration which is defined as m/M_rV where V, m, and M_r are volume, mass, and the molecular weight of the inclusion, respectively. The general formula for the dimensionless α in m-dimensions is [46]

$$\alpha = m\frac{\varepsilon_t - \varepsilon_b}{\varepsilon_t + (m-1)\varepsilon_b} \tag{9}$$

Based on (8) and (9), the two-dimensional α in the form of the Maxwell-Garnett formula is expressed as

$$\alpha_{2D} := \frac{\varepsilon_{mix} - \varepsilon_b}{\varepsilon_{mix} + \varepsilon_b} = \sum_{k=1}^{K} c_k \frac{\varepsilon_k - \varepsilon_b}{\varepsilon_k + \varepsilon_b} \tag{10}$$

The concentration coefficients c_k are modified based on the area of the inclusion for the 2D case.

(2) Incident Electric Field (E_{inc}) for the Microwave Breast Imaging. The microwave imaging system at Chalmers University of Technology has a circular array of monopole antennas acting

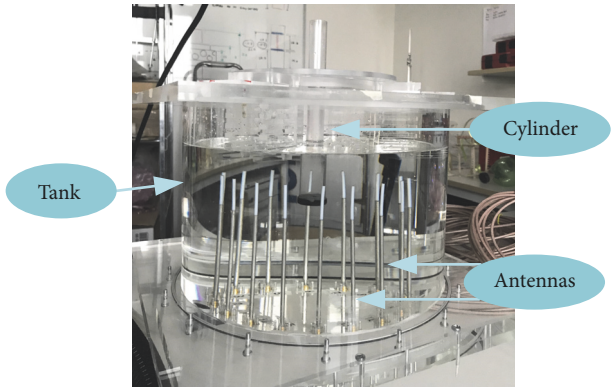

Figure 1: Photograph of the measurement setup including the tank, antennas, and the phantom cylinders.

as both transmitters and receivers (Figure 1). The transmitting antenna is modeled via the electric field distribution caused by an electrical line source (ELS). In this formulation, the 2D ELS is written in the form of

$$E_{inc}(\rho) = \frac{I_0 \omega \mu_0}{4} H_0^2 \left(k_b \left|\rho - \rho_a\right|\right) \tag{11}$$

where I_0, ω, and μ_0 are the current amplitude, operating frequency, and free-space permeability, respectively. The term $|\rho - \rho_a|$ is the distance of a dipole located at position ρ from an antenna position ρ_a.

2.2. Two-Dimensional Discrete Dipole Approximation as a System of Equations. The governing equation for the two-dimensional discrete dipole approximation is [36, 39]:

$$E_{tot}(\rho) = E_{inc}(\rho) + \sum_{\Omega_i} G(\rho, \rho') P(\rho') \tag{12}$$

Inserting (5) into (12) yields

$$E_{inc}(\rho) = \frac{P(\rho)}{\alpha(\rho)} - \sum_{\Omega_j} G(\rho, \rho') P(\rho') \tag{13}$$

For the 2D-DDA, $G(\rho, \rho')$ is the scalar Green's function for the 2D Helmholtz equation and describes the interaction between two dipoles located at ρ and ρ'. The relationship is given by

$$G(\rho, \rho') = \frac{-j}{4} H_0^2 \left(k_b \left|\rho - \rho'\right|\right) \tag{14}$$

where H_0^2 is the zero-order Hankel function of the second kind. Discretizing the forward model zone into N subdomains, (Figure 2), transforms Equation (13) into its matrix format of

$$\begin{pmatrix} \frac{1}{\alpha_1} & -G_{12} & -G_{13} & \cdots & -G_{1N} \\ -G_{21} & \frac{1}{\alpha_2} & -G_{23} & \cdots & -G_{2N} \\ -G_{31} & -G_{32} & \frac{1}{\alpha_3} & \cdots & -G_{3N} \\ \vdots & \vdots & \vdots & \ddots & \vdots \\ -G_{N1} & -G_{N2} & -G_{N3} & \cdots & \frac{1}{\alpha_N} \end{pmatrix} \begin{pmatrix} P_1 \\ P_2 \\ P_3 \\ \vdots \\ P_N \end{pmatrix} = \begin{pmatrix} E_{inc}(\rho_1) \\ E_{inc}(\rho_2) \\ E_{inc}(\rho_3) \\ \vdots \\ E_{inc}(\rho_N) \end{pmatrix} \tag{15}$$

One problematic aspect of this formulation is that some terms on the diagonal can approach infinity when any one of the α's goes to zero. This happens when the permittivity at a dipole is exactly the same as that of the background (see Equation (7)). One way to eliminate this problem is to multiply both sides of the equation by α. However, this has the unintended consequence of placing the α quantities in the off-diagonal terms of the matrix. As will be shown later, we exploit the fact that the off-diagonal terms are only functions of distance and the background permittivity which allows these portions of the matrix to become block Toeplitz and subsequently allows for important optimizations. In fact, for our imaging configuration, we regularly encounter instances where α approaches zero. Because of this conflict, we assume a uniform background medium outside of the dipoles where the properties are set to ε_{bk}. Simultaneously, for our actual measurement system, we utilize a uniform coupling bath

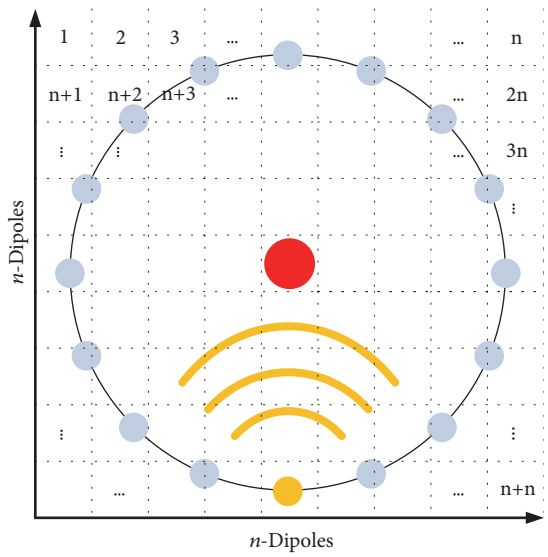

FIGURE 2: Schematic imaging plane with n^2 equally spaced dipoles on it.

everywhere outside the imaging domain, ε_{bath}. Since our forward model zone is a uniform grid, the properties at all dipoles outside of the imaging domain (a circle in this case) are set to ε_{bath}. Ideally ε_{bath} would be set to ε_{bk} to eliminate all reflections at the grid boundary. However, allowing the α's to go to zero would make the diagonal terms go to infinity. To overcome this, we artificially set ε_{bath} and ε_{bk} to be slightly different. This essentially sets many diagonal terms to a large number. In addition, it also implies that there will be nonsignificant signal reflections at the outer boundary of the dipole domain. For the latter challenge, we are fortunate in that our imaging system only uses a highly lossy coupling bath ensuring that waves reflecting back into the DDA and imaging domains will be sufficiently attenuated such that they effectively have no impact on the forward solution. The primary trade-off in this situation is between the level of reflections that can be tolerated and whether the accuracy of the forward solution is adversely affected because the condition number of the matrix in (15) becomes too great. An analysis of this issue is presented in Section 3.1.

2.3. Computational Efficient Implementation. The task of computing the electric field distribution utilizing the DDA involves two primary steps: (a) solving the dipole moments (P) and (b) multiplying P by the matrix in (15) with the diagonal, $1/\alpha$, terms removed to compute the fields. Because the matrix in (15) is full, the computational order can be as high as $2N^3/3$ when using the standard Gaussian elimination technique [47]. As N gets large, this becomes prohibitive and alternatives such as iterative solvers become attractive. In these cases, because the time limiting step involves repetitive multiplication of a length N vector by an $N \times N$ matrix, the computational cost is $O(N_{iter}N^2)$, where N_{iter} is the number of iterations required for the solution to converge. For this implementation, we exploit the special nature of the matrix derived for the DDA which ultimately allows us to employ the FFT as part of the matrix-vector multiplication to dramatically reduce the computation time within each iteration.

Different iterative solvers have been suggested with most derived from the Krylov subspace methods [39, 48, 49]. Among these methods the conjugate gradient method (CG) is the most popular. In the derivation of the CG algorithm, symmetry and positive definiteness (SPD) are assumed; however, if one of these conditions is not satisfied for the system of equations, the algorithm does not converge to a solution. In our case, the matrix in (15) is symmetric since the off-diagonal terms G_{ij} are only a function of the background medium and the distances between dipoles i and j. Unfortunately, the matrix does not meet the requirement of positive definiteness. Alternatively, there are a class of Krylov subspace methods that have been suggested for these conditions [50–57]. For our problem, we have chosen the conjugate orthogonal conjugate gradient method (COCG); it requires one time matrix-vector multiplication per iteration, but similar alternatives such as the conjugate orthogonal conjugate residual (COCR) can also be used with equivalent computational costs [57, 58].

Examination of (15) provides important insights into how best to exploit the COCG method. By breaking the matrix in Equation (15) into its diagonal and off-diagonal components, the left-hand side of (15) can be rewritten as

$$\begin{pmatrix} \frac{1}{\alpha_1} & 0 & 0 & \cdots & 0 \\ 0 & \frac{1}{\alpha_2} & 0 & \cdots & 0 \\ 0 & 0 & \frac{1}{\alpha_3} & \cdots & 0 \\ \vdots & \vdots & \vdots & \ddots & \vdots \\ 0 & 0 & 0 & \cdots & \frac{1}{\alpha_N} \end{pmatrix} \begin{pmatrix} P_1 \\ P_2 \\ P_3 \\ \vdots \\ P_N \end{pmatrix} + \begin{pmatrix} 0 & -G_{12} & -G_{13} & \cdots & -G_{1N} \\ -G_{21} & 0 & -G_{23} & \cdots & -G_{2N} \\ -G_{31} & -G_{32} & 0 & \cdots & -G_{3N} \\ \vdots & \vdots & \vdots & \ddots & \vdots \\ -G_{N1} & -G_{N2} & -G_{N3} & \cdots & 0 \end{pmatrix} \begin{pmatrix} P_1 \\ P_2 \\ P_3 \\ \vdots \\ P_N \end{pmatrix} \tag{16}$$

The first important observation is that the matrix-vector multiplication in the first term can easily be reduced to an $O(N)$ vector-vector multiplication. For the right-hand matrix, multiplication times the vector P is normally an $O(N^2)$ operation. However, in this situation, the right-hand side matrix, G, is block Toeplitz. That is, each of the N $n \times n$ (where $n = \sqrt{N}$) portions of the matrix are themselves Toeplitz matrices (Figure 3). To complete the full matrix-vector multiplication of $G \times P$, it can be performed by multiplying the smaller Toeplitz matrices times the appropriate portion of P and summing the results together afterwards.

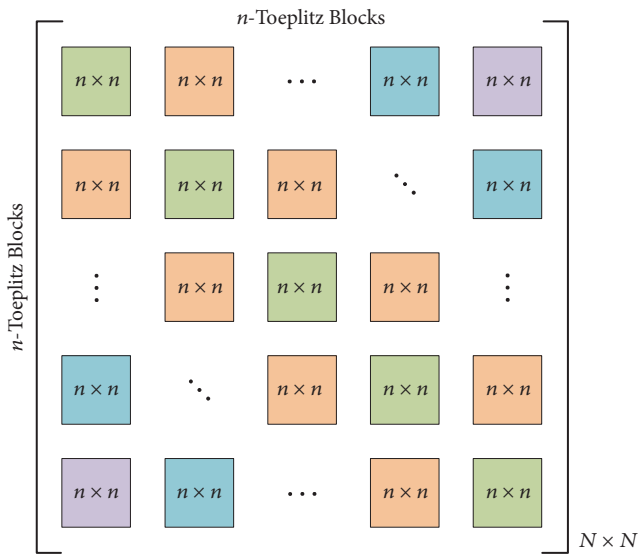

Figure 3: Block-Toeplitz matrix **G**.

Toeplitz matrices are unique in that they are not necessarily symmetric, but they have regular repetition of the individual coefficients, for example:

$$\begin{pmatrix} a & b & c & d & e \\ f & a & b & c & d \\ g & f & a & b & c \\ h & g & f & a & b \\ i & h & g & f & a \end{pmatrix} \tag{17}$$

For our case, the Toeplitz matrices are symmetric and are closely related to circulant matrices for which there are highly optimized means for performing matrix-vector multiplications (i.e., the convolution theorem). In this case, the symmetric Toeplitz matrix can be padded both in columns and rows (Figure 4) to produce a circulant matrix:

$$\underline{\underline{C}}_1 = \begin{pmatrix} g_1 & g_2 & \cdots & g_{n-1} & g_n & g_{n-1} & \cdots & g_2 \\ g_2 & g_1 & g_2 & \ddots & g_{n-1} & g_n & \cdots & g_3 \\ \vdots & g_2 & g_1 & \ddots & \vdots & g_{n-1} & \ddots & \vdots \\ g_{n-1} & \ddots & g_2 & g_1 & g_2 & \ddots & g_{n-1} & g_n \\ g_n & g_{n-1} & \ddots & g_2 & g_1 & g_2 & \ddots & g_{n-1} \\ g_{n-1} & g_n & g_{n-1} & \ddots & g_2 & g_1 & g_2 & \ddots \\ \vdots & g_{n-1} & g_n & g_{n-1} & \ddots & g_2 & g_1 & g_2 \\ g_2 & \ddots & g_{n-1} & g_n & g_{n-1} & \ddots & g_2 & g_1 \end{pmatrix} \tag{18}$$

where the upper left-hand side, $n \times n$ matrix was the original block-Toeplitz matrix. By transforming the Toeplitz matrix to this form, several key observations can be made. First, since each row is identical to the next except for a modulo shift, only one row of the matrix needs to be computed and stored. This is a substantial savings in terms of memory requirements. Secondly, because the matrix is now circulant, the convolution theorem can be used to multiply it by the associated portion of the vector (in this case the vector also needs to be padded similarly to the matrix). Taking the inverse FFT of the product of the FFT's of the first row of the matrix times the associated portion of the vector is equivalent to multiplying the whole matrix times the vector.

3. Computational Results

In this section, we discuss two different approaches to optimize the forward solver of the reconstruction algorithms. Additionally, the effects of background medium dielectric properties are investigated and its impact on the electric field distribution is presented.

3.1. Study of the Field Distributions as a Function of Permittivity Difference. As mentioned in Section 2.2, one challenge in using Equation (15) is the treatment of the diagonal of the system of equations coefficient matrix. As the α terms tend to zero, implying that the electrical properties of background liquid are the same as those of the dipoles, the corresponding diagonal terms go to infinity. For medical microwave imaging systems, a coupling liquid reducing the contrast between skin tissues and its surrounding is used. Utilizing a coupling liquid that has identical dielectric properties to that of the outside results in a matrix with infinity values on its diagonal. To accommodate this challenge, we set the properties of the dipoles within the grid to something slightly different than that for the background. This problem motivates us to study the range of acceptable permittivity values for its surrounding. For this analysis, the permittivities of the background and coupling medium are denoted as ε_{bk} and ε_{bath}, respectively.

In this situation, we set the permittivity values for the grid region directly surrounding the imaging domain to ε_{bath} and that for the surrounding background to a value slightly lower than that. We compute the electric field distributions for a single, large inclusion ($\varepsilon_{inc} = 40$, and $\sigma = 1.0$ S/m) and the bath properties of $\varepsilon_{bath} = 22$ and $\sigma = 1.0$ S/m. The imaging domain consists of 6561 dipoles. The antenna array is located on a circle of diameter 15.2 cm and the target is positioned at the origin. In this situation, the background permittivity is varied from 21.9999 down to 21 where the difference between ε_{bath} and ε_{bk} is increased in increments of multiples 10 (i.e., $\varepsilon_{bk} =$ 21.9999, 21.999, 21.99, 21.9, and 21.0) and the conductivity is kept constant at $\sigma = 1.0$ S/m. Figure 5 shows plots of (a) the condition number of the matrix using the formulation in (15), (b) the condition number of the matrix using the formulation where (15) has been multiplied by α, and (c) the relative error for the first formulation, all as a function of the difference in permittivity between the bath and background (log scale). The condition number is a useful metric because it provides a good measure of the digital accuracy of the inversion process utilizing a particular matrix [47]. Note that the condition number of the case where the matrix is multiplied by α does not change appreciably since the values on the diagonal

$$\begin{bmatrix} g_1 & g_2 & \cdots & g_{n-1} & g_n & g_{n-1} & g_{n-2} & \cdots & g_3 & g_2 \\ g_2 & g_1 & g_2 & & g_{n-1} & g_n & g_{n-1} & & g_4 & g_3 \\ \vdots & g_2 & g_1 & \ddots & \vdots & \vdots & g_n & g_{n-1} & \ddots & \vdots \\ g_{n-1} & & \ddots & \ddots & g_2 & g_3 & & \ddots & \ddots & g_{n-2} \\ g_n & g_{n-1} & \cdots & g_2 & g_1 & g_2 & g_3 & \cdots & g_n & g_{n-1} \end{bmatrix} \begin{bmatrix} p_1 \\ p_2 \\ \vdots \\ p_{n-1} \\ p_n \\ 0 \\ 0 \\ \vdots \\ 0 \\ 0 \end{bmatrix} = \begin{bmatrix} g_1 & g_2 & \cdots & g_{n-1} & g_n \\ g_2 & g_1 & g_2 & & g_{n-1} \\ \vdots & g_2 & g_1 & \ddots & \vdots \\ g_{n-1} & & \ddots & \ddots & g_2 \\ g_n & g_{n-1} & \cdots & g_2 & g_1 \end{bmatrix} \begin{bmatrix} p_1 \\ p_2 \\ \vdots \\ p_{n-1} \\ p_n \end{bmatrix}$$

Figure 4: Circulant conversion.

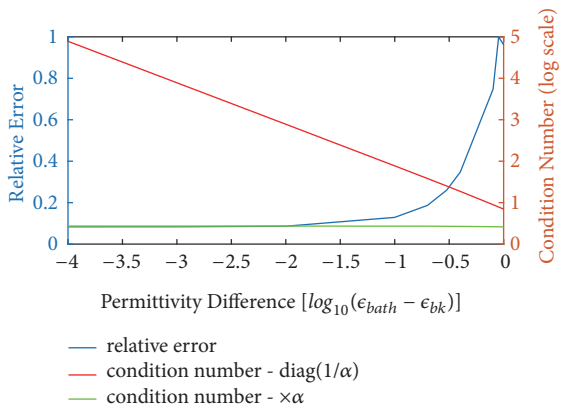

Figure 5: The relative error of the total solution, condition number of the matrix with $1/\alpha$ on the diagonal, and the condition number of the matrix that has been multiplied by α all as a function of the logarithmic difference in permittivity between the bath, $\varepsilon_{bath} = 22$ and the background. For the permittivity difference scale, -4 corresponds to a background permittivity of 21.9999 and a value of 0 corresponds to a background permittivity of 21, respectively.

remain within a relatively tight bound. The field distributions (both amplitude and phase) for the cases of background permittivities of 21, 21.9, 21.99, 21.999, and 21.999 are shown in Figures 6(a)–6(e). For the most part, these distributions are quite similar. Except for $\varepsilon_{bk} = 21$, the amplitude plots all show a primary lobe towards 12:00 (clock-face orientation) with slight nulls to either side of it. The $\varepsilon_{bk} = 21$ case does exhibit a slight bulge towards 12:00, but the nulls have been smoothed over. The phase distributions show roughly circular patterns with the sharp changes from red to blue designating phase wrapping as the distributions jump from -180° to $+180^\circ$. These distributions are roughly circular, with the cases for $\varepsilon_{bk} \geq 21.9$ exhibiting a slight flattening in the 12:00 direction. The $\varepsilon_{bk} = 21$ distribution is more circular for the entire region. From the visual examination in Figures 6(a)–6(e) and the error and condition number plots in Figure 5, it would appear that background permittivity values of 21.99 or greater would be suitable. However, our preference is to keep the condition number to a modest level, so we choose a value of 21.99 to restrain the condition number while simultaneously keeping the error low.

3.2. Computational Efficiency with the FFT. We have implemented the 2D-DDA using both MATLAB and C++. The iterative and direct solutions for the given system of equations have also been calculated. Since the main concern on the choice of these algorithms stems from optimizing computation time to obtain vector P, we have calculated and compared the computation times for each implementation and method with different numbers of dipoles. The computation times are divided into three categories based on the complexities N^3, N^2, and $N\log(N)$ for the direct solvers, the COCG iterative algorithm and the FFT-COCG algorithm, respectively. The computation time for the COCG-FFT implemented in C++ is processed in two separate software packages, Armadillo and FFTW. Armadillo is an open source C++ library for linear algebra and scientific computing which provides a high level syntax and is balanced between speed and user friendliness [59, 60]. FFTW is a C subroutine library for computing the discrete Fourier transform (DFT) in one or more dimensions, of arbitrary input size, and of both real and complex data [37]. These two packages have been used in our implementation in this study. Table 1 shows the computation times for different solvers in MATLAB and C++. For these simulations, the forward model zone contains N number of dipoles, where $N = 441, 1681$, and 6561. The computation times for these cases are given in Table 1. Table 1 shows that the MATLAB direct solver is more efficient compared to that of the C++ implementation using the Armadillo package. Generally, for the two smaller matrices, MATLAB is more efficient than C++. However, when using larger matrices with sufficient numbers of dipoles in the imaging domain ($N = 6561$) to ensure accuracy, the computation times for the direct and iterative solvers in MATLAB show that the time savings are on the order of a factor of two. Using the FFT-COCG in MATLAB, the time decreases by a factor of three. Our observations show that there is a significant difference in computation time between the Armadillo and FFTW packages using the built-in FFT algorithm.

3.3. two orders of magnitude faster than a conFurther Optimizations for Our Specific Microwave Imaging Problem. In this section, the optimal number of dipoles utilized in the imaging domain is investigated. In the previous section, it was convenient to sequentially double the number of dipoles to more easily identify the optimal number of dipoles. However, there may be more convenient intermediate values which have improved efficiency, especially with respect to the FFT.

For the block-Toeplitz matrices in the case with 6561 dipoles, the square Toeplitz matrices are 81×81. To convert

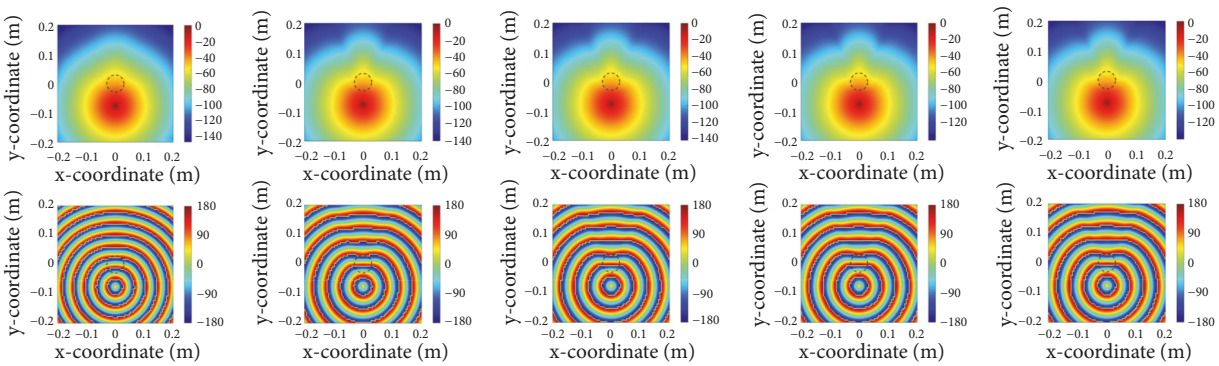

(a) 21.0 (b) 21.9 (c) 21.99 (d) 21.999 (e) 21.9999

Figure 6: Plots of magnitude (top) and phase (bottom) distributions for f =1.3 GHz, $\sigma = 1$, $\varepsilon_{r,t} = 40$, $d = 6$ (cm), forward zone of size of 40 cm and #6561 number of dipoles, for multiple background permittivity values, $\varepsilon_{r,bk}$, in range of 21 to 21.9999. The inclusion is located at (0m, 0m) and its outline is indicated by the dashed lines.

these matrices to circulant ones, the size of the matrix needs to be nearly doubled in width and height along with duplication of coefficients to that in (18). In this case, the conversion means adding 79 columns with appropriate coefficients, before performing the actual FFT. In this form, the number of columns and the length of each column increases to 160.

The fast Fourier transformations of the first row of the matrix and the column vector also require zero-padding procedures to the next power of 2 to allow use of the FFT. In this way, a vector with the size of 160 would be converted to the one of size 256. One way to optimize these cases is to restrict our number of dipoles in a way that does not require significant zero-padding. One example of exploiting this observation is to reduce the overall grid size to 65 × 65 dipoles. Without reducing the physical size of the grid, this would imply a node-to-node spacing of 6.3 mm instead of the previous 5.0 mm spacing, an increase of 25%. However, by decreasing the grid size by only 12% (corresponding to spacings of 5.5mm and an overall grid size of 35.2cm x 35.2cm), the overall change to the accuracy is only minor, and we accomplish the goal of improved efficiency. Figure 7 shows the magnitude and phase distributions for the same case in Figure 6(c), the background permittivity of 21.99, except that the overall grid size is 35.2 (cm) × 35.2 (cm). While the physical boundary is closer to the antennas, the artifacts from the boundary still have minimal impact on the fields inside the array of antennas. In terms of efficiency, Table 2 shows the performance times for this grid size. For all solution techniques, this size has substantial time improvement over the previous 6561 case, especially when the FFT is exploited, by as mush as a factor of $3x$ depending on method. This is a substantial improvement.

Moreover, for the iterative algorithms such as COCG, the number of iterations is not independent of prescribed accuracy tolerance levels. To reduce the computation time, we studied the effects of the error tolerance level on the computation time as well as the overall accuracy. Table 3 shows the corresponding computation times for tolerances of 1e-5 and 1e-3 for the 6561 dipole grid. For all implementations, there are significant time improvements, with the C++ times utilizing the FFT algorithm improving on the order of 35%.

4. Conclusion

We have implemented a version of the DDA for computing the forward solutions for a configuration used in our current 2D tomographic imaging system. 2D is intriguing in that it has already been successfully implemented for phantom and animal experiments along with considerable clinical studies. Even without the speed enhancements from the techniques presented here, the 2D approach is already considerably faster than any existing 3D inverse technique which positions it well with regard to being the foundation for a low cost and portable system that would be suitable for under-resourced settings.

We have previously demonstrated that the DDA is accurate for forward solution computation for our imaging algorithm. This study builds on that experience and formulates the problem in ways that facilitate dramatic speed optimization. Chief among these enhancements is the notion of utilizing conjugate gradient based iterative solvers in conjunction with breaking the core matrix into a simple diagonal matrix and a separate one that can be further broken into block-Toeplitz matrices. Through standard techniques, these smaller matrices can be easily expanded into circulant matrices for which the FFT can be employed to speed up the matrix/vector multiplications utilizing the convolution theorem.

Further enhancements including judicious selection of the grid size and analysis of appropriate error tolerance levels for the conjugate gradient type iterative process allow the forward solution time to decrease to the order of 0.1 second which is almost two orders of magnitude faster than a conventional COMSOL approach that is considered to be efficient. These computation time improvements along with significant reductions in memory usage because of the nature of circulant matrices make this an attractive approach for

Table 1: Computation times (s).

	Direct		COCG		COCR		COCG-FFT			COCR-FFT		
#dipoles	MATLAB	C++ (Armadillo)	MATLAB	C++ (Armadillo)	MATLAB	C++ (Armadillo)	MATLAB	C++ Armadillo	FFTW	MATLAB	C++ Armadillo	FFTW
441	0.0045	0.0540	0.0029	0.0033	0.0034	0.0037	0.0413	0.0029	0.0069	0.04123	0.0030	0.0069
1681	0.1790	2.1660	0.0790	0.0632	0.0830	0.0680	0.1869	0.0565	0.0600	0.1851	0.0589	0.0549
6561	5.3340	57.8030	1.5296	1.4693	1.6020	1.5353	1.4603	1.2336	0.6431	1.4410	1.3612	0.6512

Table 2: Computation times for the power of 2 optimized grid size.

	Direct		COCG		COCR		COCG-FFT			COCR-FFT		
#dipoles	MATLAB	C++ (Armadillo)	MATLAB	C++ (Armadillo)	MATLAB	C++ (Armadillo)	MATLAB	C++ Armadillo	FFTW	MATLAB	C++ Armadillo	FFTW
4225	1.7129	31.7440	0.6444	0.5555	0.6461	0.5836	0.7637	0.5689	0.2746	0.5785	0.5366	0.2758

Table 3: Comparison of computation times as a function of conjugate gradient scheme accuracy tolerances.

	Tolerance = 1e-5				Tolerance = 1e-3			
	COCG	COCG-FFT	COCR	COCR-FFT	COCG	COCG-FFT	COCR	COCR-FFT
MATLAB	0.3351	0.4090	0.3749	0.4042	0.2061	0.2694	0.2344	0.2613
C++	0.3470	0.1655	0.3741	0.1665	0.3237	0.1073	0.2648	0.1080

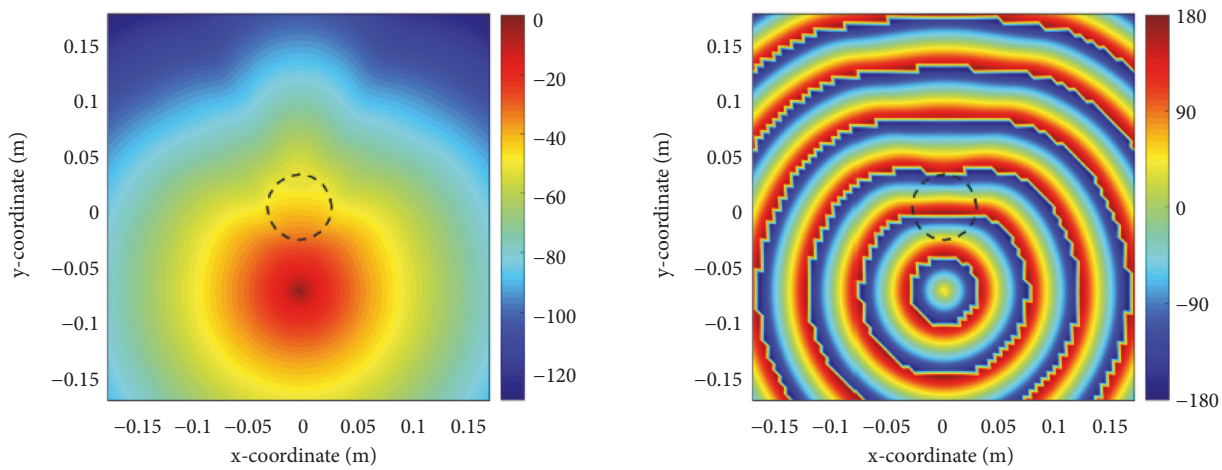

Figure 7: Plots of magnitude (left) and phase (right) distributions for f =1.3 GHz, $\sigma = 1$, $\varepsilon_{r,t} = 40$, $d = 6$ (cm), for forward zone of size 35.2 × 35.2 cm and 4225 dipoles, for background permittivity value of $\varepsilon_{r,bk} = 21.99$.

simplifying and greatly speeding up the image reconstruction process.

Data Availability

No data were used to support this study.

Conflicts of Interest

The authors declare that there are no conflicts of interest regarding the publication of this paper.

Acknowledgments

The article has been included in a thesis by the first author Samar Hosseinzadegan for the Licentiate Degree of Engineering at the Chalmers University of Technology, Göteborg, Sweden [61]. This work was sponsored by an NIH/NCI grant # R01-CA191227 and a Chalmers Foundation Excellence grant.

References

[1] D. J. Brenner and E. J. Hall, "Computed tomography—an increasing source of radiation exposure," *The New England Journal of Medicine*, vol. 357, no. 22, pp. 2277–2284, 2007.

[2] T. Jansson, J. E. Westlin, H. Ahlström, A. Lilja, B. Långström, and J. Bergh, "Positron emission tomography studies in patients with locally advanced and/or metastatic breast cancer: a method for early therapy evaluation?" *Journal of Clinical Oncology*, vol. 13, no. 6, pp. 1470–1477, 1995.

[3] D. M. Ikeda, D. R. Baker, and B. L. Daniel, "Magnetic resonance imaging of breast cancer: Clinical indications and breast MRI reporting system," *Journal of Magnetic Resonance Imaging*, vol. 12, no. 6, pp. 975–983, 2000.

[4] S. G. Orel and M. D. Schnall, "MR imaging of the breast for the detection, diagnosis, and staging of breast cancer," *Radiology*, vol. 220, no. 1, pp. 13–30, 2001.

[5] E. Porter, M. Coates, and M. Popović, "An early clinical study of time-domain microwave radar for breast health monitoring," *IEEE Transactions on Biomedical Engineering*, vol. 63, no. 3, pp. 530–539, 2016.

[6] E. C. Fear, J. Bourqui, C. Curtis, D. Mew, B. Docktor, and C. Romano, "Microwave breast imaging with a monostatic radar-based system: a study of application to patients," *IEEE Transactions on Microwave Theory and Techniques*, vol. 61, no. 5, pp. 2119–2128, 2013.

[7] A. W. Preece, I. Craddock, M. Shere, L. Jones, and H. L. Winton, "MARIA M4: Clinical evaluation of a prototype ultrawideband radar scanner for breast cancer detection," *Journal of Medical Imaging*, vol. 3, no. 3, Article ID 033502, 2016.

[8] H. Song, S. Sasada, T. Kadoya et al., "Detectability of breast tumor by a hand-held impulse-radar detector: performance evaluation and pilot clinical study," *Scientific Reports*, vol. 7, Article ID 16353, 2017.

[9] R. K. Amineh, M. Ravan, A. Khalatpour, and N. K. Nikolova, "Three-dimensional near-field microwave holography using reflected and transmitted signals," *IEEE Transactions on Antennas and Propagation*, vol. 59, no. 12, pp. 4777–4789, 2011.

[10] D. Tajik, F. Foroutan, D. S. Shumakov, A. D. Pitcher, and N. K. Nikolova, "Real-time microwave imaging of a compressed

breast phantom with planar scanning," *IEEE Journal of Electromagnetics, RF and Microwaves in Medicine and Biology*, vol. 2, pp. 154–162, 2018.

[11] R. A. Kruger, D. R. Reinecke, and G. A. Kruger, "Thermoacoustic computed tomography–technical considerations," *Medical Physics*, vol. 26, no. 9, pp. 1832–1837, 1999.

[12] G. Ku and L. V. Wang, "Scanning microwave-induced thermoacoustic tomography: signal, resolution, and contrast," *Medical physics*, vol. 28, pp. 4–10, 2001.

[13] S. P. Poplack, T. D. Tosteson, W. A. Wells et al., "Electromagnetic breast imaging: results of a pilot study in women with abnormal mammograms," *Radiology*, vol. 243, no. 2, pp. 350–359, 2007.

[14] P. M. Meaney, P. A. Kaufman, L. S. Muffly et al., "Microwave imaging for neoadjuvant chemotherapy monitoring: initial clinical experience," *Breast Cancer Research*, vol. 15, article R35, 2013.

[15] S. Y. Semenov, A. E. Bulyshev, A. Abubakar et al., "Microwave-tomographic imaging of the high dielectric-contrast objects using different image-reconstruction approaches," *IEEE Transactions on Microwave Theory and Techniques*, vol. 53, no. 7, pp. 2284–2294, 2005.

[16] J. D. Shea, P. Kosmas, S. C. Hagness, and B. D. Van Veen, "Three-dimensional microwave imaging of realistic numerical breast phantoms via a multiple-frequency inverse scattering technique," *Medical Physics*, vol. 37, no. 8, pp. 4210–4226, 2010.

[17] P. Tournier, M. Bonazzoli, V. Dolean et al., "Numerical modeling and high-speed parallel computing: new perspectives on tomographic microwave imaging for brain stroke detection and monitoring," *IEEE Antennas and Propagation Magazine*, vol. 59, no. 5, pp. 98–110, 2017.

[18] O. M. Bucci, L. Crocco, and R. Scapaticci, "On the optimal measurement configuration for magnetic nanoparticles-enhanced breast cancer microwave imaging," *IEEE Transactions on Biomedical Engineering*, vol. 62, no. 2, pp. 407–414, 2015.

[19] Z. Miao and P. Kosmas, "Multiple-frequency DBIM-TwIST algorithm for microwave breast imaging," *IEEE Transactions on Antennas and Propagation*, vol. 65, no. 5, pp. 2507–2516, 2017.

[20] I. Catapano, L. Crocco, M. D' Urso, and T. Isernia, "3D microwave imaging via preliminary support reconstruction: testing on the Fresnel 2008 database," *Inverse Problems*, vol. 25, no. 2, Article ID 024002, 23 pages, 2009.

[21] A. Fasoula, L. Duchesne, J. Gil Cano, P. Lawrence, G. Robin, and J. Bernard, "On-site validation of a microwave breast imaging system, before first patient study," *Diagnostics*, vol. 8, no. 3, article 53, 2018.

[22] R. Scapaticci, P. Kosmas, and L. Crocco, "Wavelet-based regularization for robust microwave imaging in medical applications," *IEEE Transactions on Biomedical Engineering*, vol. 62, no. 4, pp. 1195–1202, 2015.

[23] T. Rydholm, A. Fhager, M. Persson, and P. M. Meaney, "A first evaluation of the realistic supelec-breast phantom," *IEEE Journal of Electromagnetics, RF and Microwaves in Medicine and Biology*, vol. 1, pp. 59–65, 2017.

[24] T. Rydholm, A. Fhager, M. Persson, S. Geimer, and P. Meaney, "Effects of the plastic of the realistic GeePS-L2S-breast phantom," *Diagnostics*, vol. 8, article 61, 2018.

[25] P. M. Meaney, M. W. Fanning, T. Raynolds et al., "Initial clinical experience with microwave breast imaging in women with normal mammography," *Academic Radiology*, vol. 14, no. 2, pp. 207–218, 2007.

[26] P. M. Meaney, M. W. Fanning, D. Li, S. P. Poplack, and K. D. Paulsen, "A clinical prototype for active microwave imaging of the breast," *IEEE Transactions on Microwave Theory and Techniques*, vol. 48, no. 1, pp. 1841–1853, 2000.

[27] S. Semenov, R. Svenson, A. Boulyshev et al., "Microwave tomography: two-dimensional system for biological imaging," *IEEE Transactions on Biomedical Engineering*, vol. 43, no. 9, pp. 869–877, 1996.

[28] P. M. Meaney, F. Shubitidze, M. W. Fanning et al., "Surface wave multipath signals in near-field microwave imaging," *Journal of Biomedical Imaging*, vol. 2012, Article ID 697253, 8 pages, 2012.

[29] Q. Fang, P. M. Meaney, and K. D. Paulsen, "Singular value analysis of the Jacobian matrix in microwave image reconstruction," *IEEE Transactions on Antennas and Propagation*, vol. 54, no. 8, pp. 2371–2380, 2006.

[30] P. M. Meaney, Q. Fang, T. Rubaek, E. Demidenko, and K. D. Paulsen, "Log transformation benefits parameter estimation in microwave tomographic imaging," *Medical Physics*, vol. 34, no. 6, pp. 2014–2023, 2007.

[31] P. M. Meaney, S. D. Geimer, and K. D. Paulsen, "Two-step inversion in microwave imaging with a logarithmic transformation," *Medical Physics*, vol. 44, no. 8, pp. 4239–4251, 2017.

[32] A. Fhager, M. Gustafsson, and S. Nordebo, "Image reconstruction in microwave tomography using a dielectric debye model," *IEEE Transactions on Biomedical Engineering*, vol. 59, no. 1, pp. 156–166, 2012.

[33] Q. Fang, P. M. Meaney, and K. D. Paulsen, "Viable three-dimensional medical microwave tomography: theory and numerical experiments," *IEEE Transactions on Antennas and Propagation*, vol. 58, no. 2, pp. 449–458, 2010.

[34] P. Rocca, M. Benedetti, M. Donelli, D. Franceschini, and A. Massa, "Evolutionary optimization as applied to inverse scattering problems," *Inverse Problems*, vol. 25, no. 12, Article ID 123003, 2009.

[35] T. M. Grzegorczyk, P. M. Meaney, P. A. Kaufman, R. M. Diflorio-Alexander, and K. D. Paulsen, "Fast 3-D tomographic microwave imaging for breast cancer detection," *IEEE Transactions on Medical Imaging*, vol. 31, no. 8, pp. 1584–1592, 2012.

[36] S. Hosseinzadegan, A. Fhager, M. Persson, and P. Meaney, "Application of two-dimensional discrete dipole approximation in simulating electric field of a microwave breast imaging system," *IEEE Journal of Electromagnetics, RF and Microwaves in Medicine and Biology*, 2018.

[37] M. Frigo and S. G. Johnson, "The design and implementation of FFTW3," in *Proceedings of the IEEE Special Issue on Program Generation, Optimization, and Platform Adaptation*, vol. 93, pp. 216–231, 2005.

[38] E. M. Purcell and C. R. Pennypacker, "Scattering and absorption of light by nonspherical dielectric grains," *The Astrophysical Journal*, vol. 186, pp. 705–714, 1973.

[39] B. T. Draine and P. J. Flatau, "Discrete-dipole approximation for scattering calculations," *Journal of the Optical Society of America A*, vol. 11, pp. 1491–1499, 1994.

[40] K. Skorupski, "Using the DDA (discrete dipole approximation) method in determining the extinction cross section of black carbon," *Metrology and Measurement Systems*, vol. 22, no. 1, pp. 153–164, 2015.

[41] A. Lakhtakia, "Strong and weak forms of the method of moments and the coupled dipole method for scattering of time-harmonic electromagnetic fields," *International Journal of Modern Physics C*, vol. 3, pp. 583–603, 1992.

[42] W. C. Chew, *Waves and Fields in Inhomogeneous Media*, IEEE press, 1995.

[43] B. T. Draine and J. Goodman, "Beyond clausius-mossotti-wave propagation on a polarizable point lattice and the discrete dipole approximation," *The Astrophysical Journal*, vol. 405, no. 2, pp. 685–697, 1993.

[44] F. Kahnert, "Numerical methods in electromagnetic scattering theory," *Journal of Quantitative Spectroscopy & Radiative Transfer*, vol. 79-80, pp. 775–824, 2003.

[45] M. A. Yurkin, V. P. Maltsev, and A. G. Hoekstra, "Convergence of the discrete dipole approximation. I. theoretical analysis," *The Journal of the Optical Society of America A (JOSA A)*, vol. 23, pp. 2578–2591, 2006.

[46] A. Sihvola, "Peculiarities in the dielectric response of negative-permittivity scatterers," *Progress in Electromagnetics Research*, vol. 66, pp. 191–198, 2006.

[47] G. H. Golub and C. F. Van Loan, *Matrix Computations*, vol. 3, JHU Press, 2012.

[48] P. J. Flatau, "Improvements in the discrete-dipole approximation method of computing scattering and absorption," *Optics Expresss*, vol. 22, no. 16, p. 1205, 1997.

[49] J. J. Goodman, P. J. Flatau, and B. T. Draine, "Application of fast-Fourier-transform techniques to the discrete-dipole approximation," *Optics Expresss*, vol. 16, no. 15, pp. 1198–1200, 1991.

[50] P. Sonneveld, "CGS, a fast lanczos-type solver for nonsymmetric linear systems," *SIAM Journal on Scientific and Statistical Computing*, vol. 10, no. 1, pp. 36–52, 1989.

[51] H. A. van der Vorst, "BI-CGSTAB: a fast and smoothly converging variant of BI-CG for the solution of nonsymmetric linear systems," *SIAM Journal on Scientific and Statistical Computing*, vol. 13, no. 2, pp. 631–644, 1992.

[52] M. H. Gutknecht, "Variants of BICGSTAB for matrices with complex spectrum," *SIAM Journal on Scientific Computing*, vol. 14, no. 5, pp. 1020–1033, 1993.

[53] Y. Saad and M. Schultz, "GMRES: a generalized minimal residual algorithm for solving nonsymmetric linear systems," *SIAM Journal on Scientific and Statistical Computing*, vol. 7, no. 3, pp. 856–869, 1986.

[54] R. W. Freund, "A transpose-free quasi-minimal residual algorithm for non-hermitian linear systems," *SIAM Journal on Scientific Computing*, vol. 14, no. 2, pp. 470–482, 1993.

[55] R. W. Freund, "Conjugate gradient-type methods for linear systems with complex symmetric coefficient matrices," *SIAM Journal on Scientific and Statistical Computing*, vol. 13, no. 1, pp. 425–448, 1992.

[56] M. Clemens and T. Weiland, "Iterative methods for the solution of very large complex symmetric linear systems of equations in electrodynamics," Front Range Scientific Computations, Inc, Lakewood, NJ, USA, 1996.

[57] H. A. van der Vorst and J. B. M. Melissen, "Petrov-Galerkin type method for solving Ax = b, where A is symmetric complex," *IEEE Transactions on Magnetics*, vol. 26, no. 2, pp. 706–708, 1990.

[58] T. Sogabe and S.-L. Zhang, "A COCR method for solving complex symmetric linear systems," *Journal of Computational and Applied Mathematics*, vol. 199, no. 2, pp. 297–303, 2007.

[59] C. Sanderson and R. Curtin, "Armadillo: a template-based C++ library for linear algebra," *Journal of Open Source Software*, 2016.

[60] C. Sanderson and R Curtin, "A user-friendly hybrid sparse matrix class in C++," in *Proceedings of the International Congress on Mathematical Software*, pp. 422–430, 2018.

[61] S. Hosseinzadegan, *A discrete dipole approximation forward solver for microwave breast imaging [Dissertation, thesis]*, Chalmers University of Technology, 2019.

Hindawi
International Journal of Antennas and Propagation
Volume 2019, Article ID 7548243, 19 pages
https://doi.org/10.1155/2019/7548243

Research Article

Electromagnetic Model of a SPR Sensor Coupled to Array of Nanoparticles by Periodic Green's Function

André Cruz,[1] Victor Dmitriev,[1] Tommaso Del Rosso,[2] and Karlo Costa[1]

[1] *Department of Electrical Engineering, Federal University of Pará, Belém-PA, Brazil*
[2] *Department of Physics, Pontifical Catholic University of Rio de Janeiro, Rio de Janeiro-RJ, Brazil*

Correspondence should be addressed to André Cruz; andcruz@ufpa.br

Received 28 March 2019; Accepted 3 June 2019; Published 16 July 2019

Guest Editor: Sandra Costanzo

In this paper, we present a theoretical study of a Surface Plasmon Resonance Sensor in the Surface Plasmon Coupled Emission (SPCE) configuration. A periodic planar array of core-shell gold nanoparticles (AuNps), chemically functionalized to aggregate fluorescent molecules, is coupled to the sensor structure. These nanoparticles, characterized as target particles, are modeled as equivalent nanodipoles. The electromagnetic modeling of the device was performed using the spectral representation of the magnetic potential by Periodic Green's Function (PGF). Parametric results of spatial electric and magnetic fields are presented at wavelength 632.8nm. We also present a spectral analysis of the magnetic potential, where we verify the appearance of the surface plasmon polariton (SPP) waves. To validate the analytical method, we compared the limit case of small concentration of nanoparticles with published works. We also present a convergence analysis of the solution as a function of the concentration of nanoparticles in the periodic array. The results show that the theoretical method of PFG can be efficiently used as a tool for design of this sensing device.

1. Introduction

In the last two decades, the development of new optical devices based on metallic structures has been of great interest. This is due to the interesting optical and electromagnetic properties that the metals present in the regime of high frequency [1, 2]. The interaction between metals and electromagnetic waves, in the optical regime, produces a collective oscillatory behavior in the gas of free electrons in the metal in phase opposite to the incident field, resulting in the formation of a surface wave with evanescent characteristic in the metal/dielectric interface, known as surface plasmon wave [3]. This phenomenon is related to the negative real part of the dielectric function of metal, which occurs when the excitation is due by optical fields [3, 4]. In view of these properties, noble metals have been used for development of devices based on the Surface Plasmon Resonance (SPR), in planar structures, and Localized Surface Plasmon Resonance (LSPR), in isolated metallic nanoparticles [3–5].

Recently, research has shown that, on particular conditions, SPP waves can be efficiently used to control the near field intensification in metal nanostructures [6, 7]. The study of these phenomena has been of great importance for the development of SPR sensors devices for applications in biosensing, photodetection, spectroscopy, and detection of metallic nanopoluents resulting from nanofabrication processes [7, 8]. A conventional SPR sensor in the Surface Plasmon Coupled Emission (SPCE) configuration consists of a multilayer structure, generally a thin film of noble metal (gold or silver) over a dielectric prism, excited by an external laser source. On the structure of the device is coupled a microfluidic channel where, among other compounds, fluorophores are present, luminescent substances that when excited emit optical radiation [9–11]. In this configuration, it has been proposed to use chemically functionalized gold nanoparticles (AuNps) to obtain affinity with the luminescent substance, and then these AuNps couple to chemical binders on the surface of the sensor. The detection of high sensitivity is associated to the increase in the near field of nanoparticles that induce plasmon waves, amplifying the luminescence of the fluorophores and consequently, exciting SPP waves in the metal surface of the sensor [10–13]. Recently, chemical

reactions in liquid solutions have been commonly used as a low cost procedure for AuNps production. In this process there is the presence of a surfactant agent that provides chemical and mechanical stability to the nanoparticle. The result is a type of metal particle covered with a thin superficial dielectric layer, which is called Core-shell. The optical response of these spherical particles in a free space was verified in [5].

In [10, 11], spatial and spectral analyses were performed for a single particle immobilized on the SPCE sensor structure, and from this, the radiated fields in the structure were verified. However, the existence of the electromagnetic interaction of more than one particle excited by the external source must be considered, yet, the modeling of the random spatial distribution of nanoparticles in a sample is still a great challenge. A coherent way to approximate this distribution is to consider that the sample takes the form of a periodic planar array of nanoparticles uniformly distributed over the gold layer [4].

The electromagnetic response of a multilayer structure excited by a planar array of nanosources can be described by the method of discrete spectral representation by Periodic Green's Function (PGF). However, when the concentration of AuNps becomes small, the discrete spectrum converges to a continuous spectrum, which is similar to that analyzed in [10, 11]. A brief introduction about the analysis of this sensor by PGF is discussed in [14], where the authors presented only a spectral analysis of the dominant plasmonic mode in the sensor structure.

The objective of this work is to present a electromagnetic model of a surface plasmon resonance sensor in the SPCE configuration, coupled with a planar periodic array of Core-Shell AuNps. For this sensor, we obtained a spectral representation of the magnetic vector potential by the Periodic Green's Function. To validate the method, we compared the limit case of low concentration of nanoparticles with the similar case analyzed in [10, 11]; in addition, we verified the convergence of the method. Magnetic potential field and electromagnetic fields were analyzed by checking the effects of the thickness of the gold layer on the sensor structure, in addition to the effects of the dipole moment inclination induced on the nanoparticles. In this work, we expanded the spectral analysis to verify the effects of the plasmon poles on the spectral representation of the complex Fourier series.

2. Functional Description of the SPCE Sensor

The principle of operation of the SPCE sensor is based on the interaction of the field re-irradiated by the target particle on the sensor structure, exciting plasmon modes that creates polarized propagating waves at the sensor output [9–11]. As a target particle, it is proposed to use chemically-functionalized Core-Shell AuNps to attract fluorophores, enhancing the sensor's optical response. The functional illustration of the SPCE sensor is shown in Figure 1.

The physical structure of the sensor is formed by a gold layer deposited above a dielectric prism and below a microfluidic channel where multicompounds, fluorophores, and Core-Shell AuNps are present in suspension. On the gold layer there is a binding substance with gold/target particle affinity that immobilizes the AuNps aggregated with fluorophores on the surface of the sensor. This substance, considered to be electrically inert, is used as a chemical spacer and acts to separate the immobilized particles and the gold sheet.

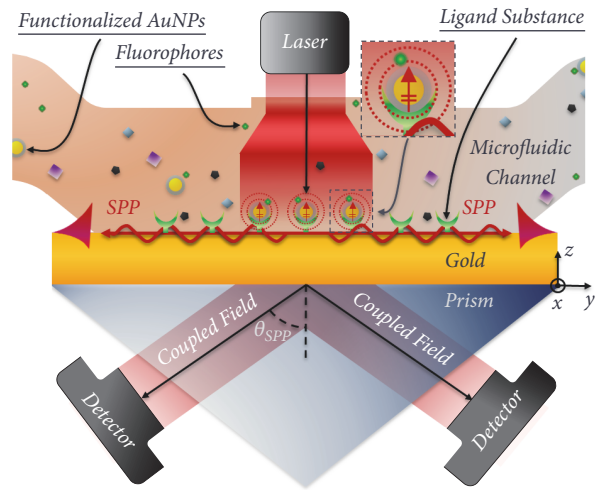

Figure 1: Functional illustration of the SPCE sensor coupled to a microfluidic channel.

The excitation, realized by a monochromatic optical laser with wavelength $\lambda = 632.8nm$, is directly applied to the sample above the gold layer, exciting the target particles, which consequently re-irradiate fields that excite SPP waves in the interface between the gold layer and the dielectric of the microfluidic channel. These SPP waves are excited by the TM evanescent radiation component of the excited particle. Thus, part of the plasmon wave is transmitted through the gold layer, coupling in the region of the prism a transversal magnetic wave as a function of the SPP wave. The formation of this TM wave provides a far field pattern like a light cone in the prism region, where θ_{SPP} is the characteristic plasmonic angle of this cone (Figure 1).

Although the radiation scattered by the target particle is not polarized, the field that mates in the region of the prism is highly polarized in TM. This characteristic can be understood by the opposite process, which occurs in the excitation of SPP waves by plane waves, exclusively polarized in TM, as in the Kretschmann configuration. For this reason, the SPCE sensor acts as a natural filter for TM polarization.

Depending on the electromagnetic characteristics of the sample formed by the multicompounds, in other words, the dielectric characteristics of the environment formed by the medium and multicompounds, in the microfluidic channel, the intensity, geometry, and angle θ_{SPP} of the light cone, measured by a detector, are changed, thus defining the output of the sensor.

3. Electromagnetic Model of Sensor

3.1. Description of the Problem. The electromagnetic interaction between the laser source and the Core-Shell AuNps

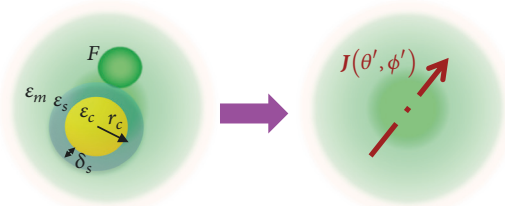

Figure 2: Equivalent between excited target particle and hertzian dipole.

can be described by the quasi-static Rayleigh scattering, since the wavelength of the source is much larger than the particle dimensions [5]; thus the radiation scattered by the nanoparticle is described by the fundamental dipole moment $p_{cs} = \alpha_{cs}E_0$, characterized by polarizability (1), excited by electric field E_0.

$$\alpha_{cs} = 4\pi\varepsilon_m (r_c + \delta_s)^3 \cdot \left[\frac{f(\varepsilon_c - \varepsilon_m)(2\varepsilon_s + \varepsilon_m) + (2\varepsilon_s + \varepsilon_c)(\varepsilon_s - \varepsilon_m)}{f(\varepsilon_c - \varepsilon_m)(2\varepsilon_s - 2\varepsilon_m) + (2\varepsilon_s + \varepsilon_c)(\varepsilon_s + 2\varepsilon_m)} \right] \quad (1)$$

with $f = r_c^3/(r_c + \delta_s)^3$ being the fraction of the total volume of the particle occupied by the core, r_c and δ_s the radius of the core and the thickness of the nanoparticle shell, respectively, and ε_c, ε_s, and ε_m the permittivities of the core, shell, and medium where the nanoparticles are inserted. Similarly, the spectral emission of the fluorescence for the excitation wavelength can be modeled by the polarizability of the fluorophore α_{FF} [15].

Due to the dimensions of the Core-Shell AuNps and the fluorophores, we can characterize the target particle excited by an effective dipole moment:

$$p_{eff} = p_{cs} + \alpha_{FF} R_e^{FF} \quad (2)$$

where R_e^{FF} is the field reaction to the excitation of the fluorophore, which is a function of the excitation intensity and the Fluorescence F. From (2), target particles excited by the external (suppressed) source are modeled as sources of concentrated electric current J (3) (hertzian dipoles), with current moments $I_0 l = j\omega p_{eff}$ in the direction $\hat{a}_r$ oriented by the parametric elevation θ' and azimuth ϕ' angles. The equivalence is shown in Figure 2.

$$\mathbf{J}(\theta', \phi') = j\omega p_{eff} \delta(x)\delta(y)\delta(z-h)\hat{a}_r(\theta', \phi') \quad (3)$$

In the microfluidic channel, the target particles are distributed randomly in space. Due to the fact that these are immobilized near the surface of the sensor, and the low concentration, we can approximate the sample as a planar array of uniformly distributed nanodipoles, equally distant from the gold sheet.

Since the sample was modeled as a periodic planar array, we can perform the field analysis by defining a particular cell with width $2a$ at x, $2b$ at y, and with the current source located at a height h by the chemical spacer (Figure 3).

The analysis region is delimited by three volumes $V1$, $V2$, and $V3$; medium 1, medium 2, and medium 3, respectively, are enclosed by the closed surfaces $S_1 = S_{11} + S_{12} + S_{13} + S_{14} + S_{15} + S_{16}$; $S_2 = S_{21} + S_{22} + S_{23} + S_{24} + S_{25} + S_{26}$; and $S_3 = S_{31} + S_{32} + S_{33} + S_{34} + S_{35} + S_{36}$, thus forming three six-sided prisms (Figure 4).

The electric and magnetic fields were determined by the magnetic potential method, defined by the solution of the Helmholtz equation in the three media [16]:

$$\begin{aligned} -\left(\nabla^2 + k_1^2\right)\mathbf{A}_1 &= \mu_1 \mathbf{J} \\ -\left(\nabla^2 + k_{2,3}^2\right)\mathbf{A}_{2,3} &= 0 \end{aligned} \quad (4)$$

In order for the electromagnetic field to obey the periodic conditions, the potential field on surfaces $S_{v1}, S_{v2}, S_{v3}, S_{v4}$ must satisfy the boundary conditions (5) in the medium $v = 1$, 2 and 3. In regions distant from the source, the potential field must satisfy the limit boundary conditions (6).

$$\begin{aligned} \mathbf{A}_{[v]}(a, y, z)\big|_{S_{[v]1}} &= \mathbf{A}_{[v]}(-a, y, z)\big|_{S_{[v]2}}, \\ \frac{\partial \mathbf{A}_{[v]}}{\partial x}(a, y, z)\bigg|_{S_{[v]1}} &= \frac{\partial \mathbf{A}_{[v]}}{\partial x}(-a, y, z)\bigg|_{S_{[v]2}} \\ \mathbf{A}_{[v]}(x, b, z)\big|_{S_{[v]3}} &= \mathbf{A}_{[v]}(x, -b, z)\big|_{S_{[v]4}}, \\ \frac{\partial \mathbf{A}_{[v]}}{\partial y}(x, b, z)\bigg|_{S_{[v]3}} &= \frac{\partial \mathbf{A}_{[v]}}{\partial y}(x, -b, z)\bigg|_{S_{[v]4}} \end{aligned} \quad (5)$$

$$\begin{aligned} \lim_{z \longrightarrow +\infty} \mathbf{A}_1(x, y, z)\big|_{S_{15}} &= 0, \\ \lim_{z \longrightarrow -\infty} \mathbf{A}_3(x, y, z)\big|_{S_{36}} &= 0 \end{aligned} \quad (6)$$

At the interfaces $z = d_u$ $(u = 1,2)$, formed by the surfaces S_{u6} and $S_{[u+1]5}$, the potential field must obey (7) and (8), so that the conditions of continuity of tangential fields and normal flows are met.

$$\begin{aligned} A_{x_{[u+1]}, y_{[u+1]}}\big|_{z=d_{[u]}} &= A_{x_{[u]}, y_{[u]}}\big|_{z=d_{[u]}} \\ \frac{1}{\mu_{[u+1]}} \frac{\partial}{\partial z}\left[A_{x_{[u+1]}, y_{[u+1]}}\right]\bigg|_{z=d_{[u]}} &= \frac{1}{\mu_{[u]}} \frac{\partial}{\partial z}\left[A_{x_{[u]}, y_{[u]}}\right]\bigg|_{z=d_{[u]}} \end{aligned} \quad (7)$$

$$\begin{aligned} \frac{1}{\mu_{[u+1]}} A_{z_{[u+1]}}\bigg|_{z=d_{[u]}} &= \frac{1}{\mu_{[u]}} A_{z_{[u]}}\bigg|_{z=d_{[u]}} \\ \frac{1}{\mu_{[u+1]}\varepsilon_{[u+1]}}\left(\nabla \cdot \mathbf{A}_{[u+1]}\right)\bigg|_{z=d_{[u]}} &= \frac{1}{\mu_{[u]}\varepsilon_{[u]}}\left(\nabla \cdot \mathbf{A}_{[u]}\right)\bigg|_{z=d_{[u]}} \end{aligned} \quad (8)$$

From the Partial Differential Equation (PDE) defined in (4) and the conditions in (5)-(8), the fields were determined

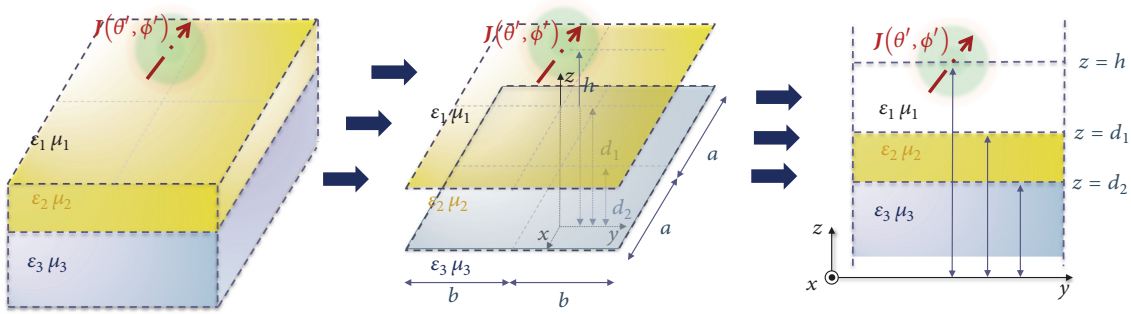

Figure 3: Definition of the analysis cell. (Left) 3D view of the three layers (microfluidic region (1), gold layer (2), and prism (3)) and one point dipole. (Middle) 3D view of the interfaces and geometry of the unit cell. (Right) Side view of the unit cell.

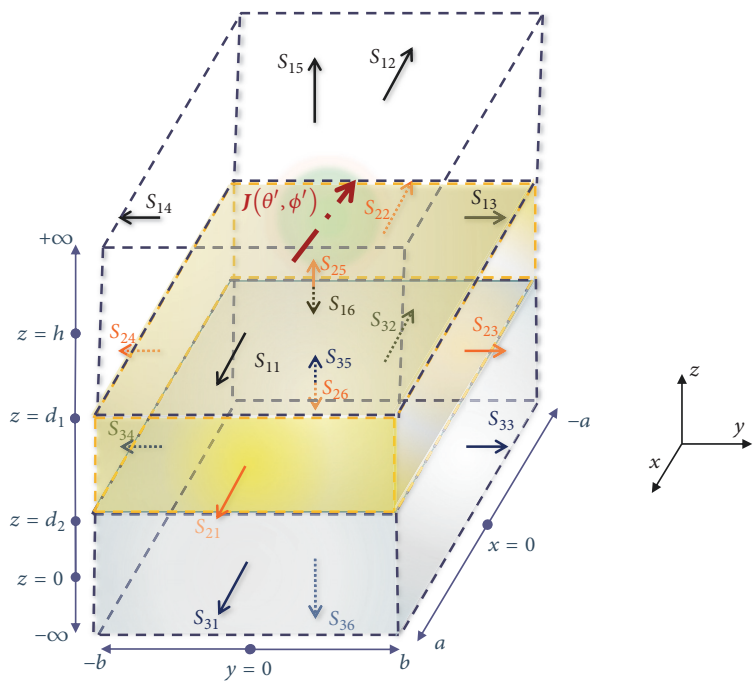

Figure 4: Analysis volume.

by the Periodic Green's Function in xy, with Limit and Neumann boundary conditions in z.

3.2. Magnetic Potential Tensor by PGF Method. The Periodic Green's Function is written in terms of the discrete spectral expansion in xy (9), defined by the inverse transform of the complex Fourier series, applied to one-dimensional Green's function problem at z in the media 1, 2, and 3 [16].

$$g_{1,2,3}\left(\mathbf{r},\mathbf{r}'\right) = \sum_{m=-\infty}^{\infty}\sum_{n=-\infty}^{\infty} g_{1,2,3_{mn}}\left(z,\mathbf{r}'\right) u_m\left(x\right) u_n\left(y\right) \quad (9)$$

$$u_m\left(x\right) = \frac{1}{\sqrt{2a}} e^{jk_x x} \quad (10)$$

$$u_n\left(y\right) = \frac{1}{\sqrt{2b}} e^{jk_y y} \quad (11)$$

where $u_m(x)$ and $u_n(y)$ are the eigenfunctions of the periodic problem at x and y, with eigenvalues $k_x = m\pi/a$ and $k_y = n\pi/b$. In the spectral domain mn, the one-dimensional Green's functions z in the media 1, 2, and 3 are, respectively, $g_{1_{mn}}$ in $(z > d_1)$, $g_{2_{mn}}$ in $(d_1 \geq z \geq d_2)$, and $g_{3_{mn}}$ in $(z < d_2)$.

$$g_{1_{mn}}\left(z,\mathbf{r}'\right)=\frac{1}{2jk_{z1}}\left[e^{-jk_{z1}|z-z'|}+e^{-jk_{z1}(z+z'-2d_1)}\right]\overline{u}_m\left(x'\right)\overline{u}_n\left(y'\right) \tag{12}$$

$$g_{2_{mn}}\left(z,\mathbf{r}'\right)=\left[\frac{\cos k_{z2}\left(\left|z-z'\right|+\left[d_2-d_1\right]\right)+\cos k_{z2}\left(\left[z'+z\right]-\left[d_2+d_1\right]\right)}{2k_{z2}\sin k_{z2}\left(d_2-d_1\right)}\right]\overline{u}_m\left(x'\right)\overline{u}_n\left(y'\right) \tag{13}$$

$$g_{3_{mn}}\left(z,\mathbf{r}'\right)=\frac{1}{2jk_{z3}}\left[e^{-jk_{z3}|z'-z|}+e^{jk_{z3}(z+z'-2d_2)}\right]\overline{u}_m\left(x'\right)\overline{u}_n\left(y'\right) \tag{14}$$

where k_{zv} is the z-propagation constant in the medium $v = 1, 2, 3$.

$$k_{z[v]}=\sqrt{k_{[v]}^2-k_x^2-k_y^2} \tag{15}$$

Applying the Green identity in each medium, using the boundary conditions defined in (5)-(8) and solving the system of equations, the magnetic potential field in the tensor form is given by [16]:

$$\begin{aligned}\mathbf{A}_{1,2,3}(\mathbf{r}) &= \sum_{m=-\infty}^{\infty}\sum_{n=-\infty}^{\infty}\begin{bmatrix} A_{xx_{1,2,3}}^{mn} & 0 & 0\\ 0 & A_{yy_{1,2,3}}^{mn} & 0\\ -jk_xA_{zx_{1,2,3}}^{mn} & -jk_yA_{zy_{1,2,3}}^{mn} & A_{zz_{1,2,3}}^{mn}\end{bmatrix}\\ &\cdot\mathbf{I}\left(\theta',\phi'\right)e^{-j[k_xx+k_yy]}\end{aligned} \tag{16}$$

the element A_{ij} being the component i, excited by the component j of the current density per cell $\mathbf{I}$.

$$\begin{aligned}\mathbf{I}\left(\theta',\phi'\right) &= \frac{j\omega p_{eff}}{8ab}\left[\cos\phi'\sin\theta' \quad \sin\phi'\sin\theta' \quad \cos\theta'\right]^t\end{aligned} \tag{17}$$

The elements of the magnetic potential tensor (16), in the mn spectral domain and z spatial domain, are, in medium 1,

$$\begin{aligned}A_{xx_1}^{mn}(z) &= A_{yy_1}^{mn}(z)\\ &= -j\mu_1\frac{1}{k_{z1}}\left[e^{-jk_{z1}|z-h|}+\widetilde{R}_{12}^{TE}e^{-jk_{z1}(z+h-2d_1)}\right]\end{aligned} \tag{18}$$

$$A_{zx_1}^{mn}(z)=A_{zy_1}^{mn}(z)=-\mu_1S_{1d1}^{EM}\frac{1}{k_{z1}}e^{-jk_{z1}(z+h-2d_1)} \tag{19}$$

$$A_{zz_1}^{mn}(z)=-j\mu_1\frac{1}{k_{z1}}\left[e^{-jk_{z1}|z-h|}+\widetilde{R}_{12}^{TM}e^{-jk_{z1}(z+h-2d_1)}\right] \tag{20}$$

In medium 2,

$$\begin{aligned}A_{xx_2}^{mn}(z) &= A_{yy_2}^{mn}(z)=-j\mu_2\\ &\cdot\frac{1}{k_{z2}}\left[e^{jk_{z2}(z-d_2)}+R_{23}^{TE}e^{-jk_{z2}(z-d_2)}\right]\frac{\widetilde{T}_{23}^{TE}}{T_{23}^{TE}}e^{-jk_{z1}(h-d_1)}\end{aligned} \tag{21}$$

$$\begin{aligned}A_{zx_2}^{mn}(z) &= A_{zy_2}^{mn}(z)=-\mu_2\\ &\cdot\frac{1}{k_{z2}}\left[S_{2d1}^{EM}e^{jk_{z2}(z-d_2)}+S_{2d2}^{EM}e^{-jk_{z2}(z-d_2)}\right]\\ &\cdot\widetilde{T}_{23}^{TM}e^{-jk_{z1}(h-d_1)}\end{aligned} \tag{22}$$

$$\begin{aligned}A_{zz_2}^{mn}(z) &= -j\mu_2\frac{1}{k_{z2}}\left[e^{jk_{z2}(z-d_2)}+R_{23}^{TM}e^{-jk_{z2}(z-d_2)}\right]\frac{\varepsilon_2}{\varepsilon_1}\\ &\cdot\frac{\widetilde{T}_{23}^{TM}}{T_{23}^{TM}}e^{-jk_{z1}(h-d_1)}\end{aligned} \tag{23}$$

In medium 3,

$$\begin{aligned}A_{xx_3}^{mn}(z) &= A_{yy_3}^{mn}(z)\\ &= -j\mu_3\frac{1}{k_{z3}}e^{j[k_{z3}(z-d_2)-k_{z1}(h-d_1)]}\frac{\mu_2k_{z3}}{\mu_3k_{z2}}\widetilde{T}_{23}^{TE}\end{aligned} \tag{24}$$

$$A_{zx_3}^{mn}(z)=A_{zy_3}^{mn}(z)=-\mu_3\frac{1}{k_{z3}}e^{j[k_{z3}(z-d_2)-k_{z1}(h-d_1)]}S_{3d2}^{EM} \tag{25}$$

$$A_{zz_3}^{mn}(z)=-j\mu_3\frac{1}{k_{z3}}e^{j[k_{z3}(z-d_2)-k_{z1}(h-d_1)]}\frac{\varepsilon_2k_{z3}}{\varepsilon_1k_{z2}}\widetilde{T}_{23}^{TM} \tag{26}$$

The Fresnel transmission and reflection coefficients of the TE and TM modes follow the definition [17]:

$$T_{ab}^{TE}=1+R_{ab}^{TE}=1+\frac{\mu_bk_{za}-\mu_ak_{zb}}{\mu_bk_{za}+\mu_ak_{zb}} \tag{27}$$

$$T_{ab}^{TM}=1+R_{ab}^{TM}=1+\frac{\varepsilon_bk_{za}-\varepsilon_ak_{zb}}{\varepsilon_bk_{za}+\varepsilon_ak_{zb}} \tag{28}$$

The generalized reflection and transmission coefficients TE and TM are defined in (29)-(32).

$$\widetilde{R}_{12}^{TE}=1-\frac{T_{21}^{TE}\left[1-R_{23}^{TE}e^{2jk_{z2}(d_2-d_1)}\right]}{\left[1-R_{21}^{TE}R_{23}^{TE}e^{2jk_{z2}(d_2-d_1)}\right]} \tag{29}$$

$$\widetilde{T}_{23}^{TE} = \frac{T_{21}^{TE} T_{23}^{TE} e^{jk_{z2}(d_2-d_1)}}{\left[1 - R_{21}^{TE} R_{23}^{TE} e^{2jk_{z2}(d_2-d_1)}\right]} \tag{30}$$

$$\widetilde{R}_{u2}^{TM} = 1 - \frac{T_{2u}^{TM}\left[1 - R_{2u}^{TM} e^{2jk_{z2}(d_2-d_1)}\right]}{\left[1 - R_{2u}^{TM} R_{2u}^{TM} e^{2jk_{z2}(d_2-d_1)}\right]}, \quad u = 1, 3 \tag{31}$$

$$\widetilde{T}_{23}^{TM} = \frac{T_{21}^{TM} T_{23}^{TM} e^{jk_{z2}(d_2-d_1)}}{\left[1 - R_{21}^{TM} R_{23}^{TM} e^{2jk_{z2}(d_2-d_1)}\right]} \tag{32}$$

The S^{EM} coupling coefficients relate the reflection and transmission coefficients of TE and TM modes:

$$S_{1d1}^{EM} = \frac{1}{2k_{z2}}\left[\zeta_{12}\frac{\varepsilon_1 k_{z2}}{\varepsilon_2 k_{z1}}\frac{\mu_1}{\mu_2}\left[1 + \widetilde{R}_{12}^{TM}\right]\left[1 + \widetilde{R}_{12}^{TE}\right] + \zeta_{23}\frac{\varepsilon_2 k_{z1}}{\varepsilon_3 k_{z2}}\frac{\mu_2}{\mu_3}\widetilde{T}_{23}^{TM}\widetilde{T}_{23}^{TE}\right] \tag{33}$$

$$S_{2d1}^{EM} = \frac{1}{2}\left[\zeta_{12}\frac{1}{k_{z1}}\frac{\mu_1}{\mu_2}\frac{1}{T_{23}^{TM}}\left[1 + \widetilde{R}_{12}^{TE}\right] + \zeta_{23}\frac{1}{k_{z2}}\frac{\varepsilon_2\mu_2}{\varepsilon_3\mu_3}\frac{R_{21}^{TM}}{T_{21}^{TM}}\widetilde{T}_{23}^{TE} e^{jk_{z2}(d_2-d_1)}\right] \tag{34}$$

$$S_{2d2}^{EM} = \frac{1}{2}\left[\zeta_{12}\frac{1}{k_{z1}}\frac{\mu_1}{\mu_2}\frac{R_{23}^{TM}}{T_{23}^{TM}}\left[1 + \widetilde{R}_{12}^{TE}\right] + \zeta_{23}\frac{1}{k_{z2}}\frac{\varepsilon_2\mu_2}{\varepsilon_3\mu_3}\frac{1}{T_{21}^{TM}}\widetilde{T}_{23}^{TE} e^{-jk_{z2}(d_2-d_1)}\right] \tag{35}$$

$$S_{3d2}^{EM} = \frac{1}{2k_{z2}}\left[\zeta_{12}\frac{\mu_1 k_{z3}}{\mu_2 k_{z1}}\widetilde{T}_{23}^{TM}\left[1 + \widetilde{R}_{12}^{TE}\right] + \zeta_{23}\frac{\mu_2}{\mu_3}\left[1 + \widetilde{R}_{32}^{TM}\right]\widetilde{T}_{23}^{TE}\right] \tag{36}$$

being ζ coupling parameters at interfaces d_1 and d_2:

$$\zeta_{ab} = \left[\frac{\varepsilon_b\mu_b - \varepsilon_a\mu_a}{\varepsilon_a\mu_a}\right] \tag{37}$$

Given the magnetic potential, the magnetic and electric fields can be easily obtained through differential operations [18].

$$\mathbf{H} = \frac{1}{\mu}\nabla \times \mathbf{A} \tag{38}$$

$$\mathbf{E} = \frac{1}{j\omega\mu\varepsilon}\nabla\left(\nabla \cdot \mathbf{A}\right) - j\omega\mathbf{A} \tag{39}$$

3.3. Alternative Form of PGF Spectral Representation. The discrete spectral representations in the solutions of the PGF in (16) are done as double sums of $-\infty$ to $+\infty$, which may require a reasonable computational cost in the simulations. To reduce such cost, it is proposed to change the base functions in the sums using the Euler identity, provided that the spectral terms in (16) obey the following conditions:

$$\begin{aligned} c_{m,n}(z) &= c_{-m,-n}(z) = c_{m,-n}(z) = c_{-m,n}(z), \\ c_{m,0}(z) &= c_{-m,0}(z), \\ c_{0,n}(z) &= c_{0,-n}(z) \end{aligned} \tag{40}$$

That is, these spectral terms are even functions with the variables m and n. The proposed identities are

$$\begin{aligned} S(z) &= \sum_{m=-\infty}^{\infty}\sum_{m=-\infty}^{\infty} c_{mn}(z)\, e^{-j[k_x x + k_y y]} \\ &= \sum_{m=0}^{\infty}\sum_{m=0}^{\infty} \epsilon_{mn} c_{mn}(z) \cos\left[k_x x\right]\cos\left[k_y y\right] \end{aligned} \tag{41}$$

$$\begin{aligned} \frac{\partial S}{\partial x}(z) &= \sum_{m=-\infty}^{\infty}\sum_{m=-\infty}^{\infty} c_{mn}(z)\left[-jk_x\right] e^{-j[k_x x + k_y y]} \\ &= \sum_{m=0}^{\infty}\sum_{m=0}^{\infty} \epsilon_{mn} c_{mn}(z)\left[-k_x\right]\sin\left[k_x x\right]\cos\left[k_y y\right] \end{aligned} \tag{42}$$

$$\begin{aligned} \frac{\partial S}{\partial y}(z) &= \sum_{m=-\infty}^{\infty}\sum_{m=-\infty}^{\infty} c_{mn}(z)\left[-jk_y\right] e^{-j[k_x x + k_y y]} \\ &= \sum_{m=0}^{\infty}\sum_{m=0}^{\infty} \epsilon_{mn} c_{mn}(z)\left[-k_y\right]\cos\left[k_x x\right]\sin\left[k_y y\right] \end{aligned} \tag{43}$$

where ϵ_{mn} is the double Neumann number:

$$\epsilon_{mn} = \begin{cases} 1, & m = 0, n = 0 \\ 2, & m = 0, n \neq 0 \text{ or } m \neq 0, n = 0 \\ 4, & m \neq 0, n \neq 0 \end{cases} \tag{44}$$

Note that, by changing the exponential base functions to cosines base functions, the domain of the spectral representation is reduced to $mn[0, \infty]$, thus reducing computational cost four times.

4. Method Validation and Convergence Analysis

In [10], authors analyzed a SPCE sensor coupled to a single nanoparticle modeled as a hertzian dipole with current momentum $I_0 l = 1Am$. In this analysis, they used the COMSOL Multiphysics, software based on the finite element method, and the DCIM (Discrete Complex Image Method), a semianalytical method used in the spectral representation of the fields in a structure.

In order to verify the validity of the PGF method, we have chosen to test the limiting case in which the nanoparticles are distant from each other in the planar array, comparing the analysis cell with the case studied in [10]. We can use this approach because, in the limiting case, the individual electromagnetic radiation of each cell does not interact with the neighboring cell, converging to the problem of a single

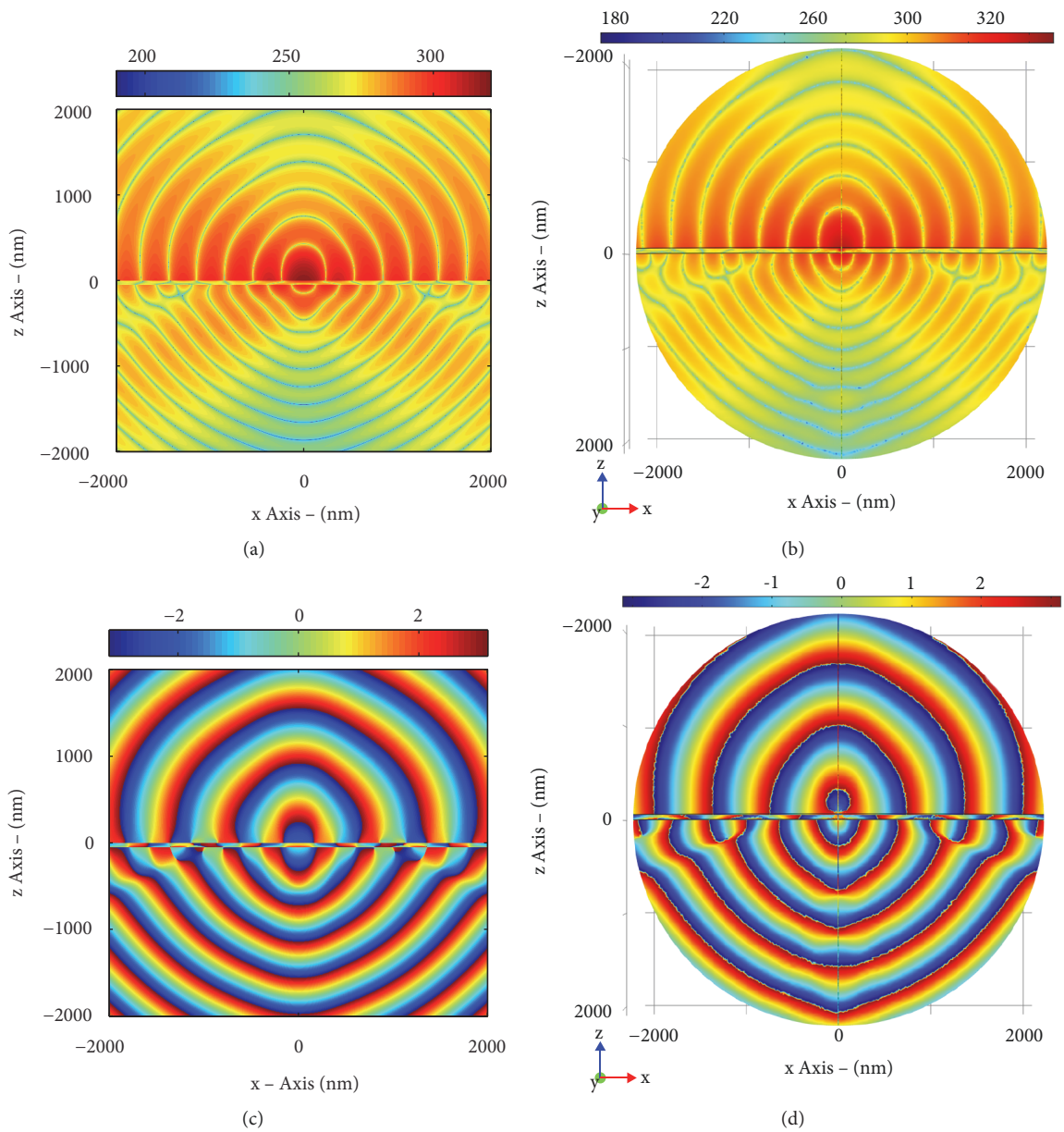

FIGURE 5: Component E_z, Amplitude (dB) ($20\log|\mathrm{Re}(E_z)|$): (a) PGF 3D, (b) [10]; Phase (rad) ($angle(E_z)$): (c) PGF, (d) [10]. In these results we set the following: $\delta_g = 50nm$, $h = 20nm$, $\theta' = \phi' = 0^\circ$, and $\lambda = 632.8nm$.

nanoparticle excited by an external source. Thus, the Core-Shell AuNps were positioned in cells of $\Delta_c = 60\mu m$ and had their current moments normalized by 1. The amplitude (dB) and phase of E_z are shown in Figures 5(a) and 5(c) by PGF method and in Figures 5(b) and 5(d) obtained from COMSOL Multiphysics.

According to [10], simulations performed on a 32GB RAM computer with a 3.8GHz processor required a total time of 5 hours, 12 minutes, and 57 seconds. By the PGF method, the simulation required a time of 17 minutes and 27 seconds. This was done with the discretized mesh at 500 × 500, with the series truncated at mn [0 : 150] (corresponding to 22801 iterations), on an 8GB RAM computer with a 1.70GHz-2.40 GHz processor.

We have also compared the results obtained from the numerical integration technique of the spectral representation used in [10] with the PGF method. Figure 15 shows these results for the component E_z on the x axis, at $z = y = 0$, and on the z axis, at $x = y = 0$.

As can be seen in Figures 5 and 6, the results show good concordance, demonstrating that, in the limit case of low concentration of nanoparticles, the discrete spectrum approaches to the continuous spectrum; consequently, the PGF representation approaches to the representation by the Fourier integral. However, it was necessary to verify the convergence of the method and the necessity of the number of terms in the series of (44). In Figure 7, the convergence of $A_z(0,0,z)$ in terms of the number of iterations $m \times n$

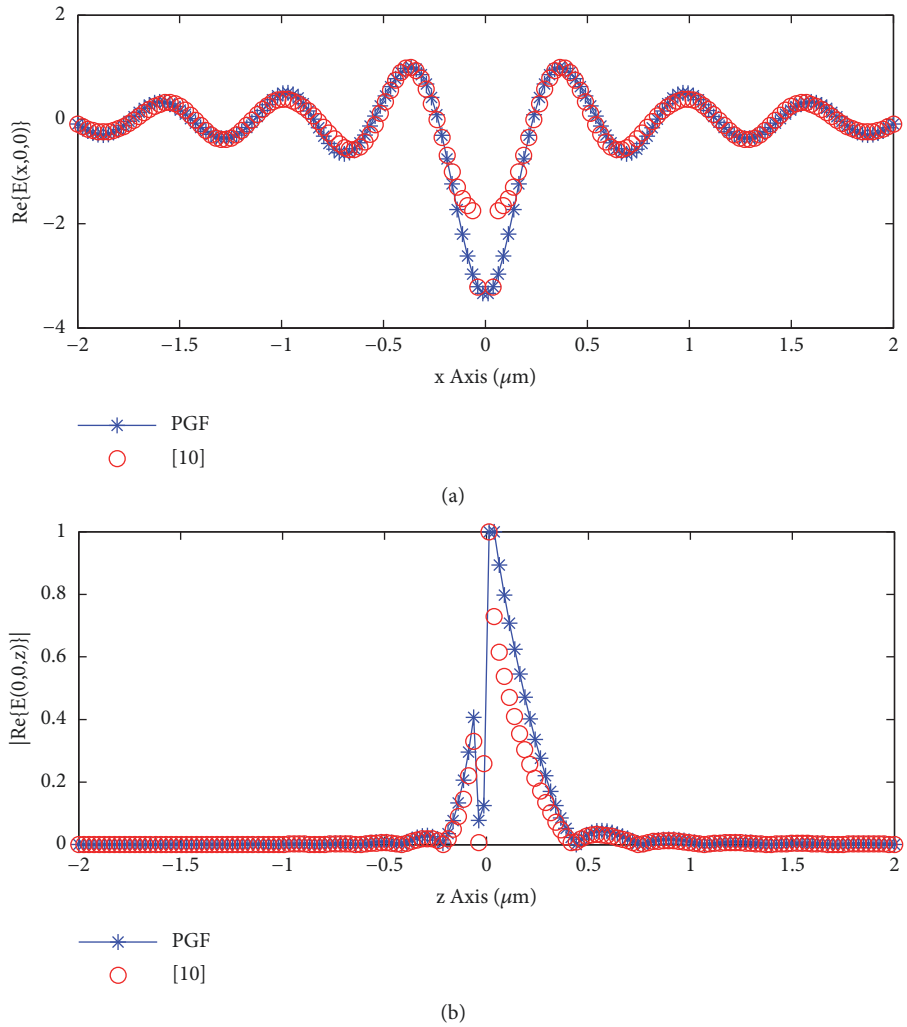

Figure 6: Results of the PGF and [10] for the component E_z: (a) $\mathrm{Re}\{E_z(x,0,0)\}$, (b) $|\mathrm{Re}\{E_z(0,0,z)\}|$. In these results we set the following: $\delta_g = 50nm$, $h = 20nm$, $\theta' = \phi' = 0°$, and $\lambda = 632.8nm$.

is demonstrated. To elucidate the convergence in the three media, we choose three points in space: above the gold layer $z = h$, inside the gold layer $z = -\delta_g/2$, and in the prism region $z = \delta_g - h$. In the spectral analysis, we will verify that the position of the dominant poles in the spectral representation is function of the cell period. For this reason we will check for three cases of Δ_c.

From the graphical results of Figure 7, we see that the potential field in all situations converges but requires a larger number of terms in the series for the case with larger cell. In fact, as the analysis cell increases, we approach more the limit case, where the discrete spectral representation becomes a continuous spectral representation; in other words, the summation becomes an integral.

5. Results and Discussion

Based on the model presented in Section 3, several Matlab codes were developed to simulate the SPCE sensor response. In this section, we considered a reference sample containing only a concentration of Core-Shell AuNps functionalized with fluorophores. Thus, the medium 1 is formed by the periodic planar array of equivalent dipoles, uniformly distributed at a distance h from the surface of the sensor ($z = d_1 = 0$) by the chemical spacer. The gold thin film has thickness δ_g ($z = d_2 = -\delta_g$). Core-Shell AuNps are excited by an external source of $\lambda = 632.8nm$ (suppressed). Thus, the fundamental dipole moment is excited in the direction $\hat{a}_r(\theta', \phi')$, re-radiating waves on the SPCE sensor structure of the same wavelength. In the periodic array, for simplicity, we consider the cell period in x and y equal, so that $\Delta_c = 2a = 2b$ is the period of the cell in the two dimensions. The particularization of the equivalent electromagnetic model is shown in Figure 8.

Considering medium 1, where the nanoparticles are immobilized, as the reference medium and electrically inert (i.e., any variation in the refractive index will be compared with the reference medium), we can approximate their relative permittivity by $\varepsilon_1 = 1$. All the structure is nonmagnetic structure ($\mu_{1,2,3} = 1$), the permittivity of the prism (BK7 optical glass) is $\varepsilon_3 = 2.30$, and the gold layer is $\varepsilon_2 = -11.63 - 1.34j$, with the latter described by the Lorentz-Drude model

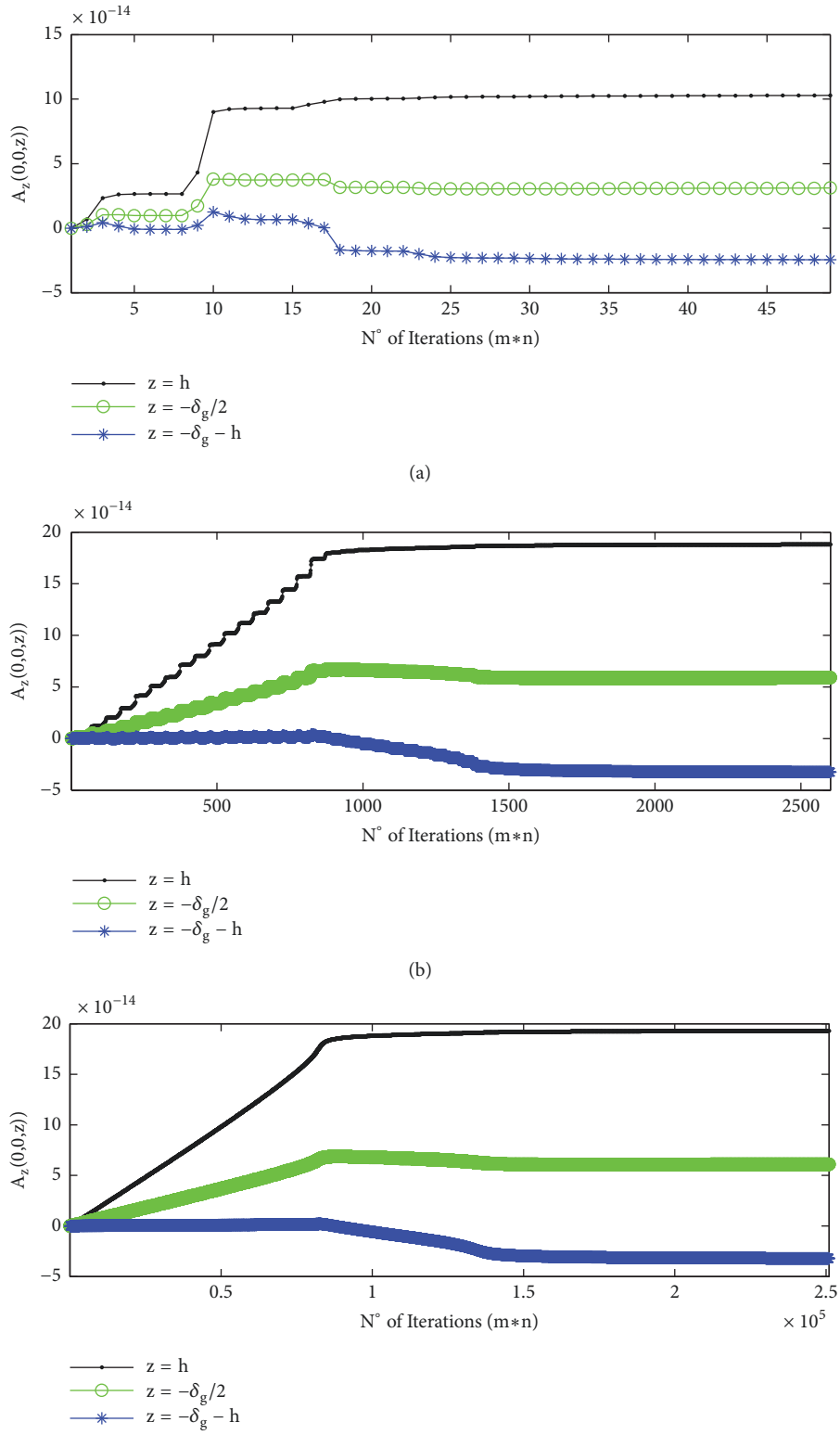

FIGURE 7: $A_z(0,0,z)$ convergence for the following: (a)$\Delta_c = 1\mu m$, (b)$\Delta_c = 10\mu m$, and (c) $\Delta_c = 100\mu m$. In these results we set the following: $\delta_g = 50nm$, $h = 20nm$, $\theta' = \phi' = 0^\circ$, and $\lambda = 632.8nm$.

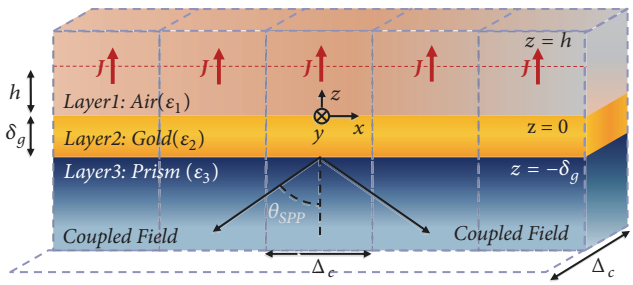

FIGURE 8: Particularization of the equivalent electromagnetic model for the SPCE sensor.

with excellent accuracy. In this step, we do not intend to verify the influence of the AuNPs dimensions on the optical response of the sensor, but we must keep in mind the near field amplification already verified that these nanoparticles suffer by the LSPR phenomenon. As an effective dipole moment, we find $p_{eff} = (7.17 + j0.003)Debye$, approximated by (1) and (2), for a particle with gold core and dielectric shell $r_c = 20nm$, $\delta_c = 10nm$, respectively, aggregated with a fluorophore with polarizability $\alpha_{FF} = (7.1 \pm 1.1)Debye/Vm^{-1}$ [19].

5.1. Spatial Analysis of Magnetic Potential and Electromagnetic Fields. First, the magnetic potential field (16) was used to verify the influence of the gold layer thickness to $\delta_g = 10nm, 50nm$, and $100nm$, with the dipole at a height $h = 200nm$, oriented in three distinct directions, $\theta = 0^\circ, 45^\circ$, and 90°, with $\phi' = 0^\circ$, in the analysis cell with period $\Delta_c = 10\mu m$. The graphs were generated in the xz plane at $y = 0$, for the normal component A_z of the magnetic potential field.

For better visualization and analysis, the graphical results in Figure 9 were normalized to $[-2, 6] \times 10^{-14} Wb/m$ and limited to $[-2, 2]\mu m$ in xz plane. The main objective of these analyses is to verify the influence of the thickness of the gold layer δ_g and the orientation of the equivalent dipoles defined by the angles θ' and ϕ'. We can verify that, as the orientation of the dipoles changes from $\theta' = 0^\circ$ to $\theta' = 90^\circ$, less the normal component A_z contributes to the magnetic potential field. This is in accordance with (18)-(26), where we can show that, in general $|\tilde{R}^{TM}| > |S^{EM}|$, in other words, the component A_z is more effectively excited by J_z than J_x or J_y. In general, for all cases with different dipole orientation, we have a better field transmission in the region of the dielectric prism for $\delta_g = 10nm$. In the case where $\delta_g = 100nm$, we have a larger field reflection in the sample region, which may reduce the signal reading at the SPCE sensor output. However, for this gold thickness, we can verify the appearance of SPP waves, mainly for vertical orientation. We found the best thickness of $\delta_g = 50nm$, where we have the two basic needs in the sensor structure at the same time: the considerable capacity of transmitting TM radiation waves through the prisma medium and the excitation of SPP waves on the gold layer.

From the differential relations (38) and (39), we can now analyze the Electric and Magnetic fields in Figure 10.

In order to verify the influence of the dipole orientation in the array, electric and magnetic field results of the E_x, E_z, and H_y components were generated for the orientations $\theta' = 0^\circ$ (VED: Vertical Electric Dipole), intermediate $\theta' = 45^\circ$, and $\theta' = 90^\circ$ (HED: Horizontal Electric Dipole), with the array positioned at a height $h = 20nm$ in a cell of period $\Delta_c = 10\mu m$ (Figure 10). For better visualization, the fields were normalized to $[-50, 50]dB$ and limited to $[-2, 2]\mu m$ x and z.

Differently from the results of magnetic potential (Figure 9), we can now verify more accurately the inclination of the equivalent dipole for the VED, intermediate, and HED cases. For the HED case (Figures 10(c), 10(f), and 10(i)), we can see a considerable field transmission in the prism region. However, note that there is no excitation of SPP waves at the sample/gold interface; that is, the field comes only from the dipole radiation, and it has no directional characteristic as a function of SPP wave excitation. For the intermediate case (Figures 10(b), 10(e), and 10(h)), the considerable excitation of SPP waves and asymmetric field characteristic in the three media is verified. In the VED orientation (Figures 10(a), 10(d), and 10(g)), also a considerable SPP wave component in the sample-gold interface is verified. This is due to the light excitation of TM waves in the VED case, in accordance with (18)-(26) and the TM nature of the SPP waves. The radiation in the prism region has a highly directional characteristic, being derived from the radiation of the VED coupled by the excitation of the SPP waves.

In summary, we can see that the HED mode, which predominantly excites TE modes, does not efficiently excite plasmons. In contrast, the VED mode actively excites SPP waves, thus, coupling highly polarized TM waves in the prism region, with the latter being the mode that presents the best feature in relation to the SPCE sensor. From this point, we will adopt the VED polarization as effective and consider only the case $\theta' = 0$. This choice cancels the tangential components of the magnetic potential field (A_x and A_y), leaving only the normal component A_z:

$$\mathbf{A}_{1,2,3}(\mathbf{r}) = \sum_{m=0}^{\infty}\sum_{n=0}^{\infty} \epsilon_{mn} A_{zz_{1,2,3}}^{mn}(z) \cos[k_x x] \cos[k_y y] \quad (45)$$

Finally, it is worth showing that the periodic conditions are met, for both the electric and magnetic field. Figure 11 shows the field result for two cells with period $\Delta_c = 4\mu m$, in the xy plane at $z = 0$ and xz plane at $y = 0$.

From this result, the interaction (interference) between the fields re-irradiated by two near dipoles is verified, where, at the boundary of the cells of analysis, the periodic boundary conditions are obeyed.

5.2. Spectral Analysis. Originally, in the inverse double transform of the Fourier series, which defines the magnetic potential at (45), the sum of complex exponentials with the double summation is performed by $m = -\infty : +\infty$ and $n = -\infty : +\infty$, defining the discrete spectral domain mn. It was proposed to use Euler's identity to change the representation in terms of exponentials by a representation in terms of cosine functions, thus reducing the spectral domain to $m = 0 : +\infty$

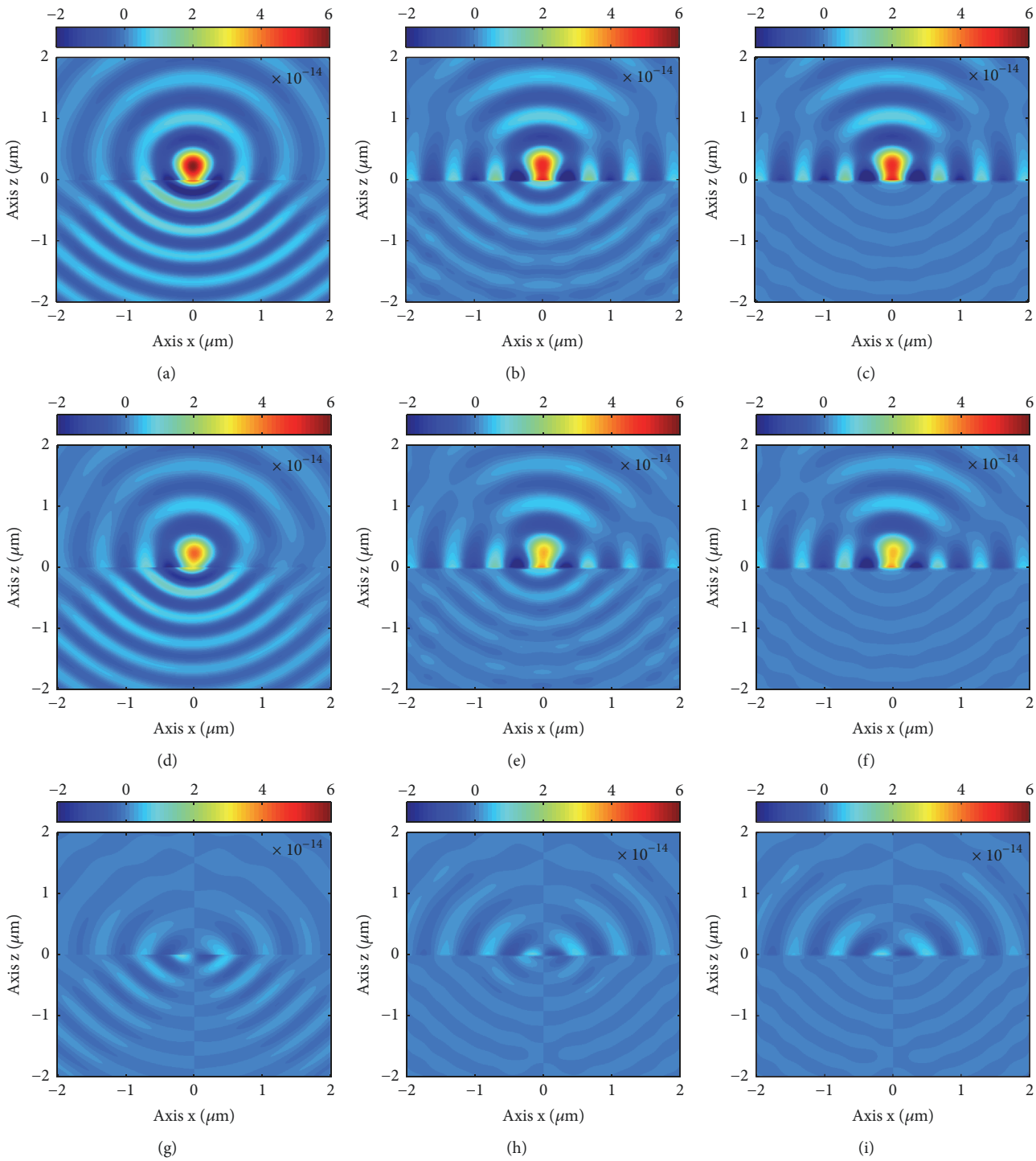

Figure 9: Magnetic Potential Field A_z for $\theta' = 0^\circ$: (a) $\delta_g = 10nm$, (b) $\delta_g = 50nm$, and (c) $\delta_g = 100nm$; $\theta' = 45^\circ$: (d) $\delta_g = 10nm$, (e) $\delta_g = 50nm$, and (f) $\delta_g = 100nm$; $\theta' = 90^\circ$: (g) $\delta_g = 10nm$, (h) $\delta_g = 50nm$, and (i) $\delta_g = 100nm$. In these results we set the following: $h = 200nm$, $\Delta_c = 10\mu m$, $\lambda = 632.8nm$, and $\phi' = 0^\circ$.

and $n = 0 : +\infty$, reducing the computational cost. In other words, the coefficients of (45) are even functions of m and n.

The analysis of the spectral terms A_{zz}^{mn} and the generalized reflection and transmission coefficients can give us important information about the dominant terms in the representation of the potential field (45). In Figure 12 the spectral distributions of the generalized reflection and transmission coefficients in the mn plane are shown for $\Delta_c = 1\mu m$, $\Delta_c = 10\mu m$, and $\Delta_c = 100\mu m$.

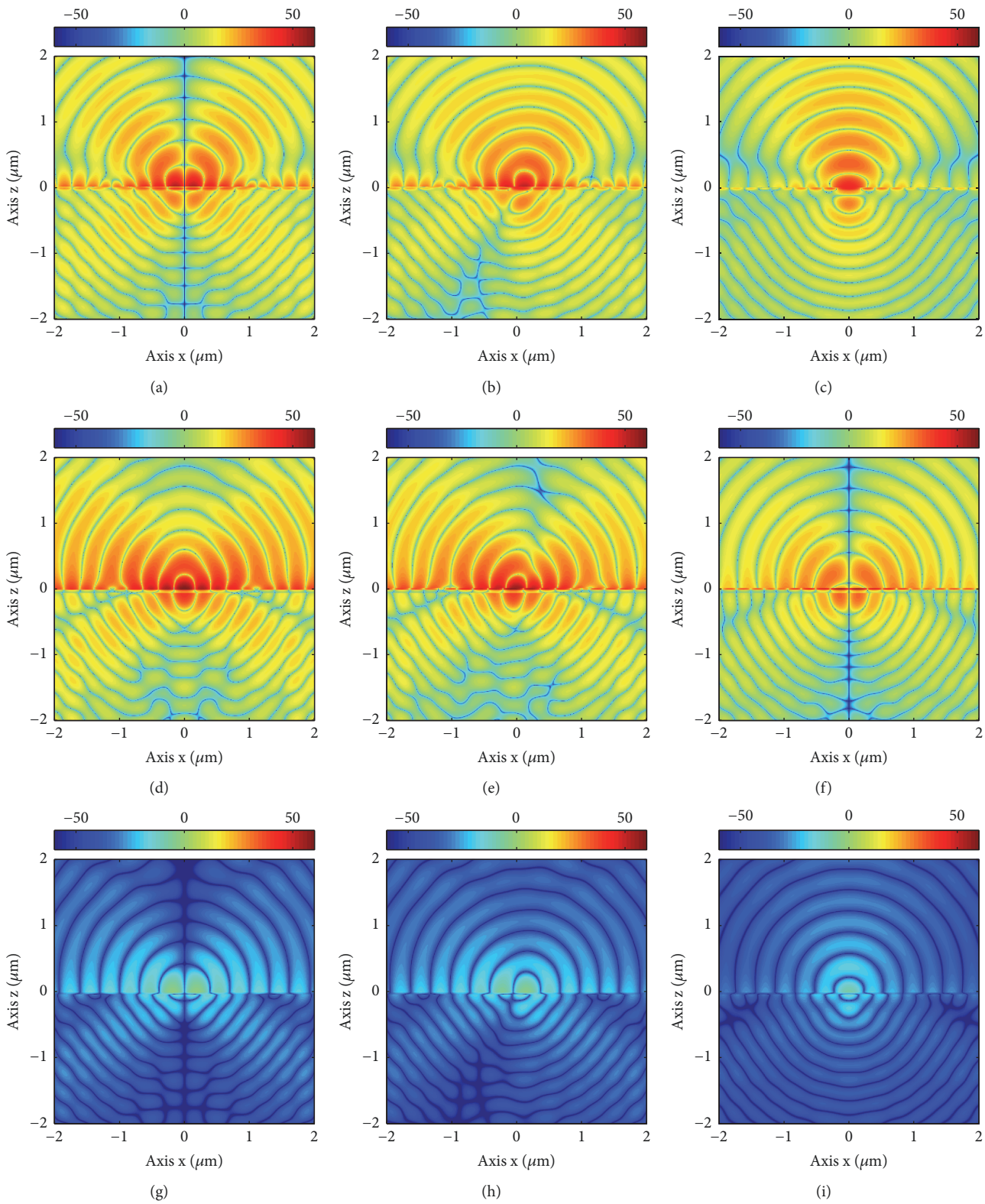

Figure 10: Electric and Magnetic Field. $20\log|\mathrm{Re}\{Ex\}|$: (a) $\theta' = 0^\circ$, (b) $\theta' = 45^\circ$, and (c) $\theta' = 90^\circ$; $20\log|\mathrm{Re}\{Ez\}|$: (d) $\theta' = 0^\circ$, (e) $\theta' = 45^\circ$, and (f) $\theta' = 90^\circ$; $20\log|\mathrm{Re}\{Hy\}|$: (g) $\theta' = 0^\circ$, (h) $\theta' = 45^\circ$, and (i) $\theta' = 90^\circ$. In these results we set the following: $\delta_g = 50nm$, $h = 20nm$, $\Delta_c = 10\mu m$, $\lambda = 632.8nm$, and $\phi' = 0^\circ$.

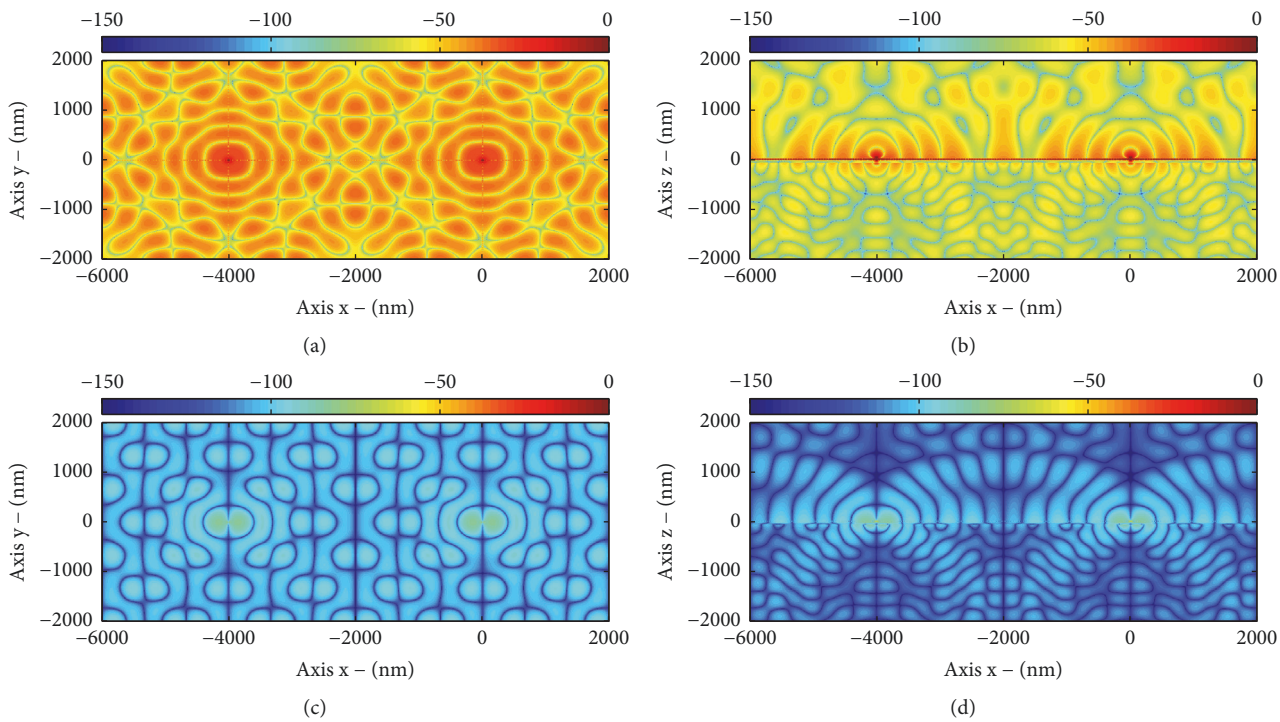

Figure 11: Component z of the electric field $20\log|\mathrm{Re}\{Ez\}|$, in dB, in the planes: (a) xy and (b) xz; Component y of the magnetic field $20\log|\mathrm{Re}\{Hy\}|$, in dB, in the planes: (c) xy and (d) xz. In these results we set the following: $\delta_g = 50nm$, $h = 20nm$, $\Delta_c = 4\mu m$, $\lambda = 632.8nm$, $\theta' = 0^\circ$, and $\phi' = 0^\circ$.

For the case of Figures 12(a) and 12(d), the terms of greater dominance are close to the origin and converge rapidly to fixed values. Also, in these cases, the spectrum does not present a cylindrical symmetry with mn because the geometry of the AuNps array is rectangular. In the case of Figures 12(c) and 12(f), we can verify that the dominance terms (peaks of resonance) occur far from the origin. Also, we observe in these cases a cylindrical symmetry in the spectrum mn. This happens because, for larger Δ_c, the AuNps array converges (behaves) to an isolated single dipole, which presents cylindrical symmetry in the xy plane, and consequently, a cylindrical symmetry in the mn plane. This characteristic of cylindrical convergence of the spectrum will be considered in the next paragraphs.

A fundamental result is the characteristic of cylindrical symmetry that the spectral terms present. This is because the eigenvalues k_x and k_y have the same structure, and they perform similar roles in the spectral representation. Due to symmetry, we can express the eigenvalues by a $k_\rho = \sqrt{k_x^2 + k_y^2}$ and express the propagation constant $k_{z_u} = \sqrt{k_u^2 - k_\rho^2}$. Also, due to the cylindrical symmetry, we can limit the spectral analysis to the domain $mn[0, +\infty]$. Even stronger, we can fix n at any value and perform the one-dimensional analysis in m. For $n = 0$, we obtain $k_\rho = [2\pi m/\Delta_c]$.

Setting $n = 0$, for $\Delta_c = 1\mu m, 10\mu m$ and $100\mu m$, Figure 13 shows the generalized reflection and transmission coefficients and in Figure 14 the spectral terms of the potential field component A_z, all in the discrete spectral domain m, in the range $[0, M]$.

Figure 13 shows the rise of two resonance peaks; these points arise from the poles of the generalized coefficients at the interfaces of the structure. Therefore, the spectral position of these resonances is dependent on the thickness of the gold layer. However, [10] found that for $\delta_g = 5nm$ the poles of the generalized and Fresnel coefficients are practically the same. Thus, the first resonance comes from the $R_{21}^{TM}(\varepsilon_2 k_{z1} + \varepsilon_1 k_{z2} = 0)$ and is related to the surface plasmon mode at the Air/Gold interface. The second resonance is the result of the $R_{23}^{TM}(\varepsilon_2 k_{z3} + \varepsilon_3 k_{z2} = 0)$, being related to the surface plasmon wave mode that appears in the Gold/Prism interface. These are the two dominant modes in the spectral representation of the fields in (44). An approximate way to determine the spectral position of these poles in m is from the dispersion relation at the interfaces, given that any n. Thus, the poles m_{SPP1} and m_{SPP2} are located, respectively, in (46) and (47).

$$m_{SPP1} = \mathrm{Re}\left\{\frac{\Delta_c k_0}{2\pi}\sqrt{\frac{\varepsilon_{r2}\varepsilon_{r1}}{\varepsilon_{r2}+\varepsilon_{r1}} - \left[\frac{2\pi n}{\Delta_c k_0}\right]^2}\right\} \quad (46)$$

$$m_{SPP2} = \mathrm{Re}\left\{\frac{\Delta_c k_0}{2\pi}\sqrt{\frac{\varepsilon_{r3}\varepsilon_{r2}}{\varepsilon_{r3}+\varepsilon_{r2}} - \left[\frac{2\pi n}{\Delta_c k_0}\right]^2}\right\} \quad (47)$$

where k_0 is the propagation constant of the free space and ε_{ru} the relative permissiveness of the medium u ($u = 1, 2, 3$). From Figure 14, we can verify that the pole m_{SPP1} is more

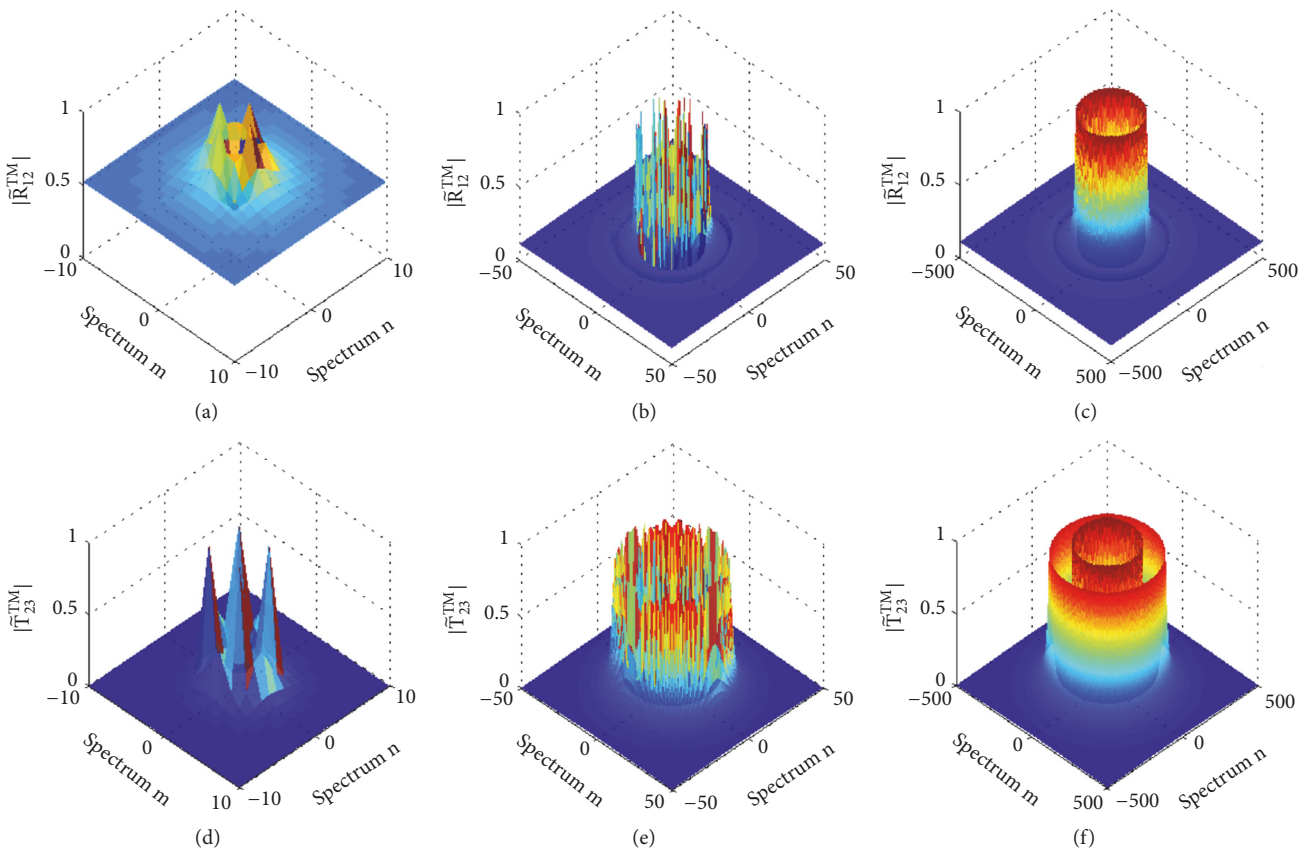

Figure 12: Spectral distribution in the mn plane: $|\tilde{R}_{12}^{TM}|$ for (a) $\Delta_c = 1\mu m$, (b) $\Delta_c = 10\mu m$, and (c) $\Delta_c = 100\mu m$; and $|\tilde{T}_{23}^{TM}|$ for (d) $\Delta_c = 1\mu m$, (e) $\Delta_c = 10\mu m$, and (f) $\Delta_c = 100\mu m$. In these results we set the following: $\delta_g = 50nm$.

intense than m_{SPP2}; for this reason, this will be the dominant pole in the calculation of the plasmon propagation constant k_ρ^{SPP}. In fact, since $k_\rho^{SPP} = (2\pi m_{SPP1})/\Delta_c$, we can approximate the resonance plasmonic angle by

$$\theta_{SPP} \simeq \sin^{-1}\left[\frac{k_\rho^{SPP}}{k_3}\right] \tag{48}$$

It is also seen that, as the period of the cell Δ_c increases, there is a shift to the right of the resonances, which, in terms of the spectral representation, means a greater amount of terms to be computed in the sum of (45).

The results in Figure 14 were generated for the spectral terms of the magnetic potential at three points in the z-space, above the gold layer $z = h$, inside the gold layer $z = -\delta_g/2$, and below the gold layer $z = -(\delta_g + h)$. For $\Delta_c = 1\mu m$, at $n = 0$, the SPP poles appear in $m_{SPP1} = 2$ and $m_{SPP2} = 3$, the plasmon propagation constant is $k_\rho^{SPP} = 1.2660k_0$, and the plasmonic coupling angle $\theta_{SPP} = 56.57^\circ$. Note that convergence occurs rapidly in m approximately $M = 10$. For $\Delta_c = 10\mu m$, the SPP poles appear in $m_{SPP1} = 17$ and $m_{SPP2} = 27$, the plasmon propagation constant is $k_\rho^{SPP} = 1.0761k_0$, and the plasmonic coupling angle $\theta_{SPP} = 45.18^\circ$. For $\Delta_c = 100\mu m$, the SPP poles appear in $m_{SPP1} = 165$ and $m_{SPP2} = 267$, the plasmon propagation constant is $k_\rho^{SPP} = 1.0444k_0$, and the plasmonic coupling angle $\theta_{SPP} = 43.51^\circ$.

As the cell period increases, we approach the limiting case, where the radiation comes from a single isolated particle. This case was studied in [10], where a plasmon propagation constant $k_\rho^{SPP} = (1.0458 - j0.0051)k_0$ and plasmonic coupling angle 43.7° were obtained. Note that the results found for $\Delta_c = 100\mu m$ are close to the results obtained in the limit case in [10]. It is also verified that the discrete spectrum gains characteristic of the continuous spectrum as we approach the limiting case.

In order to verify the effect of the SPP1 and SPP2 poles for different values of term m, in the spatial domain, Figure 15 shows the electric and magnetic field graphs to $\Delta_c = 10\mu m$, for terms $m = 7, m = m_{SPP1} = 17$ and $m = m_{SPP2} = 27$, with $n = 0$.

By the graphical analysis of the spectral distribution in Figures 13 and 14, we can note that for points near the sensor the spectral terms $m > m_{SPP2}$ contributes less to the composition of the total field. This information gives us a good idea of the number of terms needed for the field representation in a cell. In Figure 16 the electric and magnetic fields are shown for $\Delta_c = 10\mu m$, with the truncated series $m = 0 : 50$ and $n = 0 : 50$, which corresponds to 51^2 terms in the spectral representation.

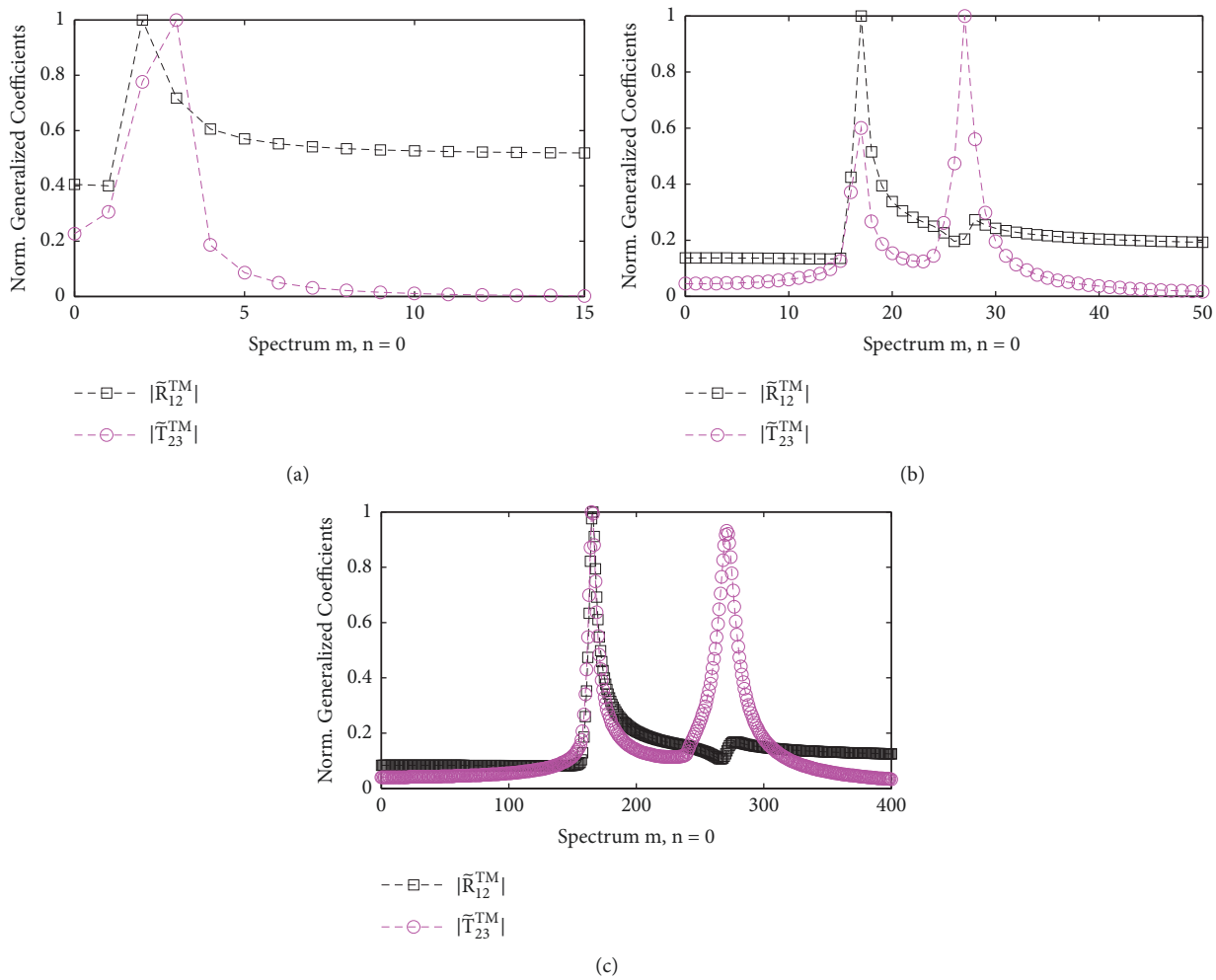

FIGURE 13: Normalized spectral distribution of $|\tilde{R}_{21}^{TM}|$ and $|\tilde{T}_{23}^{TM}|$ in m, with $n = 0$, for (a) $\Delta_c = 1\mu m$; (b) $\Delta_c = 10\mu m$; (c) $\Delta_c = 100\mu m$. In these results we set the following: $\delta_g = 50nm$ and $\lambda = 632.8nm$.

For better visualization the graphs in Figure 15 were generated in the xz plane $[-2, 2]\mu m$. For the three cases of Δ_c, we can verify that the three types of fields contribute in different ways to the total field in the sensor structure. The SPP1 pole contributes to field coupling in the prism region, a fundamental feature of the SPCE sensor. Note that the field distribution in these cases is equivalent to SPP waves excited by plane waves at metal/dielectric interfaces, analogous to what occurs in the Kretschmann configuration. The SPP2 pole plays a similar role to that of the SPP1 pole, but less intense because of the dispersion relation calculated at the gold/prism interface. Radiation fields terms also play a fundamental role in the field distribution which, in fact, is the composition of several terms with varying wavelengths that compose the total field, be it electric or magnetic, by the spectral representation; of course, some of these terms will contribute in a more significant way than others.

Note in Figure 16(a) that the intensity of the electric field of the SPP wave, near the gold layer, is higher than the radiation fields in z points far away from the gold layer.

By the relation (48) it is possible to carry out a preliminary analysis of the variation of the plasma angle depending on the relative permittivity in medium 1, for the SPCE sensor coupled to a nanoparticle array with period $\Delta_c = 100$nm (we made it clear that this is a preliminary analysis because it is not the current purpose of the work). Figure 17 shows the generalized transmission coefficient in terms of the coupling angle.

At first, we can verify that, with the increase of refractivity index in medium 1, we have a displacement of the plasmonic angle in the 90° direction and decay of the transmitted signal. For this reason, we can assume that these will be the changes in the optical response of the sensor.

6. Conclusions

In this work a theoretical electromagnetic model was presented for a SPR sensor in the SPCE configuration, coupled with a periodic planar array of equivalent nanodipoles. The Periodic Green's Function method was applied

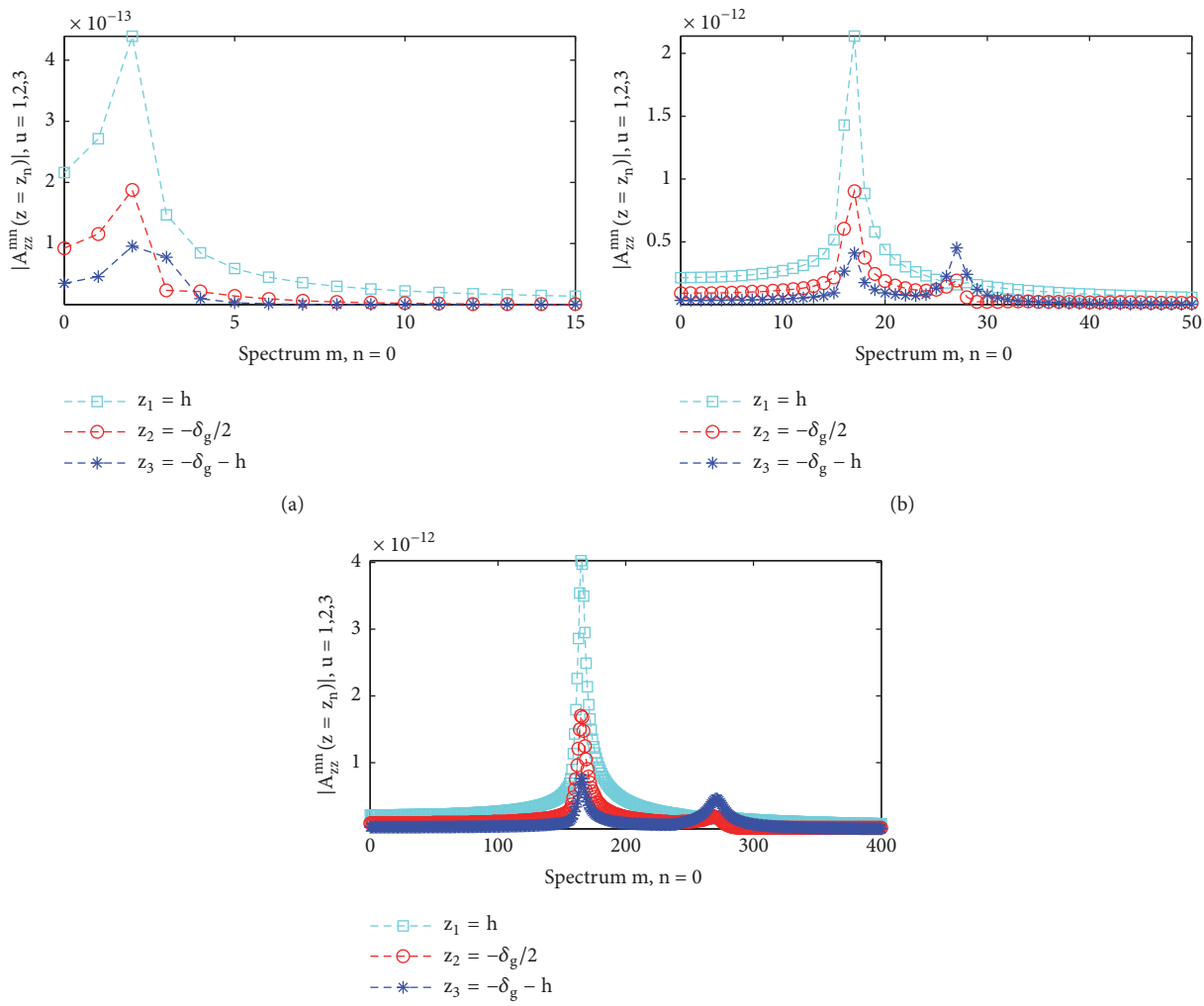

FIGURE 14: Spectral Coefficient $A_{zz}^{mn}(z)$ at $z = z_u$, with $u = 1, 2, 3$ and $n = 0$, for (a) $\Delta_c = 1\mu m$; (b) $\Delta_c = 10\mu m$; (c) $\Delta_c = 100\mu m$. In these results we set the following: $\delta_g = 50nm$, $h = 20nm$, $\theta' = \phi' = 0^\circ$, and $\lambda = 632.8nm$.

to the magnetic potential, where the spectral representation method of the Fourier Double Complex Series was used.

From the magnetic potential field results, we find that $\delta_g = 50nm$ has been the ideal thickness of the gold layer in the sensor structure for the operating frequency. The electric and magnetic field results showed that the excitation of SPP waves, such as the coupling of highly polarized TM waves, arises most efficiently when the equivalent dipoles are oriented at $\theta' = 0^\circ$ (VED). In the case of the relative distance between the array and the surface of the sensor, defined by the chemical spacer, no major changes in the results were observed for the variation of parameter h, only simple changes of intensity in the prism region.

In the spectral analysis, we verified the emergence of the SPP poles in the spectral domain mn, for three cell periods. Also, we presented a convergence analysis of the series, where the terms of greater contribution in the spectral representation of PGF were identified. Despite the appearance of the SPP2 pole, at the gold/prism interface, the SPP1 pole was shown to contribute predominantly to the spectral representation.

As the period of the analysis cell increases, the results approach the limiting case, where there are no interactions between the nanoparticles in the array. The convergence of the method depends strongly on the cell period, being faster for relatively smaller cells and becoming slow as the cell period increased. Thus, we see the need for a greater number of terms, in the convergence of the method, for relatively larger cell periods. In this situation, we have the transition from the discrete spectrum to the continuous spectrum, when the summation in the spectral representation becomes an integral. However, the transition from discrete to continuous spectrum still encounters some difficulties, since in the discrete spectrum the propagation constant k_ρ is purely real; on the other hand, in the continuous spectrum

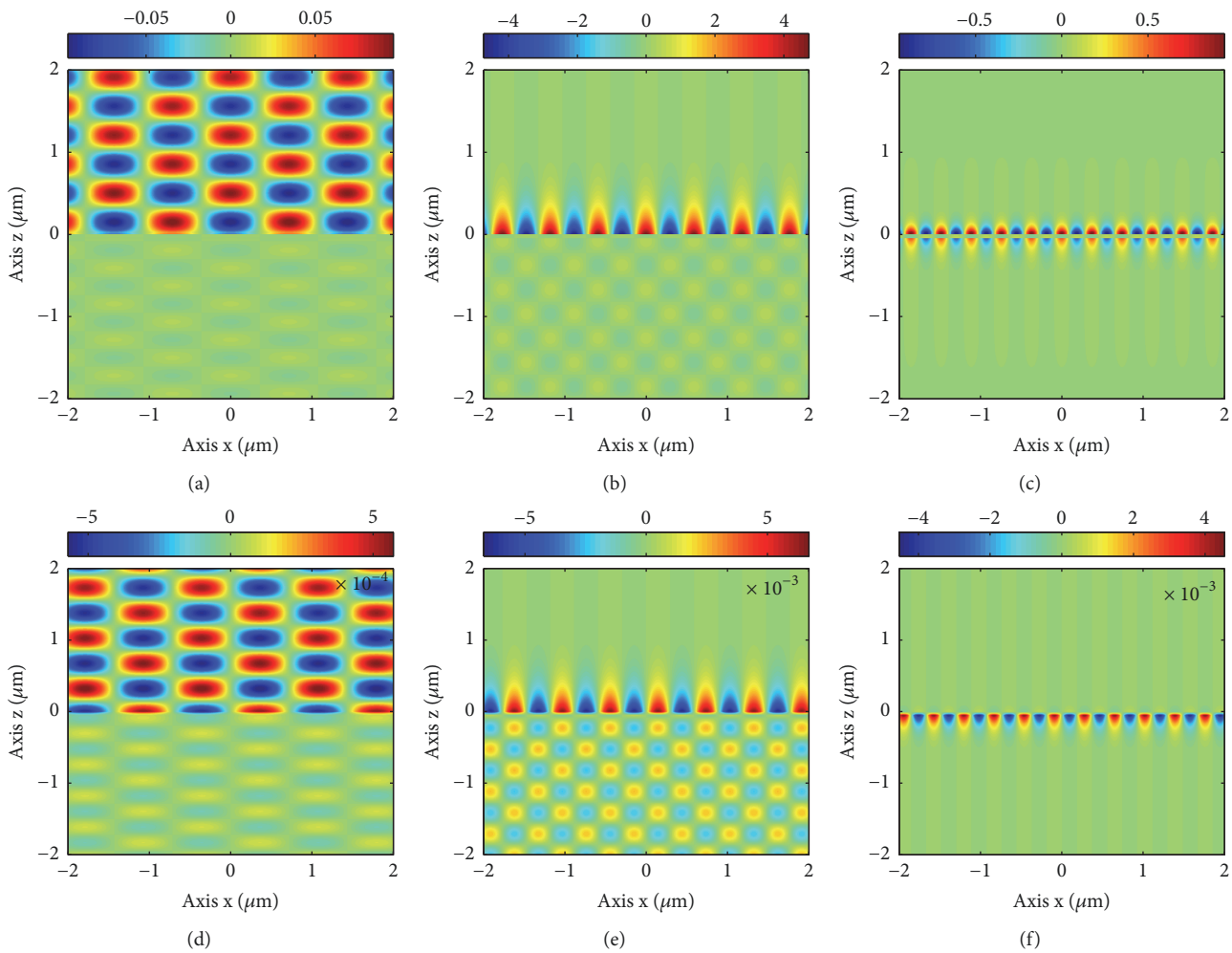

FIGURE 15: E_z and H_y in the xz plane, at $y = 0$, with $\Delta_c = 10\mu m$. Re$\{E_z\}$ for the term $n = 0$ and (a) $m = 7$, (b) $m = m_{SPP1} = 17$, and (c) $m = m_{SPP2} = 27$; Re$\{H_y\}$ for the term $n = 0$ and (d) $m = 7$, (e) $m = m_{SPP1} = 17$, and (f) $m = m_{SPP2} = 27$. In these results we set the following: $\delta_g = 50nm$, $h = 20nm$, $\theta' = \phi' = 0^\circ$, and $\lambda = 632.8nm$.

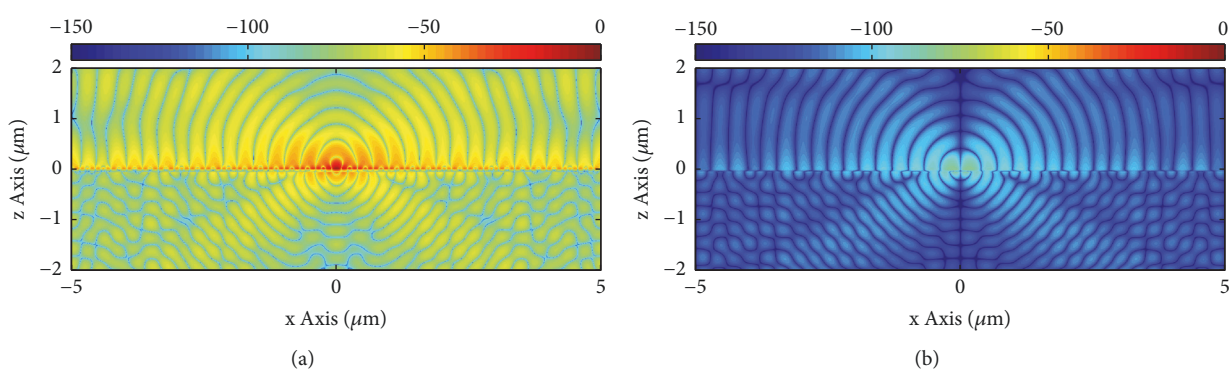

FIGURE 16: Electric and Magnetic Fields in the xz plane, at $y = 0$, with $\Delta_c = 10\mu m$: (a) $20 \log |\text{Re}\{E_z\}|$; (b) $20 \log |\text{Re}\{H_y\}|$. In these results we set the following: $\delta_g = 50nm$, $h = 20nm$, $\theta' = \phi' = 0^\circ$, and $\lambda = 632.8nm$.

k_ρ presents a small imaginary part, as verified by [10]. This small imaginary part can be seen as the losses in the material.

The field results showed consistency with the observation of polarized TM waves, with high directivity in the prism region, which in the far field should form the characteristic of the sensor output, the light cone. In general, the results obtained showed good agreement, both mathematical and physical, demonstrating that the PGF method is efficient and

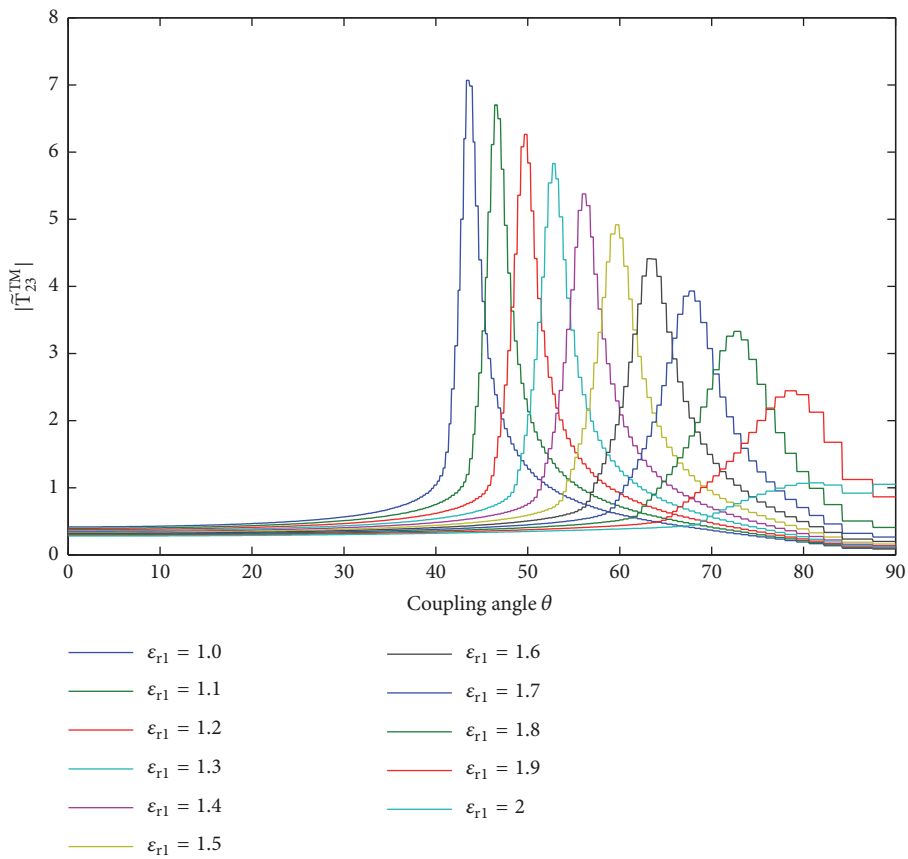

Figure 17: Generalized transmission coefficient in the gold/prism interface as a function of the coupling angle θ.

can be used as a tool in the design and optimization of the sensor in the SPCE configuration.

For future work, we propose to verify the possibility of far field calculation from the obtained electromagnetic model, thus verifying the directivity and intensity of far field in function of the refractive characteristics of the sample. In addition, we will verify the temporal decay characteristics of the radiation emitted by the fluorophores and the total response of the sensor excited by a plane wave.

Abbreviations

The following abbreviations are used in this paper:

SPR: Surface Plasmon Resonance
RSPL: Localized Surface Plasmon Resonance
SPP: Surface Plasmon Polaritons
PGF: Periodic Green's Function
SPCE: Surface Plasmon Coupled Emission
AuNps: Gold Nanoparticles
DCIM: Discrete Complex Images Method
SW: Surface Wave.

Data Availability

The data used to support the findings of this study are available from the corresponding author upon request.

Conflicts of Interest

The authors declare no conflicts of interest.

Acknowledgments

Thanks are due to the members of the Nanophotonics and Nanoelectronics Laboratory from UFPA, Nanotribo. National Council for Scientific and Technological Development - CNPq (grant numbers: 423614/2018-5).

References

[1] D. W. Pohl, A. Alu, N. Engheta, and F. Marquier, *Optical Antennas*, Forthcoming Publications: Science, PRL, 2013.

[2] J. Homola, *Surface Plasmon Resonance Based Sensors*, Springer Series on Chemical Sensors and Biosensors, Springer, Berlin, Germany, 2006.

[3] S. A. Maier, *Plasmonics: Fundamentals and Applications*, Springer, NewYork, NY, USA, 1st edition, 2007.

[4] K. Q. Da Costa, J. S. Costa, V. Dmitriev, T. Del Rosso, O. Pandoli, and R. Q. Aucelio, "Analysis of surface plasmon resonance sensor coupled to periodic array of gold nanoparticles," in *Proceedings of the SBMO/IEEE MTT-S International Microwave and Optoelectronics Conference, IMOC 2015*, pp. 1–5, Brazil, November 2015.

[5] A. Cruz and K. Costa, "Extinction efficiency and electromagnetic fields of isolated and coupled core-shell nanoparticles,"

Journal of Communication and Information Systems, vol. 33, no. 1, 2018.

[6] R. Marani, M. Grande, V. Petruzelli, and A. D'Orazio, "Plasmonic bandgaps in 1D arrays of slits on metal layers excited by out-of-plane sources," *International Journal of Optics*, vol. 2012, Article ID 146396, 12 pages, 2012.

[7] T. Špringer, M. L. Ermini, B. Špačková, J. Jabloňků, and J. Homola, "Enhancing sensitivity of surface plasmon resonance biosensors by functionalized gold nanoparticles: size matters," *Analytical Chemistry*, vol. 86, no. 20, pp. 10350–10356, 2014.

[8] M. A. Cooper, "Optical biosensors in drug discovery," *Nature Reviews Drug Discovery*, vol. 1, no. 7, pp. 515–528, 2002.

[9] J. Malicka, I. Gryczynski, Z. Gryczynski, and J. R. Lakowicz, "Use of surface plasmon-coupled emission to measure DNA hybridization," *Journal of Biomolecular Screening*, vol. 9, no. 3, pp. 208–215, 2004.

[10] N. W. P. Souza, *Análise de Sensores Plasmônicos Baseados em Nano Estruturas Estratificadas Utilizando o Método das Imagens Complexas Discretas [Doctoral thesis]*, PPGEE, UFPA, Belém-PA, Brazil, 2018.

[11] N. W. P. de Souza, J. S. Costa, R. C. Santos, A. F. S. da Cruz, T. D. Rosso, and K. Q. da Costa, "Modal analysis of surface plasmon resonance sensor coupled to periodic array of core-shell metallic nanoparticles," in *Resonance*, J. Awrejcewicz, Ed., InTech, 2017.

[12] A. F. S. Cruz, N. W. P. de Souza, V. Dmitriev, and K. Q. Costa, "Modelo Eletromagnético de Sensor Plasmônico Acoplado a Arranjo de Nanopartículas via PGF 3D," in *MOMAG 2018, 2018, Santa Rita do Sapucaí - MG. 13ºCBMag - Congresso Brasileiro de Eletromagnetismo 18ž SBMO - Simpósio Brasileiro de Microondas e Optoeletrônica INATEL, 2018*, 2018.

[13] T. Del Rosso, Q. Zaman, M. Cremona, O. Pandoli, and A. R. J. Barreto, "SPR sensors for monitoring the degradation processes of Eu (dbm) 3 (phen) and Alq3 thin films under atmospheric and UVA exposure," *Applied Surface Science*, vol. 442, pp. 759–766, 2018.

[14] A. F. Cruz, K. Q. Costa, V. Dmitriev, and T. Del Rosso, "Spectral analysis of a surface plasmon resonance sensor of nanoparticles by periodic green function," in *Proceedings of the 2018 SBFoton International Optics and Photonics Conference (SBFoton IOPC)*, pp. 1–5, Campinas, Brazil, October 2018.

[15] D. Marsh, "Reaction fields in the environment of fluorescent probes: polarity profiles in membranes," *Biophysical Journal*, vol. 96, no. 7, pp. 2549–2558, 2009.

[16] D. G. Dudley, *Mathematical Foundations for Electromagnetic Theory*, IEEE press, New York, NY, USA, 1994.

[17] W. C. Chew, *Waves and Fields in Inhomogeneous Media*, IEEE press, 1995.

[18] C. A. Balanis, *Advanced Engineering Electromagnetics*, John Wiley & Sons, 1999.

[19] P. H. Chung, C. Tregidgo, and K. Suhling, "Determining a fluorophore's transition dipole moment from fluorescence lifetime measurements in solvents of varying refractive index," *Methods and Applications in Fluorescence*, vol. 4, no. 4, Article ID 045001, 2016.

Hindawi
International Journal of Antennas and Propagation
Volume 2019, Article ID 6956809, 13 pages
https://doi.org/10.1155/2019/6956809

Research Article

Imaging Internal Defects with Synthetic and Experimental Data

Hongwei Zhou,[1] Guanghui Hu,[2] and Ling Ma [1]

[1]*Northeast Forestry University, Harbin 150040, China*
[2]*Beijing Computational Science Research Center, Beijing 100193, China*

Correspondence should be addressed to Ling Ma; maling63@163.com

Received 29 March 2019; Accepted 19 June 2019; Published 14 July 2019

Guest Editor: Lulu Wang

This work concerns an inverse time-dependent electromagnetic scattering problem of imaging internal defects in a homogeneous isotropic medium. The position and cross section of the defects are detected by transient electromagnetic pulses in the case of TE polarization. We apply the Kirchhoff migration scheme to locate the position of small objects from both synthetic and experimental data. The multiple-input-multiple-out scheme is used to recover extended scatterers from the data generated by the software GprMax. Numerical experiments show that the Kirchhoff migration method is not only efficient but also robust with respect to polluted data at high noise levels. Experimental results show good quantitative agreement with numerical simulations.

1. Introduction

Inverse scattering is to recover physical and geometrical information of inaccessible objects from scattered fields measured outside. It has been one of the most challenging problems with considerable practical applications in many areas of technology such as nondestructive evaluation, subsurface and ground-penetrating radar, geophysical remote sensing, medical imaging, seismology, and target identification; see [1–5]. One of the most prominent features of inverse scattering problem is its noninvasiveness, along with the affordability due to cheap nonionizing sensors. However, solving inverse scattering problems is difficult due to the inherent ill-posedness and nonlinearity. Small variation in the measured data can lead to large errors in the reconstruction of the scatterer, unless regularization methods are used. Extensive investigation has been carried out and a variety of inversion algorithms have been proposed.

In the time-harmonic regime, Kirsch and Kress [6, 7], Colton and Monk [8, 9], and Angrll, Kleiman, and Roach [10] theoretically separate the nonlinearity and the ill-posedness of inverse obstacle problems, giving rise to the decomposition method. Saqib et al. [11], Yang et al. [12], and Gan et al. [13] employed iterative methods to solve inverse obstacle problems. In these optimization-based iterative approaches, an efficient forward solver is needed for each iteration, and good a priori information might be required in order to choose an initial guess that ensures numerical convergence. Noniterative sampling methods were intensively studied over the last twenty years, for instance, linear sampling method [14], factorization method [15], enclosure method [16], and singular point source method [17]. The key ingredient of the sampling approach is to design an appropriate indicator function from measured data for characterizing the region occupied by the scatterer. Forward solvers are not needed in the process of inversion. The above-mentioned approaches are mostly applicable to measured data irradiated at a fixed energy with many incoming directions. A recursive linearization method with multifrequency data was investigated in [18–22].

There exist a number of reconstruction algorithms in the time domain with dynamic measurement data. Here we mention the time reversal techniques [23, 24], the reversed time migration [25], and the boundary control method [26]. For time-dependent sampling type methods, we refer to the point source method [27], the enclosure method [28], and the total focusing method (TFM) arising from nondestructive evaluation [29, 30]. In one of the author's previous works [31], the TFM (which is also known as the Kirchhoff migration approach used in geophysics; see, e.g., [32]) was examined for imaging acoustically extended scatterers in two dimensions and the indicator behavior was mathematically analyzed. This

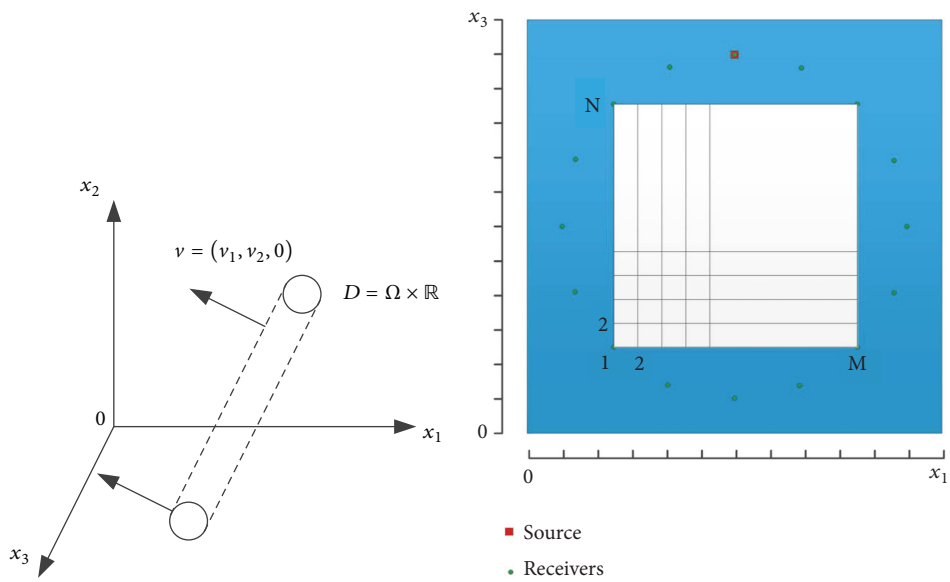

(a) Geometrical model (b) Sample grid subdivision

Figure 1: Geometrical schematic.

work concerns imaging internal defects in a homogeneous isotropic medium. It is shown that the TFM is not only efficient but also robust to measurement noise. The aim of this paper is to test the TFM for inverse electromagnetic scattering problem of imaging perfectly conducting cylinders buried in a half-space homogeneous isotropic background medium. Such kind of inverse problems has many applications in searching for internal defects with radar techniques like ground-penetrating radar (GPR); see, e.g., [5, 33, 34]. We note that the light speed is much faster than the sound speed, leading to additional difficulties in computational simulation [35]. In this paper, we make use of the open software GprMax [35, 36] to generate the forward scattering data. The GprMax is an electromagnetic simulation tool based on the Finite-Difference Time-Domain (FDTD) approach coupled with the perfectly matched layer (PML) technique. In our experiments, the real data are gained by GPR.

In this paper, we apply the TFM (or Kirchhoff migration scheme) to inverse electromagnetic scattering problems. In comparison to other algorithms, the implementation of TFM is quite simple, since the image is formed through a superposition of the scattered signals irradiated by each transducer. In fact, our imaging functions are explicit and involve only integral calculations on the measurement surface. Hence, our inversion algorithm is totally "direct". This also explains why this method is very robust with respect to measurement noise at high levels. Although the inverse scattering problem is difficult due to the inherent ill-posedness and nonlinearity, we do not need to solve the ill-posed and nonlinear problems, even without approximation and iteration. In this work, experiments with synthetic and experimental data are conducted to demonstrate the feasibility and applicability of this approach in the TE polarization case of inverse electromagnetic scattering problems.

The remaining part of this paper is organized as follows. In Section 2 we rigorously formulate the forward and inverse electromagnetic scattering problems. Section 3 is devoted to the description and implementation of the TFM for imaging small scatterers from both synthetic and real data. Extended scatterers will be reconstructed in Section 4 by using GprMax simulated data. Conclusion follows in Section 5.

2. Problem Setting

Consider the electromagnetic wave propagation in a homogeneous isotropic medium. This background medium can be characterized by the electric permittivity ε, magnetic permeability μ, and electric conductivity σ, all of which are assumed to be constant. The propagation of the electric and magnetic fields (E, H) is governed by the Maxwell system.

$$\operatorname{curl} E + \mu \frac{\partial H}{\partial t} = 0 \tag{1}$$

$$\operatorname{curl} H - \varepsilon \frac{\partial E}{\partial t} = \sigma E \tag{2}$$

Assume that $D = \Omega \times \mathbb{R}$ is an infinitely long perfectly conducting cylinder buried in the lower half-space $x_2 < 0$, which remains invariant in x_3-direction; see Figure 1(a). The medium in the exterior $D^e := \mathbb{R}^3 \setminus \overline{D}$ of D is assumed to be dielectric, which means that $\sigma = 0$. The cross section of D in the ox_1x_2-plane is denoted by $\Omega \subset \mathbb{R}^2_- := \{x = (x_1, x_2) : x_2 < 0\}$. Incident cylindrical source waves emitted from the surface $\Gamma \subset (\mathbb{R}^3 \setminus \overline{D}) \cap \{x_3 = 0\}$ will be utilized for the purpose of detecting the position and shape of Ω. Throughout the paper, we assume that the incident wave $E^i_\chi(\mathrm{x}, t; \mathrm{y})$ with $\mathrm{x} = (x, x_3)$, $\mathrm{y} = (y, y_3) \in \mathbb{R}^3$, $t > 0$ is a filamentary current

generated at the source location $y \in \Gamma$ with a temporal pulse signal $\chi : \mathbb{R} \longrightarrow \mathbb{R}$. The temporal function is supposed to have a compact support $(\chi)(t) \in (0, T_0)$ for some $T_0 > 0$. Moreover, we consider the Transverse Electric (TE) case of the monopole with the polarization direction $e_3 = (0, 0, 1)$. Then, the incident electric and magnetic waves (E^i, H^i) are governed by the system

$$\begin{aligned} \operatorname{curl} E^i(\mathrm{x}, t; \mathrm{y}) + \mu \frac{\partial H^i(\mathrm{x}, t; \mathrm{y})}{\partial t} &= 0 \\ \operatorname{curl} H^i(\mathrm{x}, t; \mathrm{y}) - \varepsilon \frac{\partial E^i(\mathrm{x}, t; \mathrm{y})}{\partial t} &= -\delta(\mathrm{x} - \mathrm{y}) \chi(t) e_3 \end{aligned} \tag{3}$$

for all $\mathrm{x} \neq \mathrm{y}$, $\mathrm{x} \in D^e$, and $t > 0$, where δ is the Dirac distribution. Denote by (E^s, H^s) the scattered fields and write the total field as $E = E^i + E^s$, $H = H^i + H^s$. Then, we have

$$\begin{aligned} \operatorname{curl} E(\mathrm{x}, t; \mathrm{y}) + \mu \frac{\partial H(\mathrm{x}, t; \mathrm{y})}{\partial t} &= 0 \quad \text{in } D^e \setminus \{\mathrm{y}\} \times \mathbb{R}_+, \\ \operatorname{curl} H(\mathrm{x}, t; \mathrm{y}) - \varepsilon \frac{\partial E(\mathrm{x}, t; \mathrm{y})}{\partial t} &= -\delta(\mathrm{x} - \mathrm{y}) \chi(t) e_3 \\ &\qquad \text{in } D^e \setminus \{\mathrm{y}\} \times \mathbb{R}_+, \\ \nu \times E(\mathrm{x}, t; \mathrm{y}) &= 0 \quad \text{on } \partial D \times \mathbb{R}_+, \end{aligned} \tag{4}$$

together with the zero initial condition at $t = 0$ in $\mathbb{R}^3$. Here $\nu = (\nu_1, \nu_2, \nu_3)$ is the unit outward normal to the boundary ∂D. Eliminating the magnetic field, we arrive at

$$\begin{aligned} \frac{\partial^2 E(\mathrm{x}, t; \mathrm{y})}{\partial t^2} &= -\frac{1}{\varepsilon\mu} \operatorname{curl} \operatorname{curl} E(\mathrm{x}, t; \mathrm{y}) \\ &\quad + \frac{1}{\varepsilon} \delta(\mathrm{x} - \mathrm{y}) \partial_t \chi(t) e_3, \quad \mathrm{x} \neq \mathrm{y}. \end{aligned} \tag{5}$$

In the TM polarization case, the electric field takes the form $E(\mathrm{x}) = (0, 0, u(x))$. Hence, the perfectly conducting boundary condition can be written as

$$\nu \times E = \begin{bmatrix} i & j & k \\ \nu_1 & \nu_2 & 0 \\ 0 & 0 & u \end{bmatrix} = (\nu_2 u, -\nu_1 u, 0) \quad \text{on } \partial D \times \mathbb{R}_+, \tag{6}$$

implying that $u = 0$ on $\partial D \times \mathbb{R}_+$. Using

$$\operatorname{curl} \operatorname{curl} E(\mathrm{x}) = -\Delta E(\mathrm{x}) + \operatorname{grad} \operatorname{div} E(\mathrm{x}), \tag{7}$$

we deduce the reduced wave equation from the Maxwell system (5) as follows:

$$\begin{aligned} \frac{\partial^2 u(\mathrm{x}, t; \mathrm{y})}{\partial t^2} &= \frac{1}{\varepsilon\mu} \Delta u(\mathrm{x}, t; \mathrm{y}) + \frac{1}{\varepsilon} \delta(\mathrm{x} - \mathrm{y}) \partial_t \chi(t), \\ &\qquad \mathrm{x} \in \mathbb{R}^2 \setminus \left\{\overline{\Omega} \cup \{\mathrm{y}\}\right\} \times \mathbb{R}_+. \end{aligned} \tag{8}$$

In the particular case that $\chi(t) = \sin(\omega t)$ is a 2π-periodic function, where ω denotes the frequency, the incident field u^{in} can be explicitly represented as

$$u^{in}(\mathrm{x}, t; \mathrm{y}) = \mu\omega \operatorname{Re}\left\{\frac{i}{4} H_0^{(1)}\left(\frac{\omega}{c}|\mathrm{x} - \mathrm{y}|\right) e^{i\omega t}\right\}, \quad \mathrm{x} \neq \mathrm{y}. \tag{9}$$

Here $H_0^{(1)}$ is the Hankel function of first kind of order zero; see [37, Chapter 3.4].

In this paper we shall consider the following inverse problem:

> (IP): determine the position and shape of $\partial\Omega$ from knowledge of $u^s(x, t; y)$ irradiated by incident dipoles located at $y \in \Gamma$.

Throughout this paper, we use the temporal function of the form

$$\chi(t) = -A\left[2\pi^2 f^2 \left(t - \frac{\sqrt{2}}{f}\right)^2 - 1\right] e^{-\pi^2 f^2 (t - \sqrt{2}/f)^2}, \quad t > 0, \tag{10}$$

which is known as the Ricker pulse. Here $f > 0$ is the center frequency and $A > 0\ 0$ is the amplitude. The incident pulse function $\chi(t)$ with $f = 6$ GHz is depicted in Figure 2.

We shall consider two cases:

(i) $\Omega \in \mathbb{R}^2_-$ is a small object (compared to the incident wavelength), $\Gamma = \{(x_1, b) : a_1 < x_1 < a_2\}$ is a finite line segment, and the data are given by $\{u^s(x, t; x)\}$ for all $(x, t) \in \Gamma \times (0, T)$.

(ii) Ω is an extended scatterer, $\Gamma = \{x \in \mathbb{R}^2 : |x| = R\}$ for some $R > 0$ such that $\Omega \subset B_R := \{x \in \mathbb{R}^2 : |x| < R\}$, and the data are given by $\{u^s(\mathrm{x}, t; \mathrm{y})\}$ for all $(\mathrm{x}, t) \in \Gamma \times (0, T)$ irradiated by many dipoles emitted from Γ.

Note that in case (i), the positions of the receivers and transmitters are identical, leading to the so-called inverse back scattering problem, whereas the case (ii) corresponds to a multiple-input-multiple-output (MIMO) radar system. The aim of this paper is to apply the total focusing method to the above inverse electromagnetic scattering problems with synthetic and experimental data. The TFM is sometimes described as the "gold standard" in the classical beamforming. Both TFM and the Kirchhoff migration form the image with the superposition of the scattered signals irradiated by each transmitter.

3. Imaging Small Scatterers

In this section we suppose that a single metal stick is buried in sand below the ground plane $\{x_2 = b\}$. The cross section Ω of the metal is so small compared to the wavelength such that Ω can be regarded as a point-like object. The electric dipoles are generated on part of the ground plane $\Gamma = \{(x_1, b) : a_1 < x_1 < a_2\}$ for some $a_j > 0$ $(j = 1, 2)$. The Kirchhoff migration imaging scheme for inverse back scattering consists of the following three steps:

Firstly, we take the searching area as a rectangular domain in the lower half-space $\mathbb{R}^2_-$ and divide it into an $M \times N$ grid. The grid points, as shown in Figure 1(b), will be referred to as sampling points $z \in \mathbb{R}^2_-$. We shall design an imaging function defined on these grid points.

Secondly, the filamentary current is transmitted from the source position $\{x^{(k)} = (k(a_2 - a_1)/N, 0)\}$ and the scattered signals are also recorded at the same position $x^{(k)}$, which we

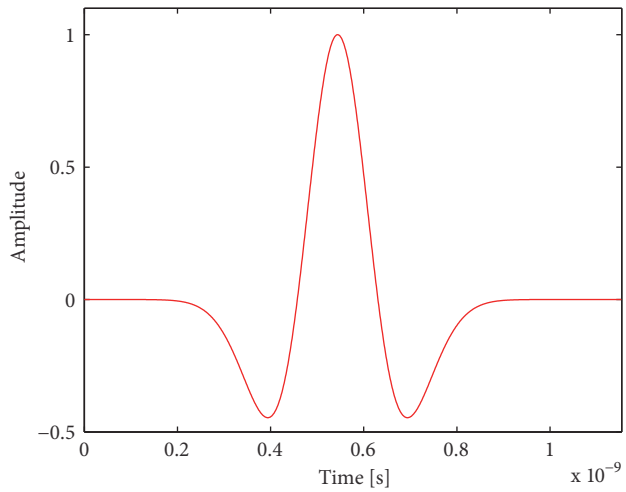

FIGURE 2: The Ricker pulse with $f = 6$ GHz and $A = 1$.

denote by $u_k^s(t) := u^s(x^{(k)}, t; x^{(k)})$ for $k = 1, 2, \ldots, N$. Note that $u^s(x, t; y) = u(x, t; y) - u^i(x, t; y)$ stands for the scattered wave field. Calculate the flight time of the signal emitted from $x^{(k)}$ to a sampling point z and then returned back to the receiver $x^{(k)}$, given by

$$t_k(z) = \frac{2\left|x^{(k)} - z\right|}{c}, \quad k = 1, 2, \ldots, N. \tag{11}$$

Here $c = \sqrt{1/(\varepsilon\mu)} > 0$ denotes the light speed in the background medium. In particular, we have $c = c_0\sqrt{\varepsilon}$ in terms of the light speed c_0 in the vacuum.

Thirdly, collect all signals u_k^s for $k = 1, 2, \ldots, N$ and plot the indicator function

$$I(z) = \left|\sum_{k=1}^{N} u_k^s(t_k(z))\right|^2 > 0. \tag{12}$$

Here we have assumed that the terminal T is large enough. By the mathematical analysis performed in [21], the local maximizers of I can represent the location of the small scatterer.

3.1. Imaging with Synthetic Data. To implement the Kirchhoff migration scheme, we assume that the interface between the air and the sand is given by $\{(x_1, b) : x_1 \in \mathbb{R}\}$ with $= -0.1$. The dielectric properties of the sand are considered as 4. We choose $N = 41$ receivers and transmitters uniformly lying between $(0.1, -0.1)$ and $(0.1, -0.3)$. The cross section of the metal stick is supposed to be the circle of radius 0.009 centered at $(0.2, -0.167)$; see Figure 3 for the locations of the metal stick in the ox_1x_2-plane and the first transmitter (receiver). The center frequency of Ricker waves is uniformly taken as $f = 2.6$ GHz and the amplitude is set to be $A = 1$. The terminal time is taken as

$$T = \frac{2h}{c} + \frac{1}{f}, \tag{13}$$

where $h > 0$ denotes the travel distance of the radar. In our simulations we take $T = 7 \times 10^{-9}s$.

The scattered data were generated by GprMax based on the FDTD method (see [20, 38]). The unbounded exterior domain is truncated by an absorbing boundary condition. The mesh of the forward solver is successively refined until the relative error of the successive measured scattered data is below 0.1%.

For the k-th transmitter, the scattered data u_k^s are recorded at 1063 time points given by

$$t_k = \frac{k}{1063}T, \quad k = 1, 2, \ldots, 1063. \tag{14}$$

Linear interpolation is adopted to obtain the value of $u_k^s(t)$ for an arbitrary $t \in (0, T)$. In Figure 4, we show the signals of the incident electric field and the total fields irradiated by the first transmitter. The incident field obviously has a launch waveform, as shown in Figure 4(a). The significant changes before 0.2ns are due to the transmitter itself rather than the reflected wave field from the metal stick. In Figure 4(b), one can observe the changes of the signal at about 0.4ns caused by the presence of the object. Subtracting the incident field from the total field, one can obtain the scattered signal, which will be utilized to locate the position of the stick.

For $x = (x_1, x_2) \in \mathbb{R}^2$ with $x_1 \in [0.1 + kh, 0.1 + (k+1)h]$, $h = (a_2 - a_1)/N = 0.2/268$, we first plot the function

$$B(x) := u_k^s\left(\frac{2\left|x_2 - 0.1\right|}{c}\right), \quad -0.4 < x_2 < -0.1, \tag{15}$$

which forms the B-scan image of the object. Note that only the information of the signal of u_k^s is involved in B-scan for $x_1 \in [0.1 + kh, 0.1 + (k+1)h]$, whereas all signals are required in our indicator equation (15). Figure 5(a) shows the B-scan image of the small object located at (0.2, 0.167). The x_1-coordinate of the location corresponds to the trace number 100. In Figure 5(b), one can see an approximate location of the target using our indicator (15). Numerical experiments show that the Kirchhoff migration method is not only efficient but

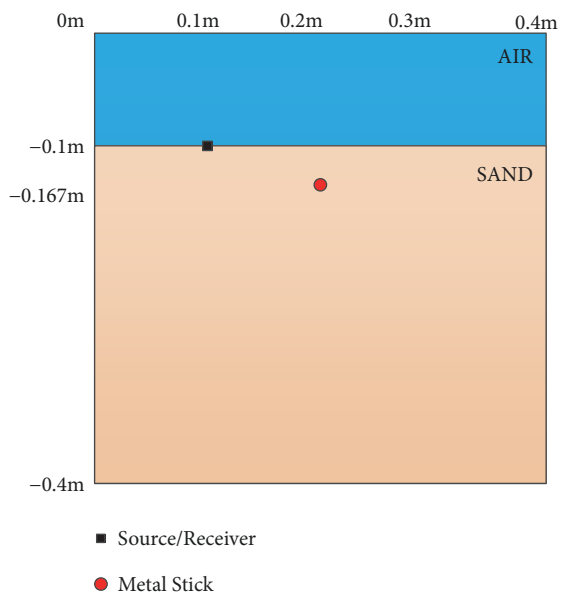

Figure 3: Locations of the first transmitter/receiver and the target.

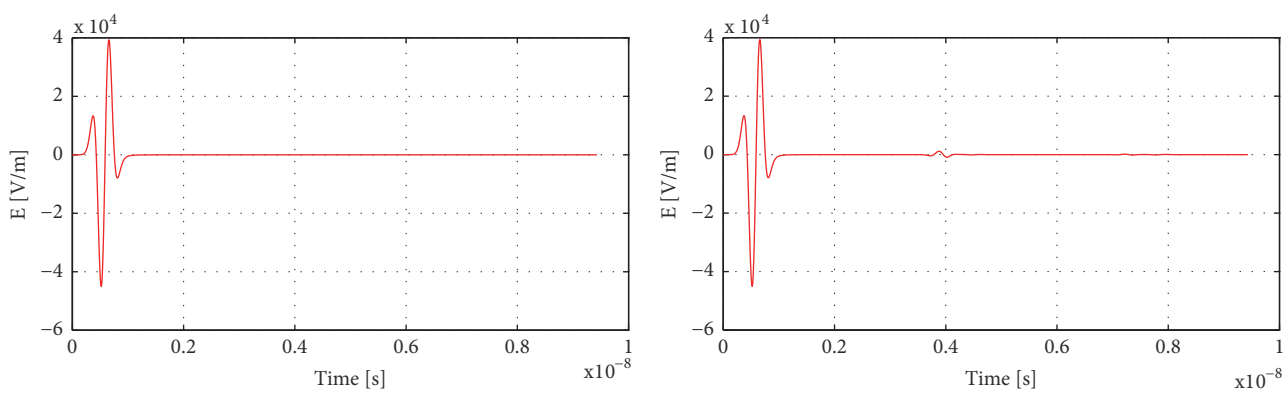

(a) Incident field (b) Total field

Figure 4: Electric signals generated by the first transmitter.

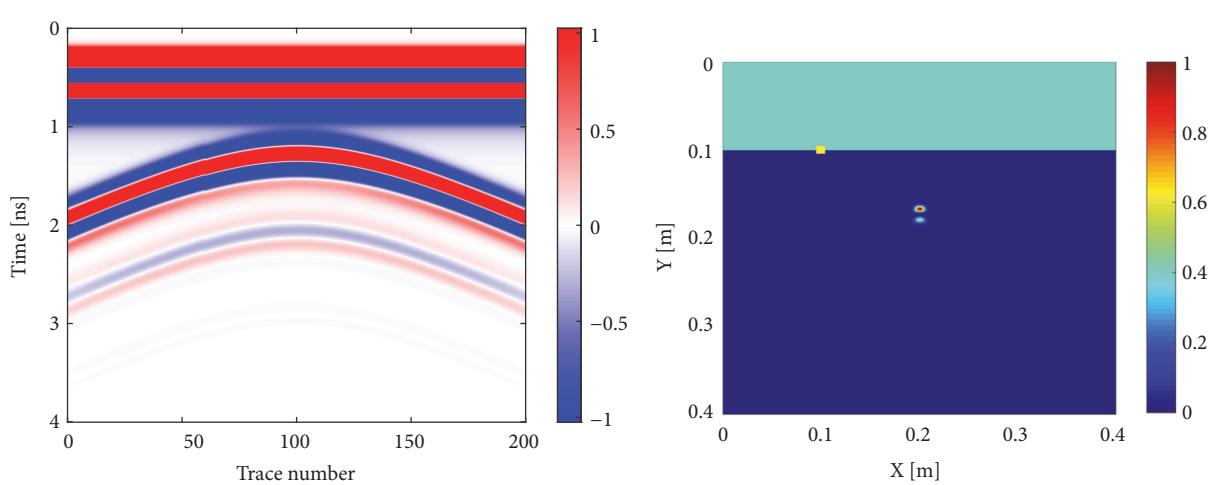

(a) B-scan image formed by the indicator equation (15) (b) The Kirchhoff migration image

Figure 5: Imaging a small scatterer using synthetic data without noise.

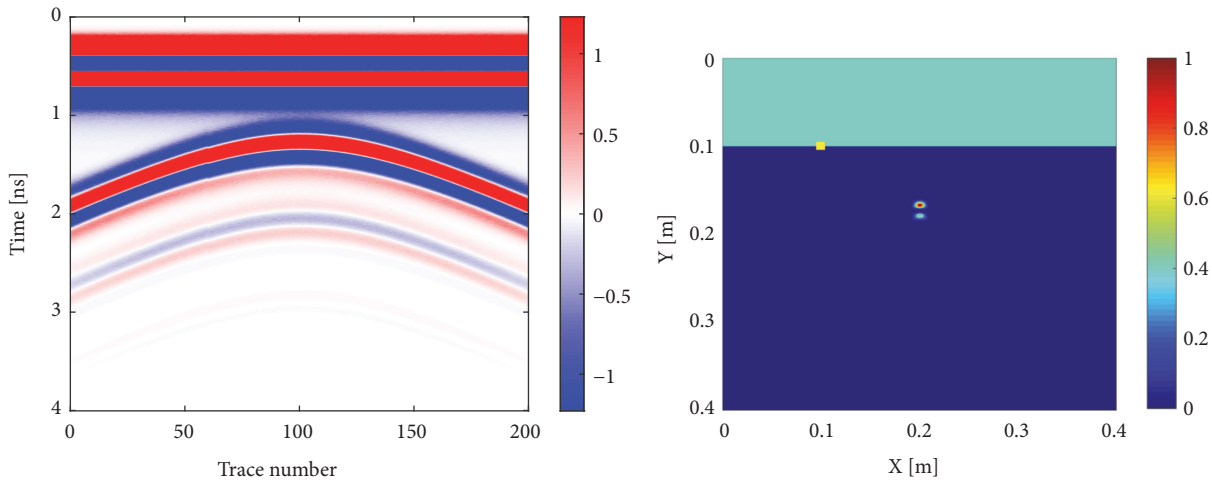

(a) B-scan image formed by the indicator equation (15)

(b) The Kirchhoff migration image

Figure 6: Imaging a small scatterer using polluted synthetic data at the noise level $\delta = 100\%$.

Figure 7: Experiment site.

also robust with respect to polluted data at high noise levels (Figure 6). Note that in this paper the scattered near-field data is polluted by

$$u_{\delta}^{sc}(x,t) = u^{sc}(x,t) + \delta\zeta u^{sc}(x,t), \tag{16}$$

where δ is the noise ratio and ζ is the standard normal distribution.

3.2. Imaging with Experimental Data. In our experiment settings, a metal stick is detected in a sand box by a GSSI Mini HR hand-held ground-penetrating radar; see Figure 7 for the experiment site. The size of the sand box is 0.45 m×0.3m×0.2m, the thickness of the wooden shell is 0.015m, the dielectric properties of the sand are 4, and the dielectric properties of the wooden box are considered approximately the same as the sand. For electric dipoles with TE polarization, the three-dimensional Maxwell equation can be reduced to a two-dimensional model for scalar wave equations. We set up a two-dimensional coordinate system and take the initial position of the source and receiver of the radar at (0.1, 0.1). The metal stick is centered at (0.2, 0.167) with the radius 0.009. The radar rolls along the straight line $x_2 = 0.1$ on the wooden shell and moves forward in the positive x_1-direction at an even pace. In this process there are totally 268 electric dipoles excited by the radar before it reaches the ending point (0.25, 0.1). The temporal function of the incident wave is a Ricker wavelet excited at the frequency 2.6GHz with the amplitude 1.

The B-scan image formed by our experimental data is plotted with Matlab R2013b, as shown in Figure 8(a). Figure 8(b) shows the image using the indicator (12), where the position of the target is precisely located. In comparison with the counterpart from synthetic data (see Figure 5(b)), we find that the inversion of the depth of the stick contains relatively large errors.

Next, we want to find two metal sticks with different positions. The centers of the cross section in the ox_1x_2-plane are given by (0.15, 0.15) and (0.25, 0.17), respectively. The other parameters in our experiment are the same as before. See Figure 9(b) for the experiment site and Figure 9(a) for the location of the two sticks.

The B-scan images with synthetic and experimental data are shown in Figures 10(a) and 10(b), respectively. The final inversion images based on the Kirchhoff migration are illustrated in Figures 11(a) and 11(b), respectively.

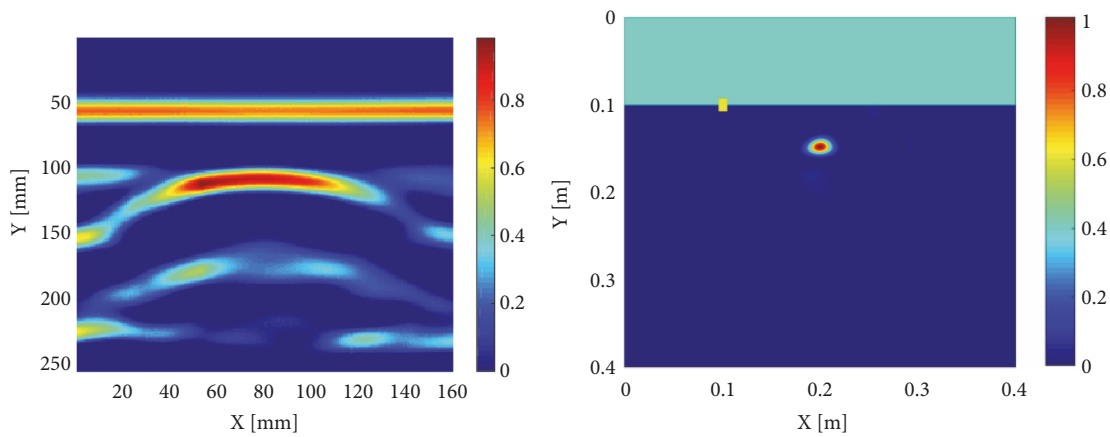

(a) B-scan image

(b) Imaging by using the Kirchhoff migration

Figure 8: Imaging with experimental data.

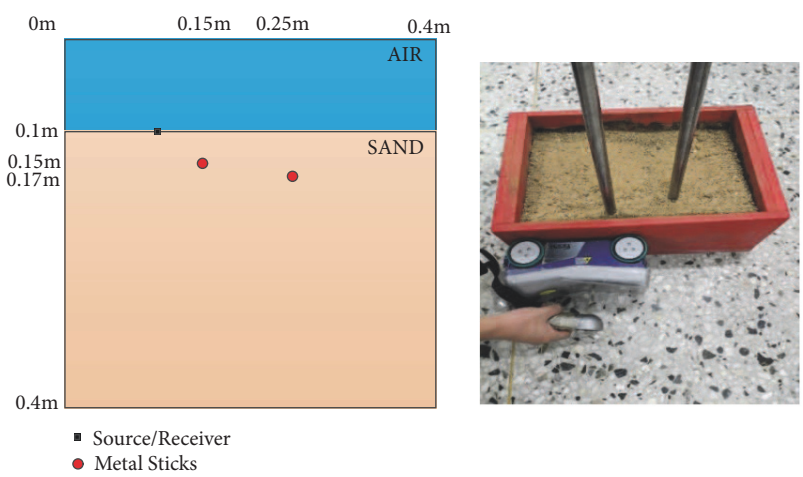

(a) Locations of the first transmitter/receiver and the two small targets

(b) Experiment site

Figure 9: Locating two small scatterers buried in sand.

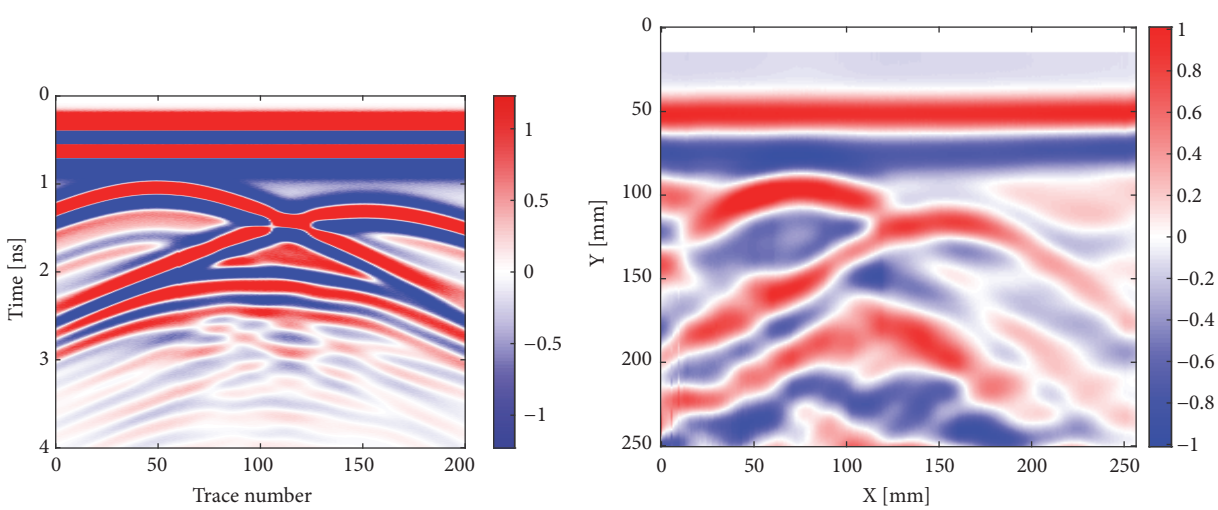

(a) Synthetic data at the noise level 20%

(b) Experimental data

Figure 10: Comparison of the B-scan images with the synthetic data at noise level 20% (a) and experimental data (b).

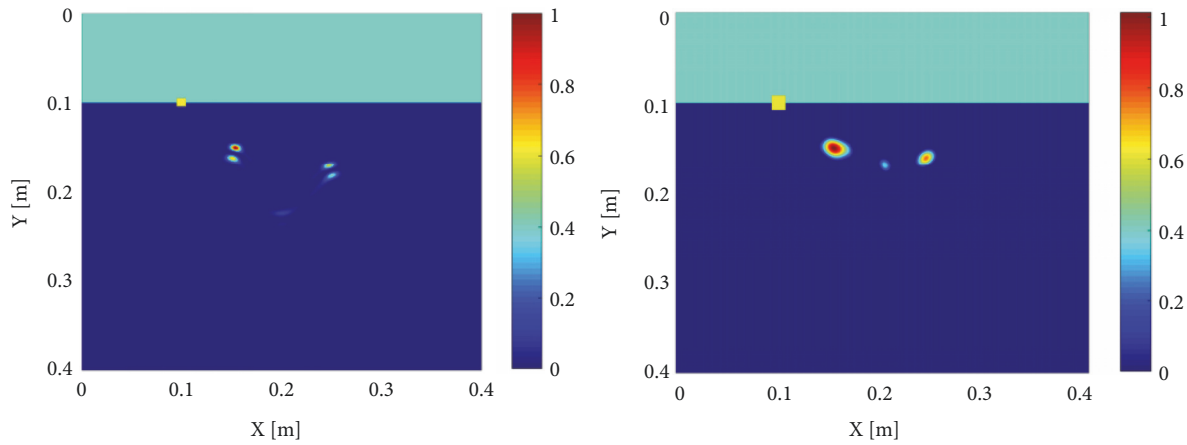

(a) Synthetic data at the noise level 20%

(b) Experimental data

Figure 11: Comparison of the images formed by the Kirchhoff migration scheme.

As shown in Figure 10, the B-scan results in both simulation and experiment can indicate a local peak in the position of the metal sticks, verifying the correctness of the inversion scheme. In Figure 11, the local maximum values of the indicator function are obtained approximately at (0.15, 0.15) and (0.25, 0.17), which agree well with the positions of the targets in our model. From the experiment image, it can be concluded that the contour image and the position of the left metal stick agree well with the true scatterers, but the size of the right one is not well reconstructed. Further, there is an untrustworthy imaging area between the two metal sticks, maybe due to the offset of the two maximizes nearby.

4. Imaging Extended Scatterers

The main purpose of this section is to test the Kirchhoff migration for imaging extended scatterers from synthetic data of several incident electric dipoles. As in the previous section, the forward data are obtained by the software GprMax. We consider the second case of our inverse electromagnetic scattering problem formulated at the end of Section 2, where the source positions are uniformly distributed on the circle $|x-O| = R$ for some $R > 0$, where $O = (o_1, o_2) \in \mathbb{R}^2$. Denote by $M > 0$ the number of incident dipoles. The Cartesian coordinates of the m-th dipole can be formulated as

$$y^{(m)} = O + R\left(\cos\theta_m, \sin\theta_m\right),$$
$$\theta_m := \frac{2m\pi}{M}, \qquad m = 1, 2, \ldots, M. \tag{17}$$

In all examples we use $N = 16$ receivers $x^{(n)}$ $(n = 1, 2, \ldots, 16)$ equally spaced on $|x - O| = R$. For notational convenience, we use $u^s_{n.m}(t) = u^s_{n,m}(x^{(m)}, t; x^{(n)})$ to represent the scattered signal excited by the n-th transmitter recorded at the m-th receiver. The flight time of an impulsive signal from $y^{(n)}$ to a sampling point $z = (z_1, z_2)$ and then back to $x^{(m)}$ is then given by

$$t_{n,m}(z) = \frac{\left|y^{(n)} - z\right| + \left|z - x^{(m)}\right|}{c}, \quad n, m = 1, 2, \ldots, 16. \tag{18}$$

In this case the imaging function based on Kirchhoff migration scheme can be formulated as

$$I(z) = \left|\sum_{n=1}^{N}\sum_{m=1}^{M} u^s_{n,m}\left(t_{n,m}(z)\right)\right|^2 > 0. \tag{19}$$

In all of our numerical examples to be reported below, we set $O = (0.35, 0.35)$. The sampling region is set to be the rectangular domain $(0, 0.7) \times (0, 0.7)$. The homogeneous background medium is set to be air, with the dielectric constant $\varepsilon = 1$ and the electric conductivity $\sigma = 0$. Unless otherwise stated, the excitation frequency of a Ricker wave is taken as $f = 10$GHz. The amplitude is set to be $A = 1$ and the time window is $T = 4$ns.

In the first example, we excite only one electric dipole located at $y^{(4)}$ and measure the scattered field at $x^{(n)}$ for $n = 1, 2, \ldots, 16$. Three types of scatterers will be recovered: two small circular metals, a square-like metal, and an L-shaped metal; see Figures 12(a), 12(c), and 12(e). The last two targets will be referred to as extended scatterers, since their size is much bigger than the incident wavelength. The circular metals are centered at A(0.25, 0.35) and B(0.45, 0.35) with the radius 0.01 m. They can be treated as point-like scatterers, because their radiuses are both much smaller than the wavelength $\lambda = 0.3$m corresponding to $f = 10$GHz. The coordinates of the corners of the square-like metal are given by A(0.275, 0.425), B(0.425, 0.425), C(0.425, 0.275), and B(0.275, 0.275), and those for the L-shaped metal are A(0.275, 0.475), B(0.35, 0.475), C(0.35, 0.35), D(0.475, 0.35), E(0.475, 0.275), and F(0.275, 0.275). Figures 12(b), 12(d), and 12(f) show the reconstructions from the data of one dipole only. It can be seen that a single source can be used to capture the position of point scatterers and the illuminated boundary

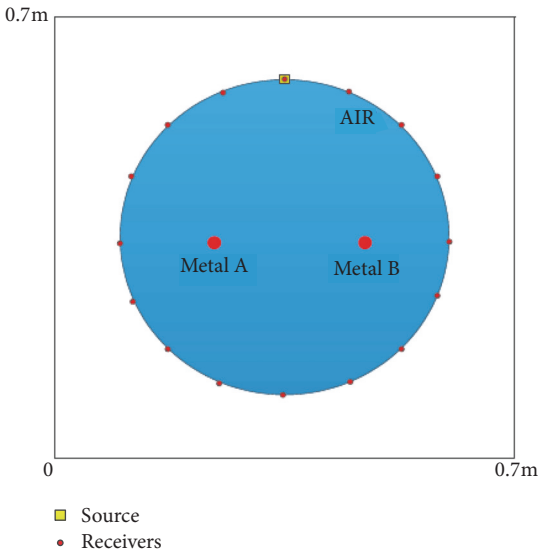

(a) Two small objects

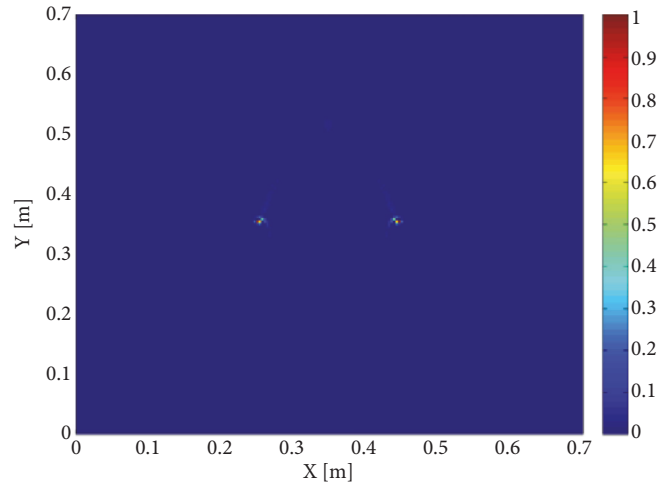

(b) Location of the two small objects

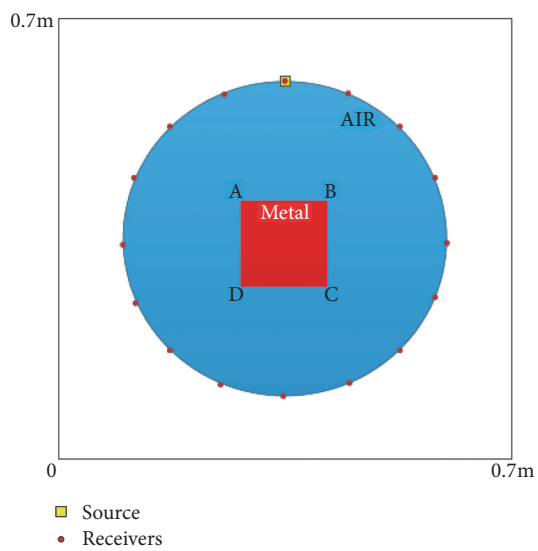

(c) A square-like metal

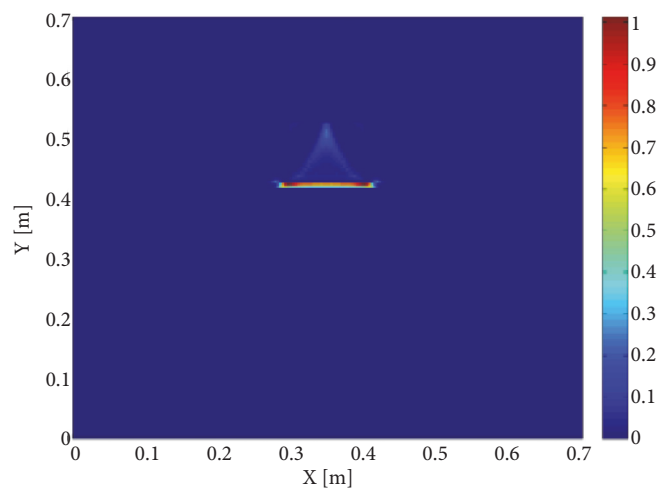

(d) Imaging of the square-like metal

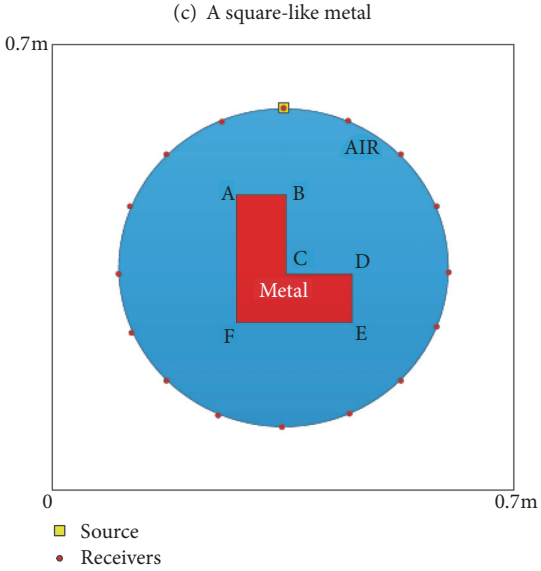

(e) An L-shaped metal

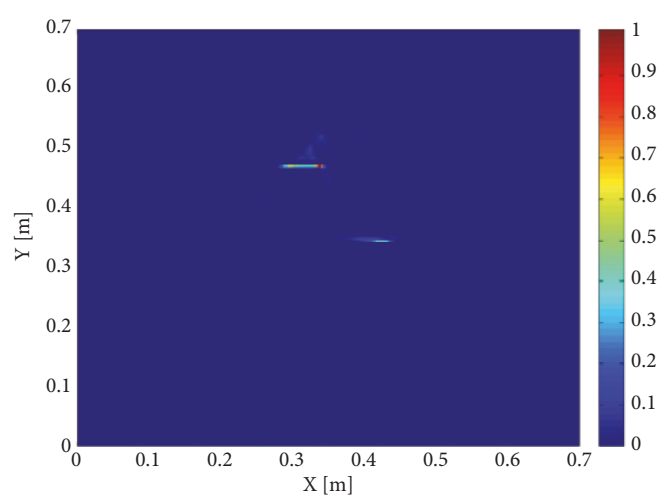

(f) Imaging of the L-shaped metal

Figure 12: Imaging small and extended metals with a single incoming dipole.

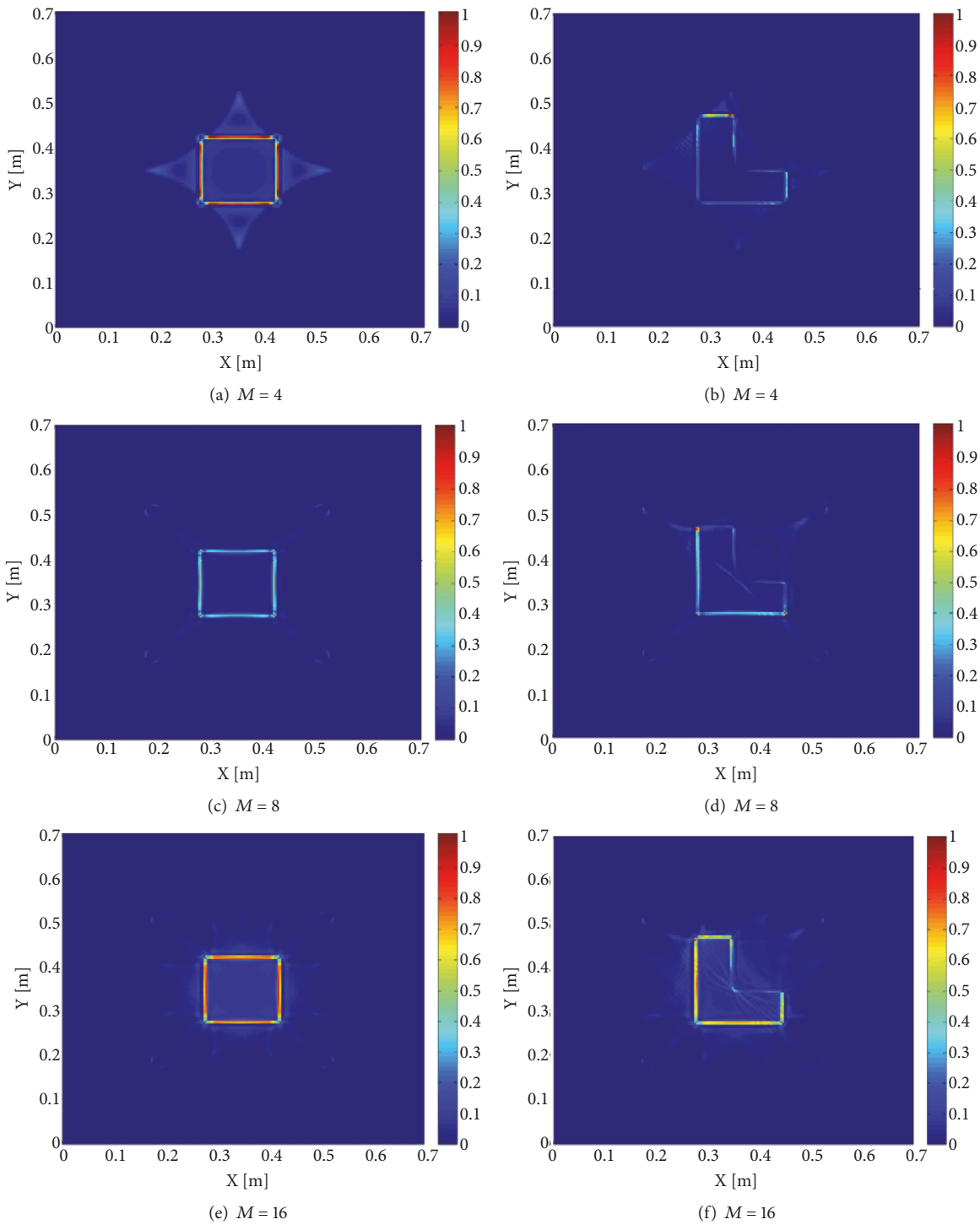

(a) $M = 4$ (b) $M = 4$

(c) $M = 8$ (d) $M = 8$

(e) $M = 16$ (f) $M = 16$

Figure 13: Imaging a square-like object (left) and an L-shape object (right) by M transmitters and $N = 16$ receivers.

of the square-like and L-shaped scatterers. However, the entire shape of extended objects cannot be well reconstructed.

In the second example, we increase the number of incident dipoles for reconstructing the entire shape; see Figure 13. The data of four incident waves without noise can generally produce a full-range image of an extended scatterer. However, there are bigger background disturbances and the scatterer cannot be accurately recovered. Using eight and sixteen incoming sources can image the outline of the scatterer. In Figures 13(e) and 13(f), the maximum values of the indicator are almost distributed on the contour of the object and the imaging is better than the case of eight dipoles. This means that sixteen sources are capable of imaging the scatterer, and therefore it is not necessary to use additional

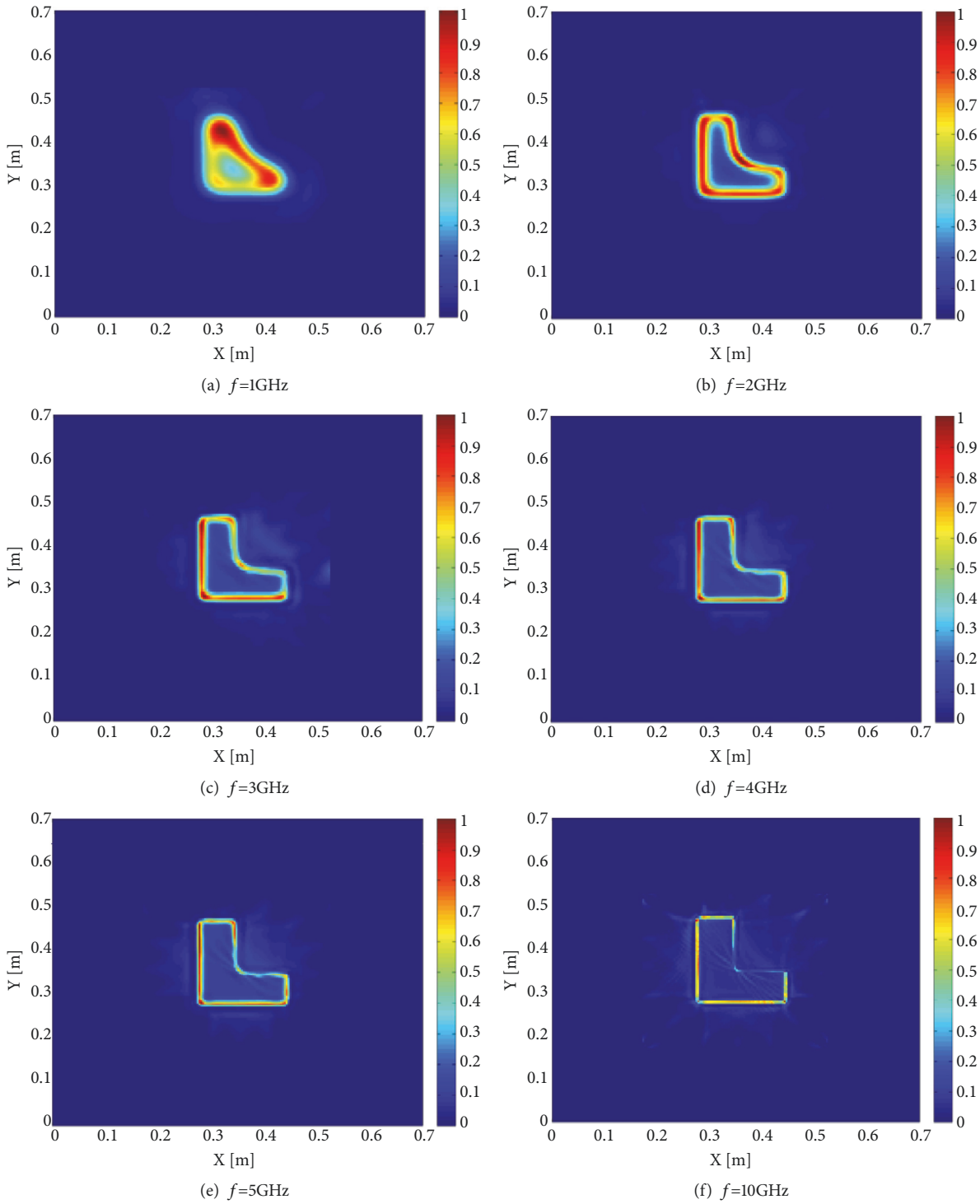

(a) f=1GHz (b) f=2GHz (c) f=3GHz (d) f=4GHz (e) f=5GHz (f) f=10GHz

Figure 14: Imaging an L-shape object by M=16 transmitters and N=64 receivers (f is the excitation frequency of the sources).

sources. Hence, the data of multiple point sources in different directions need to be measured in order to better capture the shape of the target.

In the third example, we discuss the sensitivity of the imaging quality to the center frequency of incident pulse functions. We use M=16 incident dipoles and N=64 receivers. As shown in Figure 14, the shape of an extended object can be imaged at various frequencies from 1GHz to 10GHz. However, at lower frequencies the target cannot be accurately recovered. Increasing the excitation frequency of the source (which means a shorter wavelength) may lead to an image with higher resolutions.

5. Conclusions

We apply the Kirchhoff migration approach to solve inverse scattering problems for time-dependent electromagnetic waves. The inversion scheme involves only integral calculations and is robust to polluted data at high noisy levels. We use both synthetic and experimental data to examine the performance of such a direct sampling scheme for locating point-like scatterers. The multiple-input-multiple-out scheme is used for imaging extended scatterers from the data generated by the software GprMax. Our experiments show that the data of one electric dipole can correctly reconstruct the location of two small scatterers, and that sixteen incoming sources can perfectly reconstruct the shape of an extended target. In addition, the source irradiated at 10GHz can be used to more clearly reconstruct the geometrical shape than the data of lower frequencies ranging from 1GHz to 5GHz. Our future work consists of imaging extended obstacles from experimental data buried in a random background medium, which is more challenging than the problem in a stationary homogeneous medium.

Data Availability

The data used to support the findings of this study are included within the supplementary information files.

Conflicts of Interest

The authors declare that there are no conflicts of interest regarding the publication of this paper.

Acknowledgments

The work of Hongwei Zhou and Ling Ma was supported by the National Key Research and Development Program (Grant No. 2017YFD0600101), the Fundamental Research Funds for the Central Universities (Grant No. 2572019BF08), the China Postdoctoral Science Foundation (Grant No. 2018M640288), and the Heilongjiang Postdoctoral Fund (Grant No. LBH-Z18004). The work of Guanghui Hu is supported by NSFC (Grant No. 11671028) and NSAF (Grant No. U1530401).

Supplementary Materials

We used the GSSI Mini HR hand-held ground-penetrating radar to scan the sand box in Figure 7. The ground-penetrating radar had a transmitting antenna and a receiving antenna, the transmitting antenna transmitted a Ricker wavelet excited at the frequency 2.6GHz with the amplitude 1, and the receiving antenna received data as in the supplementary information files of "data of fig7.CSV" and "data of fig9b". The difference between "data of fig7.CSV" and "data of fig9b" is that the file "data of fig7.CSV" is for one metal stick, and the file "data of fig9b" is for two metal sticks. *(Supplementary Materials)*

References

[1] J. C. Bolomey, D. Lesselier, C. Pichot, and W. Tabbara, "Physically motivated approximations in some inverse scattering problems," *Radio Science*, vol. 17, no. 6, pp. 1567–1578, 2016.

[2] V. K. Chillara and C. J. Lissenden, "Review of nonlinear ultrasonic guided wave nondestructive evaluation: theory, numerics, and experiments," *Optical Engineering*, vol. 55, no. 1, Article ID 011002, 2015.

[3] P. Lobel, R. E. Kleinman, C. Pichot, L. Blanc-Féraud, and M. Borlaud, "Conjugate-gradient method for solving inverse scattering with experimental data," *IEEE Antennas and Propagation Magazine*, vol. 38, p. 35, 1996.

[4] G. Oliveri, M. Salucci, N. Anselmi, and A. Massa, "Compressive sensing as applied to inverse problems for imaging: theory, applications, current trends, and open challenges," *IEEE Antennas and Propagation Magazine*, vol. 59, no. 5, pp. 34–46, 2017.

[5] R. Persico, "On the role of measurement configuration in contactless GPR data processing by means of linear inverse scattering," *IEEE Transactions on Antennas and Propagation*, vol. 54, no. 7, pp. 2062–2071, 2006.

[6] A. Kirsch and R. Kress, "On an integral equation of the first kind in inverse acoustic scattering," in *Inverse Problems*, J. R. Cannon and U. Hornung, Eds., vol. 77 of *International Series of Numerical Mathematics*, pp. 93–102, Birkhäuser Basel, 1986.

[7] A. Kirsch and R. Kress, "An optimization method in inverse acoustic scattering," in *Boundary Elements IX, Fluid Flow and Potential Applications*, C. A. Brebbia et al., Ed., vol. 3, pp. 3–18, Springer, Berlin, Germany, 1987.

[8] D. Colton and P. Monk, "A novel method for solving the inverse scattering problem for time-harmonic acoustic waves in the resonance region," *SIAM Journal on Applied Mathematics*, vol. 45, no. 6, pp. 1039–1053, 1985.

[9] D. Colton and P. Mon, "The numerical solution of the three-dimensional inverse scattering problem for time-harmonic acoustic waves," *Society for Industrial and Applied Mathematics*, vol. 8, no. 3, pp. 278–291, 1987.

[10] T. S. Angell, R. E. Kleinman, and G. F. Roach, "An inverse transmission problem for the Helmholtz equation," *Inverse Problems*, vol. 3, no. 2, pp. 149–180, 1987.

[11] M. Saqib, S. Hasnain, and D. S. Mashat, "Highly efficient computational methods for two-dimensional coupled nonlinear unsteady convection-diffusion problems," *IEEE Access*, vol. 5, pp. 7139–7148, 2017.

[12] L. Yang, J. Tian, K. Z. Rajab, and Y. Hao, "FDTD modeling of nonlinear phenomena in wave transmission through graphene," *IEEE Antennas and Wireless Propagation Letters*, vol. 17, no. 1, pp. 126–129, 2018.

[13] H. H. Gan, T. Xia, Q. I. Dai, Y. Li, and W. C. Chew, "Augmented electric-field integral equation for inhomogeneous media," *IEEE Antennas and Wireless Propagation Letters*, vol. 16, pp. 2967–2970, 2017.

[14] D. Colton and A. Kirsch, "A simple method for solving inverse scattering problems in the resonance region," *Inverse Problems*, vol. 12, no. 4, pp. 383–393, 1996.

[15] C. Bilen, A. Ozerov, and P. Pérez, "Solving time-domain audio inverse problems using nonnegative tensor factorization," *IEEE Transactions on Signal Processing*, vol. 66, no. 21, pp. 5604–5617, 2018.

[16] M. Ikehata, "Reconstruction of an obstacle from the scattering amplitude at a fixed frequency," *Inverse Problems*, vol. 14, no. 4, pp. 949–954, 1998.

[17] M. N. Akinci, M. Cayoren, and I. Akduman, "Near-field orthogonality sampling method for microwave imaging: theory and experimental verification," *IEEE Transactions on Microwave Theory and Techniques*, vol. 64, no. 8, pp. 2489–2501, 2016.

[18] G. Bao, P. Li, J. Lin, and F. Triki, "Inverse scattering problems with multi-frequencies," *Inverse Problems*, vol. 31, no. 9, Article ID 093001, 2015.

[19] G. Bao, J. Lin, and F. Triki, "A multi-frequency inverse source problem," *Journal of Differential Equations*, vol. 249, no. 12, pp. 3443–3465, 2010.

[20] G. Bao and P. Li, "Inverse medium scattering problems in near-field optics," *Journal of Computational Mathematics*, vol. 25, no. 3, pp. 252–265, 2007.

[21] G. Bao and F. Triki, "Reconstruction of a defect in an open waveguide," *Science China Mathematics*, vol. 56, no. 12, pp. 2539–2548, 2013.

[22] H. Wang and J. Liu, "On the reconstruction of Dirichlet-to-Neumann map in inverse scattering problems with stability estimates," *Science China Mathematics*, vol. 53, no. 8, pp. 2069–2084, 2010.

[23] M. Sheikholeslami, H. Keramati, A. Shafee, Z. Li, O. A. Alawad, and I. Tlili, "Nanofluid MHD forced convection heat transfer around the elliptic obstacle inside a permeable lid drive 3D enclosure considering lattice Boltzmann method," *Physica A: Statistical Mechanics and its Applications*, vol. 523, pp. 87–104, 2019.

[24] M. Fink, "Time reversed acoustics," *Physics Today*, vol. 50, no. 3, pp. 34–40, 1997.

[25] E. Baysal, D. D. Kosloff, and J. W. C. Sherwood, "Reverse time migration," *Geophysics*, vol. 48, no. 11, pp. 1514–1524, 1983.

[26] L. Oksanen, "Solving an inverse obstacle problem for the wave equation by using the boundary control method," *Inverse Problems*, vol. 29, no. 3, pp. 35004–35015, 2013.

[27] D. Russell Luke and R. Potthast, "The point source method for inverse scattering in the time domain," *Mathematical Methods in the Applied Sciences*, vol. 29, no. 13, pp. 1501–1521, 2006.

[28] M. Ikehata, "Extracting the geometry of an obstacle and a zeroth-order coefficient of a boundary condition via the enclosure method using a single reflected wave over a finite time interval," *Inverse Problems*, vol. 30, no. 4, Article ID 045011, 2014.

[29] B. W. Drinkwater and P. D. Wilcox, "Ultrasonic array for non-destructive evaluation: a review," *NDT & E International*, vol. 39, no. 7, pp. 525–541, 2006.

[30] C. Holmes, B. W. Drinkwater, and P. D. Wilcox, "Post-processing of the full matrix of ultrasonic transmit-receive array data for non-destructive evaluation," *NDT & E International*, vol. 38, no. 8, pp. 701–711, 2005.

[31] Y. Guo, D. Hömberg, G. Hu, J. Li, and H. Liu, "A time domain sampling method for inverse acoustic scattering problems," *Journal of Computational Physics*, vol. 314, pp. 647–660, 2016.

[32] V. Metelka, L. Baratoux, M. W. Jessell, A. Barth, J. Ježek, and S. Naba, "Automated regolith landform mapping using airborne geophysics and remote sensing data, Burkina Faso, West Africa," *Remote Sensing of Environment*, vol. 204, pp. 964–978, 2018.

[33] I. Catapano, A. Affinito, A. Del Moro, G. Alli, and F. Soldovieri, "Forward-looking ground-penetrating radar via a linear inverse scattering approach," *IEEE Transactions on Geoscience and Remote Sensing*, vol. 53, no. 10, pp. 5624–5633, 2015.

[34] L. Langhammer, L. Rabenstein, A. Bauder, and H. Maurer, "Ground-penetrating radar antenna orientation effects on temperate mountain glaciers," *Geophysics*, vol. 82, no. 3, pp. H15–H24, 2017.

[35] M. Zhong and J. Liu, "On the reconstruction of media inhomogeneity by inverse wave scattering model," *Science China Mathematics*, vol. 60, no. 10, pp. 1825–1836, 2017.

[36] A. Giannopoulos, "Modelling ground penetrating radar by GprMax," *Construction and Building Materials*, vol. 19, no. 10, pp. 755–762, 2005.

[37] M. Berk, C. Loo, C. G. Davey, and B. H. Harvey, "Ketamine and rapidly acting antidepressants: breaking the speed of sound or light?" *Australian & New Zealand Journal of Psychiatry*, vol. 52, no. 11, pp. 1026–1029, 2018.

[38] C. Warren, A. Giannopoulos, and I. Giannakis, "gprMax: Open source software to simulate electromagnetic wave propagation for ground penetrating radar," *Computer Physics Communications*, vol. 209, pp. 163–170, 2016.

Hindawi
International Journal of Antennas and Propagation
Volume 2019, Article ID 8065036, 12 pages
https://doi.org/10.1155/2019/8065036

Research Article

Design and Experimental Assessment of a 2D Microwave Imaging System for Brain Stroke Monitoring

Jorge A. Tobon Vasquez,[1] Rosa Scapaticci,[2] Giovanna Turvani,[1] Gennaro Bellizzi,[3] Nadine Joachimowicz,[4] Bernard Duchêne,[5] Enrico Tedeschi,[6] Mario R. Casu,[1] Lorenzo Crocco,[2] and Francesca Vipiana[1]

[1]*Department of Electronics and Telecommunications, Politecnico di Torino, 10129 Torino, Italy*
[2]*Institute for the Electromagnetic Sensing of the Environment, National Research Council of Italy, 80124 Naples, Italy*
[3]*Department of Electric Engineering and Information Technologies, University of Naples Federico II, 80125 Naples, Italy*
[4]*Group of Electrical Engineering-Paris (GeePs: CNRS-CentraleSupélec, Univ Paris-Sud, Université Paris-Saclay, Sorbonne Université), 91190 Gif-sur-Yvette, France*
[5]*Laboratoire des Signaux et Systèmes (L2S: CNRS-CentraleSupélec-Univ Paris-Sud), 91190 Gif-sur-Yvette, France*
[6]*Department of Advanced Biomedical Sciences, University of Naples Federico II, 80131 Napoli, Italy*

Correspondence should be addressed to Lorenzo Crocco; crocco.l@irea.cnr.it

Received 6 December 2018; Accepted 19 February 2019; Published 5 May 2019

Guest Editor: Alvaro Rocha

The aim of this paper is to present and experimentally verify the first prototype of a microwave imaging system specifically designed and realized for the continuous monitoring of patients affected by brain stroke, immediately after its onset and diagnosis. The device is a 2D version of the 3D system, currently under construction, and consists of an array of 12 printed monopole antennas connected to a two-port vector network analyzer through a switching matrix so that each antenna can act as a transmitter or receiver, thereby allowing the acquisition of the entire multistatic multiview scattering matrix required for the imaging. The system has been experimentally tested on 2D phantoms with electric properties mimicking the brain. The presence and the evolution of the stroke have been reproduced by filling a proper cavity in the phantom with a liquid having the electric properties of blood. A differential approach has been adopted by acquiring the scattering matrix before and after the filling of the blood cavity. The so achieved differential dataset has been processed by means of a linear imaging algorithm in order to reconstruct the stroke location and dimension. Moreover, the effect of pre- and postprocessing operations on the measured data is investigated. A good agreement has been obtained between the reconstructions and the actual scenario. As a final remark, it is worth noting that the entire data acquisition and processing are sufficiently fast to allow a real-time monitoring.

1. Introduction

In recent years, microwave tomography (MWT) has attracted an increasing interest as an alternative diagnostic tool for medical imaging. Among the various applications, diagnoses of breast cancer [1] and brain stroke [2] are certainly the most prominent examples.

Low cost, reduced size of the equipment, and the use of low-intensity and nonionizing radiations make MWT particularly appealing as compared to standard diagnostic tools for brain stroke, such as magnetic resonance imaging (MRI) and X-ray computerized tomography (CT), which are indeed much more expensive, bulky, and harmful for the patient.

Based on such observations, different microwave system prototypes have been proposed for brain stroke diagnostics in the literature. To the best of our knowledge, the most advanced system for brain stroke diagnosis is the one developed at Chalmers University [3, 4]. In agreement with the fact that microwave technology must be a support and not a substitute for standard diagnostic tools, this system aims

at classifying stroke to give the clinicians a prompt information on the kind of stroke they are faced with, which is crucial for an early intervention. The advantages of this device are its small size and weight, as well as a short measurement time that allows real-time diagnosis. Its drawback is that the only information provided is the presence and the kind of stroke, while no information is provided on the size and location. Another crucial point is the need to collect a significant amount of training data to make classification reliable.

As far as stroke imaging is concerned, several systems have been proposed, which are at different stages of development [5–8]. In particular, the BRIM G2 developed at EMTensor [5] for brain stroke tomography and the device developed at the University of Queensland, devoted to intracranial hemorrhage imaging [6, 9, 10], have been both tested on phantoms as well as on some volunteers with encouraging results.

An application which has been to some extent overlooked for which MWT appears to be particularly promising is the continuous monitoring of the time evolution of the stroke growth after its onset [11]. In fact, monitoring the stroke evolution would give clinicians the possibility to promptly set the therapy and verify its effectiveness, aimed at stopping the growth of the stroke and so at reducing the risk of death or permanent injuries [12–14]. However, frequent, bedside monitoring cannot be done with MRI or X-ray CT, because it requires a completely safe, relatively cheap, and not bulky technology, such as MWT. This is because MWT would allow a repeated long-time exposure of the patient and its embedding at the bedside in the early stages of hospitalization.

In [15], the authors of this contribution have presented the design of a system based on a conformal antenna array adapted to the head, specifically meant for the continuous monitoring of patients affected by brain stroke, immediately after its onset. Starting from the guidelines given therein, this paper presents the ongoing work towards the realization of the first complete prototype of such a system. In particular, we present and experimentally test an initial prototype representing a simplified 2D version of the device.

In such a prototype, the electronics and the antennas are already the ones of the final system, but instead of a conformal array, a simple circular array of 12 printed monopole antennas is used to image 2D cylindrical phantoms. In particular, the array is connected to a two-port vector network analyzer (VNA) through a purposely designed switching matrix, so that each antenna can act as a transmitter or as a receiver, thereby allowing the acquisition of the entire multistatic multiview scattering matrix required for imaging. The antenna array is immersed in a coupling medium contained in a tank, acting as a holder.

This 2D system, for which preliminary results are reported in [16, 17], has been experimentally tested on phantoms made of a thin plastic material and consisting of waterproof compartments which can be filled with proper liquid mixtures mimicking the electric properties of the different head tissues. The presence and the evolution of the stroke have been reproduced and measured by filling a proper cavity in the phantom with a liquid having the same electric properties than blood and by acquiring the scattering matrix before and after the filling of the cavity. The differential dataset obtained in this way has been then processed by a linear inversion algorithm [11, 18] in order to reconstruct the stroke variation. A good agreement has been obtained between the reconstructions and the real positions and sizes assumed for the stroke in the phantom. Moreover, the effect of different pre- and postprocessing operations on the measured data is investigated. The entire data acquisition and processing are sufficiently fast to allow a real-time diagnosis. Notice that it is also possible to accelerate this kind of algorithm with proper specialized hardware, as shown in [19].

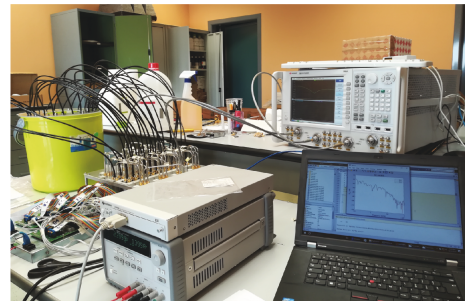

Figure 1: Overview of the realized microwave imaging system.

The paper is organized as follows. In Section 2, the overall MWT system, including the coupling medium, the antenna array, the switching matrix, the phantom, and the imaging algorithm, is described and characterized. Section 3 describes different pre- and postprocessings applied on the measurement data, in order to assess their influence on the reconstruction. The reconstruction results are reported in Section 4, and conclusion and perspectives follow in Section 5.

2. Microwave Imaging System

An overview of the microwave imaging system designed and realized in this work is shown in Figure 1. The system consists of a set of 12 or 24 antennas, placed around the considered phantom, inside a tank filled with the chosen coupling liquid, as shown in Figure 2 in the case of 12 antennas. To act as transmitters and receivers (RX/TX), the antennas are connected to a custom 24×2 switching matrix, then connected to a vector network analyzer (VNA). Finally, all the signals received by the VNA are used as input data for the implemented imaging algorithm. In the following subsections, all the different parts of the microwave imaging system are detailed, together with the main design constraints.

2.1. Frequency Range and Coupling Liquid. The choice of the working frequency range and the dielectric characteristics of the coupling medium are strictly related to the final use of the realized microwave imaging system, i.e., brain stroke monitoring. According to previous theoretical studies [20, 21], the transmission coefficient through a layered medium representing the different tissues of the brain exhibits a "forbidden" band between around 1.5 GHz and 2.5 GHz. The frequency behavior of the transmission coefficient depends slightly on the dielectric characteristics of the

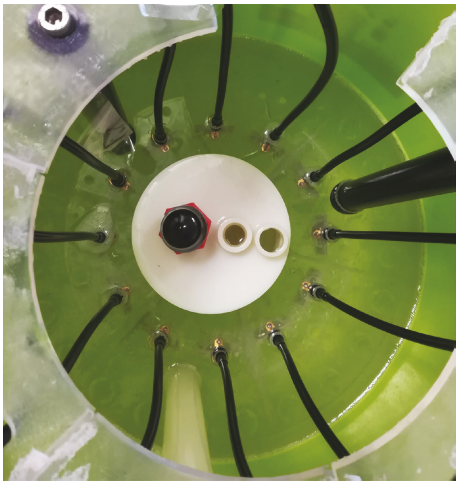

Figure 2: Microwave imaging system: tank filled with the coupling liquid with phantom and RX/TX antennas inside.

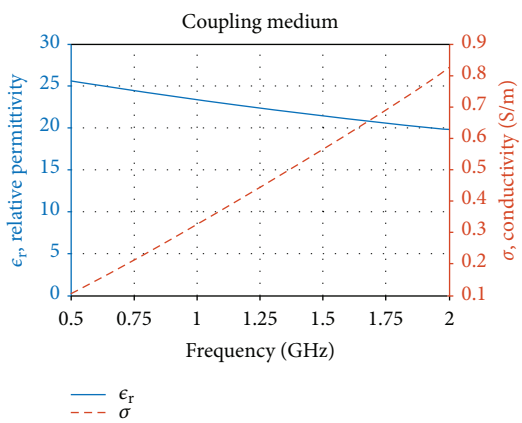

Figure 3: Microwave imaging system: coupling medium relative permittivity and conductivity.

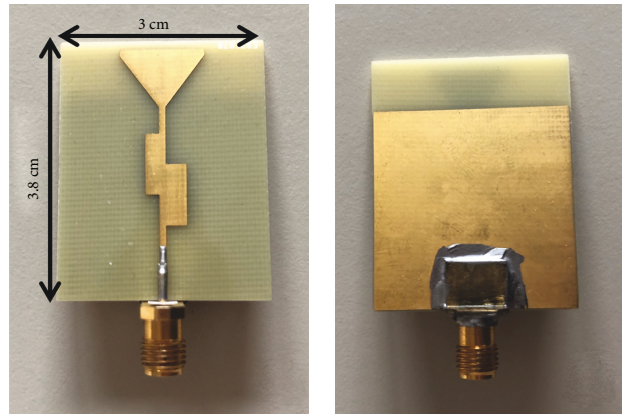

(a) (b)

Figure 4: Microwave imaging system: RX/TX antennas; (a): top side; (b): bottom side.

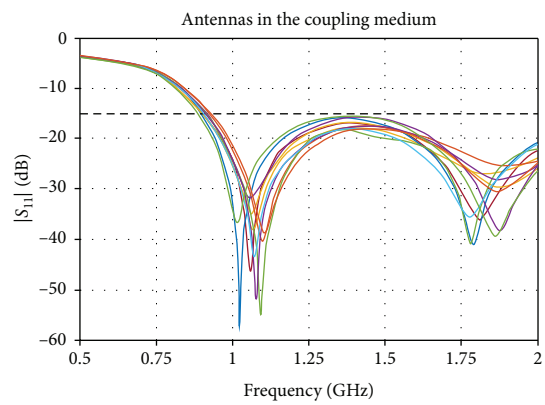

Figure 5: Microwave imaging system: amplitude of the input reflection coefficient of the antennas immersed in the coupling medium.

coupling medium; in particular, the starting frequency of the forbidden band is a bit higher if its relative permittivity is around 20 or lower. Moreover, working at frequencies higher than 2.5 GHz could be possible but is not convenient, due to the low penetration depth in the inspected tissues. Hence, the chosen working frequency range for the antenna design and image reconstruction algorithms is 1-1.75 GHz with a coupling medium relative permittivity of around 20.

The desired dielectric characteristics of the coupling medium are obtained with a mixture of Triton X-100 and water in the volume percentage of 70/30; the relative permittivity and conductivity, measured in the working frequency range by means of an open-ended coaxial probe connected to the VNA, are shown in Figure 3. We have chosen a mixture of Triton X-100 and water mainly because it has been verified to be very stable in time and easy to prepare (the two liquids are simply mixed together at room temperature) [22–24]. Moreover, the corresponding attenuation in the considered frequency band (see the conductivity behavior in Figure 3) is much lower than other mixtures proposed in literature, such as the ones based on glycerine [25], allowing to work with less noisy measurements.

2.2. Antennas. The radiating part of the realized microwave imaging system is a set of antennas placed on a circumference, around the considered phantom, and immersed in the coupling medium. The antenna support, inside the tank, allows us to place 24 or 12 antennas on a circumference with a diameter of 24 cm or 16 cm, respectively, with a distance between adjacent antennas of around 1 cm.

Each antenna of the microwave imaging system is a wideband monopole antenna, printed on a standard FR4 dielectric substrate with thickness equal to 1.6 mm, as shown in Figure 4. The top side consists of a transmission line with a double-stub matching circuit and ended with a triangular-shaped radiating part (see Figure 4(a)). The bottom side is made of a ground plane that terminates close to the beginning of the radiating triangle (see Figure 4(b)).

Figure 5 reports the amplitude of the input reflection coefficient of the realized antennas immersed in the coupling medium: the matching is always below −15 dB all over the frequency range (1–1.75 GHz). The differences in

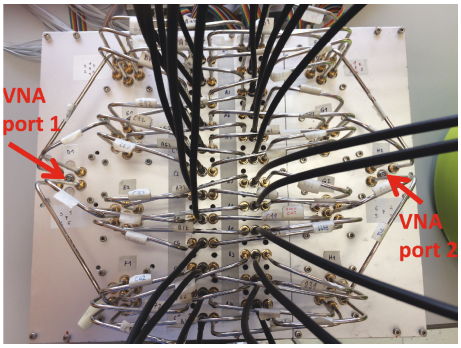

Figure 6: Microwave imaging system: switching matrix.

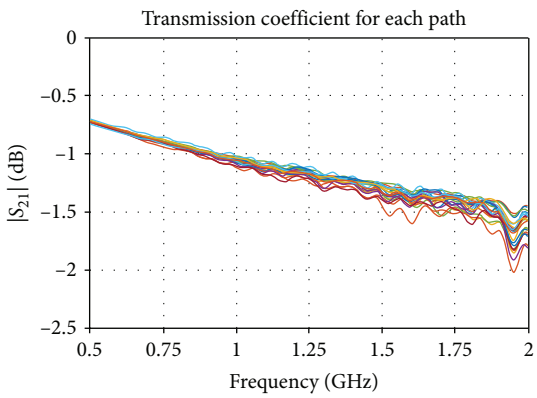

Figure 7: Microwave imaging system: amplitude of the transmission coefficient of each path of the switching matrix.

the behavior of the measured antennas are expected to be related mainly to the slightly different welding of the connector (see Figure 4) and also to the possible presence of air bubbles in the coupling liquid wherein they are immersed. Moreover, the presence of a double resonance at the two limits of the frequency range allows us to work also in an almost "flat" region (around 1.5 GHz), where the matching is still below −15 dB and the $|S_{11}|$ coefficient differs much less with respect to the resonant regions. This is an interesting feature because it has been verified that the implemented imaging algorithm performs better in this flat region (see Section 4).

The realized antennas are wide-band monopoles, hence with an omnidirectional radiation pattern in the plane orthogonal to the antenna plane (see Figure 4). This plane corresponds to the one where the antennas are placed on a circumference (see Figure 2); hence, a high coupling is expected between adjacent antennas. In order to mitigate this effect, the scattering parameters between adjacent antennas are discarded in the implemented imaging algorithm (see Section 4).

2.3. Switching Matrix. In the microwave imaging system, each antenna acts as a transmitter and as a receiver, in order to have multistatic multiview measurements of the phantom. Hence, all the antennas are connected to the VNA through a switching matrix, shown in Figure 6. The switching matrix consists of two single-pole-four-throw (SP4T), eight single-pole-six-throw (SP6T), and twenty-four single-pole-double-throw (SPDT) electromechanical coaxial switches. The pole of the two SP4T switches is connected via a flexible coaxial cable to one port of the VNA, and the pole of the twenty-four SPDT switches is connected, in the same way, to one antenna port. The other ports of the switches are properly connected together via semirigid coaxial cables in order to implement a 2×24 switching matrix. The semirigid coaxial connections among the SP4T, SP6T, and SPDT switches have been realized in order to have very similar path lengths between the VNA port and any antenna port.

To create the proper connections between the antennas and the VNA, all the switches are connected to the control board. The Ethernet connectivity available on the board enables the connection to the network, which allows us to control the entire system from a standard laptop. The board provides a built-in graphical web interface which enables a full manual configuration of the matrix. Moreover, in order to make fast and automated measurements, the switches can also be controlled through the VISA/TCPIP (VXI-11) protocol by using standard scripting languages such as MATLAB. This approach has been followed in the present prototype in order to enable a software integration of the measurement data and the imaging algorithm. In this way, complete automated scans of the target can be run providing the reconstructed images in almost real time. In the current prototype, the measurement time is around three minutes, considering the frequency range 0.5–3 GHz with 1001 sample points and an intermediate-frequency (IF) bandwidth equal to 1 kHz, and the processing of the measured data thought the imaging algorithm needs a few seconds.

In the implementation of the switching matrix, we have chosen electromechanical coaxial switches in order to minimize the insertion loss (<0.3 dB) and maximize the isolation (>90 dB), because it is expected that the useful signal (i.e., the one due to the stroke variation) is typically about 70 dB below that measured at two monitoring times (which is due to the scattering from the whole head); hence, it is a very critical signal to be detected [15, 26]. Figure 7 shows the amplitude of the transmission coefficient of each path of the switching matrix from the VNA port to the antenna port, including also the 1 m flexible coaxial cable connecting the antenna to the matrix; it has been verified that the introduced attenuation is no more than 2 dB in the considered frequency range.

2.4. 2D Phantom. The experiments presented herein (see Section 4) have been carried out with a 3D-printed phantom [22, 23] designed to model the possible presence of a stroke area inside the brain. The phantom, shown in Figure 8, is a 10 cm diameter, 16 cm high circular cylindrical cavity made of acrylonitrile butadiene styrene (ABS) and closed by a cap with three holes where smaller ABS cylinders can be inserted; the larger hole has a diameter of 1.8 cm and the other two have a diameter of 1.4 cm. Note that this phantom is meant to carry out preliminary 2D measurements and, as such, one dimension (the height) is dominant with respect to the other (diameter) and it does not take into account the actual dimensions of a human head. Of course, the 3D head phantom will be developed with realistic dimensions.

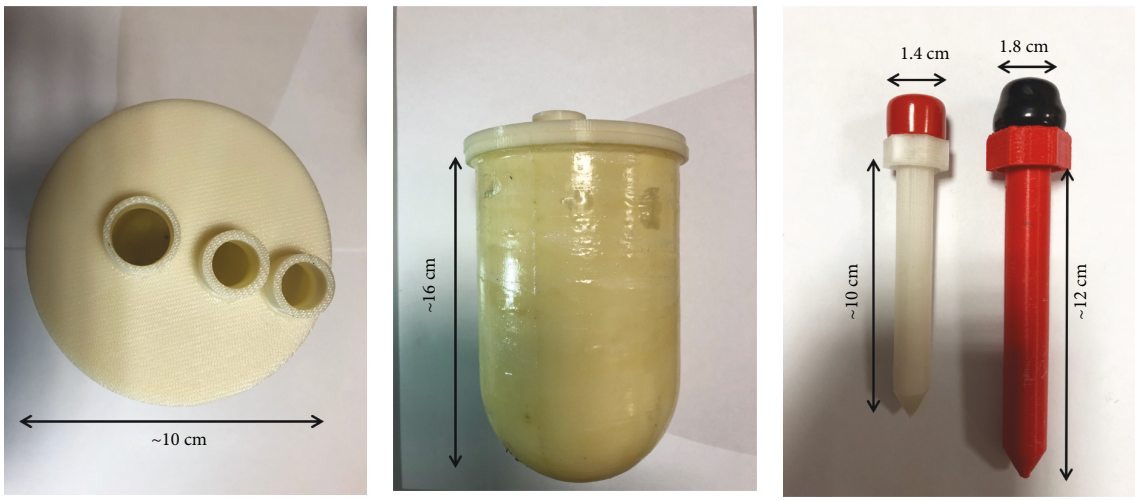

(a) (b) (c)

Figure 8: 2D phantom: (a): top view; (b): side view; (c): inserted cylinders.

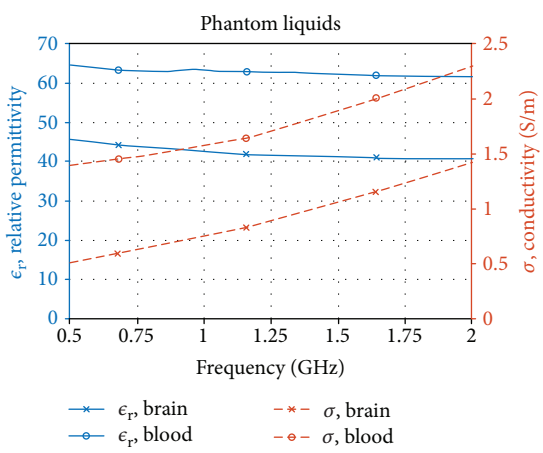

Figure 9: 2D phantom: dielectric properties of the liquids used to fill the different parts of the phantom.

As shown in Figure 2, the phantom is immersed in a coupling liquid and placed at the center of the circular antenna support. The distance between the antennas and the phantom external surface is about 3 cm; in the operating frequency range, this corresponds to a distance in between 0.5λ and 0.8λ, where λ is the wavelength in the coupling medium. This choice results from a trade-off in minimizing the attenuation of the useful signal on one hand and, on the other hand, the near-field effects that are hard to model and that could perturb the measured fields [15, 27]. It can be noted that, considering the location of the antennas and the cylindrical shape of the phantom, the latter is assumed to be a 2D target and the images are built up in the antenna support plane, orthogonal to the cylindrical cavity axis (see Section 4).

The phantom cavity is filled up with a liquid that mimics the brain, the latter being modeled as a blend of white and grey matters (75% of white matter and 25% of grey matter), while the inner cavity is filled up with another mixture representing the blood. The brain- and blood-mimicking mixtures are made of Triton X-100 (TX-100), water, and salt with respective volume fractions and salt quantities of 38% of TX-100, 72% of water, and 5.2 g/L of salt for the brain and 14% of TX-100, 86% of water, and 9.4 g/L of salt for the blood [28]. Finally, Figure 9 reports the dielectric properties of the tissue-mimicking mixtures measured by means of an open-ended coaxial probe connected to the VNA in the 0.5-2 GHz operating frequency range.

2.5. Imaging Algorithm. The data collected with the system are processed by means of a simple and well-assessed approach, based on the singular value decomposition (SVD) of the scattering operator relating the data of the problem to the unknown contrast function [18].

Since the target application of the system at hand is monitoring the time evolution of the stroke after its onset, i.e., the variation of the electric contrast of the brain tissues at two different times, the data of the imaging problem are represented by the difference between the scattering matrices measured at these two different times. This differential scattering matrix will be denoted as ΔS in the following.

Typically, the differential contrast, say $\Delta\chi$, associated to ΔS is localized in a small portion of the imaging domain. Accordingly, it is possible to take advantage of the distorted Born approximation, so that ΔS and $\Delta\chi$ become linearly related through the following relationship:

$$\Delta S(r_p, r_q) = \mathcal{S}(\Delta\chi), \tag{1}$$

where $\mathcal{S}$ is a linear and compact integral operator, whose kernel is $-j\omega\epsilon_b/4E_b(r_m, r_p)\cdot E_b(r_m, r_q)$, with $r_m \in D$, $E_b(r_m, r_p)$ being the *background* field in the unperturbed scenario, while r_p and r_q denote the positions of the transmitting and receiving antennas, and r_m are the positions of the points in which the imaging domain D is discretized. The symbol "·" denotes the dot product between vectors, $\omega = 2\pi f$ is the angular frequency, ϵ_b the relative dielectric constant of the background medium, and j the imaginary unit.

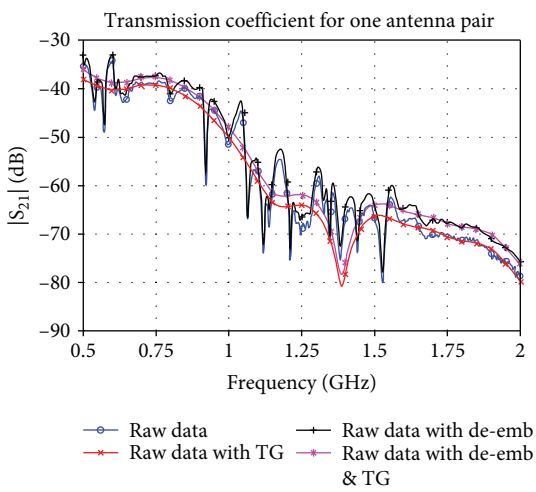

Figure 10: Amplitude in dB of the transmission coefficient versus frequency for a pair of antennas comparing the raw measured data, the data with time gating (TG), the data with deembedding, and the data with TG and deembedding.

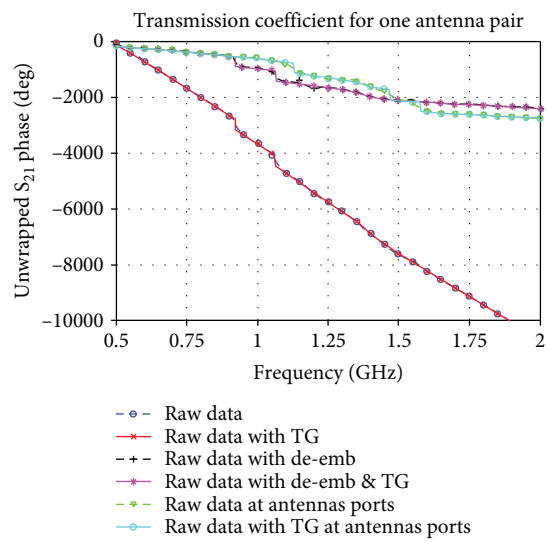

Figure 11: Unwrapped phase in degrees of the transmission coefficient versus frequency for a pair of antennas comparing the raw measured data, the data with time gating (TG), the data with deembedding, and the data with TG and deembedding; the raw data measured directly at the antenna ports are shown as reference.

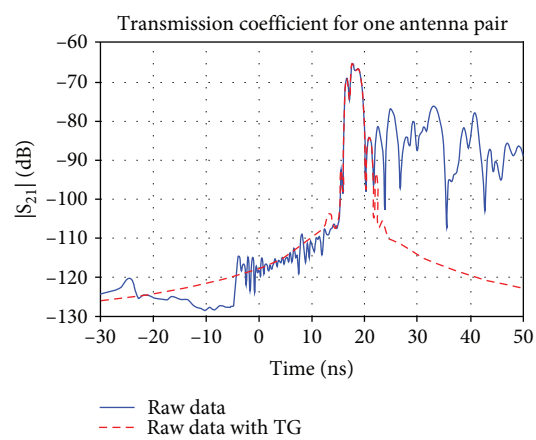

Figure 12: Amplitude in dB of the transmission coefficient versus time for a pair of antennas comparing raw measured data and data with time gating (TG).

The linear problem in (1) can be inverted by means of the truncated singular value decomposition (TSVD) scheme [18], and the retrieved differential contrast reads

$$\Delta_\chi = \sum_{n=1}^{L_t} \frac{1}{\sigma_n} \langle \Delta S, [u_n] \rangle [v_n], \tag{2}$$

where $\langle [u], [\sigma], [v] \rangle$ is the SVD of the discretized scattering operator $\mathcal{S}$. L_t is the truncation index of the SVD, which acts as a regularization parameter.

3. Pre- and Postmeasurement Processing

As described in Section 2.3, the VNA is connected to the two input ports of the switching matrix, whose output ports are then connected, via flexible coaxial cables, to the TX/RX antennas. The VNA is a N5227A PNA Microwave Network Analyzer, with an output power of 0 dBm and calibrated with a full two-port (twelve terms) calibration at the end of its high-precision coaxial cables (then connected to the switching matrix), in order to eliminate the directivity error, the cross-talk, the source match error, and the frequency response reflection tracking error.

Figures 10 and 11 show the amplitude and unwrapped phase, respectively, of the measured S_{21} coefficient for one antenna pair of the realized microwave imaging system. The data, labelled as "raw data," are the S_{21} coefficients measured at the calibrated VNA ports, while the "raw data with TG" are the measured data with a time gating applied in order to reduce multiple reflections within the tank. To get the S_{21} coefficient in the time domain, an Inverse Fourier Transform (IFT) is performed on the measured data points, as shown in Figure 12 (solid line). Then, a windowed gating function, centered at 17.5 ns and with a time span of 9 ns, is applied. The corresponding time-gated data, shown in Figure 12 (dashed line), contain the main impulse received by the considered antenna with less reflections from the tank. The gated time domain response is then transformed back to the frequency domain with the effect that most of the multiple reflections are removed, as shown in Figure 10. Comparing the amplitude of the measured S_{21} coefficient in the frequency domain, it is evident that the time-gated data are, as expected, much smoother than the initial data; on the contrary, there are no changes in the measured phase (see Figure 11).

In order to obtain the transmission coefficients directly at the antenna ports for all the considered paths (as expected by most imaging algorithms), a deembedding technique is applied to the measured data. Each measured 2×2 $[S]$ matrix includes three 2-port parts, each one represented by its own 2×2 scattering matrix: the input (left) path between the port 1 of the VNA and the TX antenna through the switching

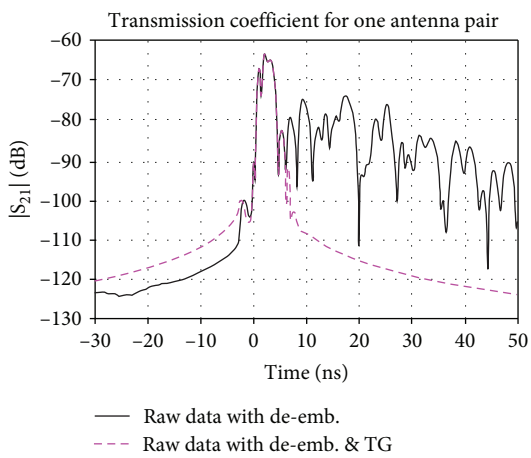

Figure 13: Amplitude in dB of the transmission coefficient versus time for a pair of antennas comparing deembedded raw measured data and deembedded data with time gating (TG).

matrix represented by $[S_L]$, the TX/RX antenna pair represented by $[S_{DUT}]$, and the output (right) path between the RX antenna and the port 2 of the VNA via the switching matrix represented by $[S_R]$. In order to "extract" the desired $[S_{DUT}]$, the corresponding $[S_L]$ and $[S_R]$ are measured with the calibrated VNA. Then, all the measured scattering matrices, $[S]$, $[S_L]$, and $[S_R]$, are rewritten into the corresponding transmission matrices, $[T]$, $[T_L]$, and $[T_R]$, respectively [29]. Considering that

$$[T] = [T_L][T_{DUT}][T_R], \tag{3}$$

where $[T_{DUT}]$ is the unknown transmission matrix of the considered TX/RX antenna pair, the $[T_{DUT}]$ matrix is obtained as

$$[T_{DUT}] = [T_L]^{-1}[T][T_R]^{-1} \tag{4}$$

and rewritten as a scattering matrix in $[S_{DUT}]$.

For the considered antenna pair, Figures 10 and 11 show the amplitude and unwrapped phase of the measured S_{21} coefficient after the application of the described deembedding (lines labelled as "raw data with de-emb"). We can observe that the amplitude of the S_{21} coefficient, after deembedding, is very similar to the initial one, which just shifted up of around 1.5–4 dB (within the considered frequency range) due to removal of the attenuation through the scattering matrix (see Figure 7, considering two paths). On the contrary, the phase is changed and, as expected, it is superimposed to the one measured directly at the antenna ports (labelled as "raw data at antenna ports" in Figure 11).

As for the previous case, a time gating is then applied to the deembedded data in order to mitigate multiple reflections within the tank. Hence, the deembedded data are transformed in the time domain (see Figure 13, solid line) and a windowed gating function, centered at 2 ns and with the same time span as before (9 ns), is applied. The gating function is now applied at the beginning of the time domain S_{21} coefficient because, due to the deembedding, the reference planes are at the antenna ports. The gated time domain response is then transformed back to the frequency domain, as shown in Figures 10 and 11 (lines labelled as "raw data with de-emb. & TG").

All the previously described kinds of measured data, with or without time gating and with or without deembedding, are used in Section 4 to generate the images via the implemented imaging algorithm.

4. Experimental Results and Discussion

The experimental measurement campaign is reported in this section in order to test the developed system; it has been carried out with the phantom described in Section 2.4 and with the imaging algorithm detailed in Section 2.5.

Three cases are considered according to the available holes in which the inner cylinder, mimicking the hemorrhagic stroke, can be inserted in the phantom, mimicking the brain. In particular, the following three cases are reported:

(i) Case 1: 1.4 cm cylinder positioned nearby the center of the phantom, centered at −13 and −7.5 mm

(ii) Case 2: 1.8 cm cylinder positioned nearby the center of the phantom, centered at 7.5 and 13 mm

(iii) Case 3: 1.4 cm cylinder positioned close to the periphery of the phantom, centered at −32.5 and 18.75 mm

For each case, the differential measurements have been obtained by subtracting the scattering parameters gathered in the presence of the phantom without the target cylinder. Moreover, to minimize the antenna coupling effects, the nearest antenna contributions are removed from the differential scattering matrix given in input to the reconstruction algorithm.

The performance of the system is analyzed with respect to the working frequency band (within the operative range of the antennas), with respect to the adopted pre- and post-measurement operations, as discussed in Section 3, and with respect to the knowledge of a priori information on the background scenario, i.e., the scenario with the phantom and without the target cylinder. As far as the frequency range is concerned, with reference to the matching of the antennas summarized in Figure 5, we have identified two possible operative situations: the first range is 1–1.5 GHz, including the main resonance of the antennas, and the second one is 1.5–1.75 GHz, where the S_{11} coefficient still confirms a good matching, even outside the main resonance. In the following analysis, we refer to *low-frequency range* when processing multifrequency data in the range 1–1.5 GHz, while *high-frequency range* denotes the processing of multifrequency data in the range 1.5–1.75 GHz. Concerning pre- and postmeasurement procedures, we have analyzed all the four possible solutions identified in Section 3, namely, raw data, raw data with time gating, raw data with deembedding, and raw data with deembedding and time gating. Finally, the robustness with respect to a priori knowledge on the reference scenario

has been evaluated by comparing results obtained with Green's function of the homogeneous coupling medium with and without the presence of the brain phantom. Both Green's functions have been numerically obtained by full-fledged simulations of the system by means of an in-house vectorial 3D finite element method (FEM) solver [15]. Finally, to quantitatively appraise the quality of the reconstructions, three metrics have been defined and evaluated for the considered examples:

(i) *Dimensional error (Dim)*, defined as the ratio between the retrieved dimension of the target (once the image has been binarized through a -3 dB thresholding) and the actual dimension of the target

(ii) *Localization error (Loc)*, defined as the distance between the retrieved and the actual centers of the target

(iii) *Side lobe level (SLL)*, defined as the ratio of the highest value of the retrieved differential contrast falling outside the target with respect to the highest value attained inside the target

For the sake of brevity, the complete analysis for Case 1 is reported in the following, while for Case 2 and Case 3, only the best condition results (coming from the previous analysis) are shown.

Figure 14 and Table 1 summarize the analysis of performances in Case 1. First, we can observe that the application of time gating to raw data as well as to deembedded data improves the accuracy of the reconstructions, mainly in terms of side lobe level, even if a reconstruction is feasible also without applying it. On the contrary, the deembedding operation seems to bring only a slight improvement in the reconstructed images, despite the significant improvement of the phase estimation of the measured data (see Figure 11), probably due to the fact that the switching matrix has been built such to keep all the patterns of the same length and hence, the correction of the phase is not significant in the developed system. As far as the frequency range is concerned, from both Figure 14 and Table 1, it can be concluded that the high-frequency ranges are to be preferred. It is worth to note that the thresholds of the singular values for the low- and high-frequency range are different ($\tau = 20\log_{10}(\sigma_{Lt}/\sigma_1) = -22$ dB for low frequencies and $\tau = -32$ dB for high frequencies). This is in agreement with their decay in the two cases, reported in Figure 15, where it can be seen that at these different threshold values correspond around the same number of singular values (and hence basis functions used in the reconstruction formula in (2)).

As far as it concerns the adopted a priori information on the scenario, the results show that using Green's function that takes into account the presence of the brain phantom does not bring to significant improvements with respect to the simple Green function of the homogeneous coupling medium. This is possibly due to the fact that the features of the phantom (i.e., geometry, electric properties, and position with respect to the antenna array) are not known with sufficient accuracy such to allow a remarkable improvement. As this is even more true in practical applications, we can expect that the TSVD reconstruction of the stroke evolution is not likely to be significantly improved by exploiting patient-specific prior knowledge (e.g., geometry and electric properties of the head).

Given the above analysis, the selected settings for the processing of data related to Case 2 and Case 3 are summarized as follows:

(i) High-frequency range data (1.5–1.75 GHz)

(ii) Green's function of the homogeneous coupling medium

(iii) Time-gating measurement data processing

Figures 16 and 17 show the obtained reconstructions, while Table 2 summarizes the quantitative metrics evaluated for these examples. As can be noticed, the 1.8 cm cylinder is accurately reconstructed. The size and shape of the 1.4 cm cylinder are also correctly imaged, but the retrieved target position is radially displaced towards the center. Such an outcome could have been to some extent expected, since the 1.4 cm cylinder is placed close to the phantom boundary, whose effect is not taken into account in the homogeneous Green function. The boundary represents a significant electric discontinuity and therefore introduces a modeling error, especially for targets located in its proximity. On the other hand, given the already mentioned circumstance that the phantom is not known with sufficient precision, no significant improvements are obtained using the more accurate (but still approximated) Green function.

5. Conclusion and Perspectives

In this paper, the prototype of a MWT system designed for the continuous imaging of the brain stroke evolution, after its onset, has been presented and experimentally tested. The system is composed of a ring of twelve printed monopole antennas, designed to work in the band 1–1.75 GHz; a switching matrix enabling the acquisition of the entire scattering matrix through a two-port VNA; and a coupling medium whose electric properties have been tuned such to enable a good trade-off between wave penetration and attenuation inside the phantom. Moreover, a phantom has been built up, which can be filled with different liquids, mimicking a human brain affected by a hemorrhagic stroke. Each part of the system has been experimentally characterized in order to set the best working frequency and to accurately compute Green's function used in the reconstruction algorithm, which is a linear imaging algorithm based on TSVD. The input differential data, arising from the stroke evolution, have been simulated by measuring the scattering matrix before and after the filling of the cavity of the phantom mimicking the stroke.

Different pre- and postprocessing operations have been applied to the measured differential scattering matrix in order to assess their effect on the quality of the image reconstruction. In particular, in order to reduce the effect of the antenna mutual coupling, in all cases, the scattering

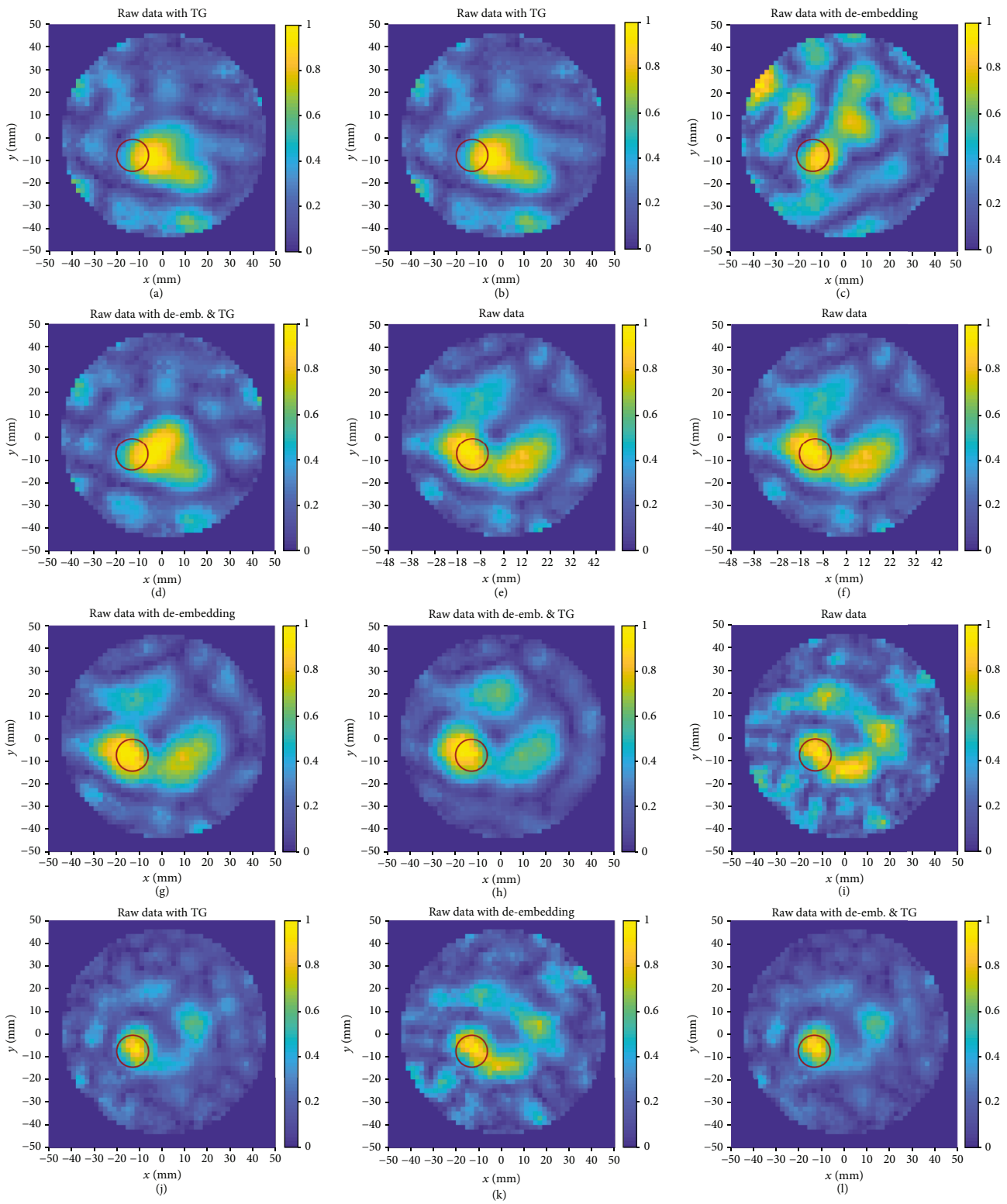

Figure 14: Reconstruction images for Case 1: first column: raw data, second column: raw data with time gating (TG), third column: raw data with deembedding, and fourth column: raw data with deembedding and TG; first row: 1, 1.25, and 1.5 GHz with Green's function of the homogeneous coupling medium and $\tau = -22$ dB; second row: 1.5 and 1.75 GHz with Green's function of the homogeneous coupling medium and $\tau = -32$ dB; third row: 1.5 and 1.75 GHz with Green's function of the homogeneous coupling medium inside the phantom and $\tau = -32$ dB.

Table 1: Case 1 evaluated metrics.

	Green's function of the homogeneous coupling medium			
	Raw data at 1-1.5 GHz	TG data at 1-1.5 GHz	De-emb. data at 1-1.5 GHz	TG de-emb. data at 1-1.5 GHz
Dim	0.83	1.31	0.86	1.31
Loc	3.03 mm	4.71 mm	2.5 mm	6.9 mm
SLL	0.88 dB	-2.38 dB	0.73 dB	-3.1 dB
	Raw data at 1.5-1.75 GHz	TG data at 1.5-1.75 GHz	De-emb. data at 1.5-1.75 GHz	TG de-emb. data at 1.5-1.75 GHz
Dim	1.33	1.1	1.14	1
Loc	2.51 mm	2 mm	3 mm	4.2 mm
SLL	-1.41 dB	-4.4 dB	-1.94 dB	-4 dB
	Green's function of the homogeneous coupling medium with inside the brain phantom			
	Raw data at 1.5-1.75 GHz	TG data at 1.5-1.75 GHz	De-emb. data at 1.5-1.75 GHz	TG de-emb. data at 1.5-1.75 GHz
Dim	1.17	0.53	1.08	0.58
Loc	2.5 mm	1.8 mm	1.8 mm	1.5 mm
SLL	-0.5 dB	-4.44 dB	-1.83 dB	-4.73 dB

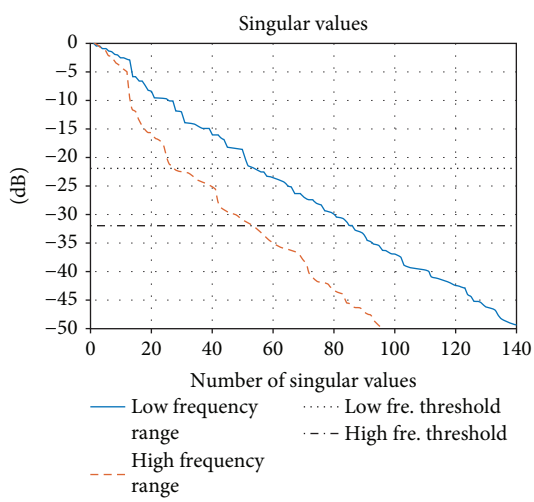

Figure 15: Singular value behavior of the scattering operator for low-frequency range (solid blue line) and high-frequency range (dashed red line).

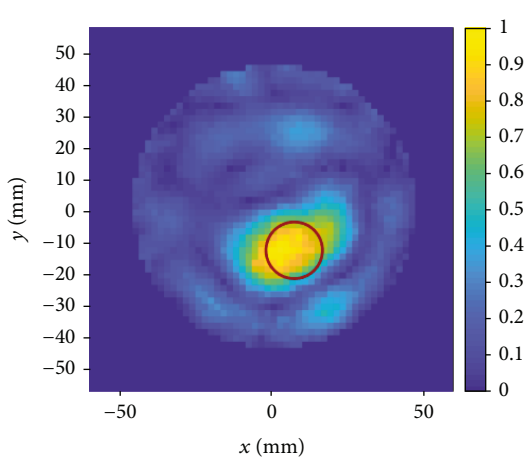

Figure 16: Reconstruction image for Case 2: 1.8 cm cylinder, raw data with time gating, 1.5 and 1.75 GHz, Green's function of the homogeneous coupling medium, and $\tau = -32$ dB.

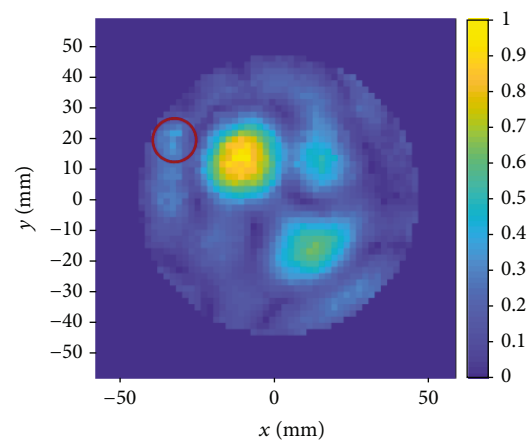

Figure 17: Reconstruction image for Case 3: 1.4 cm cylinder in the outer position, raw data with time gating, 1.5 and 1.75 GHz, Green's function of the homogeneous coupling medium, and $\tau = -32$ dB.

Table 2: Cases 2 and 3: evaluated metrics.

Green's function of the coupling medium, TG data, at 1.5-1.75 GHz		
	Case 2	Case 3
Dim	1.41	1.39
Loc	0.5 mm	38 mm
SLL	-8.4 dB	-4.44 dB

parameters measured for adjacent antennas have been enforced to zero (raw data). Moreover, a deembedding operation, allowing at shifting the reference planes directly at the antenna ports, and a time gating, allowing at mitigating the multiple reflections of the signal inside the system, have been alternatively or jointly applied to the raw data. All these different kinds of processed measured data have been analyzed, and the reconstructions have been compared to each other.

The ongoing work concerns the realization and characterization of a 3D and clinically usable version of the MWT system, where the antennas are mounted on a conformable

helmet adapted to the patient head and of a 3D realistic phantom of the head that will be used to experimentally test the system before proceeding with the preclinical assessment on patients.

Data Availability

The data used to support the findings of this study are available from the corresponding author upon request.

Conflicts of Interest

The authors declare that there is no conflict of interests regarding the publication of this paper.

Acknowledgments

This work was supported by the Italian Ministry of University and Research (MIUR) under the PRIN project "MiBraScan—Microwave Brain Scanner for Cerebrovascular Diseases Monitoring". The authors would like to acknowledge the valuable help of Eng. G. Dassano for the realization of the switching matrix and of the antenna supports.

References

[1] R. C. Conceição, J. J. Mohr, and M. O'Halloran, *An Introduction to Microwave Imaging for Breast Cancer Detection*, Springer International Publishing, 2016.

[2] L. Crocco, Ed.I. Karanasiou, M. L. James, and R. C. Conceição, *Emerging Electromagnetic Technologies for Brain Diseases Diagnostics, Monitoring and Therapy*, L. Crocco, Ed., Springer International Publishing, 2018.

[3] M. Persson, A. Fhager, H. D. Trefna et al., "Microwave-based stroke diagnosis making global prehospital thrombolytic treatment possible," *IEEE Transactions on Biomedical Engineering*, vol. 61, no. 11, pp. 2806–2817, 2014.

[4] A. Fhager, S. Candefjord, M. Elam, and M. Persson, "Microwave diagnostics ahead: saving time and the lives of trauma and stroke patients," *IEEE Microwave Magazine*, vol. 19, no. 3, pp. 78–90, 2018.

[5] M. Hopfer, R. Planas, A. Hamidipour, T. Henriksson, and S. Semenov, "Electromagnetic tomography for detection, differentiation, and monitoring of brain stroke: a virtual data and human head phantom study," *IEEE Antennas and Propagation Magazine*, vol. 59, no. 5, pp. 86–97, 2017.

[6] A. T. Mobashsher, K. S. Bialkowski, A. M. Abbosh, and S. Crozier, "Design and experimental evaluation of a non-invasive microwave head imaging system for intracranial haemorrhage detection," *PLoS One*, vol. 11, no. 4, article e0152351, 2016.

[7] M. Maffongelli, S. Poretti, A. Salvade et al., "Design and experimental test of a microwave system for quantitative biomedical imaging," in *2018 IEEE International Symposium on Medical Measurements and Applications (MeMeA)*, Rome, Italy, June 2018.

[8] Z. Miao, P. Kosmas, and S. Ahsan, "Impact of information loss on reconstruction quality in microwave tomography for medical imaging," *Diagnostics*, vol. 8, no. 3, p. 52, 2018.

[9] A. Afsari, A. M. Abbosh, and Y. Rahmat-Samii, "A rapid medical microwave tomography based on partial differential equations," *IEEE Transactions on Antennas and Propagation*, vol. 66, no. 10, pp. 5521–5535, 2018.

[10] A. Afsari, A. M. Abbosh, and Y. Rahmat-Samii, "Modified born iterative method in medical electromagnetic tomography using magnetic field fluctuation contrast source operator," *IEEE Transactions on Microwave Theory and Techniques*, vol. 67, no. 1, pp. 454–463, 2019.

[11] R. Scapaticci, O. M. Bucci, I. Catapano, and L. Crocco, "Differential microwave imaging for brain stroke followup," *International Journal of Antennas and Propagation*, vol. 2014, Article ID 312528, 11 pages, 2014.

[12] A. Cavallini, G. Micieli, S. Marcheselli, and S. Quaglini, "Role of monitoring in management of acute ischemic stroke patients," *Stroke*, vol. 34, no. 11, pp. 2599–2603, 2003.

[13] A. Rocco, M. Pasquini, E. Cecconi et al., "Monitoring after the acute stage of stroke: a prospective study," *Stroke*, vol. 38, no. 4, pp. 1225–1228, 2007.

[14] J. Gubbi, A. S. Rao, K. Fang, B. Yan, and M. Palaniswami, "Motor recovery monitoring using acceleration measurements in post acute stroke patients," *Biomedical Engineering Online*, vol. 12, no. 1, p. 33, 2013.

[15] R. Scapaticci, J. Tobon, G. Bellizzi, F. Vipiana, and L. Crocco, "Design and numerical characterization of a low-complexity microwave device for brain stroke monitoring," *IEEE Transactions on Antennas and Propagation*, vol. 66, no. 12, pp. 7328–7338, 2018.

[16] J. A. Tobon Vasquez, R. Scapaticci, G. Turvani et al., "First experimental assessment of a microwave imaging prototype for cerebrovascular diseases monitoring," in *2018 International Conference on Electromagnetics in Advanced Applications (ICEAA)*, Verona, Italy, September 2018.

[17] J. A. Tobon Vasquez, G. Turvani, G. Dassano et al., "Ongoing developments towards the realization of a microwave device for brain stroke monitoring," in *2018 IEEE International Symposium on Antennas and Propagation & USNC/URSI National Radio Science Meeting*, Boston, MA, USA, July 2018.

[18] M. Bertero and P. Boccacci, *Introduction to Inverse Problems in Imaging*, Institute of Physics, Bristol, U.K., 1998.

[19] I. Sarwar, G. Turvani, M. Casu et al., "Low-cost low-power acceleration of a microwave imaging algorithm for brain stroke monitoring," *Journal of Low Power Electronics and Applications*, vol. 8, no. 4, p. 43, 2018.

[20] R. Scapaticci, M. Bjelogrlic, J. A. Tobon Vasquez, F. Vipiana, M. Mattes, and L. Crocco, "Microwave technology for brain imaging and monitoring: physical foundations, potential and limitations," in *Emerging Electromagnetic Technologies for Brain Diseases Diagnostics, Monitoring and Therapy*pp. 7–35, Springer, Cham.

[21] R. Scapaticci, L. di Donato, I. Catapano, and L. Crocco, "A feasibility study on microwave imaging for brain stroke monitoring," *Progress In Electromagnetics Research B*, vol. 40, pp. 305–324, 2012.

[22] N. Joachimowicz, B. Duchene, C. Conessa, and O. Meyer, "Reference phantoms for microwave imaging," in *2017 11th European Conference on Antennas and Propagation (EUCAP)*, pp. 2719–2722, Paris, France, March 2017.

[23] N. Joachimowicz, C. Conessa, T. Henriksson, and B. Duchene, "Breast phantoms for microwave imaging," *IEEE Antennas and Wireless Propagation Letters*, vol. 13, pp. 1333–1336, 2014.

[24] S. Romeo, L. di Donato, O. M. Bucci et al., "Dielectric characterization study of liquid-based materials for mimicking breast

tissues," *Microwave and Optical Technology Letters*, vol. 53, no. 6, pp. 1276–1280, 2011.

[25] P. M. Meaney, F. Shubitidze, M. W. Fanning, M. Kmiec, N. R. Epstein, and K. D. Paulsen, "Surface wave multipath signals in near-field microwave imaging," *International Journal of Biomedical Imaging*, vol. 2012, Article ID 697253, 11 pages, 2012.

[26] O. M. Bucci, L. Crocco, R. Scapaticci, and G. Bellizzi, "On the design of phased arrays for medical applications," *Proceedings of the IEEE*, vol. 104, no. 3, pp. 633–648, 2016.

[27] O. M. Bucci, L. Crocco, and T. Isernia, "Improving the reconstruction capabilities in inverse scattering problems by exploitation of close-proximity setups," *Journal of the Optical Society of America. A*, vol. 16, no. 7, pp. 1788–1798, 1999.

[28] N. Joachimowicz, B. Duchene, J. A. Tobon Vasquez et al., "Head phantoms for a microwave imaging system dedicated to cerebrovascular disease monitoring," in *2018 IEEE Conference on Antenna Measurements & Applications (CAMA)*, Västerås, Sweden, September 2018.

[29] D. M. Pozar, *Microwave Engineering*, John Wiley and Sons Inc, second edition edition, 1998.

Hindawi
International Journal of Antennas and Propagation
Volume 2019, Article ID 4074862, 9 pages
https://doi.org/10.1155/2019/4074862

Research Article

Microwave Tomography System for Methodical Testing of Human Brain Stroke Detection Approaches

Ilja Merunka,[1] Andrea Massa,[2] David Vrba,[3] Ondrej Fiser,[3] Marco Salucci,[2] and Jan Vrba[3]

[1]*Department of Electromagnetic Field, Czech Technical University in Prague, Prague, Czech Republic*
[2]*ELEDIA Research Center (ELEDIA@UniTN-University of Trento), Via Sommarive 9, I-38123 Trento, Italy*
[3]*Department of Biomedical Technology, Czech Technical University in Prague, Prague, Czech Republic*

Correspondence should be addressed to Ilja Merunka; merunilj@fel.cvut.cz

Received 19 October 2018; Revised 16 January 2019; Accepted 23 January 2019; Published 31 March 2019

Guest Editor: Sandra Costanzo

In this work, a prototype of a laboratory microwave imaging system suitable to methodically test the ability to image, detect, and classify human brain strokes using microwave technology is presented. It consists of an antenna array holder equipped with ten newly developed slot bowtie antennas, a 2.5 D reconfigurable and replaceable human head phantom, stroke phantoms, and related measuring technology and software. This prototype was designed to allow measurement of a complete S-matrix of the antenna array. The reconfigurable and replaceable phantom has currently 23 different predefined positions for stroke phantom placement. This setting allows repeated measurements for the stroke phantoms of different types, sizes/shapes, and at different positions. It is therefore suitable for large-scale measurements with high variability of measured data for stroke detection and classification based on machine learning methods. In order to verify the functionality of the measuring system, S-parameters were measured for a hemorrhagic phantom sequentially placed on 23 different positions and distributions of dielectric parameters were reconstructed using the Gauss-Newton iterative reconstruction algorithm. The results correlate well with the actual position of the stroke phantom and its type.

1. Introduction

Microwave tomography (MWT) is an emerging imaging technique for retrieving the spatial distribution of dielectric parameters of biological tissues [1].

In microwave imaging, the imaged area is typically exposed to electromagnetic (EM) waves radiated by antenna(s) positioned around the imaged area. The spatial distribution of the dielectric parameters in the imaged area influences the way of propagation of these waves, and the resulting EM field is subsequently measured by the same antennas. The measured data is used to estimate the distribution of dielectric properties within the imaged area.

While the use of nonionizing radiation in MWT systems is a good argument when looking for benefits over a computed tomography and mammography (nonionizing radiation would allow frequent screenings), portability and cost effectiveness are good points when comparing MWT with magnetic resonance imaging [2].

Although one of the first reference of microwave hemorrhagic stroke detector can be found in the US patent by inventors Haddad and Trebes [3], there are nowadays several research groups working towards early stroke detection and differentiation systems. Just to name few leaders of the groups active in this field—Mikael Persson from Medfield Diagnostics AB, Sweden [4], Serguei Semenov from EMTensor GmbH, Austria [5], Amin Abbosch from The University of Queensland, Australia [6], and Lorenzo Crocco from the National Research Council of Italy, Italy [7–9]. Thorougher review can be found in [10].

In general, two different approaches for detection and classification of strokes can be found in literature: methods

based on visualization (image reconstruction) of dielectric parameters distribution in the region of interests [6, 11] and methods based on machine learning algorithms [4, 12, 13].

Most of the published systems (both hardware and reconstruction/classification algorithms) have not been systematically tested. Typically, one or two stroke phantom positions are selected, and the results obtained are evaluated and presented.

In this paper, we designed and tested a laboratory microwave imaging system suitable for measuring head and stroke phantoms of various types, shapes, and sizes. The stroke phantoms could be placed at any of 23 predefined positions covering almost all the volume of the head phantom. Such a system is especially suited for testing methods for stroke detection and classification based on machine learning algorithms, but it can be used for testing image reconstruction methods as well. Additionally, the proposed system allows testing of the two approaches for phantoms of different complexities and matching liquids of various dielectric properties. The system was tested using a simple 2.5 D reconfigurable head phantom with hemorrhagic stroke phantom, which was sequentially placed at some of the predefined positions. The system, phantoms, and measurements are described in Section 2. Section 3 includes an analysis of the measured data as a function of stroke phantom position. Finally, a deterministic iterative algorithm for the reconstruction of the dielectric properties distribution was applied in Section 4 to the measured data in order to verify functionality of the presented system.

2. Microwave Imaging System Description

2.1. Phantoms of Head and Brain Strokes, Antenna Array. The shape of the head phantom was designed with respect to the main objective of the article, namely, to systematically test the use of microwave imaging for the purpose of detection and classification of brain strokes occurring anywhere in the volume of human brain. For this, it is necessary to be able to place a stroke phantom on a predefined position in the entire head phantom. Towards this end, a liquid head phantom has been chosen to fill an elliptical container with a human head-shaped cross section in a transverse plane. The head phantom vessel is placed into the antenna element holder. The space between the vessel and the holder is filled with a matching liquid, see Figure 1. Both the antenna holder and the head phantom vessel have a height of 200 mm (including a base of 4 mm) and a wall thickness of 2 mm. The numerical model of the proposed system and its physical form are shown in Figure 2. 23 octagonal pins are designed at the bottom of this container and are used to define the positions of phantoms of strokes. These latter are made by hollow cylinders filled by liquids of desired dielectric parameters, having an octagonal opening in their bottom. This ensures accurate and repeatable placement of phantoms of strokes in the head phantom. The containers for stroke phantoms have an internal diameter of 40 mm, a height of 196 mm, and a wall thickness of 1 mm. All the parts were made by 3D printing using Prusa i3 MK2 (Prusa Research, Czech Republic) and PETG material.

2.2. Antenna Elements. Ten identical slot bowtie antennas (antenna design is described in [14]) were placed on the walls of the antenna array holder. The antennas were made of two layers of 1.5 mm RF substrates Rogers R04003C with the dimensions of 59×59 mm^2 and realized by Pragoboard s.r.o., Prague, Czech Republic. The main advantages of this antenna element design are suppressed radiation outside the imaging area, symmetry of radiated field, mechanical stiffness, and easy, inexpensive, and repeatable production. The front side of the realized antenna and the modules of measured reflection coefficients of all 10 antenna elements laid on the surface of a liquid head phantom are illustrated in Figure 3. The reflection coefficients of all ten antenna elements show virtually identical values and a low amplitude (less than -10 dB) in the frequency range from nearly 0.9 to 1.3 MHz. The system introduced in this work can therefore be used at any frequency in this frequency band. The frequency band was chosen in view of the fact that it fits into frequency bands already considered the most suitable for this application [7] considering attenuation of EM waves inside the human head and resolution of the imaging method. Although the authors believe that the higher number of antennas would lead to better results, the maximal number of antennas is determined by the actual dimensions of the container and the used antenna elements.

2.3. Measurement Setup and Settings. The measuring instruments used in the presented MWI system are the microwave switching matrix ZN-Z84-B42 (Rohde & Schwarz, Germany) and the vector network analyzer (VNA) ZNB4-B32 (Rohde & Schwarz, Germany). The antennas were connected to the switching matrix test ports using semirigid coaxial cables (Rohde & Schwarz, Czech Republic). Although the isolation between all tested matrix ports should be greater than 90 dB, 10 out of 24 ports of the switching matrix test ports involved in the measurement were selected for the highest possible isolation between channels. The fact that 90 dB isolation should be sufficient is supported by another group that used an 80 dB [4] custom-made switching matrix. All high-frequency connections were tightened by a torque wrench 0.9 Nm. Setting and triggering of measurements together with reading out of the measured data were done with MATLAB scripts written in-house (MathWorks, MA, USA). The photograph of the MWI system is shown in Figure 2. The following parameters of the measurement instruments were used: operating frequency 1 GHz, intermediate frequency bandwidth 30 Hz, and output power of the VNA 13 dBm. The working frequency 1 GHz was selected with respect to penetration depth, spatial resolution, and last but not least the fact that it fits into the frequency interval preferred for the same application in [7].

2.4. Calibration. A full-port calibration was performed just before the measurement using the automatic calibration unit ZN-Z153 (Rohde & Schwarz, Germany).

Throughout the calibration period, the antenna elements were disconnected from the coaxial cables leading into the switching matrix. To these open ends of the coaxial cables,

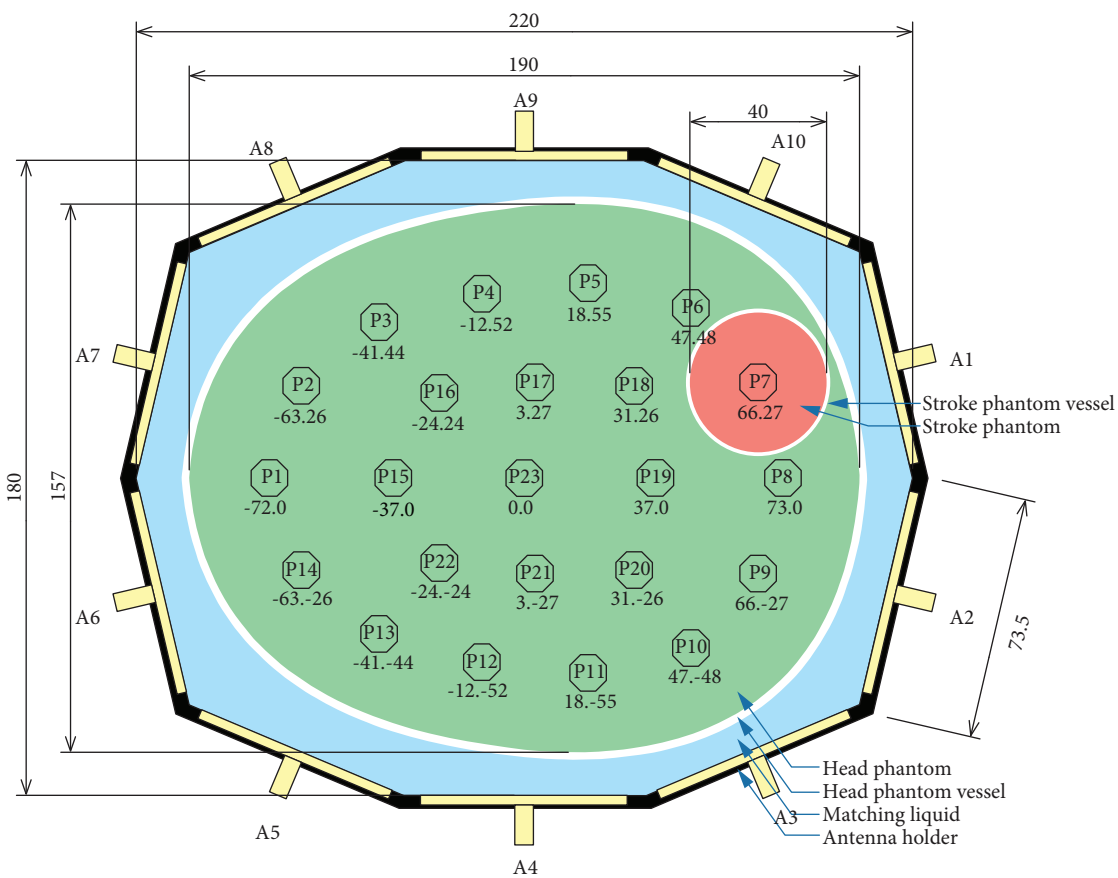

Figure 1: Bottom view of measuring container with marked positions of the stroke phantoms. Black: walls of the antenna holder, yellow: antennas with ports, blue: matching liquid, white: head phantom vessel, green: liquid phantom of human head, and red: liquid phantom of stroke at position P7 (all dimensions are in mm).

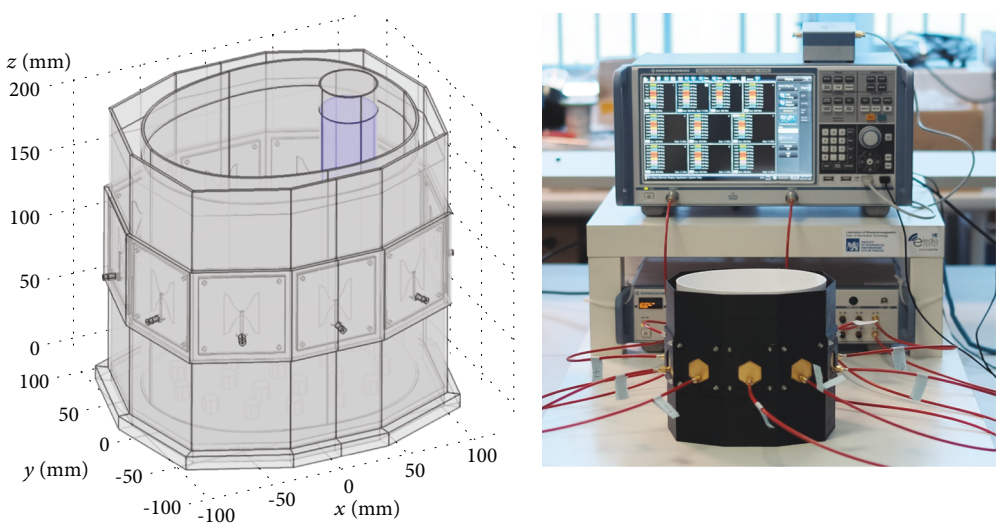

(a) (b)

Figure 2: 3D model of measuring container with antennas and cylindrical phantom of stroke marked blue (a) and the photograph of the measuring setup (b).

the calibration unit was three times reconnected (due to the lower number of ports of the calibration unit than the number of used antenna elements/system channels) following the calibration instructions displayed on the VNA. In this way, the switching matrix was included in the full-port VNA calibration.

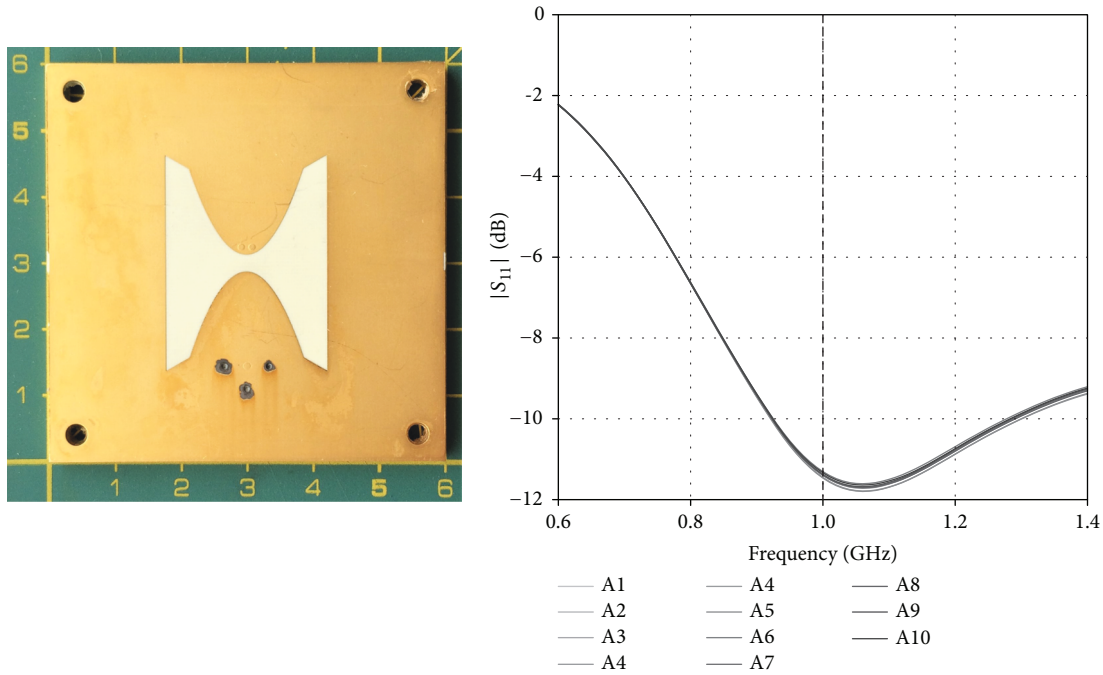

(a) (b)

Figure 3: Photograph of the antenna element from the side facing to the phantom (a) (dimensions in cm) and measured magnitude of S_{11} for all antennas in frequency range 0.6 - 1.4 GHz heading to the liquid homogeneous phantom of human head (b). Central operating frequency is marked by a dashed line.

The VNA, switching matrix, and automatic calibration unit were turned on 90 minutes before the calibration onset. Calibration data was saved and reloaded before each measurement.

2.5. Liquid Phantom Composition and Dielectric Properties. Two liquid phantoms substituting healthy head and brain hemorrhagic stroke tissue were prepared. The dielectric properties of the head phantom are equal to average dielectric parameters of a human head ($\varepsilon_{r,HH} = 39.8$, $\sigma_{HH} = 0.94$ S/m) [15]. The dielectric properties of the hemorrhagic stroke phantom are chosen based on the knowledge of the dielectric properties of blood [16], where the contrast to brain tissues is about 50 - 60%. A conservative change at the level of 30% is chosen here ($\varepsilon_{r,HR} = 51.4$, $\sigma_{HR} = 1.22$ S/m) as in [5]. Dielectric properties of the phantoms were measured using DAK (Schmid & Partner Engineering AG, Switzerland) just before the measurement in the MWI system prototype. Compositions in weight percent and comparison of target and measured dielectric properties of the phantoms are listed in Table 1. In this table, the HEAD marks the column devoted to the phantom of the head and the HEM marks the column devoted to the hemorrhagic stroke phantom. The dielectric parameters listed in rows following the compositions were measured at a frequency of 1 GHz and 25°C before the measurement in the MWI system. In order to eliminate the reflections from the interface matching liquid-head, the head phantom material was also used as the matching liquid between the antennas and the head vessel.

Table 1: Phantom composition in weight percent, target, and measured dielectric parameters at 1 GHz and 25°C, immediately before the measurement in the MWI system.

	HEAD	HEM
Isopropyl alcohol (wt%)	50.48	34.00
Deionized water (wt%)	48.35	64.67
NaCl (wt%)	1.16	1.33
Target ϵ_r (-)	39.60	51.48
Measured ϵ_r (-)	39.80	51.37
U ($k = 2$) (%)	1.7	2.1
Target σ (S/m)	0.94	1.220
Measured σ (S/m)	0.94	1.224
U ($k = 2$) (%)	2.7	2.7

U: expanded uncertainty of type B, HEAD: head phantom, HEM: hemorrhagic phantom.

2.6. Measuring Procedure. The antenna array holder and the head phantom vessel were firstly filled with homogeneous head phantom liquid. Special attention was paid to elimination of bubbles which appeared on the surface of antennas during the filling procedure of the container. Finally, the container was enclosed by microwave pyramid absorbers. The measurement procedure is composed from two main steps: (1) measurement of the MWI system filled with the head phantom only and (2) measurement with the head phantom including the hemorrhagic stroke phantom. The phantom of stroke was subsequently positioned and measured in all 23 positions (Figure 1). Whole S-matrix was measured 10 times

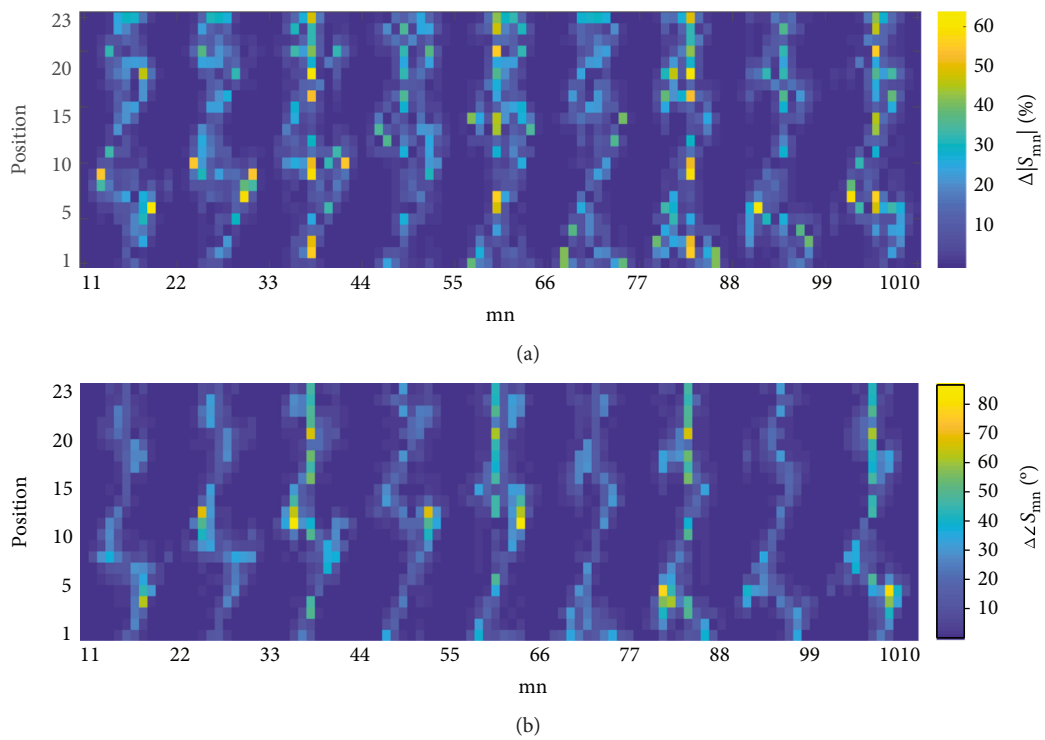

Figure 4: Response of the system ((a) relative change in the modulus of S-matrix and (b) change in the phase of S-matrix in degrees) to a presence of the hemorrhagic stroke phantom at 23 different positions (y axes) in the phantom of human head.

in series to cover fluctuations that could appear during the measurement for every position of the stroke. One measurement of the full S-matrix took about 12 s.

3. Measured Data

The response of the system to a presence of the phantom of hemorrhagic stroke at all 23 positions is visualized in Figure 4. It is calculated as the relative difference in the modules (equation (1)) and as the absolute difference in the arguments (equation (2)) of the S-parameters measured with (S_{mn}^{STROKE}) and without (S_{mn}^{HOMO}) the stroke phantom, respectively

$$\Delta|S_{mn}| = \frac{\left||S_{mn}^{STROKE}| - |S_{mn}^{HOMO}|\right|}{|S_{mn}^{HOMO}|}, \quad (1)$$

$$\Delta\angle S_{mn} = \left|\angle S_{mn}^{STROKE} - \angle S_{mn}^{HOMO}\right|. \quad (2)$$

The most responding S-parameters to the stroke at the specific position can be deduced from those images. The characteristic patterns in both amplitude and phase images indicate the strongest responses in transmission coefficients.

4. Application of Image Reconstruction Algorithm to Measured Data

A reconstruction algorithm based on Gauss-Newton algorithm with Tikhonov regularization [17] was used to reconstruct the dielectric image in the central plane of the antennas from the measured S-parameters. This algorithm is based on deterministic optimization procedure, assuming linear behavior of outcome in every iteration when only a small change in dielectric properties is introduced. In order to reduce the building time of the Jacobian matrix, the so-called adjoint method was used [18]. The value of the Tikhonov parameter was determined using the procedure described in [17].

4.1. Image Reconstruction Procedure. The image reconstruction procedure includes solution of forward problem (computation of electromagnetic field distribution and S-matrix), extraction of E-fields and S-matrix, computation of Jacobian, and computation of step in dielectric properties of the material domains. To model the propagation of E-field in the forward step, the 3D numerical version of the real measuring system was modeled in COMSOL Multiphysics (Figure 2(a)). Models of the real antennas together with SMA ports were used in the numerical model. Special attention was payed to correctly discretize all the model components. Finally, EM field was computed using the finite element method in 3D. All three components of E-field were extracted and used in the inverse step. In order to precisely represent the real-world scenario, any special assumption either simplification in the computational procedure of EM field was not made. Therefore, the framework presented in this paper can be easily adapted to the other realistic scenario by simply replacing the numerical model. Computation of the forward problem is the most computationally extensive procedure and takes about 150 minutes for all 10 antenna ports on the current PC (i7-6700 - 3.4 GHz, 64 GB DDR4

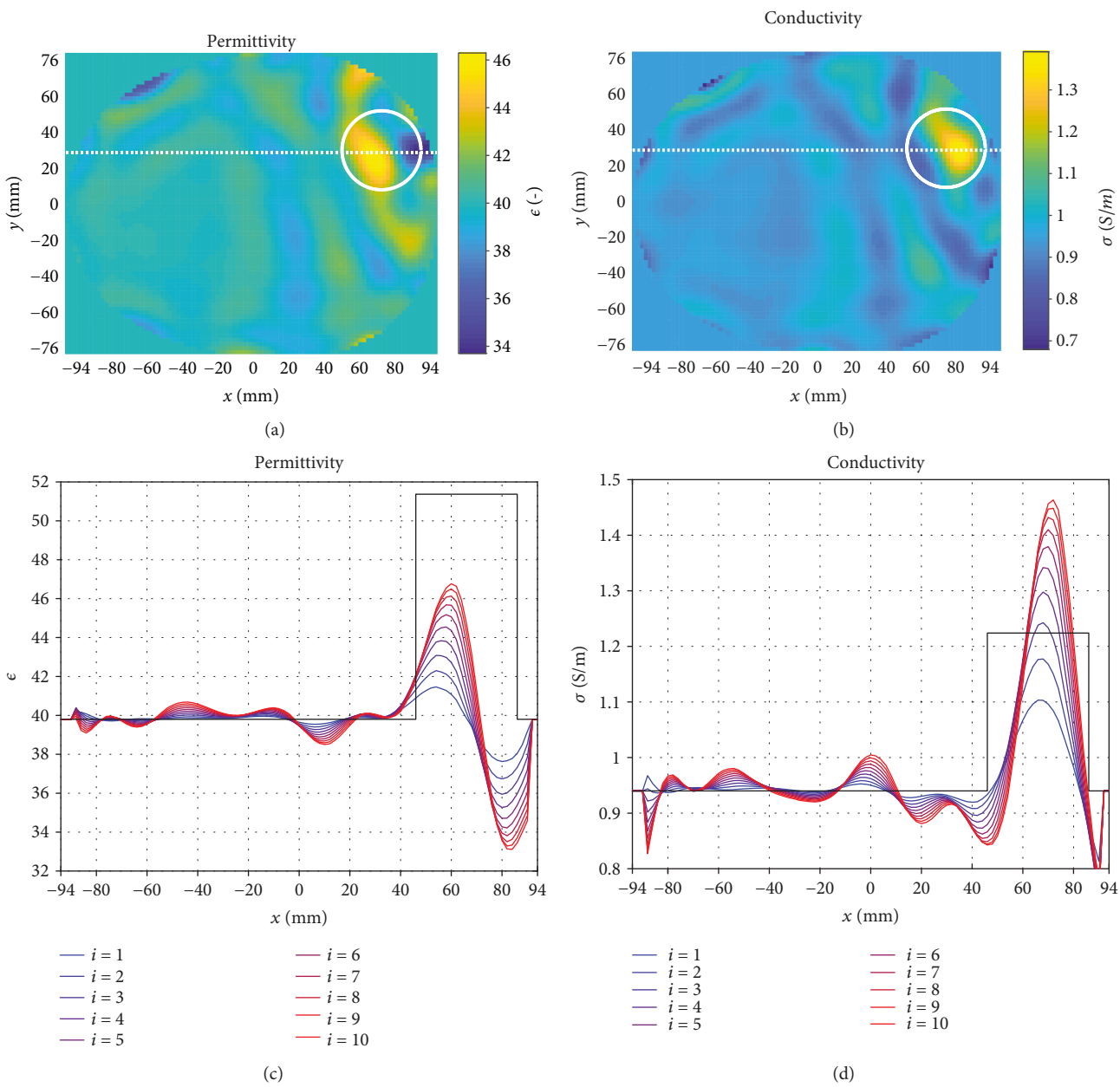

Figure 5: Results (a, b) of iterative reconstruction procedure for hemorrhagic stroke phantom at position P7 (marked by white circle) and evolution (c, d) of relative permittivity and conductivity over the iterations ($i = 1$ for the first iteration, $i = 10$ for the tenth iteration) on the line going through the center of the stroke phantom (marked by dashed white lines). Actual values of both relative permittivity and conductivity are marked by solid black lines in graphs (c) and (d).

RAM - 2133 MHz). The reconstruction algorithm was implemented in MATLAB.

In an attempt to achieve the actual values of complex permittivity in the region of interest, 10 iterations of the reconstruction algorithm were performed. Since the image reconstruction takes more than 25 hours for 10 iterations, the maximal number of iterations allowed was set to 10. Better results could be possibly achieved with higher number of iterations. However, as it can be seen from Figure 5, there is only a small change in the dielectric parameters over the last few iterations. Results of the reconstruction in a plane going through the center of the antennas for hemorrhagic stroke at position P7 are shown in Figure 5. Even though values of relative permittivity and conductivity in the reconstructed images did not reach the actual values and shape of the stroke, the biggest change in those quantities can be observed in the area of the stroke phantom (white circle).

Nine different unique positions of the stroke phantom inside the head phantom were selected, and the measured data were processed with the image reconstruction algorithm. In order to show the results of the reconstruction for all the positions of the stroke in one image, 350 values of relative permittivity and conductivity differing the most from the background matching liquid were detected in all

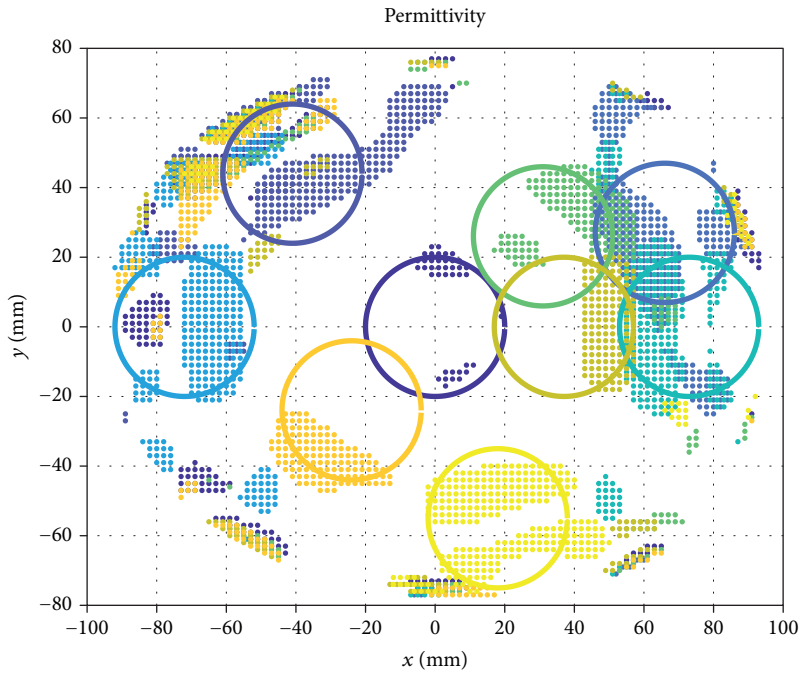

(a)

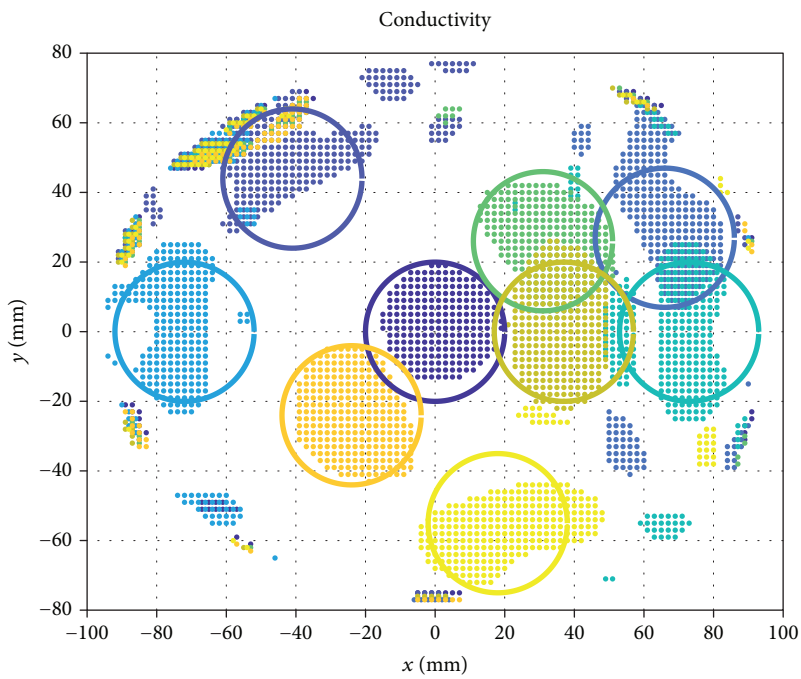

(b)

Figure 6: Detection of position of the strokes from reconstructed images. Circles mark the actual position of the stroke; dots of adequate color show the detected positions.

Table 2: Maximal values of dielectric parameters for the selected positions of the stroke phantom after the reconstruction.

Position	P1	P3	P7	P8	P11	P18	P19	P22	P23
max ϵ_r (-)	48.13	51.34	46.30	47.60	44.87	44.71	44.71	45.23	44.48
max σ (S/m)	1.42	1.32	1.39	1.38	1.30	1.23	1.24	1.22	1.24

9 images and its positions plotted together for every stroke phantom position, see Figures 6(a) and 6(b). In this figure, the threshold used to allow the binarization is based on the assumption that the size of the stroke phantom is known. And so, the size of the area covered by the dots of the specific color in Figure 6 is equaled to the size of the area of the cross-section of the stroke phantom. Positions of the stroke phantom can be better recognized from images depicting conductivity. Since the quantitative information is lost in Figure 6, the maximal values of dielectric parameters are listed in Table 2.

5. Discussion

The MWI systems are very sensitive to the quality of conducted microwave measurement. There are many cofounders, including temperature drift of measuring devices, changes in complex permittivity of phantoms due to the changes in temperature, evaporation and possible leak of liquids during stroke phantom replacement procedure, appearance of bubbles in the liquid phantoms, and quality of multiport calibration procedure, that the experimenter has to deal with during the measuring procedure. All those sources of noise negatively impact the quality of reconstructed images.

Conservative estimates of the differences between the dielectric properties of brain tissues and areas affected by strokes were considered. It can be assumed that a higher contrast in the dielectric properties of the head phantom and stroke phantoms would yield in better reconstruction results.

The number of antennas/channels of the presented system was determined by the dimensions of the human head/head phantom and the antenna element. For the used antenna elements, only limited size reductions can be achieved. Metamaterial-based structures such as described in [19–21] could be suitable for systems with a higher number of the antenna elements.

The forward problem in every iteration is solved for every antenna element. This can be done in parallel and thus reduce the total computational time. Further reduction of the computational time could be achieved by using the Finite Differences in Time-Domain Method (FDTD) which can be accelerated using GPU. If a broadband formulation of FDTD is used, it is possible to obtain results for multiple frequencies in a single simulation without a significant computational time increase.

In this work, imaging results for only 9 stroke phantom positions are presented, although there are in total of 23 positions available. This step is only motivated by the clarity of the imaging results presented. The 9 positions considered were carefully selected based on the geometric symmetry of the head phantom and antenna array. In other words, the imaging results for each of the remaining 14 positions would not differ much from the results corresponding to one of the 9 positions.

6. Conclusion

The prototype of the MWT system allowing systematic evaluation of human brain stroke detection and classification approaches has been presented in this paper. In order to prove the capabilities of the presented system, hemorrhagic phantom of human brain stroke was prepared and the experimental measurements were conducted with this stroke sequentially placed at 23 different positions in the head phantom. Achieved results support the statements of another groups working in this field that the detection and differentiation of the strokes by means of microwave technique should be possible at least in the laboratory conditions. In our future work, we are going to improve our system in several ways to deal with some major known issues such as low sensitivity, spatial resolution, and sensitivity to noise. A 2.5 D anatomically realistic head phantom consisting of three solid layers with shape and dielectric properties corresponding to skin, skull, and cerebrospinal fluid is currently under development. We also plan to combine the reconstructed images with detection and classification by algorithms of machine learning.

Data Availability

The data used to support the findings of this study are available from the corresponding author upon request.

Conflicts of Interest

The authors declare that there is no conflict of interest regarding the publication of this paper.

Acknowledgments

This work has been supported by a grant from the Czech Science Foundation, number 17-00477Y.

References

[1] A. Fhager, P. Hashemzadeh, and M. Persson, "Reconstruction quality and spectral content of an electromagnetic time-domain inversion algorithm," *IEEE Transactions on Biomedical Engineering*, vol. 53, no. 8, pp. 1594–1604, 2006.

[2] P. M. Meaney, "Microwave imaging and emerging applications," *International Journal of Biomedical Imaging*, vol. 2012, Article ID 252093, 2 pages, 2012.

[3] W. Haddad and J. Trebes, "Microwave hemorrhagic stroke detector," US Patent US20 030 018 244 A1, 2003, US Classification 600/371; International Classification A61B5/05; Cooperative Classification A61B5/4076, A61B5/0507, A61B5/05; European Classification A61B5/05M, A61B5/05, https://www.google.ch/patents/US20030018244.

[4] M. Persson, A. Fhager, H. D. Trefna et al., "Microwave-based stroke diagnosis making global prehospital thrombolytic treatment possible," *IEEE Transactions on Biomedical Engineering*, vol. 61, no. 11, pp. 2806–2817, 2014.

[5] M. Hopfer, R. Planas, A. Hamidipour, T. Henriksson, and S. Semenov, "Electromagnetic tomography for detection, differentiation, and monitoring of brain stroke: a virtual data and human head phantom study," *IEEE Antennas and Propagation Magazine*, vol. 59, no. 5, pp. 86–97, 2017.

[6] D. Ireland, K. Bialkowski, and A. Abbosh, "Microwave imaging for brain stroke detection using Born iterative method,"

IET Microwaves, Antennas & Propagation, vol. 7, no. 11, pp. 909–915, 2013.

[7] R. Scapaticci, L. Di Donato, I. Catapano, and L. Crocco, "A feasibility study on microwave imaging for brain stroke monitoring," *Progress In Electromagnetics Research B*, vol. 40, pp. 305–324, 2012.

[8] R. Scapaticci, O. M. Bucci, I. Catapano, and L. Crocco, "Differential microwave imaging for brain stroke followup," *International Journal of Antennas and Propagation*, vol. 2014, Article ID 312528, 11 pages, 2014.

[9] R. Scapaticci, J. Tobon, G. Bellizzi, F. Vipiana, and L. Crocco, "Design and numerical characterization of a low-complexity microwave device for brain stroke monitoring," *IEEE Transactions on Antennas and Propagation*, vol. 66, no. 12, pp. 7328–7338, 2018.

[10] L. Crocco, I. Karanasiou, M. L. James, and R. C. Conceição, Eds., *Emerging Electromagnetic Technologies for Brain Diseases Diagnostics, Monitoring and Therapy*, Springer International Publishing, 2018, https://www.springer.com/la/book/9783319750064.

[11] A. Abbosh, "Microwave systems for head imaging: challenges and recent developments," in *2013 IEEE MTT-S International Microwave Workshop Series on RF and Wireless Technologies for Biomedical and Healthcare Applications (IMWS-BIO)*, pp. 1–3, Singapore, December 2013.

[12] M. Salucci, J. Vrba, I. Merunka, and A. Massa, "Real-time brain stroke detection through a learning-by-examples technique - an experimental assessment," *Microwave and Optical Technology Letters*, vol. 59, no. 11, pp. 2796–2799, 2017.

[13] M. Salucci, A. Gelmini, J. Vrba, I. Merunka, G. Oliveri, and P. Rocca, "Instantaneous brain stroke classification and localization from real scattering data," *Microwave and Optical Technology Letters*, vol. 61, no. 3, pp. 805–808, 2019.

[14] I. Merunka, J. Vrba, O. Fiser, and D. Vrba, "Comparison of bowtie slot and rectangular waveguide-based antennas for microwave medical imaging," in *12th European Conference on Antennas and Propagation (EuCAP 2018)*, pp. 1–5, London, UK, April 2018.

[15] IEEE Std 1528-2013 (Revision of IEEE Std 1528-2003), *IEEE Recommended Practice for Determining the Peak Spatial-Average Specific Absorption Rate (SAR) in the Human Head from Wireless Communications Devices: Measurement Techniques*, IEEE, 2013, https://search.library.wisc.edu/catalog/9912350582702121.

[16] P. A. Hasgall, F. Di Gennaro, C. Baumgartner et al., "IT'IS database for thermal and electromagnetic parameters of biological tissues," January 2015, http://www.itis.ethz.ch/database.

[17] N. Joachimowicz, C. Pichot, and J. P. Hugonin, "Inverse scattering: an iterative numerical method for electromagnetic imaging," *IEEE Transactions on Antennas and Propagation*, vol. 39, no. 12, pp. 1742–1753, 1991.

[18] Q. Fang, P. M. Meaney, S. D. Geimer, A. V. Streltsov, and K. D. Paulsen, "Microwave image reconstruction from 3-D fields coupled to 2-D parameter estimation," *IEEE Transactions on Medical Imaging*, vol. 23, no. 4, pp. 475–484, 2004.

[19] M. Polívka and D. Vrba, "Shielded micro-coplanar CRLH TL zeroth-order resonator antenna: critical performance evaluation," *Radioengineering*, vol. 18, no. 1, pp. 1592–1595, 2009.

[20] J. Vrba and D. Vrba, "A microwave metamaterial inspired sensor for non-invasive blood glucose monitoring," *Radioengineering*, vol. 24, no. 4, pp. 877–884, 2015.

[21] D. Vrba, J. Vrba, D. B. Rodrigues, and P. Stauffer, "Numerical investigation of novel microwave applicators based on zero-order mode resonance for hyperthermia treatment of cancer," *Journal of the Franklin Institute*, vol. 354, no. 18, pp. 8734–8746, 2017.

Hindawi
International Journal of Antennas and Propagation
Volume 2019, Article ID 4640925, 7 pages
https://doi.org/10.1155/2019/4640925

Research Article

Uncertainty Quantification for the Transient Response of Human Equivalent Antenna Using the Stochastic Collocation Approach

Anna Šušnjara and Dragan Poljak

Faculty of Electrical Engineering, Mechanical Engineering and Naval Architecture, Department of Electronics, University of Split, 21000 Split, Croatia

Correspondence should be addressed to Dragan Poljak; dpoljak@fesb.hr

Received 12 October 2018; Accepted 30 December 2018; Published 28 March 2019

Guest Editor: Sandra Costanzo

The paper deals with the uncertainty quantification of the transient axial current induced along the human body exposed to electromagnetic pulse radiation. The body is modeled as a straight wire antenna whose length and radius exhibit random nature. The uncertainty is propagated to the output transient current by means of the stochastic collocation method. The stochastic approach is entirely nonintrusive and serves as a wrapper around the deterministic code. The numerical deterministic model is based on the time domain Hallen integral equation solved by means of the Galerkin-Bubnov indirect boundary element method (GB-IBEM). The stochastic moments, i.e., the mean and the variance of the transient current, are calculated. Confidence margins are obtained for the whole duration of the transient response as well as for the maximal current value. The presented approach enables the estimation of the probability for the induced current to exceed the basic restrictions prescribed by regulatory bodies. The sensitivity analysis of the input parameters indicates to which extent the variation of the input parameter set influences the output values which is particularly interesting for the design of the human equivalent antenna.

1. Introduction

Axial current distribution has been one of the quantities of interest not only to quantify human exposure to low-frequency fields by determining the current density/induced fields but also to compute specific absorption (SA) for the case of human exposure to transient radiation [1]. Thus, these quantities are the first step in quantifying the effects of EM exposure. On the other hand, biological effects depend on the frequency of the EM field. Due to the absence of resonance effects at low frequencies (LF), the thermal effects are negligible while the nonthermal effects could possibly have severe effects on membrane cells [2, 3]. On the contrary, in a high-frequency (HF) range, where the body dimensions are comparable to external field wavelength and resonances become significant, thermal effects are dominant [4, 5]. In any case, there is no way to directly measure the induced electric fields in humans and related biological effects; hence, the use of reliable computational models is mandatory.

However, computational models used in EM dosimetry, simplified or anatomically realistic ones, are subjected to variation of input parameters' values. The morphology (dimensions), the tissue conductivity and relative permittivity, and other constants related to the model description are often partially or even entirely unknown. In the past decade, some efforts have been made to provide the means to include the parameter variability into the model and propagate it to the output value of interest. A term "stochastic dosimetry" has been coined under the idea that by using only average values, the computational models are rough approximation of the real scenarios in EM dosimetry [6]. Some examples of stochastic dosimetry simulations are presented in [7–10]. Such an approach becomes even more important when it comes to international and national guidelines and standards, respectively, which ought to account for the stochastic nature of the input variables thus providing certain expected values for the restrictions along with the confidence margins and worst-case predictions [11, 12].

Generally, the Monte Carlo simulation (MCS) method is considered to be the most reliable and robust stochastic method [13]. However, relatively slow convergence makes this somewhat unattractive and sometimes inconvenient even for the validation of results with respect to other methods. Among various alternative methods reported in the literature, the generalized polynomial chaos expansion (gPCE) emerged as the most often used approach in the stochastic computational electromagnetics (SCEM). This technique for solving stochastic equations is based on spectral discretization, and it comprises the stochastic Galerkin method (SGM) and stochastic collocation method (SCM) [13]. The main difference between the two methods is their intrusive/nonintrusive approach to computational models. The intrusive nature of SGM implies a more demanding implementation since the development of new codes is required. On the other hand, the nonintrusiveness of SCM enables the use of previously validated deterministic models as black boxes. Still, both approaches exhibit fast convergence and high accuracy under different conditions. The analysis regarding the applications in computational electromagnetics may be found elsewhere, e.g., in [14].

The properties of the field induced in the human body due to EM exposure could be studied by means of a simple but rather useful cylindrical model of the human body [1]. This model has been widely used for LF ranges. First, King and Sandler proposed the parasitic-antenna model of the human body exposed to extremely low-frequency (ELF) and very-low-frequency (VLF) sources providing some closed-form expressions for the induced current [15]. An overview of some numerical methods for human exposure from ELF to a microwave region is reported in [16]. Furthermore, for the case of ELF range, the loaded thick-wire model of human body based on Pocklington's integrodifferential equation in FD has been proposed by Poljak and Rashed [17]. The model is based on the solution of Pocklington's equation via the Galerkin-Bubnov boundary element method (GB-BEM).

Although FD techniques enable the use of simpler formulations and therefore the numerical treatment is less complicated, when the human body is exposed to transient radiation, a direct time domain approach offers a better insight into the physical behavior of the phenomena [18]. One possible approach would be to use an indirect approach, i.e., to implement the FD-based models along with the IFFT algorithm. However, the thick-wire model from [17] suffers from some numerical instabilities when used for TD response, and moreover, coupling of such approach with nonintrusive and sampling-based stochastic methods would imply a significant burden on computational resources.

A human equivalent thin-wire antenna model has been proposed for experimental dosimetry [19], and it is valid in the frequency region from 50 Hz to 110 MHz. Therefore, TD simulation of the body based on the human equivalent antenna model is proposed in [20]. The formulation is based on Hallen's type of integral equation numerically treated via the GB-IBEM. This deterministic model has been validated providing the stable numerical results.

This paper presents a step forward towards the deterministic-stochastic coupling of TD Hallen's equation GB-IBEM solver, for the unknown current induced along the antenna, and the SCM, respectively. The SCM treats the deterministic part as a black box, thus preserving the functionalities of validated codes from [20]. The novel stochastic approach treats the dimensions of the antenna, namely, its length and radius, as random variables (RV) with predefined stochastic distributions. The aim is to obtain the expected value of the induced current and provide the estimation of confidence margins. The results will also show which of the two parameters have a higher impact on the output value and to which extent. The modeling carried out in the presented stochastic-deterministic approach may be useful in designing such antennas like in Gandhi and Aslan's patent in [19]. The present work could be regarded as a follow-up to the stochastic-deterministic coupling of the FD thick-wire model and the SCM approach for the LF exposure assessment reported in [21]. Though such a canonical representation can be regarded as a rather simplified deterministic-stochastic model of the body for a transient plane wave exposure, it still ensures a rapid estimation of the phenomenon. Moreover, this cylindrical model could be considered as a starting point to establish a more realistic and eventually anatomically based direct time domain model. To the best of our knowledge, even oversimplified models of this kind are rather rare in the relevant literature if they are available at all.

This paper is organized as follows. Section 1 introduces the basic concept of the time domain model of the human equivalent antenna. Section 2 outlines the fundamentals of the stochastic collocation method. Numerical examples are presented in Section 3 while some concluding remarks and considerations related to the future work are given in Section 4.

2. Time Domain Model of Human Equivalent Antenna

As it has been shown by King and Sandler in [15], the perpendicular component of the incident electric field tangential to the body can be assumed constant along the body. This field component induces the axial current not forming a closed loop but ending on charge density induced on the surface of the body. Provided that the human body is represented by a cylindrical antenna, the first task of the electromagnetic dosimetry is to calculate the current distribution induced along the antenna. Once the axial current is known, it is possible to calculate the electric field, the power density, and the specific absorption (SA) induced in the body. Furthermore, the macroscopic average electric field can be subsequently used for the calculation of the corresponding local electric fields induced in different organs [15].

The TD model of the human equivalent antenna used in this work has been proposed in [20]. The antenna with radius a and length L representing the human body is assumed to be insulated in the free space. The arms are positioned close to the body. All body organs are considered to behave as good conductors for a given frequency range. As the impact of the conductivity variations on the results is negligible [20],

the antenna is considered to be perfectly conducting (PEC). The cylindrical antenna of length L and radius a representing the human body is presented in Figure 1.

The formulation is based on the Hallen space-time integral equation [20]:

$$\int_0^L \frac{I\left(z', t - R/c\right)}{4\pi R} dz' = F_0\left(t - \frac{z}{c}\right) + F_L\left(t - \frac{L-z}{c}\right) + \frac{1}{2Z_0}\int E_z^{\text{inc}}\left(z', t - \frac{|z-z'|}{c}\right) dz', \tag{1}$$

where $I(z', t - R/c)$ is the unknown space-time dependent current to be determined for a given incident electric field E_z^{inc}, c is the light velocity, and Z_0 is the free-space wave impedance. Multiple reflections of the current wave from the wire free ends are taken into account via unknown time signals $F_0(t)$ and $F_L(t)$. A detailed derivation of (1) could be found elsewhere, e.g., in [20].

In the past two decades, some studies have provided evidence of greater effect on biological systems when exposed to pulsed signals such as radar or mobile radio telephones than to nonpulsed signals [22]. In this paper, the excitation field is given as the standard double-exponential EMP waveform [20]:

$$E_z^{\text{inc}}(t) = E_0\left(e^{-\alpha t} - e^{-\beta t}\right), \tag{2}$$

where $E_0 = 1$ kVm^{-1}, $\alpha = 4 * 10^6$ s^{-1}, and $\beta = 4.76 * 10^8$ s^{-1}. The EMP is chosen in such a way that its frequency range corresponds to the frequency range of the human equivalent antenna presented in [19].

The transient current induced in the human body due to a particular EMP excitation is obtained by solving TD Hallen's integral equation (1) via the TD version of Galerkin-Bubnov indirect boundary element method (GB-IBEM). The mathematical details concerning the method of solution are given in [20].

3. Stochastic Collocation Method

3.1. Uncertainty Quantification. The process of quantifying the uncertainty in the output value of interest due to the uncertain nature of input parameters is usually referred to as the uncertainty quantification (UQ). The aim is to calculate the stochastic moments, namely, the expected value and variance, and provide confidence margins and probability density function.

The fundamental principle of the stochastic collocation method lies in the polynomial approximation of the considered output Y in the stochastic space that consists of N previously selected collocation points [23]:

$$\widehat{Y}(X) = \sum_{i=1}^{N} L_i(X) \bullet Y^{(i)}, \tag{3}$$

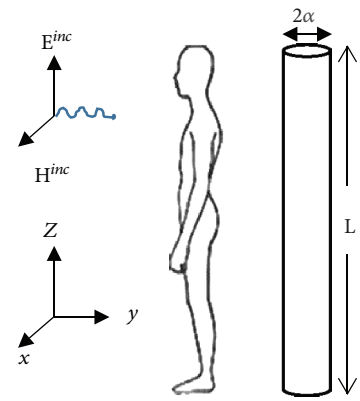

Figure 1: The cylindrical model of the body exposed to transient radiation.

where $L_i(X)$ are basis functions and $Y^{(i)}$ is the output realization for the ith input point $X^{(i)}$. The stochastic space is d dimensional as there are d random input variables, each prescribed with the corresponding probability density functions (pdf). The input variables are defined as vector $X = [x_1, \ldots, x_d]$; therefore, $X^{(i)} = [x_1^{(i)}, \ldots, x_d^{(i)}]$ is the ith input point. In this work, input variables are considered independent, an assumption valid for majority of applications in the computational electromagnetics (CEM).

The simplest way to interpolate in the multivariate dimension space is to use the tensor product in each random dimension and this approach is valid for $d < 5$. Thus, the basis function $L_i(X)$ from equation (3) is constructed as follows [23]:

$$L_k(X) = l_1^{m_1} \otimes \cdots \otimes l_d^{m_d}, \quad k = 1, \ldots N, \tag{4}$$

where l_i, $i = 1, \ldots, d$, is the one-dimensional Lagrange polynomial and the maximal value of m_j equals to the number of points in the corresponding stochastic dimension. Successful applications of a fully tensorised SCM model can be found in [23–25].

For the univariate case and m collocation points, the Lagrange basis function is given as follows:

$$l_i(x) = \prod_{k=0, k\neq i}^{m} \frac{x - x_k}{x_i - x_k}, \tag{5}$$

with the property $l_i(x_i) = \delta_{ij}$, where δ_{ij} denotes the Kronecker symbol. Other types of basis functions are possible, e.g., piecewise multilinear basis functions as in [26].

The expression in equation (3) can be used as a surrogate for the given mathematical model such as the one in equation (1). Namely, the expression may be used to estimate the probability density function since the MC sampling of this equation is more practical than the MC sampling of the original mathematical model.

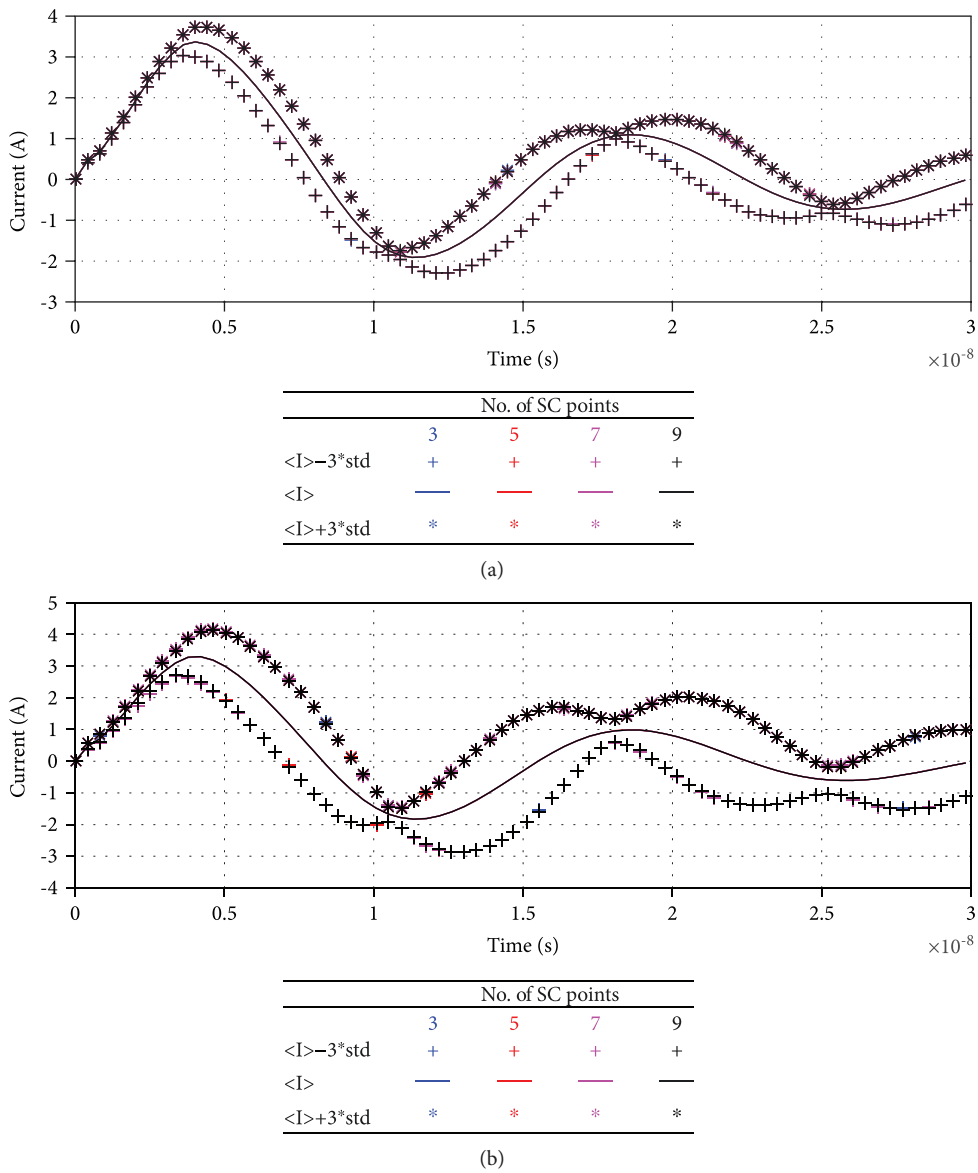

Figure 2: The stochastic transient current induced in the human body exposed to the double-exponential EMP. The observation point is the middle point of the antenna. The stochastic mean is denoted with $<I>$ and std stands for standard deviation. (a) The coefficient of variation CF = 5.71%; (b) CF = 12%.

Furthermore, the expressions for the stochastic moments are derived following their definitions from the statistics. Thus, the expectation (mean) of $\widehat{Y}(X)$ is computed as [13]

$$\begin{aligned}\mu\left(\widehat{Y}(X)\right) &= \int_{-\infty}^{+\infty} \widehat{Y}(\boldsymbol{X})p(\boldsymbol{X})d\boldsymbol{X} \\ &= \int_{-\infty}^{+\infty} \sum_{i=1}^{N} L_i(X)\bullet Y^{(i)}p(X)dX \\ &= \sum_{i=1}^{N} Y^{(i)}\bullet w_i,\end{aligned} \tag{6}$$

where $p(X)$ represents the joint probability density function of random variables in X and w_i are weights that can be precomputed as follows:

$$w_i = \int_{-\infty}^{+\infty} L_i(X)p(X)dX. \tag{7}$$

Accordingly, the variance is given as follows:

$$V\left(\widehat{Y}(X)\right) = \sum_{i=1}^{N} \left(\widehat{Y}^{(i)} - \mu\left(\widehat{Y}(X)\right)\right)^2 \bullet w_i. \tag{8}$$

It is worth noting that to calculate the stochastic moments, it is not necessary to build the polynomial form equation (3) which further reduces the computational burden.

The choice of the interpolation points $X^{(i)}$ in equation (3) can follow several approaches. In this work, the choice of

Table 1: The estimate of the confidence intervals based on quantile computation.

Quantiles	#1 CF = 5.71%	#2 CF = 12%
10.0%, 90%	[3.23, 3.54] A	[3.03, 3.65] A
5.00%, 95%	[3.20, 3.57] A	[2.96, 3.71] A
1.00%, 99%	[3.15, 3.61] A	[2.87, 3.80] A

points corresponds to the Gauss quadrature rule related to the probability distribution of random inputs, e.g., Legendre polynomials for a uniform distribution and Hermite polynomials for a Gaussian distribution [13]. Other formulas may be used to generate the abscissas for the interpolation in equation (3) such as the Clenshaw-Curtis formula with nonequidistant abscissas given as zeros of the extreme points of Chebyshev polynomials or equidistant points [26, 27]. These sets of points exhibit a nested fashion unlike Gauss points which are desirable in certain applications such as sparse grid interpolation [26, 27].

3.2. Sensitivity Analysis. The definition of sensitivity analysis (SA) according to [28] defines it as the study of how uncertainty in the output of a model (numerical or otherwise) can be apportioned to different sources of uncertainty in the model input. The variance-based SA presented in this work follows the "one at a time" principle for calculating sensitivity indices. The impact factors are thus calculated in the following way:

$$I_i = \frac{V(Y\,;X_i)}{V(Y)}, \quad i = 1, \dots, d, \tag{9}$$

where I_i stands for the influence of a single input parameter's uncertainty.

4. Numerical Results

The TD human equivalent antenna model outlined in Section 1 is coupled with the SCM method presented in Section 2. The random dimension is $d = 2$ with the antenna length and antenna radius modeled as random variables (RVs). Both RVs are prescribed with uniform distributions whose range is defined as follows:

$$\langle x_i \rangle \pm \langle x_i \rangle \cdot \mathrm{CF}, \quad i = 1, 2, \tag{10}$$

where $\langle x_i \rangle$ is the mean value of the input parameter and CF is the coefficient of variation. The mean value of the antenna length and radius is $L = 1.75$ m and $a = 5$ cm, respectively. The coefficient of variation CF is chosen as 5.71% for the first test case and 12% in the second case.

Since this model approximates the antenna as perfectly conducting, the results are given in terms of the induced current instead of the induced electric field which would be appropriate according to the latest updates in international standards and guidelines [11, 12]. However, the results are still valid and can be readily interpreted.

First, to test the convergence of the stochastic approach, the full tensor model was built with 3×3, 5×5, 7×7, and 9×9 collocation points in the case of CF = 5.71% and 12%. The results presented in Figure 2 exhibit a satisfactory convergence rate of the method. The change in the CF value does not deteriorate the convergence of the SCM. The chosen observation point is the middle point of the antenna which corresponds to the body waist. Similar results are obtained for other space coordinates. The size of confidence margins doubles when CF is changed from 5.71% to 12%.

The estimation of confidence intervals (CI) for the maximal possible value of current based on quantile estimation is given in Table 1. The results are obtained as MC simulation of the surrogate model from equation (3) with 10^6 samples. The shape of the corresponding probability density function is given in Figure 3 for both test cases. The maximal possible value of the current appears in the early time of response (within 5 ns), and it is within the recommended intervals.

The presented stochastic-deterministic model is simple in terms of stochastic dimension, since there are only two random input variables. However, the information on the influence of the input parameters to the output value deserves some merit. The impact factors I_1 and I_2 for the antenna length and radius, respectively, are calculated according to equation (9), and the results are depicted in Figure 4. It is worth noting that, although the impact of the antenna length, i.e., body height, is overwhelming throughout the simulation period, the antenna radius exhibits much higher influence in the early time behavior of the transient response. This is exactly the time period in which the current reaches its maximal possible value; hence, the radius is the parameter that has very high impact to maximum current. The mutual interaction between the two parameters is obviously very weak, as the summation of I_1 and I_2 adds up to 1 almost everywhere.

5. Concluding Remarks

A stochastic perspective for the exposure of human body to electromagnetic pulse radiation is presented. The human body is modeled as a straight thin-wire antenna whose length and radius are considered to be random variables with associated uniform distribution. A nonintrusive stochastic collocation method is used to propagate the uncertainty to the output transient current. The mean value along with the confidence margins is presented for the current values, and it is shown that the obtained values are inside the recommended ranges for the presented exposure scenario. The probability density function of the maximal value of the transient current is presented. The impact of each input variable is calculated, and it is shown that the radius of the antenna has much higher impact on the maximal current value than the length, while for the rest of the impulse duration, the antenna length is more significant. The results may be taken into account when designing the human equivalent antenna that is used to replace the real body in experimental dosimetry

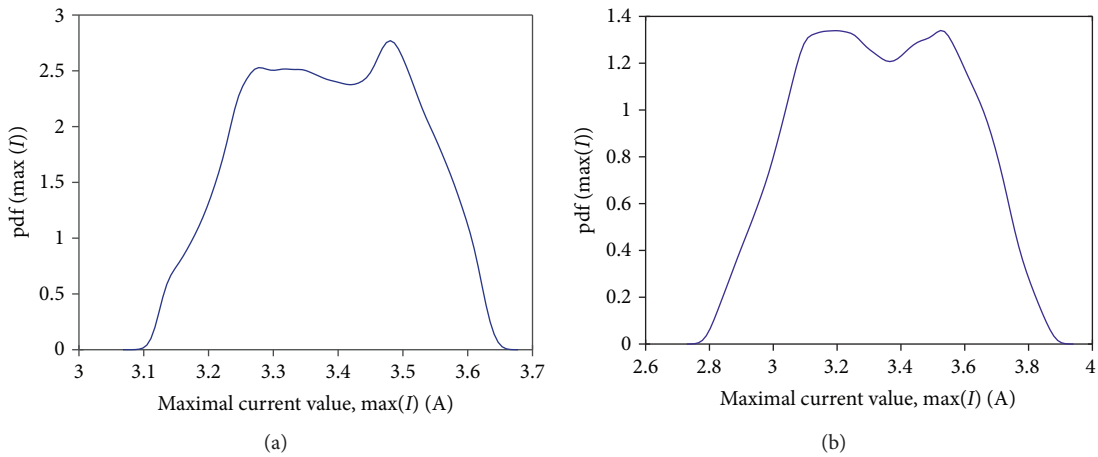

Figure 3: The probability density function of the maximal possible current value in the case of CF = 5.71% (a) and CF = 12% (b). The results are based on the MC sampling of the surrogate model from equation (3) with 106 samples.

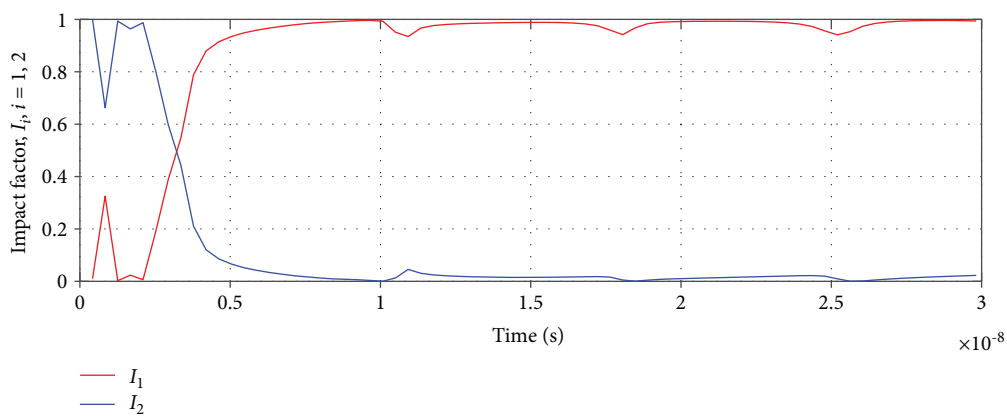

Figure 4: The impact factor of the antenna parameters: I_1 represents the influence of the antenna length and I_2 represents the influence of the antenna radius.

measurements. Also, the stochastic-deterministic approach offers a new perspective providing a deeper understanding of the influence of input parameters to the output values.

A first step to enhance the time domain cylindrical model is to include the body permittivity and conductivity into a deterministic and stochastic analysis, respectively. Furthermore, a future work would likely deal with anatomically realistic time domain body representations which were already developed by the authors in the frequency domain.

Data Availability

The data used to support the findings of this study are included within the article.

Conflicts of Interest

The authors declare that they have no conflicts of interest.

References

[1] D. Poljak, "Postprocessing of the human body response to transient electromagnetic fields," *Progress In Electromagnetics Research*, vol. 49, pp. 219–238, 2004.

[2] R. W. P. King, "Fields and currents in the organs of the human body when exposed to power lines and VLF transmitters," *IEEE Transactions on Biomedical Engineering*, vol. 45, no. 4, pp. 520–530, 1998.

[3] R. W. P. King, "A review of analyticaly determined electric fields and currents induced in the human body when exposed to 50-60 Hz electromagnetic fields," *IEEE Transactions on Antennas and Propagation*, vol. 52, no. 5, pp. 1186–1192, 2004.

[4] B. Kibret and A. K. Teshome, "Characterizing the human body as a monopole antenna," *IEEE Transactions on Antennas and Propagation*, vol. 63, no. 10, pp. 4384–4392, 2015.

[5] B. Kibret and A. K. Teshome, "Cylindrical antenna theory for the analysis of whole-body averaged specific absorption rate," *IEEE Transactions on Antennas and Propagation*, vol. 63, no. 11, pp. 5224–5229, 2015.

[6] J. Wiart, *Radio-Frequency Human Exposure Assessment: from Deterministic to Stochastic Methods*, John Wiley & Sons, 2016.

[7] E. Chiaramello, M. Parazzini, S. Fiocchi, P. Ravazzani, and J. Wiart, "Assessment of fetal exposure to 4G LTE tablet in realistic scenarios: effect of position, gestational age, and frequency," *IEEE Journal of electromagnetics, RF and Microwaves in Medicine and Biology*, vol. 1, no. 1, pp. 26–33, 2017.

[8] Y. Pinto and J. Wiart, "Surrogate model based on polynomial chaos of indoor exposure induced from a WLAN source," in *2017 XXXIInd General Assembly and Scientific Symposium of the International Union of Radio Science (URSI GASS)*, Montreal, QC, Canada, August 2017.

[9] X. Cheng and V. Monebhurrun, "Application of different methods to quantify uncertainty in specific absorption rate calculation using a CAD-based mobile phone model," *IEEE Transactions on Electromagnetic Compatibility*, vol. 59, no. 1, pp. 14–23, 2017.

[10] M. A. Drissaoui, S. Lanteri, P. Leveque, and F. Mu, "A stochastic collocation method combined with a reduced basis method to compute uncertainties in numerical dosimetry," *IEEE Transactions on Magnetics*, vol. 48, no. 2, pp. 563–566, 2012.

[11] ICNIRP, "ICNIRP guidelines for limiting exposure to time-varying electric and magnetic fields (1 Hz – 100 kHz)," *Health Physics*, vol. 99, no. 6, pp. 818–836, 2010.

[12] I. S. C. TM, *IEEE Standard for Safety Levels with respect to Human Exposure to Electromagnetic Fields, 0–3 kHz*, The Institute of Electrical and Electronics Engineers, Inc., New York, NY, USA, 2002.

[13] D. Xiu, "Fast numerical methods for stochastic computations: a review," *Communications in Computational Physics*, vol. 5, no. 2-4, pp. 242–272, 2009.

[14] J. Bai, G. Zhang, D. Wang, A. P. Duffy, and L. Wan, "Performance comparison of the SGM and the SCM in EMC simulation," *IEEE Transactions on Electromagnetic Compatibility*, vol. 58, no. 6, pp. 1739–1746, 2016.

[15] R. W. P. King and S. S. Sandler, "Electric fields and currents induced in organs of the human body when exposed to ELF and VLF electromagnetic fields," *Radio Science*, vol. 31, no. 5, pp. 1153–1167, 1996.

[16] O. P. Gandhi, "Some numerical methods for dosimetry: extremely low frequencies to microwave frequencies," *Radio Science*, vol. 30, no. 1, pp. 161–177, 1995.

[17] D. Poljak and Y. F. Rashed, "The boundary element modelling of the human body exposed to the ELF electromagnetic fields," *Engineering Analysis with Boundary Elements*, vol. 26, no. 10, pp. 871–875, 2002.

[18] D. Poljak, *Advanced Modelling in Computational Electromagnetic Compatibility*, John Wiley and Sons, New York, NY, USA, 2007.

[19] O. P. Gandhi and E. Aslan, "Human equivalent antenna for electromagnetic fields," US Patent 5394164, 1995.

[20] D. Poljak, C. Y. Tham, O. Gandhi, and A. Sarolic, "Human equivalent antenna model for transient electromagnetic radiation exposure," *IEEE Transactions on Electromagnetic Compatibility*, vol. 45, no. 1, pp. 141–145, 2003.

[21] A. Susnjara and D. Poljak, "An efficient deterministic-stochastic model of the human body exposed to ELF electric field," *International Journal of Antennas and Propagation*, vol. 2016, Article ID 6153620, 8 pages, 2016.

[22] J. Y. Chen and O. P. Gandhi, "Currents induced in an anatomically based model of a human for exposure to vertically polarized electromagnetic pulses," *IEEE Transactions on Microwave Theory and Techniques*, vol. 39, no. 1, pp. 31–39, 1991.

[23] L. Mathelin and M. Y. Hussaini, "A stochastic collocation algorithm for uncertainty analysis," Tech. Rep. NASA/CR-2003-212153, NAS 1.26:212153, 2003, NASA STI report series.

[24] I. Babuuska, F. Nobile, and R. Tempone, "A stochastic collocation method for elliptic partial differential equations with random input data," *Society for Industrial and Applied Mathematics*, vol. 52, no. 2, pp. 317–355, 2010, 10.1137/100786356.

[25] S. Lalléchère, P. Bonnet, I. El Baba, and F. Paladian, "Unscented transform and stochastic collocation methods for stochastic electromagnetic compatibility," in *Computational Electromagnetics International Workshop (CEM)*, Izmir, 2011.

[26] P. Li and L. J. Jiang, "Uncertainty quantification for electromagnetic systems using ASGC and DGTD method," *IEEE Transactions on Electromagnetic Compatibility*, vol. 57, no. 4, pp. 754–763, 2015.

[27] N. Agarwal and N. R. Aluru, "Stochastic analysis of electrostatic MEMS subjected to parameter variations," *Journal of Microelectromechanical Systems*, vol. 18, no. 6, pp. 1454–1468, 2009.

[28] A. Saltelli, P. Annoni, I. Azzini et al., "Variance based sensitivity analysis of model output. Design and estimator for the total sensitivity index," *Computer Physics Communications*, vol. 181, no. 2, pp. 259–270, 2010.